

BARBARA GENOCCHI

# Astrocyte regulation of neuronal activity in *vitro* and *in silico*

From computation to data analysis



BARBARA GENOCCHI

Astrocyte regulation of neuronal activity  
*in vitro* and *in silico*

From computation to data analysis

ACADEMIC DISSERTATION

To be presented, with the permission of  
the Faculty of Medicine and Health Technology  
of Tampere University,  
for public discussion in the Auditorium F114  
of the Arvo Building, Arvo Ylpön katu 34, Tampere,  
on 22 November 2023 at 12 o'clock.

## ACADEMIC DISSERTATION

Tampere University, Faculty of Medicine and Health Technology  
Finland

<i>Responsible supervisor and Custos</i>	Professor Jari Hyttinen Tampere University Finland	
<i>Supervisor</i>	Assistant Professor Kerstin Lenk Graz University of Technology Austria	
<i>Pre-examiners</i>	Professor Michael van Putten University of Twente Netherlands	PhD João Oliveira University of Minho Portugal
<i>Opponent</i>	Professor Ulrich Egert Albert-Ludwig-Universität Freiburg Germany	

The originality of this thesis has been checked using the Turnitin OriginalityCheck service.

Copyright ©2023 author

Cover design: Roihu Inc.

ISBN 978-952-03-3138-2 (print)

ISBN 978-952-03-3139-9 (pdf)

ISSN 2489-9860 (print)

ISSN 2490-0028 (pdf)

<http://urn.fi/URN:ISBN:978-952-03-3139-9>



ClimateCalc CC-000025FI  
PunaMusta Printing

Carbon dioxide emissions from printing Tampere University dissertations have been compensated.

PunaMusta Oy – Yliopistopaino  
Joensuu 2023



# ACKNOWLEDGEMENTS

The studies presented in this thesis were carried out at the Faculty of Medicine and Health Technology at Tampere University (formerly Tampere University of Technology) between the years 2017 and 2023.

I would like to express my gratitude to the financial supporters of my work: the BioMEP doctoral programme funded by the European Union's Horizon 2020 research and innovation programme under the Marie Skłodowska-Curie grant agreement No 713645, the Pirkanmaa Regional Fund of the Finnish Cultural Foundation and the doctoral programme at the Faculty of Medicine and Health Technology, Tampere University.

My greatest gratitude goes to my supervisor, Professor Jari Hyttinen, leader of the Computational Biophysics and Imaging Group, for believing in me and giving me the opportunity to start this path, and for the support through all the years. I also would like to thank my scientific supervisor Assistant Professor Kerstin Lenk, TU Graz, for the help, support, and advice during my PhD. I would also like to express my gratitude to PhD Hugues Berry, INRIA Lyon (France), and Prof. Katja Nieweg, Philipps-Universität Marburg (Germany), for hosting me in their groups and giving me the opportunity to develop new skills, and to Professor Michel van Putten and to PhD João Filipe Oliveira for their valuable comments that helped me improve this thesis.

Thank you to all the members of the CBIG group, for the lunches and the laughs which brightened many dark winter days. Among my group colleagues, a special thank you goes to Annika Ahtiainen, for the chit-chatting and for all the hours spent in the lab to provide the data used in this thesis, to Docent Jarno Tanskanen for the endless availability and help, and to all the coauthors of the papers of this thesis, for your inputs and help in shaping this project.

To all the people I met during these years in Tampere, thank you for being part of my life in one way or another. I am particularly grateful for meeting my Italian

family in Tampere and for the laughs, the dinners, the gossip, and the drama which made my time in Tampere memorable. In particular, thank you to Michelangelo for lending me half of his desk, but especially a hand when I most needed it. Thank you to Chiara and Sergio for being the sister and the brother I never had.

Thank you to my parents for always believing in me, rooting for me, and letting me be wrong to then say "told you": if now I am the person I am, most of the merit (or blame) is yours.

And last but not least, a big colorful thank you goes to my husband Francesco. Thank you for brightening the last ten years of my life with your presence and your jokes (sometimes questionable), turning every bad day into a good day with just a smile and a hug. Thank you for being my best fan and for pushing me when I thought I couldn't do something. How was it? *There is always a great man behind a great woman!*

We shaped our life by traveling the world together, leaving in five different countries, and growing together. Looking back, I wouldn't have it any other way!

Tampere, September 2023

Barbara

# ABSTRACT

The human brain is composed of more than 86 billion neurons, interconnected in synapses and in constant communication with other cell types, like for example the astrocytes. Astrocytes shape the cytoarchitecture of the brain and provide metabolic support to the neurons. Furthermore, they promote synapse formation, maturation, and elimination by exchanging transmitters with them. Thus, astrocytes can modulate neuronal activity. Impairments in astrocytes may lead to hyper- or hypoactivity and thus to diseases like Alzheimer's and epilepsy. Computational models became more commonly used to better understand unanswered questions on the astrocytic modulation of neuronal activity.

This thesis combines computational studies and *in vitro* experiments. We first utilized computational methods to study how astrocyte network topology affects neuronal spiking and synchronization in neuron-astrocyte networks. Then, we examined *in vitro* how astrocytic ionic and gliotransmitter regulation controls neuronal activity. In the computational studies, we extended a computational model previously developed in our group to: i) test the role of gap junction uncoupling in hyperactivity control, ii) compare 2D and 3D co-culture network topology effects on neuronal activity and iii) compare the results obtained from the model with experimental results obtained using microelectrode arrays recording of neuron-astrocyte co-cultures with fixed relative amounts of neurons and astrocytes. In the second part of the thesis, which is focused on the *in vitro* experiments conducted, we explored the role of astrocytes in counteracting the effect of convulsant drugs applied to the different *in vitro* cultures. Furthermore, we studied how astrocytes and extracellular ionic clearance affect the spike shape and the activity patterning during development.

The results of the computational studies suggest that the topology of both the astrocyte and neuron networks is crucial for the activity propagation in the neurons. The topology, in fact, affects how the transmitters are distributed in the astrocytes, resulting in an up- or down-regulation of the activity in the neighboring

neurons. The experimental studies, moreover, show that blocking the activity of either voltage-gated  $K^+$  channels with 4AP or of  $GABA_A$  receptors with gabazine resulted in effects that depended on the particular relative proportions of neuron and astrocytes in the co-culture. This suggested that the amount of astrocytes in the networks is fundamental for proper control of alterations of the ionic and transmitter homeostasis.

The collective findings of this thesis indicate that indeed astrocytes have a regulatory effect on neuronal activity, probably by eliminating ions and gliotransmitters from the extracellular space, thereby controlling the neuronal action potentials, signal propagation within the network, and synchronicity and patterning of the signals. Astrocytes induced desynchronization in the signals and led to less patterned signals; *in vivo* this effect might be reflected in a reduced seizure susceptibility. This thesis presents the first studies where the cultures had defined relative neuron-astrocytes proportions. Overall, our studies stress the importance of considering the ratio of astrocytes in the cultures when testing new drugs or in general in co-culture experiments.

# TIIVISTELMÄ

Yli 86 miljoonaa synapsein yhdistettyä hermosolua muodostaa ihmisäivot jatkuvassa vuorovaikutuksessa muiden solutyyppeiden, kuten astroosyyttien kanssa. Astroosyytit ovat hermotukisoluja, jotka muovaavat aivojen solurakennetta, tarjoavat aineenvaihdunnallista tukea hermosoluille sekä edistävät synapsien muodostumista, kypsymistä ja poistoa välittäjäaineiden avulla. Täten astroosyytit vaikuttavat merkittävästi hermosolujen sähköiseen aktiivisuuteen. Astroosyyttien toimintahäiriöt voivat johtaa yliaktiivisuuteen (hyperaktiivisuus) tai aliaktiivisuuteen (hypoaktiivisuus) ja siten myös hermostollisiin sairauksiin, kuten Alzheimerin tautiin ja epilepsiaan.

Lakennallisia malleja hyödynnetään yhä enemmän tutkittaessa astroosyyttien vaikutuksia hermosolujen sähköiseen aktiivisuuteen.

Tässä väitöskirjatyössä yhdistyvät laskennalliset menetelmät ja *in vitro*-laboratoriokokeet. Ensinnäkin hyödynsimme laskennallisia menetelmiä tutkiaksemme, miten astroosyyttien verkoston topologia vaikuttaa hermosolujen sähköiseen aktiivisuuteen ja sen ja sen synkronisuuteen hermosolu-astroosyyttiverkostossa. Seuraavaksi tutkimme *in vitro* laboratoriokokeilla, miten astroosyyttien ioni- ja välittäjäainesäätely ohjaa hermosolujen aktiivisuutta. Laajensimme jo aiemmin ryhmässämme kehitettyä laskennallista mallia tutkiaksemme: i) aukkoliitosten roolia hyperaktiivisuuden säätelyssä, ii) kaksi- ja kolmiulotteisen verkkotopologian vaikutusta hermosolujen aktiivisuuteen, iii) laskennallisten mallien ja laboratoriokokeiden vertailua, hyödyntäen erityisiä hermosolu-astroosyyttiviljelmiä mikroelektrodimatriisialustalla (MEA).

Väitöskirjatyön toisessa osassa, jossa keskityttiin laboratoriotuloksiin, tutkimme astroosyyttien roolia lääkeaineiden neutraloimisessa, jotka aiheuttavat hermosoluissa konvulsivisia vaikutuksia (lisääntynyttä sähköistä aktiivisuutta tai kouristuksia). Näitä lääkkeitä annettiin suoraan erilaisiin *in vitro*-viljelmiin. Tutkimme, miten astroosyytit ja niiden solunulkoinen ionien puhdistus vaikuttavat hermosolujen aktiopotentiaalien muotoon ja aktiivisuuden kaavoittumiseen kehityksen aikana.

Laskennalliset tulokset osoittavat, että sekä astroosyyttien että hermosolujen verkos-

ton rakenteella on merkittävä rooli hermosolujen toimintapotentialin leviämisessä hermoverkostossa. Itse asiassa tämä rakenne vaikuttaa siihen, kuinka astrozyytit jakelevat välittäjäaineita, mikä puolestaan vaikuttaa niiden lähialueen hermosolujen aktiivisuuden lisääntymiseen tai vähenemiseen. Lisäksi laboratorionkokeet osoittavat, että hermosolujen sähköinen vaste estettäessä jänniteherkkien kaliumkanavien toimintaa 4-aminopyridiinillä, tai gamma-aminovoihappo tyyppin A reseptoreja gabatsiinilla, riippuu astrozyyttien määrästä viljelmissä. Tämä viittaa siihen, että astrozyyttien lukumäärä hermoverkostossa on olennaisen tärkeä ioni- ja välittäjäainetasapanon ylläpitämiselle.

Väitöskirjan yhteenvedona voidaan todeta, että astrozyytit todennäköisesti säätelevät hermosolujen toimintaa poistamalla ioneja ja välittäjäaineita solunulkoisesta tilasta, mikä puolestaan säätelee hermosolujen aktiopotentiaaleja ja niiden etenemistä hermoverkostossa. Astrozyytit aiheuttavat signaalien eriaikaistumista, mikä voi viitata in vivo ihmis- ja eläinkokeissa vähentyneeseen alttiuteen epileptisille kohtauksille. Tämä väitöskirjatyö esittelee ensimmäiset tutkimukset, jossa on käytetty tarkasti määriteltyjä viljelmiä eri hermosolujen ja astrozyyttien määrällisillä suhteilla. Kaiken kaikkiaan tämä työ korostaa hermosolujen ja astrozyyttien suhteellisten osuuksien huomioimisen tärkeyttä uusien lääkeaineiden arvioitaessa ja yleisesti yhteisviljelmiä hyödyntävissä laboratorionkokeissa.

# CONTENTS

1	Introduction . . . . .	27
2	Literature review . . . . .	31
2.1	Neuron physiology . . . . .	31
2.2	Astrocyte physiology . . . . .	32
2.3	Tripartite synapse . . . . .	34
2.4	Astrocytes and epilepsy . . . . .	37
2.4.1	Epilepsy . . . . .	37
2.4.2	Role of the astrocytes in epilepsy . . . . .	38
2.5	Techniques to monitor neuronal and astrocytic activity . . . . .	40
2.5.1	Fluorescence microscopy and immunostaining . . . . .	40
2.5.2	Microelectrode Arrays . . . . .	41
2.5.3	Calcium imaging . . . . .	44
2.6	Computational modeling of neuron-astrocyte networks in health and disease . . . . .	45
2.6.1	Neuron-astrocyte network models . . . . .	45
3	Aims of the study . . . . .	49
4	Methods overview . . . . .	51
5	Aim 1: Computational study of the astrocyte network topology effects of neuronal activity . . . . .	53
5.1	Methods . . . . .	53
5.1.1	Computational description of the neuron-astrocyte net- work and its pathways . . . . .	53
5.1.2	Data acquisition . . . . .	60
5.1.3	Data analysis . . . . .	61

5.2	Results . . . . .	63
5.2.1	Gap junction uncoupling increases spike and burst rate .	63
5.2.2	Network topology comparison between the planar and the 3D networks . . . . .	65
5.2.3	Comparison between the activity and the topology of in vitro and in silico neuron-astrocyte networks . . . . .	70
6	Aim 2: Experimental study of the astrocytic ionic clearance and its effects on neuronal spiking . . . . .	77
6.1	Methods . . . . .	77
6.1.1	Experimental data acquisition. . . . .	77
6.1.2	Data analysis . . . . .	81
6.2	Results . . . . .	90
6.2.1	Astrocyte response to chemically induced hyperactivity .	90
6.2.2	Neuronal signal development and control in co-cultures. .	96
7	Discussion . . . . .	101
7.1	Higher astrocyte presence reduces astrocytic activation . . . . .	101
7.2	Astrocytes and the plating conditions affect the network topology	102
7.3	Astrocytes prevent neuronal hyperactivity induced by extracellu- lar $K^+$ . . . . .	103
7.4	Astrocytes increase chaotic behaviors in neuronal spiking . . . . .	104
7.5	Astrocytes regulate neuronal depolarization and repolarization . .	105
8	Conclusions . . . . .	109
	References . . . . .	111
	Publication I . . . . .	129
	Publication II . . . . .	139
	Publication III . . . . .	147
	Publication IV . . . . .	157
	Publication V . . . . .	183



*List of Figures*

2.1 A) Graphical description of a neuron. The soma contains the nucleus, and several branches extend from the soma. The dendrites transfer information, in the shape of electrical signals to the soma, while the axon transfers them from the soma to the axon terminals. B) Chemical description of the saltatory conduction in the nodes of Ranvier and through the myelin sheaths. C) Description of an action potential and its phases. All the original images were licensed under a Creative Commons Attribution-ShareAlike 3.0 Unported License. . . . . 33

2.2 Fluorescence imaging of (a) fibrous astrocytes from rodents and humans, and (b) protoplasmic astrocytes from rodents and humans. . . . 35

2.3 Glutamate and ATP released from the presynaptic neuron activate mGluR and PY2R, which in turn lead to the release of  $Ca^{2+}$  from intracellular stores via an  $IP_3$ -evoked mechanism. The resultant increase in  $Ca^{2+}$  levels stimulates the release of glutamate, GABA, ATP, and D-serine into the synaptic cleft. Reproduced with permission from: Bazargani and Attwell, 2016b. . . . . 37

2.4 Astrocytes dysfunctions scheme in mesial temporal lobe epilepsy with hippocampal sclerosis (MTLE-HS). 1) Down-regulation in Kir4.1 channels lead to an increased  $K^+$  extracellular concentration. 2) Gap-junctions impairment leads to a dysregulated redistribution of  $K^+$  ions. 3) Dislocated or decreased water channels lead to impaired  $K^+$  buffering. 4) Reduced expression of EAAT1 and EAAT2, glutamate transporters, reduced glutamate uptake leading to an increased extracellular glutamate concentration. 5) Loss of GS lead to reduced synthesis and release of GABA. Reproduced with permission from: Coulter and Steinhäuser, 2015. . . . . 39

2.5	Immunostaining and fluorescence imaging. When a primary and a secondary antibody are bound to a protein antigen, these can be imaged with a fluorescence microscope. The secondary antibody is bound with a fluorophore and selecting the right excitation wavelength with the excitation filter allows to excite the fluorophore and elicits an emission in a longer wavelength which will be detected by the detector. Figure created with BioRender.com. . . . .	42
2.6	Ca <sup>2+</sup> imaging. Chemical Ca <sup>2+</sup> indicators when injected in the cell culture can specifically bind Ca <sup>2+</sup> ions. Chemical Ca <sup>2+</sup> indicators are bound to a fluorophore and when binding Ca <sup>2+</sup> ions they change their fluorescence intensity. By mapping the fluorescence intensity over time it is possible to study the response of the cell culture to some manipulation. Figure created with BioRender.com. . . . .	44
4.1	Design of the computational studies which will be explained in Chapter 5. Created with BioRender.com. . . . .	52
4.2	Design of the experimental studies described in Chapter 6. Created with BioRender.com. . . . .	52
5.1	Pathway scheme of the INEXA model. The colored boxes describe the elements comprised in the model and which original model was used to describe these parts. The model consists of multiple excitatory synapses, each of which can be connected to an astrocyte. The communication pathways of each individual tripartite synapse in the network are illustrated in the figure. The pre- and post-synaptic spiking were modeled similarly to the INEX model (depicted in blue boxes). The Tsodyks-Markram synapse model (in orange) and De Pittà's astrocyte gliotransmitter model (in red) were added to the spiking generation. The local astrocyte Ca <sup>2+</sup> dynamics (in green) trigger gliotransmission to the synapse. The Ca <sup>2+</sup> signaling was modeled according to the UAR model (in violet) by Lallouette et al. The local and global Ca <sup>2+</sup> dynamics stimulate the release of GABA into the extracellular space by the astrocyte (in yellow) to restrict the spiking of nearby post-synaptic neurons. . . . .	54

5.2	A) Planar topology of the neuron-astrocyte network. Neurons are displayed as green dots and astrocytes as red triangles. Astrocyte-astrocyte connections are shown as red links. B) Connection probability rules used in the model. Neuron-neuron connections (in red) follow a Gaussian probability based on the distance between the neurons. Astrocyte-neuron connection probability (in blue) follows a Gaussian distribution until it reaches a max distance limitation which drops the probability to zero. Astrocyte-astrocyte connections (in green) are formed only if the distance between the two cells is comprised in the limits. Illustrations reproduced with permission from: Lenk et al., 2020. . . .	55
5.3	Comparison between the planar (left) and the 3D (right) network structures in the neuron-astrocyte computational model INEXA. Neurons are in red and astrocytes are shown in blue, together with their connections. Figure reproduced with permission from <b>Publication II</b> . . .	60
5.4	Astrocyte networks couplings in neuron-astrocyte networks. A) Graphic representation of one of the ten networks created for each coupling level, from fully uncoupled to high connectivity. Astrocytes are displayed as diamonds in magenta, with their connections also shown in magenta. Neurons are represented by blue dots. Neuronal connections are not displayed for image clarity. B) Average gap junctions of each astrocyte for each of the ten runs for each coupling condition. C) Number of connected synapses on average to each of the astrocytes in the different coupling conditions. . . . .	64
5.5	Gap junction coupling activity analysis. The figure shows the spike rate (spikes/minute), burst rate (bursts/minute), burst duration (ms), spikes/burst, and astrocyte activation for the three simulated noise levels. The results for the low noise case are displayed in violet, for the medium noise in blue, and for the high noise in yellow. * $p < 0.05$ ; ** $p < 0.01$ ; *** $p < 0.001$ ; **** $p < 0.0001$ . . . . .	66
5.6	Comparison between the graph analysis conducted on the astrocytic networks and the neuronal activity features for the different astrocytic link distances $d$ simulated. $k$ represent the astrocytic mean degree, $L$ describes the mean shortest path Figure reproduced with permission from <b>Publication II</b> . . . . .	70

5.7 Network topologies with mean degree  $k$  for the two distances  $d = 70$  m and  $d = 120$  m. The degree of the node is represented by the dimension and the color of the node itself. Light blue bars between the nodes represent the links. The black arrows in  $d = 120$  m represent the hub astrocytes. Figure reproduced with permission from **Publication II**. . . . . 70

5.8 Spike rate graph for the neuronal network for the six different max astrocyte connection distances. The neuronal topology here shown was kept constant. The nodes represent the neurons, and their color and dimension are the spike rate expressed in spikes/min. Axes are in  $\mu$ m. Figure modified with permission from **Publication II**. . . . . 71

5.9 Comparison between experimental data and simulated data. A) Spike rate (spikes/min), and B) burst rate (bursts/min) for NS and the co-cultures. Experimental data is shown in solid colors, while simulated data is shown with the square patterned filling. Statistical comparisons between the experimental cultures are shown in black, while the comparisons between experimental and simulated data are in red. <sup>ns</sup>  $p > 0.05$ ; \*  $p < 0.05$ ; \*\*  $p < 0.01$ ; \*\*\*  $p < 0.001$ ; \*\*\*\*  $p < 0.0001$ . . . . . 72

5.10 Comparison between the graph analysis features in the experimental data and simulated data. A) Nodes, B) mean degree, and C) mean shortest path for NS and the co-cultures. Experimental data is shown in solid colors, while simulated data is shown with the square patterned filling. Statistical comparisons between the experimental cultures are shown in black, while the comparisons between experimental and simulated data are in red. <sup>ns</sup>  $p > 0.05$ ; \*  $p < 0.05$ ; \*\*  $p < 0.01$ ; \*\*\*  $p < 0.001$ ; \*\*\*\*  $p < 0.0001$ . . . . . 73

5.11 Pearson's correlation analysis  $R$  in the experimental data to determine the relationship between the spike rate and the degree of the electrodes. Each electrode on the MEAs is represented by a circle, where the size of the circle represents the node centrality based on the cross-correlation values of the edges of the node. Linear regression models with the relative  $r^2$  are depicted by solid lines. Figure reproduced with permission from **Publication III**. . . . . 74

5.12	Astrocyte network topology graph analysis. A) Mean degree (i.e., the gap junctions), B) the mean shortest path, and C) the mean number of times in which an astrocyte entered the active state. <sup>ns</sup> p > 0.05; * p < 0.05; ** p < 0.01; *** p < 0.001; **** p < 0.0001. Figure reproduced with permission from <b>Publication III</b> .. . . . .	75
5.13	Activity response to the astrocyte network topology. The figure displays the response of activity to the topology of the astrocyte network. It depicts 60 selected neurons as dots, with solid blue lines indicating the neuronal connections based on cross-correlation (edge weight > 0.65). The dot diameter indicates the mean degree of the neuron, while the dot color represents the spike rate expressed in spikes/min and ranges from blue (low) to green (high). The astrocytes are shown in a diamond shape, and their gap junctions are represented by dot-dashed red lines. The color of the diamond reflects the astrocyte activation, defined as the number of times the particular astrocyte was activated and ranges from red (low) to yellow (high). The size of the diamond indicates the degree of the astrocyte. Figure reproduced with permission from <b>Publication III</b> .. . . . .	76
6.1	Graphical description of the cell plating protocols used in <b>Publication III-V</b> . Astrocytes were plated and left in the incubator until confluent. When they reached confluency astrocytes were treated with ara-C for 5 days. At this point in <b>Publication III-IV</b> astrocytes and neurons were mixed together based on the desired cell proportions and then plated. In <b>Publication V</b> the neurons were plated first and left settling for 1 hour and then the different amounts of astrocytes were plated based on the desired final neuron-astrocyte ratio. Figure created with BioRender.com. . . . .	79
6.2	Graphical description of the used protocol to stimulate the MEAs and register the drug-induced activity. . . . .	80
6.3	Image analysis steps used for the cell labeling and neuron and astrocyte detection. Figure created with BioRender.com . . . . .	82
6.4	Graphical representation of the selection rule for the repetitive NBs. Figure modified from <b>Publication IV</b> .. . . . .	85

6.5 **Waveform selection and features.** A) Waveform features used for the waveform analysis (modified from S. H. Sun et al., 2021); B) decision tree of the algorithm used for the waveform detection; C) Examples of the five possible waveforms: regular spiking, fast-spiking, triphasic spiking, compound spiking, and positive spiking. . . . . 89

6.6 Cell detection and count from immunolabeled images. a) relative ratios of neurons (in green), and astrocytes (in magenta) in the plated co-cultures. b) representative image of the neuronal detection (in green), where the non labeled nuclei are left in magenta. c) representative image of the astrocyte detection (in cyan), from the non labeled nuclei left from image b. . . . . 91

6.7 Activity response to the injection of 4-AP and gabazine. a) Representative raster plots of 10 electrodes of two MEAs per culture condition, at baseline (left) and after the drug application (4-AP top right, gabazine bottom right). b) SR (spikes/minute), c) BR (bursts/minute), d) the percentage of spikes in bursts, and e) IBI (ms), of the MEAs for NS, 90/10, 80/20, 70/30, and 50/50 at baseline (in grey), after 4-AP injection (in purple), and after gabazine injection (in green). \*  $p < 0.05$ ; \*\*  $p < 0.01$ . Red crosses represent the population outliers. . . . . 93

6.8 Neuronal network synchronization at baseline and after chemical stimulation. a) Correlation weights of the different cultures at baseline. b) representative correlation heatmap of one MEA from the 80/20 co-culture at baseline (bottom left half), and after 4-AP stimulation (upper right half). c) representative correlation heatmap of one MEA from the 80/20 co-culture at baseline (bottom left half), and after gabazine stimulation (upper right half). The heatmaps squares represent the correlation weight of the channel pairs; the weights span from 0 (deep blue) to 1 (dark red). Excluded channels are shown in grey. d) violin plots of the differences between the stimulated correlation weight of each channel pair and its baseline value; MEAs stimulated with 4-AP are shown in purple, and those stimulated with gabazine in green. The pink stars represent those groups with high Glass' delta effect size. \*  $p < 0.05$ ; \*\*  $p < 0.01$ ; \*\*\*\*  $p < 0.0001$ . . . . . 94

- 6.9 Gabazine-induced delayed effects on the synchronization. a) Summed spiking activity of the channels of representative MEAs in NS (blue), 90/10 (yellow), 80/20 (purple), 70/30 (green), and 50/50 (black) stimulated with 4-AP, and b) with gabazine. The network bursts (NBs) are displayed in orange or in blue. Blue dots represent highly repetitive NBs, the orange dots represent the others. When both are present the NB in the legend shows the sums of the two. The red vertical lines represent the time point at which the first NB was found. c) Shows the delays for the cell culture types in the appearance of the first NB of the highly repetitive series for the gabazine (in green), and for 4-AP (in purple), when the NB series was present. . . . . 95
- 6.10 Activity development analysis. A) spike rate (Hz), B) burst rate (Hz), C) burst duration in ms, D)% spikes in bursts, E) inter-spikes intervals in ms, and F) inter-bursts intervals in ms for NS (in blue), 80/20 (in magenta) and 50/50 (in yellow) co-cultures for 14, 19 and 28 DIV. Subfigures C, E, and F are centered where the majority of the results were located, leaving some outliers outside the figure. *ns* - non significant; \* $<0.05$ ; \*\* $<0.01$ ; \*\*\* $<0.001$ ; \*\*\*\* $<0.0001$ .. . . . 97
- 6.11 Complexity-Entropy planes and surrogates analysis. A, B, and C) show the complexity-entropy values of the single channels in the cultures at DIV 14, DIV 19, and DIV 28, respectively. NS are shown in blue, 80/20 in magenta, and 50/50 in yellow. A1, B1, and C1) present the empirical CDF of the complexity values of the cultures on each measurement day in vitro, compared to the empirical CDF of the complexity levels of the relative generated surrogates (subscript *s* in the labels). The NS<sub>*s*</sub> are shown in light blue, the 80/20<sub>*s*</sub> in pink, and the 50/50<sub>*s*</sub> in light yellow. A2, B2, and C2) show the empirical CDF of the entropy measures of the cultures on each day in vitro, compared to the empirical CDF of the entropies of the relative generated iAAFT surrogates. The original complexity and entropy values from the C-E planes, and the entropy and complexity empirical CDFs were compared at each DIV with a two-sample Kolmogorov-Smirnov test. . . . . 99

6.12 Spike waveform analysis. A, B, and C) Prevalence of the spike waveforms in the NS, 80/20, and 50/50 co-cultures (blue, magenta, and yellow) at 14, 19, and 28 DIV, respectively. RS - regular spiking, FS - fast-spiking, CS - compound spiking, TS - triphasic spiking, and PS - positive spiking. D and E) Spike amplitude in V at 14, 19, and 28 DIV for the negative and positive spikes, respectively. F) Spike duration in ms, counted as the time from the spike peak to the 2<sup>nd</sup> peak (or to the end of the time window in absence of the 2<sup>nd</sup> peak). G and H) Positive and negative slopes, respectively, to reach the spike peak for the NS, 80/20 and 50/50 co-cultures at 14, 19, and 28 DIV. *ns* - non significant; \* <0.05; \*\* <0.01; \*\*\* <0.001; \*\*\*\* <0.0001. . . . . 100



List of Tables

5.1 Parameters used to force the coupling conditions in the simulations. . . . . 59

5.2 Comparison of the characteristics of the planar and the 3D networks. Table modified with permission from **Publication II**. . . . . 60

5.3 Numerical results for the three simulated noise levels. For each noise level are shown: SR, spike rate (spikes/minute); BR, burst rate (bursts/minute); BD, burst duration (ms); spikes/burst, and astrocyte activation. The results are expressed as mean  $\pm$  standard deviation. . . . . 65

5.4 Topological features of the two network configurations, planar and 3D. The features are subdivided into those of the neuronal network in the first section (N-N network); those of the astrocyte network in the middle section (A-A network); and, those for the neuron-astrocyte network in the last section (A-N network). Table modified from **Publication II**. . . . . 67

5.5 Graph analysis comparison for the planar and the 3D networks.  $k$  and  $L$  are displayed with mean and standard deviation over all astrocytes.  $N_{act}$  has the mean and standard deviation calculated over all the ten simulation runs. Table modified from **Publication II**. . . . . 68

5.6 Activity comparison between the planar and the 3D networks. Spike rate, burst rate, and burst duration are displayed with mean and standard deviation over the ten simulation runs. Table modified from **Publication II**. . . . . 68



# GLOSSARY

4-AP	4-aminopyridine
50/50	50% neurons / 50% astrocytes co-culture
70/30	70% neurons / 30% astrocytes co-culture
80/20	80% neurons / 20% astrocytes co-culture
90/10	90% neurons / 10% astrocytes co-culture
A-N network	Astrocyte-neuron network
A-A network	Astrocyte-astrocyte network
AP	Action potential
AQP4	Aquaporin-4
ara-C	Cytosine b-D-arabinofuranoside
ATP	Adenosine triphosphate
BD	Burst duration
BR	Burst rate
BW	Black-and-white
CDF	Cumulative distribution function
C-E	Complexity-entropy
CNS	Central nervous system
CS	Compound-spiking
CV	Coefficient of variation
DAPI	4',6-diamidino-2-phenylindole
DIV	Days in vitro

$E_{astro}$	Links of astrocyte network
EAAT1	Excitatory amino acid transporter 1
EAAT2	Excitatory amino acid transporter 1
ECS	Extracellular space
ER	Endoplasmic reticulum
FS	Fast-spiking
GABA	$\gamma$ -aminobutyric acid
GFAP	Glial fibrillary acidic protein
GJ	Gap junction
GS	Glutamin synthetase
iAAFT	Iterative amplitude adjusted Fourier transform
ICC	Immunocytochemistry
IP <sub>3</sub>	Inositol triphosphate
IP <sub>3</sub> R	Inositol triphosphate receptors
ITO	Indium tin oxide
k	Mean degree
L	Shortest path
LFP	Local field potential
LTD	Long-term depression
LTP	Long-term potentiation
MAP2	Microtubule-associated protein 2
MEA	Microelectrode array
meanIBI	Mean inter-burst interval
mGluR	Metabotropic glutamate receptor
$N_{act}$	Number of active astrocytes
Na <sup>+</sup> /K <sup>+</sup> -ATPase	Na <sup>+</sup> /K <sup>+</sup> - adenosine triphosphatase
NBs	Network bursts

N-N network	Neuron-neuron network
NS	Neuron culture
P2YR	Purinergic receptor type 2
PDL	Poly-D-Lysine
PIP2	phosphatidylinositol 4,5-bisphosphate
PLC	Phospholipase C
ROI	Region of interest
RS	Regular-spiking
SiN	Silicon nitride
SR	Spike rate
stdIBI	Standard deviation of the Inter-bursts interval
TiN	Titanium nitride
TLE	Temporal lobe epilepsy
TS	Triphasic-spiking
$V_{astro}$	Vertices of astrocyte network



## ORIGINAL PUBLICATIONS

- Publication I      **Genocchi, B.**, Lenk, K., & Hyttinen, J. (2019). Influence of astrocytic gap junction coupling on in silico neuronal network activity. *Mediterranean Conference on Medical and Biological Engineering and Computing*, 480–487.
- Publication II     Lenk, K., **Genocchi, B.**, Barros, M. T., & Hyttinen, J. A. (2021). Larger connection radius increases hub astrocyte number in a 3-d neuron-astrocyte network model. *IEEE Transactions on Molecular, Biological and Multi-Scale Communications*, 7(2), 83–88.
- Publication III    **Genocchi, B.**, Ahtiainen, A., Barros, M. T., Tanskanen, J. M., Hyttinen, J., & Lenk, K. (2021). Astrocytic control in in vitro and simulated neuron-astrocyte networks. *Proceedings of the Eight Annual ACM International Conference on Nanoscale Computing and Communication*, 1–7.
- Publication IV     Ahtiainen \*, A., **Genocchi \*, B.**, Tanskanen, J. M., Barros, M. T., Hyttinen, J. A., & Lenk, K. (2021). Astrocytes exhibit a protective role in neuronal firing patterns under chemically induced seizures in neuron-astrocyte co-cultures. *International Journal of Molecular Sciences*, 22(23), 12770. \* these authors contributed equally to the manuscript.
- Publication V     **Genocchi, B.**, Ahtiainen, A., Niemi, A., Barros, M. T., Tanskanen, J. M., Lenk, K., Hyttinen, J., & Subramaniam, N. P. (n.d.). Astrocytes induce desynchronization and reduce predictability in neuron-astrocyte networks cultured on micro-electrode arrays. *Submitted*.

## *Author's contribution*

- Publication I      Genocchi, Lenk and Hyttinen conceptualized the simulation ideas for the study. Genocchi modified the existing code, performed the simulations, analysed and displayed the results. Genocchi drafted the first manuscript. All authors contributed to the final manuscript version.
- Publication II     Lenk conceptualized and performed the simulations. Lenk, Genocchi, and Barros conceptualized the analysis. Genocchi performed the data analysis and the results visualization. Lenk, Genocchi, and Barros drafted the first manuscript. All authors contributed to the discussion of the results and to the final manuscript version.
- Publication III    Genocchi and Lenk conceptualized the study. Genocchi and Ahtiainen collected the experimental data. Genocchi performed the simulations, the data analysis of the simulated and experimental results, and the data visualization. Genocchi drafted the first version of the manuscript. All authors discussed the results and contributed to the last version of the manuscript.
- Publication IV    Genocchi, Ahtiainen, Hyttinen, and Lenk conceptualized the study. Ahtiainen and Genocchi collected the data. Ahtiainen maintained the cell cultures and conducted the data analysis related to the immunocytochemistry and live/dead assay. The rest of the data analysis (activity analysis, activity correlation, cell counting, and synchronization) was performed by Genocchi. Ahtiainen and Genocchi drafted the first manuscript. All the authors discussed the results and contributed to the final version of the manuscript.
- Publication V     Genocchi, Subramaniyam, and Hyttinen conceived the study idea. Ahtiainen and Niemi maintained the cell culture and collected the data. Genocchi analyzed the data and took care of the data visualization. Genocchi drafted the first manuscript. All authors discussed the results and contributed to the last version of the manuscript.



# 1 INTRODUCTION

Astrocytes, a glial cell type, define the cytoarchitecture of the brain. They are intertwined with neurons and form networks throughout the central nervous system. The single element of these networks is represented by the *tripartite synapse*, which is formed by one presynaptic neuron, one astrocyte, and one postsynaptic neuron (Araque et al., 1999). In the tripartite synapses, astrocytes and neurons communicate and exchange neuro- and gliotransmitters. It is recognized that astrocytes facilitate the formation, maturation, and elimination of synapses (Tan et al., 2021); they provide metabolic support to the neurons (Perez-Catalan et al., 2021), maintain homeostasis by removing excessive ions and glutamate from the extracellular space (Verkhratsky et al., 2020). When glutamate is released from the presynapse and binds to glutamate receptors on the astrocytic membrane, it triggers a series of chemical reactions that ultimately result in an increase in intracellular calcium ( $\text{Ca}^{2+}$ ) levels in the astrocyte. This rise in  $\text{Ca}^{2+}$  then prompts the astrocyte to release both excitatory and inhibitory molecules (Dall rac et al., 2018; Halassa et al., 2007a, for a review: Oliveira and Araque, 2022). These molecules are normally referred to as gliotransmitters, and the phenomenon is called gliotransmission.  $\text{Ca}^{2+}$  oscillations in the astrocytes also appear spontaneously and independently from the neuronal activity (Nett et al., 2002). These oscillations appear asynchronously along the astrocytic process and often do not extend as local calcium waves or intercellular waves. Moreover,  $\text{Ca}^{2+}$  oscillations have been observed to be initiated by transmembrane  $\text{Ca}^{2+}$  entry (Srinivasan et al., 2015), and elicited by a reversed operation of sodium ( $\text{Na}^+$ )/ $\text{Ca}^{2+}$  exchangers, as a consequence of an uptake-evoked rise of intracellular  $\text{Na}^+$  (Doengi et al., 2009a).

Given the crucial functions that astrocytes perform in regulating neuronal activity, dysfunctions or impairments of these cells can result in neurological disorders. Potassium ( $\text{K}^+$ ) buffering from the extracellular space (ECS) is one of the critical functions of astrocytes (Verkhratsky et al., 2020). If impaired, it may lead to

an increased extracellular  $K^+$  concentration, which results in high neuronal activity (Bellot-Saez et al., 2017).  $K^+$  is distributed between astrocytes through the gap junctions (GJ) (i.e., intercellular connections that enable the flow of ions and small molecules between cells) (Ma et al., 2016; Rose and Ransom, 1997). Research on GJs in astrocytes, as well as investigations on GJ uncoupling in epilepsy, appear to support the idea that these cellular structures play a causal role in the onset and propagation of epileptic seizures. (Bedner et al., 2015a; Q. Li et al., 2019; Steinhäuser et al., 2012).

As mentioned above, the network structure is fundamental, especially when considering signal transmission in the neuronal and astrocytic networks. In fact, the network connectivity and the structure largely affect not only ion clearance but also  $Ca^{2+}$  signals spread (Fujii et al., 2017; Lallouette et al., 2014).

Over the past decade, computational modeling has increasingly been employed to gain a better understanding of the modulatory impact of astrocytes and to overcome experimental constraints (De Pittà and Berry, 2019). Computational models traditionally focused on neuronal electrical activity and the relative spiking, overlooking the other non-electrically excitable cells in the central nervous system. Recent work by Armbruster et al., 2022 observed activity-dependent depolarizations in the peripheral astrocytic processes of *circa* 20 mV, in response to  $K^+$  handling in the extracellular space. However, it is mostly accepted by researchers in the glial physiology field that astrocytes use chemical signaling as a communication code. The most researched and modeled is nowadays  $Ca^{2+}$  signaling (De Pittà and Berry, 2019), because of higher access to data from  $Ca^{2+}$  imaging. The models currently available span from the single cell level to the neuron-astrocyte network level and focus on both healthy and diseased states (reviewed in Manninen et al., 2018; Oschmann et al., 2018).

The aim of my doctoral thesis was to investigate the functions of astrocytes in both healthy and epileptic-like states. Initially, I focused on exploring the impact of astrocyte network topology on the diffusion and synchronization of neuronal signals in neuron-astrocyte networks. In **Publication I**, we simulated the effect of GJ uncoupling in the generation of hyperactivity. In **Publication II** and **Publication III**, we examined how the astrocytic network topology influences neuronal activity in both 3D and planar networks. Moreover, we studied how astrocytes counteract hyperactivity in rat cortical co-cultures *in vitro* (**Publication IV**); in this work, two

convulsant drugs targeting, respectively, voltage-gated  $K^+$  channels and  $GABA_A$  receptors were used to study the ionic and transmitters pathways likely activated in astrocytes to counteract hyperactivity. The main innovation of this research was the utilization of fixed quantities of neurons and astrocytes in co-cultures, which enabled us to investigate the diverse drug responses in cultures containing varying quantities of astrocytes. Lastly, in **Publication V**, we studied how astrocytes shape neuronal activity patterns and the local field potentials in microelectrode arrays (MEA). Altogether, these results show that astrocytes modulate neuronal activity and by clearing the extracellular space from ions and gliotransmitters shape the neuronal action potentials and the signal transmission in the network.



## 2 LITERATURE REVIEW

### 2.1 Neuron physiology

The average weight of an adult male human brain is approximately 1.5 kg, and it contains around 86 billion neurons and 85 billion non-neuronal cells (Herculano-Houzel, 2009). Although it is challenging to differentiate glia from small neurons using histology-based counting methods, it has been estimated that there are between 18.2 and 38.9 billion glial cells in the human cortex (von Bartheld et al., 2016).

A neuron consists of a cell body, or soma, which houses the nucleus and organelles, as well as numerous branches extending from the soma. These branches can either be dendrites, which receive signals from other neurons, or an axon, which carries the neuronal signal from the cell body to the axon terminals (see Fig.2.1-A)(Brodal, 2016). Each neuron may have multiple dendrites, but it has only one axon. The end terminal of the axon can present several ramifications, allowing the neuron to contact and influence many other cells (Brodal, 2016). At these terminals the neurons contact with each other and exchange molecules, which in this way transfer information (O'Rourke et al., 2012). These contacts are called *synapses*. Traditionally, synapses are divided into *electrical*, if the transmission happens through the direct flow of charges in the GJ, or *chemical*, if the communication is mediated by an exchange of neurotransmitters in the synaptic cleft. Synapses can also be divided into excitatory or inhibitory based on the neurotransmitter effect, or also based on the type of neurotransmitter, e.g. GABAergic, or glutamatergic synapses (O'Rourke et al., 2012).

The majority of the axons are wrapped in myelin sheets, an isolating layer, that allows for faster electrical signal propagation. This is made possible because the signal potentiation happens only in particular portions of the axon called nodes of Ranvier and travels isolated in the myelinated parts. This phenomenon is called saltatory conduction (Fig. 2.1 - B). In the nodes the opening of the voltage-gated  $K^+$  and  $Na^+$

channels allow for the generation of action potentials (AP) (Fig. 2.1 - B).

APs are rapid variations in the cell membrane potential, and are fundamental for cell-to-cell communication in all the electrically excitable cells (e.g., neurons and muscle cells) (Jackson, 2006). The rise in potential is called depolarization, while the fall back to the resting state is called repolarization. The resting potential of the neuronal membrane is in the majority of the cases between  $\approx -60$  and  $\approx -70$  mV (Jackson, 2006; Lewis et al., 2011). At this stage  $K^+$  has a high concentration inside the axon, while  $Na^+$  is instead highly concentrated outside the cell membrane, leading to a more negative inside of the cell. When a stimulus arrives this causes the opening of voltage-dependent  $Na^+$  channels, which allows the flow of  $Na^+$  toward the inside of the cell (Jackson, 2006). If the stimulus current is high enough to make the voltage overcome the threshold, which is usually  $\approx -50$  to  $-55$  mV, the  $Na^+$  channels open and the voltage rises up to  $\approx 50$  mV.

APs can also be referred to as spikes when their shape is neglected and only the peak time point is considered (Jackson, 2006). Since the AP is fired only upon overcoming the threshold and, if overcome, always rises to similar voltage levels, this behavior is called *all or nothing* (Debanne et al., 2011).

When the AP reaches its peak, the  $Na^+$  channels close, and the  $K^+$  channels open. This secondary opening allows  $K^+$  to flow from the inside of the axon to the extracellular fluid, returning the membrane potential to a negative value. Due to the fixed opening time of the  $K^+$  channels, the membrane potential decreases to lower levels than the resting state (Jackson, 2006). In this part of the AP, called *refractory period*, it is very unlikely that a stimulus is capable of initiating an AP, and the  $K^+$  and  $Na^+$  concentrations return to the resting levels through the activation of the  $Na^+/K^+$ -adenosine triphosphate ( $Na^+/K^+$ -ATPase) pump (Jackson, 2006). This pump transports  $Na^+$  outside of the cells, and  $K^+$  towards the inside. This movement is done against their electrochemical driving force, and thus the pump needs adenosine triphosphate (ATP) for its activation (Clausen et al., 2017).

## 2.2 Astrocyte physiology

Astrocytes are glial cells that are highly intertwined in the neural network; they define the cytoarchitecture of the central nervous system (CNS) by connecting the gray matter with the vasculature (Verkhatsky and Nedergaard, 2018). Astrocytes

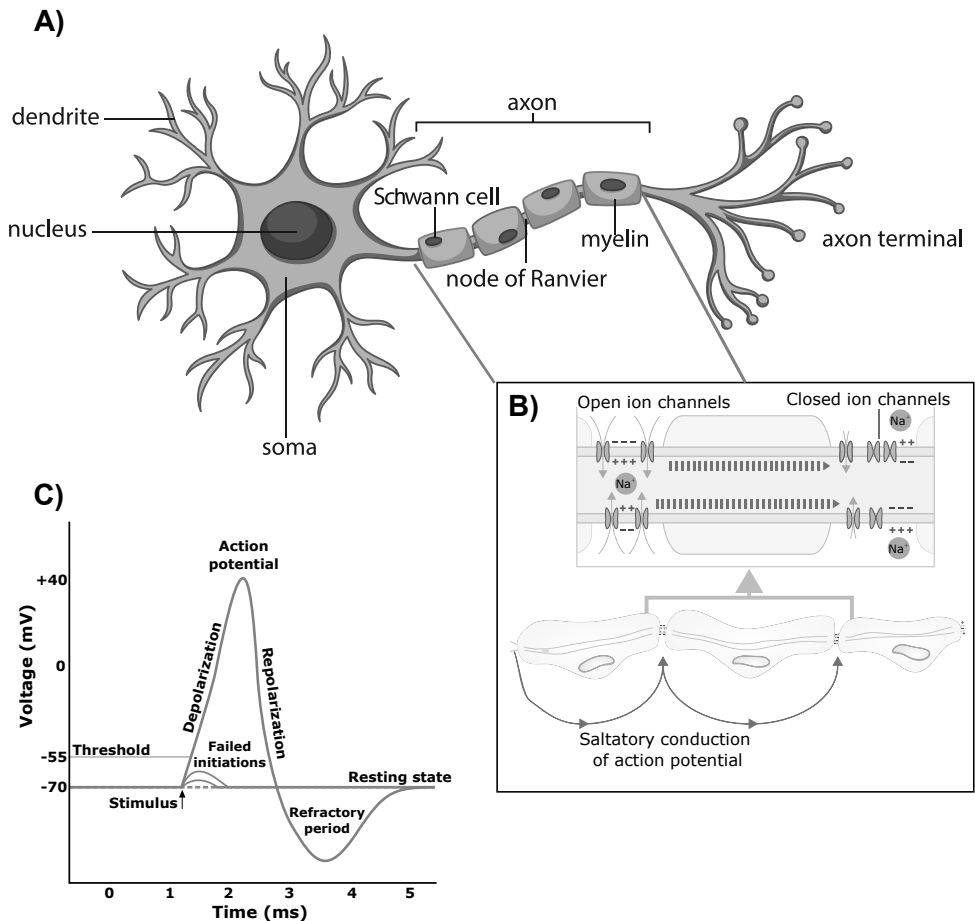


**Figure 2.1** A) Graphical description of a neuron. The soma contains the nucleus, and several branches extend from the soma. The dendrites transfer information, in the shape of electrical signals to the soma, while the axon transfers them from the soma to the axon terminals. B) Chemical description of the saltatory conduction in the nodes of Ranvier and through the myelin sheaths. C) Description of an action potential and its phases. All the original images were licensed under a Creative Commons Attribution-ShareAlike 3.0 Unported License.

are widely heterogeneous in morphology and functions, which spans from maintaining ionic and neurotransmitter homeostasis, sustaining neurotransmission, and helping neurogenesis (Oberheim et al., 2009a).

During the early 1900s, the neuroscientist Ramón y Cajal conducted studies on brain cells (Ramón y Cajal, 1911). The classifications that Ramón y Cajal made at

that time are still used nowadays; he divided the astrocytes into two main subtypes: *protoplasmic* and *fibrous* (Ramón y Cajal, 1911). The classification had been made based on morphological differences and on anatomical location.

Protoplasmic astrocytes (Fig. 2.2b) are found in the grey matter and grow a lot of branches in a globular distribution. Fibrous astrocytes (Fig. 2.2a) are instead found in the white matter and present many long fiber processes. There are also differences in how protoplasmic and fibrous astrocytes contact neurons; protoplasmic astrocytes envelop synapses, and fibrous astrocytes contact nodes of Ranvier through their processes, and both of them form gap junctions with other astrocytes (Sofroniew and Vinters, 2010). Both protoplasmic and fibrous astrocytes in humans are larger than in rodents (Fig. 2.2b, Fig. 2.2a) (Oberheim et al., 2009a). Astrocytes occupy the entire CNS in an ordered and organized non-overlapping manner (Sofroniew and Vinters, 2010). Protoplasmic astrocytes envelope 20,000 – 100,000 synapses in rodents, in humans they can envelop from 27,000 up to 2 million synapses within a single domain (Oberheim et al., 2009a).

Various studies have contributed to our current understanding of the roles played by astrocytes. Multiple reviews have focused on astrocytic  $\text{Ca}^{2+}$  signaling (Bazargani and Attwell, 2016a; Cornell-Bell et al., 1990; Haydon, 2001; Kim et al., 1994; Verkhratsky and Kettenmann, 1996; Verkhratsky et al., 1998). This signaling can be triggered by neuronal activity and stimulates the release of gliotransmitters from astrocytes to neurons, thereby modulating neuronal activity. Other studies have highlighted the importance of astrocytes in the clearance and redistribution of ions and neurotransmitters (Mennerick and Zorumski, 1994; Newman and Reichenbach, 1996). In recent years, it has become evident that abnormal functions in glial cells and astrocytes may be associated with diseases of the CNS (Rossi and Volterra, 2009; Seifert et al., 2006).

## 2.3 Tripartite synapse

The term *tripartite synapse*, meaning the complex comprising pre- and post-synaptic neuron and the astrocyte, was first proposed in 1999 by Araque et al. in their review on neuron-astrocyte signaling (Araque et al., 1999). In the 1990s several studies from different laboratories revealed a bidirectional communication between astrocytes and neurons (Fig. 2.3) (Dani et al., 1992; Nedergaard, 1994; Parpura et al.,



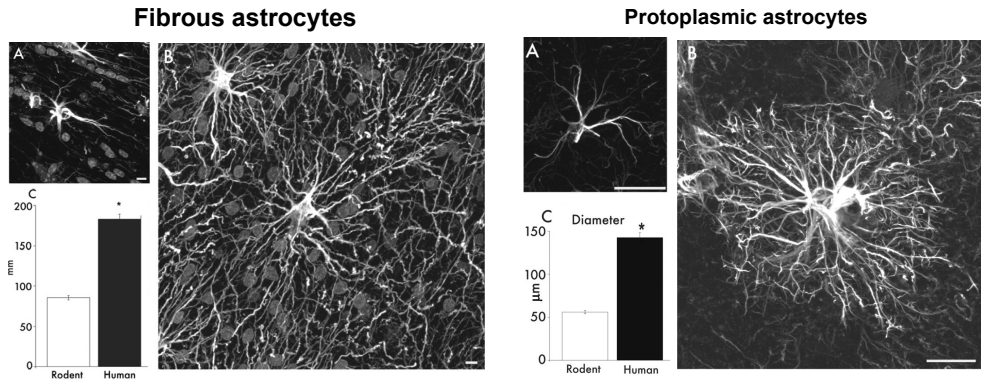


**Figure 2.2** Fluorescence imaging of (a) fibrous astrocytes from rodents and humans, and (b) protoplasmic astrocytes from rodents and humans.

1994).

This communication consists on the release from the presynaptic neuron of various neurotransmitters, e.g. glutamate and ATP, from glutamatergic presynaptic neurons, and  $\gamma$ -aminobutyric acid (GABA) from interneurons. Glutamate and ATP, when released, activate specific G protein-coupled receptors, primarily metabotropic glutamate receptors (mGluR) and type 2 purinergic receptors (P2YR), present on the astrocytic membrane. This activation triggers the phospholipase C (PLC)/inositol 1,4,5-triphosphate ( $\text{IP}_3$ ) cascade of reactions. The activation of PLC by this process hydrolyzes the membrane lipid phosphatidylinositol 4,5-bisphosphate (PIP2) to generate  $\text{IP}_3$ , leading to the activation of  $\text{IP}_3$  receptor ( $\text{IP}_3\text{R}$ ) and the release of  $\text{Ca}^{2+}$  from the endoplasmic reticulum (ER) (Agulhon et al., 2008).

The astrocytic  $\text{Ca}^{2+}$  increase leads to the release of various gliotransmitters such as glutamate, GABA, ATP, endocannabinoids, and D-serine into the synaptic cleft. These gliotransmitters modulate the activity of both pre- and post-synaptic neurons, as demonstrated by several studies (Bazargani and Attwell, 2016a).  $\text{Ca}^{2+}$  waves can propagate through the astrocytic processes, thereby regulating cerebral blood flow and energy supply based on the brain's activity level (Attwell et al., 2010; Harris et al., 2012). Through gap junctions,  $\text{IP}_3$  and  $\text{Ca}^{2+}$  waves can activate other astro-

cytes, resulting in the release of gliotransmitters in synapses distant from the initially activated one, which is facilitated by the increased IP<sub>3</sub> levels and the subsequent Ca<sup>2+</sup> release from intracellular stores (Charles et al., 1991; Cornell-Bell et al., 1990; Cornell-Bell and Finkbeiner, 1991). A detailed scheme of the signaling cascade can be seen in Fig 2.3.

The synaptic modulation can lead to various scenarios (Araque et al., 2014):

- *Astrocytic glutamate* can both potentiate excitatory transmission by activating presynaptic NMDA receptors and presynaptic mGluRs (Jourdain et al., 2007; Navarrete et al., 2012; Perea and Araque, 2007) and modulate both inhibitory and excitatory postsynaptic transmission (Kang et al., 1998).
- Networks of neurons can be modulated by gliotransmission. Astrocytic Ca<sup>2+</sup> signals can spread to different astrocytes leading to a concomitant activity of multiple synapses. The concomitant activation of the synapses can induce synaptic depression and facilitation in the network (Hebb, 1949), so astrocytes' activity can also participate in synaptic plasticity.
- Astrocytes can trigger a form of long-term potentiation (LTP) when there is a coincidence of postsynaptic activity and Ca<sup>2+</sup> elevation (Perea and Araque, 2007), while spike-timing-dependent long-term depression (LTD) of excitatory transmission is mediated by glutamate release and activation of NMDARs (Min and Nevian, 2012). These observations have been made in both *in vivo* and *in vitro*. However, it should be noted that while astrocytes play a role in some forms of synaptic plasticity, they are not involved in all phenomena of synaptic plasticity.
- Extracellular K<sup>+</sup> levels also affect neuronal excitability. The two main mechanisms thought to balance potassium concentration are K<sup>+</sup> uptake by astrocytes through Na<sup>+</sup>/K<sup>+</sup>-ATPase and Na<sup>+</sup>-K<sup>+</sup>-Cl<sup>-</sup> cotransporters, and K<sup>+</sup> buffering, which main contributors are astrocytic inwardly rectifying K<sup>+</sup> channels (Kir channels), water channels (AQP4) and gap junctions (Bellot-Saez et al., 2017; Bellot-Saez et al., 2021).
- Astrocytes uptake GABA from the ECS. Astrocytic GABA transporters near GABAergic synapses take up GABA locally and contribute to terminating or modulating GABA-mediated neuronal transmission (Chatton et al., 2003; Doengi et al., 2009b)

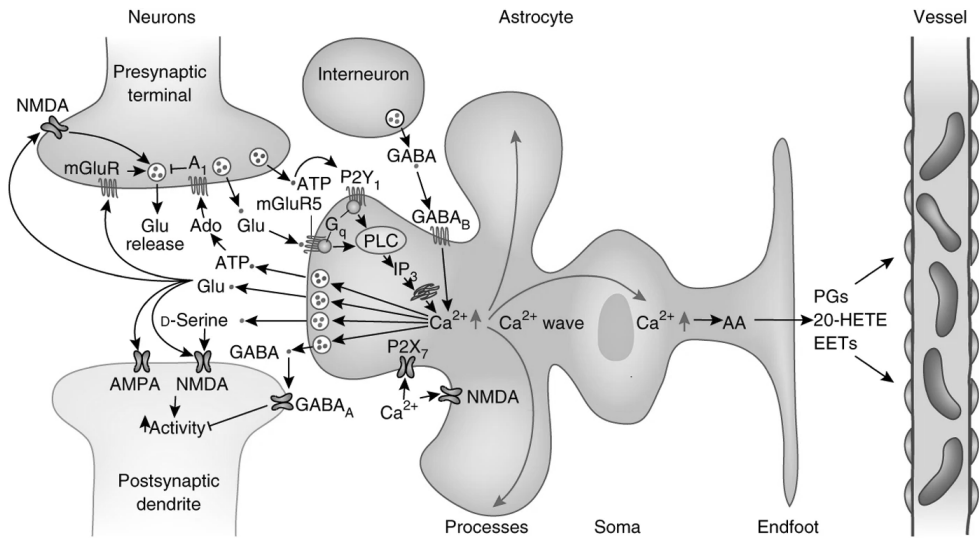


**Figure 2.3** Glutamate and ATP released from the presynaptic neuron activate mGluR and PY2R, which in turn lead to the release of  $\text{Ca}^{2+}$  from intracellular stores via an  $\text{IP}_3$ -evoked mechanism. The resultant increase in  $\text{Ca}^{2+}$  levels stimulates the release of glutamate, GABA, ATP, and D-serine into the synaptic cleft. Reproduced with permission from: Bazargani and Attwell, 2016b.

## 2.4 Astrocytes and epilepsy

### 2.4.1 Epilepsy

Epilepsy is a chronic brain disorder that can affect people of all ages and all countries (Forsgren et al., 2005). In a fact sheet of February 2018, the *World Health Organization* has counted approximately 50 million people worldwide that are affected by epilepsy (World Health Organization, 2018). Epilepsy is a condition in which repeated and unprovoked seizures occur (Dekker, 2002; Stafstrom and Carmant, 2015). It is possible to distinguish between symptomatic epilepsy if it is developed after a particular event, such as meningitis or head injury for example, and idiopathic epilepsy, if it develops without a clear cause (Dekker, 2002). An epileptic seizure is an alteration of neurologic functions due to excessive and hypersynchronous activity of neurons and occurs when excitation and inhibition in brain networks are not balanced (Stafstrom and Carmant, 2015). Genetic alterations occurring at the circuit level, or receptor level, have been seen to lead to epilepsy; for example, abnormal

synaptic connectivity, abnormal GABA and glutamate receptor subunits shape, or ionic channels densities (Stafstrom and Carmant, 2015).

## 2.4.2 Role of the astrocytes in epilepsy

Despite the traditional view focusing on the neurons as the only cause of epilepsy, researchers have proposed astrocytes as the cause as well (Dossi et al., 2018; Fellin and Haydon, 2005; Tian et al., 2005). Especially in the case of mesial temporal lobe epilepsy (MTLE), patients showed dysfunctions in astrocytic channels and receptors, suggesting a possible involvement of astrocytes in hyperexcitation, neurotoxicity, and seizure spreading (Coulter and Steinhäuser, 2015; Dossi et al., 2018). Abnormalities in astrocytes that are believed to be associated with epilepsy include reactive astrogliosis, impaired potassium buffering, dysfunction in astrocytic GJ, and abnormal uptake of glutamate (Fig. 2.4) (Bedner et al., 2015b; Bellot-Saez et al., 2017; Coulter and Steinhäuser, 2015; Dossi et al., 2018; Seifert, 2010).

### Reactive astrogliosis

Reactive astrogliosis has been noted in almost all forms of epilepsy, but especially in MTLE with hippocampal sclerosis (MTLE-HS) (Thom, 2014). In MTLE-HS, a severe loss of neurons in the CA1 region of the hippocampus is accompanied by a chronic and fibrillary gliosis (Fahrner et al., 2007). Together with the increased expression of glial fibrillary acid protein (GFAP), also a different isoform of GFAP has been identified; apparently, this isoform controls the size and motility of the astrocytes (Martinian et al., 2009).

### K<sup>+</sup> buffering: gap junctions and K<sup>+</sup> channels

From in vivo studies, it appeared that the extracellular concentration of potassium at rest,  $[K^+]_0$  is about 3 mM, but during seizures, it can increase to 10 – 12 mM (Heinemann and Lux, 1977). If the value of  $[K^+]_0$  is not restored to its homeostatic value, hyperactivity and seizures can be present.

From studies on patients with MTLE-HS, it came out that impaired K<sup>+</sup> buffering and enhanced seizure susceptibility was dependent on reduced expression of Kir channels Kir4.1 (Bordey and Sontheimer, 1998; Hinterkeuser et al., 2000) (Fig.

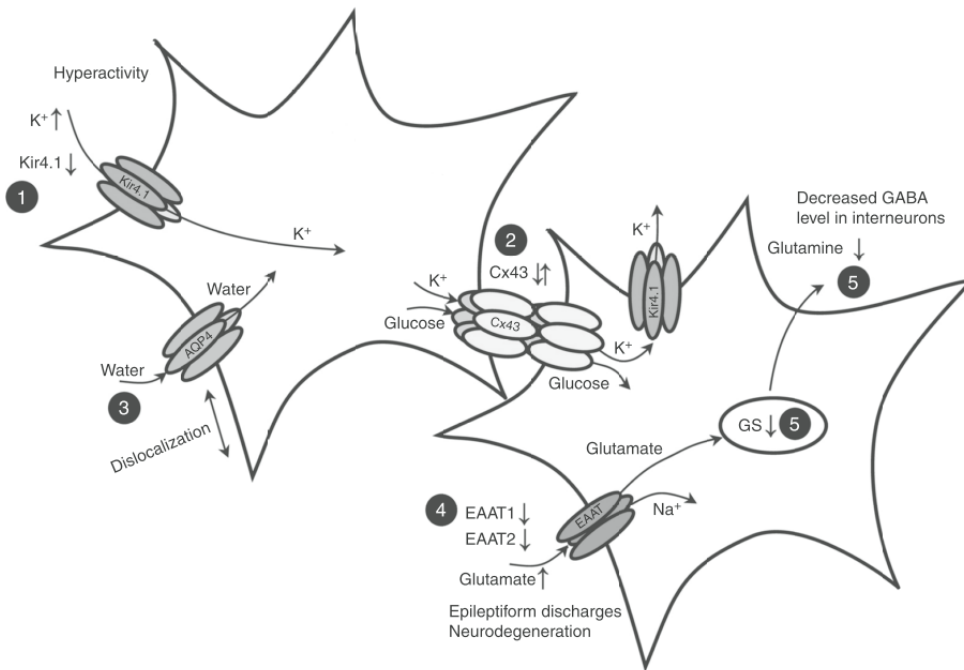


**Figure 2.4** Astrocytes dysfunctions scheme in mesial temporal lobe epilepsy with hippocampal sclerosis (MTLE-HS). 1) Down-regulation in Kir4.1 channels lead to an increased  $K^+$  extracellular concentration. 2) Gap-junctions impairment leads to a dysregulated redistribution of  $K^+$  ions. 3) Dislocated or decreased water channels lead to impaired  $K^+$  buffering. 4) Reduced expression of EAAT1 and EAAT2, glutamate transporters, reduced glutamate uptake leading to an increased extracellular glutamate concentration. 5) Loss of GS lead to reduced synthesis and release of GABA. Reproduced with permission from: Coulter and Steinhäuser, 2015.

2.4 - point 1). It has been shown that a down-regulation of Kir4.1 reduced astrocytic removal of glutamate and  $K^+$  from the extracellular space (Djukic et al., 2007). MTLE patients also showed a loss and a dislocation in AQP4 channels Heuser et al., 2010. It seems that the parallel action of AQP4 and Kir4.1 emphasize their impact on  $K^+$  homeostasis (Seifert et al., 2009) (Fig. 2.4 - point 3). Kir channels transport  $K^+$  into cells together with water entry through AQP4 in order to maintain osmotic balance (Devinsky et al., 2013).

Gap junctions are ring assemblies with a pore inside; the connection of two adjacent hemichannels forms a junction that permits the electrical coupling of the cells and ions homeostasis (Bellot-Saez et al., 2017). Wallraff and colleagues demonstrated

that gap junctions seem to help accelerate  $K^+$  clearance from extracellular space reducing the local accumulation of  $K^+$  (Wallraff, 2006). If the coupling is impaired or the expression of the gap junction-specific proteins CX43 is downregulated,  $K^+$  clearance might fail, leading to local accumulation of  $K^+$  and a consequential hyperactivation of the neurons (Fig. 2.4 - point 2).

## Glutamate uptake and synthesis

Glutamate is a neurotransmitter released during neural activity and its uptake is mainly operated by excitatory aminoacid transporter 1 and 2 (EAAT1 and EAAT2, respectively), human astrocytic glutamate transporters localized on the membrane (Bellot-Saez et al., 2017). In human temporal lobe epilepsy (TLE) has been found a downregulation in the activity of EAAT1 and EAAT2 (Seifert et al., 2006) (Fig. 2.4 - point 4). An excess of extracellular glutamate can induce recurrent seizures and neuronal cell death, and it has been often seen in human epileptic tissue (Glass and Dragunow, 1995).

The enzyme that helps the glutamate removal is the glutamine synthetase (GS), which converts glutamate into receptor-inactive glutamine (Seifert, 2010). Different studies evidence a loss of GS in epilepsy, suggesting a role for this enzyme in epileptogenesis (Cho, 2013; Eid et al., 2012; Eid et al., 2016; Mathern et al., 1999) (Fig. 2.4 - point 5). The hyperactivity after GS deficiency could be caused because glutamine is taken up by GABAergic neurons, there it is converted to glutamate again and then into GABA by glutamic acid decarboxylase. Thus, reduced GS can lead to reduced GABA release (Coulter and Steinhäuser, 2015; Seifert, 2010). In addition, studies on epilepsy models have reported increased protein levels of mGluR3, mGluR5, and mGluR8 in astrocytes (Steinhäuser and Seifert, 2002). Activation of these receptors leads to an increase in  $Ca^{2+}$  and its propagation as waves, ultimately triggering the release of gliotransmitters from astrocytes (Seifert, 2010).

## 2.5 Techniques to monitor neuronal and astrocytic activity

### 2.5.1 Fluorescence microscopy and immunostaining

In biochemistry, immunostaining refers to the detection of a specific protein in a sample by marking it with antibody-based methods (Coons et al., 1941). In this

technique, the target protein antigen is detected by a specific antibody, defined as *primary antibody*. Successively the primary antibody is detected for imaging with a species-specific *secondary antibody* combined with a fluorophore (Fig. 2.5). After labeling the desired proteins located on the membrane with the antibodies, the cells are imaged with a fluorescence microscope.

A fluorescence microscope utilizes fluorescence to generate an image (Stockert and Blazquez-Castro, 2017). The specimen is irradiated with light of a specific wavelength which is absorbed by the fluorophore, which will emit light in a longer wavelength. The excitation wavelength is selected with an excitation filter which separates the light from the source into its multiple components. Then the dichroic mirror deflects the light of the specified excitation wavelength toward the specimen. The fluorophore will then emit lights of a longer wavelength which will pass undeflected through the dichroic filter to the detector. This allows mapping the distribution of a single fluorophore at a time (Fig. 2.5). Multi-color images of several types of fluorophores, e.g. when multiple proteins are stained, must be composed by obtaining several single-color images (Stockert and Blazquez-Castro, 2017).

## 2.5.2 Microelectrode Arrays

In order to measure neuronal activity *in vitro* or *in vivo* at the network level, microelectrode arrays (MEA) have been used because of their capability to record and stimulate the neurons simultaneously (Cerina et al., 2023; Obien et al., 2015). Moreover, MEAs allow following the network development over several weeks (Charlesworth et al., 2015; Ito et al., 2014).

MEAs present different numbers of electrodes, with different electrode diameters and materials; as well as, different grid shapes. The standard MEAs used in the experiments described later in this thesis present an 8x8 grid of electrodes, with a diameter of 30  $\mu\text{m}$ , and an electrode spacing of 200  $\mu\text{m}$ . The flat and round electrodes are made of titanium nitride (TiN) or indium tin oxide (ITO), while the insulation material is silicon nitride (SiN). We used these MEAs since they are normally used for cell cultures.

The microelectrodes detect the changes in the extracellular field caused by the closest neurons. As described earlier (Section 2.1), during a spike the rapid  $\text{Na}^+$  ion influx results in a rise in the neuronal membrane potential, on the other hand, this results in a large negative spike in the extracellular action potentials, subsequently

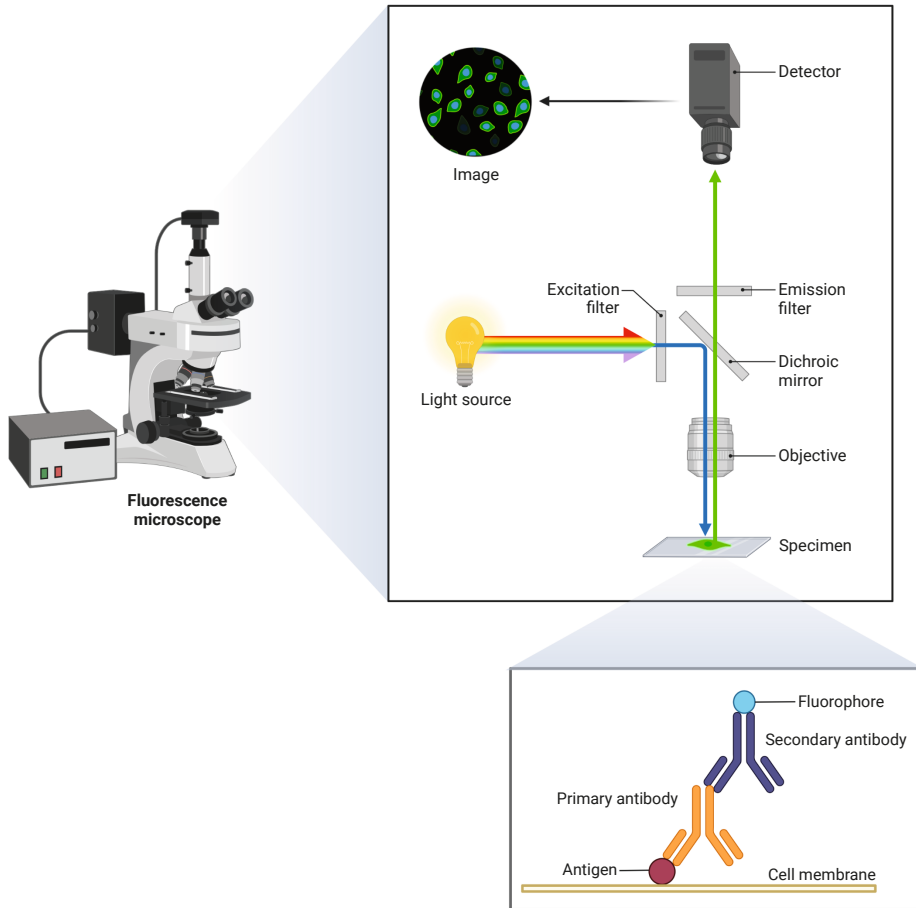


**Figure 2.5** Immunostaining and fluorescence imaging. When a primary and a secondary antibody are bound to a protein antigen, these can be imaged with a fluorescence microscope. The secondary antibody is bound with a fluorophore and selecting the right excitation wavelength with the excitation filter allows to excite the fluorophore and elicits an emission in a longer wavelength which will be detected by the detector. Figure created with BioRender.com.

inverted in a small positive spike thanks to the slow  $K^+$  efflux (Obien et al., 2015).

Extracellular action potentials are normally between tens to hundreds of microvolts in amplitude and less than 2 ms in duration; intracellular action potentials are in the range of tens of millivolts, with similar duration to those of the extracellular action potentials (Buzsáki et al., 2012).

Usually, the detected signals are single- and multi-unit spiking activity; however,



MEAs can also detect local field potentials (LFP), such as the resulting activity of a large population of neurons located in the vicinity of an electrode. LFPs present a low-frequency band, normally lower than 300 Hz, and thus can be analyzed by low-pass filtering the signals (Buzsáki et al., 2012).

Standard MEA signal processing at least includes:

- *Filtering the raw data traces.* As said earlier, filtering the signal, normally with a band-pass filter (300–3000 Hz), allows the discrimination LFPs and noise from extracellular action potentials (Quiñones Quiroga, 2009).
- *Spike detection.* Spikes are normally detected based on amplitude thresholding. Most commonly, the threshold is set to five times the baseline noise level. This is calculated either as the root mean square of the signals with a mean value of zero, or in the presence of many spikes using the median of the signal, which is less sensitive to outlier spikes (Quiroga et al., 2004; Quiroga et al., 2007).
- *Spike sorting.* Spike sorting refers to the clustering of the spike shapes. The idea behind spike sorting is that different neurons will have clearly distinct spike shapes, thus the spikes of different neurons will be clearly separated in the clusters. There are several spike sorting tools that utilize different techniques e.g., principal component analysis (Chaure et al., 2018; Quiroga et al., 2004), or extraction of template waveforms (Pachitariu et al., 2016; Yger et al., 2018).

After the signal preprocessing spikes and bursts are commonly extracted from MEA recordings. A burst is a set of spikes fired in quick succession in a short time period; it can either be stimulated by the network activity or it can be intrinsically generated by the single neuron (Cotterill et al., 2016). The reason why bursts are commonly analyzed lies in the fact that they are believed to carry information and exert several functions, for example, synchronization (Chiappalone et al., 2006; Cotterill et al., 2016; J.-J. Sun et al., 2010).

The extracted features that are commonly analyzed, and that we will mention in the thesis, are:

- *Spike rate.* Represents the number of spikes in a second (Hz) or in a minute (spikes/min).
- *Burst rate.* Represents the number of bursts in a second (Hz) or in a minute (spikes/min).

- *Burst duration.* The time expressed in milliseconds between the first and the last spike inside the same burst.
- *Inter-burst interval.* The time expressed in milliseconds between the last spike of a burst and the first one of the next burst.

### 2.5.3 Calcium imaging

Calcium is the most common second messenger in the majority of the cells, astrocytes and neurons included, and it has been widely used to study cellular activation and responses to drugs or manipulations.

Calcium imaging is used to optically measure the  $\text{Ca}^{2+}$  concentration in isolated cells, tissue, or in a medium, by binding  $\text{Ca}^{2+}$  ions to fluorescent molecules de Melo Reis et al., 2020. These molecules are called  $\text{Ca}^{2+}$  indicators and can be either chemical indicators, e.g. Fluo-4 and Fura-2, or genetically encoded  $\text{Ca}^{2+}$  indicators (GECI). The chemical indicators chelate  $\text{Ca}^{2+}$  ions and have a high selectivity for it. When the chemical indicators bind free  $\text{Ca}^{2+}$  ions a resulting increase in fluorescence intensity or a shift in the emission/excitation wavelength can be observed depending on the indicator used (Fig. 2.6). By mapping the fluorescence in a culture it is possible to study the responses of the cells to a variety of manipulations, for example, the injection of a chemical or a drug, or also monitor spontaneous  $\text{Ca}^{2+}$  activity.

GECI indicators are instead most commonly used in vivo and using a photoreceiver, it is possible to detect changes in cell fluorescence as the animal is awake and freely behaving (de Melo Reis et al., 2020).

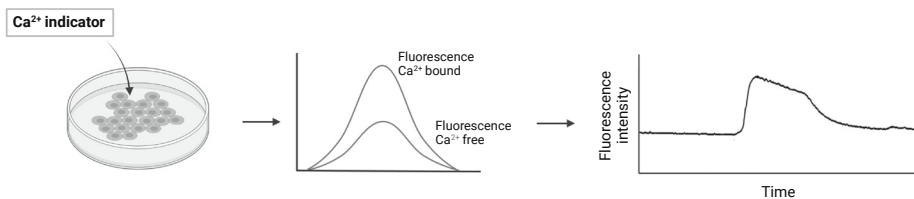


**Figure 2.6**  $\text{Ca}^{2+}$  imaging. Chemical  $\text{Ca}^{2+}$  indicators when injected in the cell culture can specifically bind  $\text{Ca}^{2+}$  ions. Chemical  $\text{Ca}^{2+}$  indicators are bound to a fluorophore and when binding  $\text{Ca}^{2+}$  ions they change their fluorescence intensity. By mapping the fluorescence intensity over time it is possible to study the response of the cell culture to some manipulation. Figure created with BioRender.com.

Calcium elevations in astrocytes are the main hallmarks of astrocyte-neuron or

astrocyte-astrocyte communication (Guerra-Gomes et al., 2018; Volterra et al., 2014), and  $\text{Ca}^{2+}$  imaging has been extensively used to study astrocyte communication. Elevations in astrocytic  $\text{Ca}^{2+}$  can arise spontaneously or be induced by either endogenous or exogenous stimuli, such as synaptic activity (Perea and Araque, 2005) (Fig. 2.3).

## 2.6 Computational modeling of neuron-astrocyte networks in health and disease

The increasing number of evidence and relative questions on the roles of astrocytes in brain diseases pushed neuroscientists at aiming to computationally model brain functions. In order to be able to study the biophysical mechanisms underlying the brain's processes, a detailed and realistic representation is needed. However, detailed biophysical models can be made at single cell level, but fail when modeling large networks of cells due to the computational power needed.

Many approaches to modeling can be used depending on the underlying questions the modeler wants to address. The most used are biophysical and phenomenological models. The first describes the molecular interactions in detail, while the latter approach reproduces the phenomena without going deep into the biophysical description of the elements (Sejnowski et al., 1988). The advantage of this latter approach is to be able to still mimic the system, but with less computational power and run time needed.

Various models have been published focusing on astrocytes and their communication with neurons; these models span different detail levels, from single astrocyte models to tripartite synapse models, to astrocyte network models, to neuron-astrocyte networks model (Manninen et al., 2018; Oschmann et al., 2018). These last ones are those of main interest for the aim of this thesis, as the objective is to study how the astrocytes control and modulate neuronal network activity.

### 2.6.1 Neuron-astrocyte network models

Neuron-astrocyte network models typically involve multiple astrocytes connected with multiple neurons and are mainly designed to investigate and clarify phenomena related to  $\text{Ca}^{2+}$  dynamics, synchronization, information transfer, plasticity, and hy-

perexcitability. In order to study neuron-astrocyte networks, phenomenological and simplified models of the network dynamics and interactions proved to be more useful. The topology in these models is not always biophysically accurate. First, I will present neuron-astrocyte network models with no biophysically accurate network topology, and then, those which instead also model the network structure.

Among the neuron-astrocyte network models with no biophysically plausible topology, Savtchenko and Rusakov, 2014, modeled a ring network of interneurons that receive excitatory synaptic input from a subnetwork of pyramidal cells. The effect of astrocytes was modeled by reducing the frequency of the discharges in randomly selected pyramidal neurons, to reproduce a partial inhibition of the excitatory inputs, and, to model volume-constrained astrocytes, the inhibitory effect was applied to only a part of the subnetwork (Savtchenko and Rusakov, 2014). The results showed a more pronounced decrease in network synchronization for the case with random inhibition. However, the decrease in mean cell firing frequency was instead more visible for the spatial-constrained inhibition.

Chan et al., 2017 modeled the role of astrocytes in ultra-slow oscillatory activity. They showed that astrocytic activation closely affected the frequency of these oscillations.  $\text{Ca}^{2+}$  rises in astrocytes elicited the release of ATP, which altered the neurotransmitter release in nearby neurons, and thus, the regulation of neural activity (Chan et al., 2017).

Gordleeva et al., 2021 modeled working memory in a spiking neuron network coupled with an astrocyte network. The neurons and the astrocytes are homogeneously distributed in a non-specific manner. Neurons are connected through synapses and astrocytes through gap junctions, neurons, and astrocytes communicate by a shared extracellular space with transmitters diffusion. Astrocytic  $\text{Ca}^{2+}$  rises occurred in response to synchronous firing from a group of neurons. Upon activation, gliotransmitter release modulated the strength of the synaptic connections of the group of spiking neurons. Gordleeva and colleagues showed that astrocytes could store information about the patterns of neuronal activation, being able to retrieve and modulate synaptic connections of the previous patterns.

For the neuron-astrocyte network models which instead models also a biophysically plausible network topology, the first model was by Postnov et al., 2009. The model creates a realistic planar pattern of astrocytes in 2D, and considers glutamate-induced  $\text{Ca}^{2+}$  signaling as a trigger for excitability and signal transmission (Postnov

et al., 2009). With this model, Postnov and colleagues studied how different stimuli durations and noise levels affected the patterns of astrocytic  $\text{Ca}^{2+}$  waves. Their results show that the propagation distance of the  $\text{Ca}^{2+}$  wave depended on the duration of the stimuli, with stimuli shorter than 320 s not able to induce  $\text{Ca}^{2+}$  wave propagation. Regarding the applied noise, instead, they found out the strength of the noise affected the velocity of the  $\text{Ca}^{2+}$  wave.

Lenk et al., 2020 created a stochastic model which simulates several astrocytes, each connected to up to hundreds of excitatory synapses and to up to five other astrocytes through gap junctions. The model combines a spiking neuronal network model (Lenk, 2011), with a presynaptic model of glutamate release (Tsodyks et al., 1998). This presynaptic description is then coupled to a model of astrocytic potentiation effect to the presynaptic neurons (De Pittà et al., 2011; De Pittà et al., 2012), and with a novel description of inhibitory effects towards the postsynaptic neurons from Lenk and colleagues. The astrocytic network topology is modeled as in Lallouette et al., 2014. The neuron-astrocyte network reproduces a planar co-culture of 250 neurons and varying ratios of astrocytes, distributed over a  $750 \times 750 \mu\text{m}^2$  culturing area, representing the electrode area of virtual MEA. The different ratios of astrocytes in the network allowed for studying how different astrocyte connectivity scenarios shape neuronal activity. The results showed that increasing the number of astrocytes, thus increasing astrocyte interconnectivity, prevented overexcitation (Lenk et al., 2020).

L. Li et al., 2020 model is analogous to the one from Lenk et al., 2020, the difference relies on the description of the potential effects of GABA on astrocytes and excitatory presynaptic terminals. The model shows that astrocytes responded to GABA with  $\text{Ca}^{2+}$  oscillations and subsequent gliotransmitter glutamate release. With the model, it is possible to study the interplay between GABA neuronal inhibition and GABA-induced glutamate release from the astrocytes, which induces neuronal excitation (L. Li et al., 2020).



### 3 AIMS OF THE STUDY

This thesis project aims at investigating the controlling roles of astrocytes on neuronal network activity. We first analyzed how astrocyte network topology affects neuronal spiking and synchronization in neuron-astrocyte networks. This part was mainly studied with the use of computational models of neuron-astrocyte networks (Chapter 5, **Publications I-II-III**). Secondly, we examined how the astrocytic ionic and gliotransmitter regulation controls the neuronal activity and signal features (Chapter 6, **Publications IV-V**).

Specifically, the aims of each study were as follows:

- **Publication I** aimed at investigating the role of gap junction coupling and uncoupling in the regulation of neuronal activity.
- **Publication II** aimed firstly at comparing the differences between a planar network topology from a 3D network topology; and secondly, at evaluating how different connectivity rules, i.e. changing the maximum connection radius, for the astrocytes changes their network connectivity and the relative neuronal activity response to the different network topologies.
- **Publication III** aimed at exploring how astrocytes affect neuronal activity, by varying the neuron/astrocyte ratios in the networks. Moreover, we compared the results obtained from the simulations with those obtained from MEAs recordings of cultures with the same cell ratios.
- **Publication IV** explored the neuronal response to two convulsant drugs, 4-AP and gabazine, and aimed at elucidating the roles of astrocytes in controlling ionic clearance and gliotransmitter clearance, and the relative induced hyperactivity.
- **Publication V** investigated how astrocytes and extracellular ionic clearance affect the spike shape during development and based on their ratio in the cultures, and how astrocytes impact signal patterning.





## 4 METHODS OVERVIEW

The studies in this thesis comprehended computational simulations and experimental work. Since only a few methods are common between the computational studies and the experimental ones, for simplicity, the methods and results of these two methodologies have been separated into two different chapters. Chapter 5 describes the computational studies (**Publications I-III**). In this section, I will present the works which concentrate on the astrocyte network topology (**Publication I, II, III**) and how this relates to the control of the neuronal activity. All those works are built upon the neuron-astrocyte network model INEXA (Lenk et al., 2020). In the chapter, the pre-existing model will be described, as well as the modification applied for each of the studies. Figure 4.1 describes the studies implementations steps and the methods used for each publication of Chapter 5.

Chapter 6 outlines the experimental work done for this thesis (**Publication IV-V**). This section of my thesis concentrates on the roles of astrocytes in controlling gliotransmission and ionic homeostasis in-vitro. In the first article described in this section, we elicited hyperactivity with two convulsant drugs, 4-aminopyridine, and gabazine, which block  $K^+$  voltage-gated channels and  $GABA_A$  receptors, respectively, thus interjecting with the ionic homeostasis and gliotransmission (**Publication IV**). The second paper described in this section concentrates on the analysis of the signal shape and patterning in rat cortical neuron cultures and rat cortical neuron-astrocyte co-cultures, in order to study the effect of astrocytes in modulating the spike shapes and the patterning of the spikes (**Publication V**). Figure 4.2 outlines the methods used for each publication of Chapter 6.

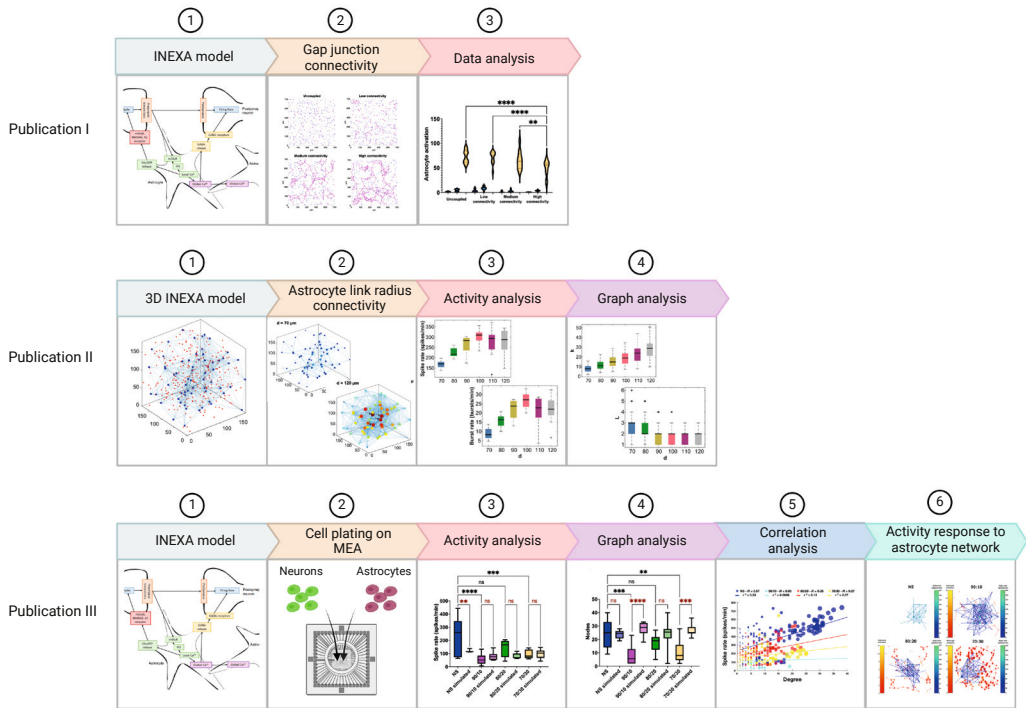


**Figure 4.1** Design of the computational studies which will be explained in Chapter 5. Created with BioRender.com.

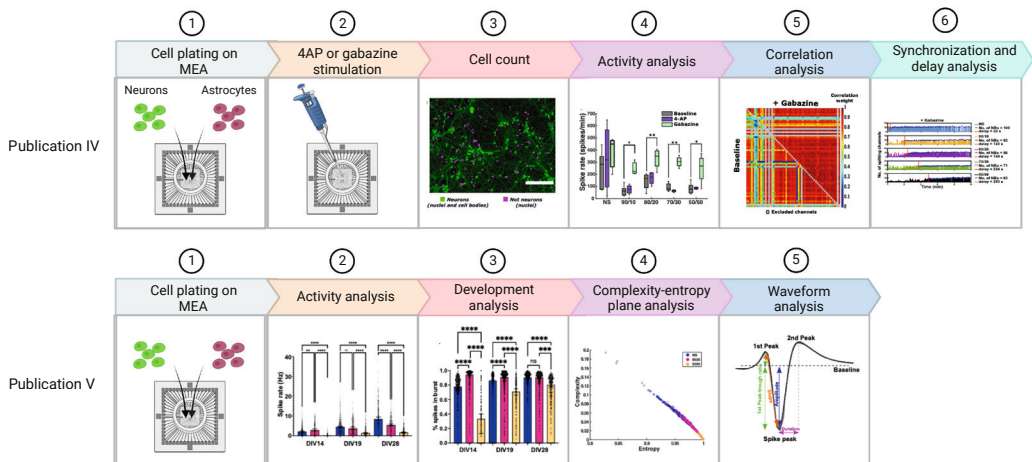


**Figure 4.2** Design of the experimental studies described in Chapter 6. Created with BioRender.com.

# 5 AIM 1: COMPUTATIONAL STUDY OF THE ASTROCYTE NETWORK TOPOLOGY EFFECTS OF NEURONAL ACTIVITY

## 5.1 Methods

### 5.1.1 Computational description of the neuron-astrocyte network and its pathways

#### INEXA model

This phenomenological model emulates a planar *in vitro* neuron-astrocyte co-culture. The neuronal and astrocytic networks are randomly created to reproduce a 2D MEA culture surface of  $750 \times 750 \mu\text{m}^2$  (Fig. 5.2A). The astrocytes and neurons nuclei were randomly placed with the following constraints: the inter-soma distances for the astrocytes had to be larger than  $30 \mu\text{m}$  and for the neurons larger than  $10 \mu\text{m}$ , otherwise, the astrocyte, or the neuron, was relocated.

After placing the cells, the connections were made between the astrocytes as a step function, where all the astrocytes with inter-soma distance smaller than  $100 \mu\text{m}$  were connected (Fig. 5.2B).

The neuronal connectivity probability ( $P_{NN}$ ) rule instead followed a scaled Gaussian probability distribution dependent on the neurons inter-soma distance ( $d$ ) (Fig. 5.2B):

$$P_{NN}(d) = e^{-\frac{d^2}{2\sigma_N^2}} \quad (5.1)$$

The connections between neurons and astrocytes, also follow a Gaussian probability distribution dependent on the distance. However, the probability was limited by a cutoff distance after which no connections are possible ( $d_A$ ), which was set equal

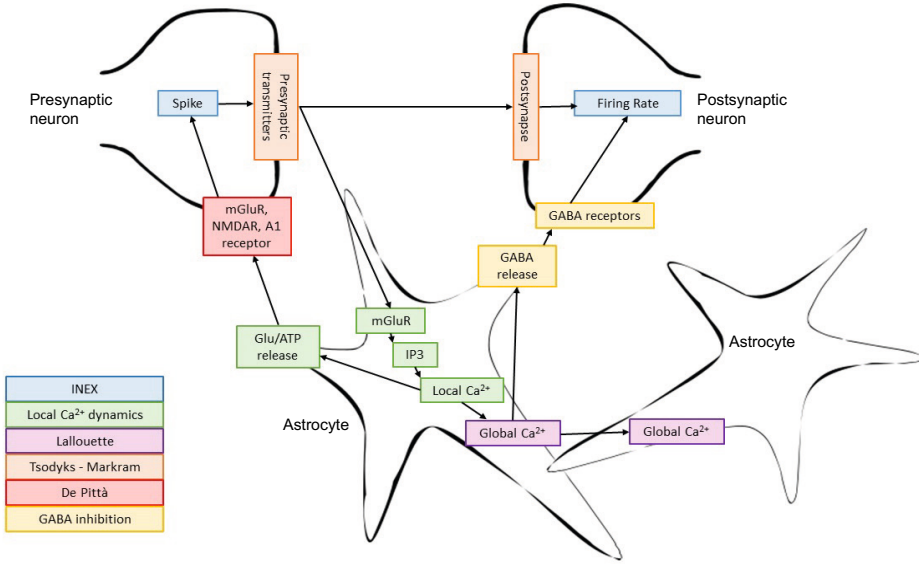


**Figure 5.1** Pathway scheme of the INEXA model. The colored boxes describe the elements comprised in the model and which original model was used to describe these parts. The model consists of multiple excitatory synapses, each of which can be connected to an astrocyte. The communication pathways of each individual tripartite synapse in the network are illustrated in the figure. The pre- and post-synaptic spiking were modeled similarly to the INEX model (depicted in blue boxes). The Tsodyks-Markram synapse model (in orange) and De Pittà's astrocyte gliotransmitter model (in red) were added to the spiking generation. The local astrocyte  $\text{Ca}^{2+}$  dynamics (in green) trigger gliotransmission to the synapse. The  $\text{Ca}^{2+}$  signaling was modeled according to the UAR model (in violet) by Lallouette et al. The local and global  $\text{Ca}^{2+}$  dynamics stimulate the release of GABA into the extracellular space by the astrocyte (in yellow) to restrict the spiking of nearby post-synaptic neurons.

to  $70 \mu\text{m}$  (Fig. 5.2B).

$$P_{AN}(d) = e^{-\frac{d^2}{2\sigma_A^2}} \cdot H(d_A - d), \quad (5.2)$$

where  $H(d_A - d)$  is the Heaviside function to limit the connection probability; in fact,  $H(d_A - d) = 1$  if  $d_A - d > 0$ , and  $H(d_A - d) = 0$  otherwise.

The neuronal part of the model is based on INEX (Lenk, 2011). INEX is a stochastic model of excitatory and inhibitory neurons connected with synapses. The astrocytes are then incorporated into the INEX model by adapting the spiking probability for the pre- and post-synaptic terminal to account for the excitatory and inhibitory effects of the astrocytes.

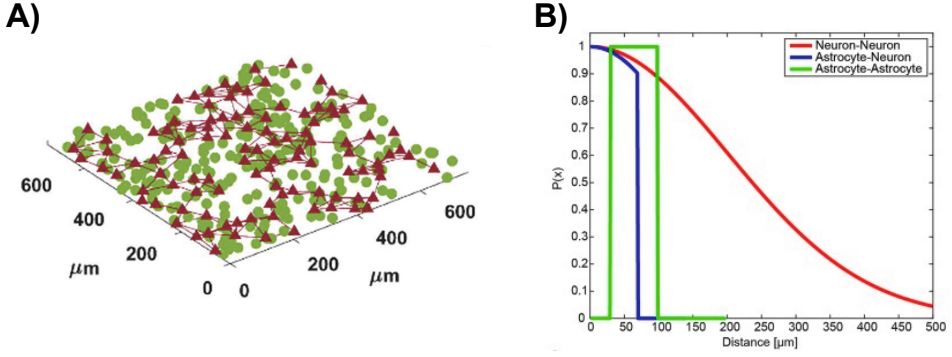


**Figure 5.2** A) Planar topology of the neuron-astrocyte network. Neurons are displayed as green dots and astrocytes as red triangles. Astrocyte-astrocyte connections are shown as red links. B) Connection probability rules used in the model. Neuron-neuron connections (in red) follow a Gaussian probability based on the distance between the neurons. Astrocyte-neuron connection probability (in blue) follows a Gaussian distribution until it reaches a max distance limitation which drops the probability to zero. Astrocyte-astrocyte connections (in green) are formed only if the distance between the two cells is comprised in the limits. Illustrations reproduced with permission from: Lenk et al., 2020

The presynaptic neuron dynamics are described by the Tsodyks-Markram (TM) model (Tsodyks et al., 1998). The TM model describes the dynamics of the fraction of neurotransmitters available in the presynaptic terminal,  $x$ , and the fraction of  $x$  that are ready for release,  $u$ . The mathematical description of the model is:

$$x_{ij}(t_k) = (x_{ij}(t_{k-1}) - RR_{ij}(t_k)) + [1 - (x_{ij}(t_{k-1}) - RR_{ij}(t_k))](1 - e^{-\Omega_d t}) \quad (5.3)$$

$$u_{ij}(t_k) = [(1 - u_{ij}(t_{k-1}))U_{ij}^*(t_k)s_j(t_k)]e^{-\Omega_f \Delta t} \quad (5.4)$$

$$RR_{ij}(t_k) = x_{ij}(t_{k-1})[(1 - u_{ij}(t_{k-1}))U_{ij}^*(t_k)s_j(t_k)]s_j(t_k) \quad (5.5)$$

where  $\Omega_d$  represents the rate of reintegration of neurotransmitters in the presynaptic terminal,  $\Omega_f$  the rate of decrease of release probability,  $RR_{ij}$  the fraction of released neurotransmitters, and  $U_{ij}^*$  describes the maximal increment of the ready-for-release fraction triggered by the arrival of a presynaptic spike. The excitatory effect of the gliotransmitters released by the astrocytes affects the value of  $U_{ij}^*$  as

follows:

$$U_{ij}^*(t_k) = \frac{y_{ij}^{base}}{Y_{max}} (1 - g_{ij}(t_k)) + \alpha g_{ij}(t_k) \quad (5.6)$$

where  $g_{ij}(t_k)$  is the fraction of bound presynaptic gliotransmitter receptors,  $Y_{max}$  represents the maximum excitatory strength a synapse can have, and  $y_{ij}^{base}$  is the basal synaptic strength of the synapse  $ij$  in absence of gliotransmission. The potentiating effect of the astrocytes is modeled as in De Pittà et al., 2011 and De Pittà et al., 2012, where the parameter  $\alpha$  describes the co-operative effect of multiple receptors. This parameter can describe both a depressing gliotransmission if  $0 < \alpha < \frac{y_{ij}^{base}}{Y_{max}}$ , and a potentiating gliotransmission if  $\frac{y_{ij}^{base}}{Y_{max}} < \alpha < 1$ . In INEXA,  $\alpha$  is set equal to 0.7 and  $\frac{y_{ij}^{base}}{Y_{max}} < 0.7$  to describe the potentiating effect of gliotransmission on the presynaptic spiking.

The spiking activity of the postsynaptic neuron depends on the activity of the presynaptic neuron, on the background noise, and on the spiking history of the presynaptic neuron. In addition to those, the INEXA model describes the depressing effect of the inhibiting gliotransmitters (e.g. adenosine or GABA) released by the astrocytes. The postsynaptic firing rate is calculated as follows:

$$\lambda_i(t_k) = \max(0, c_i + \sum_j y_{ij} s_j(t_{k-1}) - \sum_j y_{astro} A_{ija}(t_{k-1})) \quad (5.7)$$

where,  $c_i$  is the noise applied to the postsynaptic neuron  $i$ ,  $y_{ij}$  is the synaptic strength of the connection between the presynaptic neuron  $j$  and the postsynaptic neuron  $i$  and  $s_j$  represent the spiking history of the presynaptic neuron  $j$  at the previous time step. If the presynaptic neuron emitted a spike at  $t_{k-1}$ ,  $s_j$  is equal to 1, otherwise is zero. The terms accounting for the astrocytic effect are the synaptic weights  $y_{astro}$  and  $A_{ija}$ , which is equal to one if synapse  $ij$  is connected to the astrocyte  $a$  and if  $a$  was in the active state at the previous time-step. Otherwise,  $A_{ija} = 0$  and no depressing effect is applied to the synapse.

Based on the firing rate  $\lambda_i$ , the probability for the postsynaptic neuron to fire a spike at the time stamp  $t_k$  is calculated as follows:

$$P_i(t_k) = e^{-\lambda_i(t_k)\Delta t} \lambda_i(t_k)\Delta t \quad (5.8)$$

The INEXA model describes also the calcium signaling in the astrocyte network

mediated by the gap junctions. To model the activation and deactivation of the astrocytes, INEXA uses the model originally proposed by Lallouette et al., 2014 and Lallouette et al., 2018. Lallouette and colleagues describe the astrocyte network as a graph where the astrocytes are the nodes and the gap junctions are the links between the nodes. The node  $a$ , such as an astrocyte, can have three possible states  $S_a$ : active state  $A$ , inactive dormant state  $U$ , and refractory state  $R$ . The astrocyte can transition between these three states depending on the state in which currently is, and on the propagation of signals between connected astrocytes.

The probability for the transition from the dormant state to the active state,  $U \rightarrow A$ , depends on the coupling between astrocytes, and the propagation efficiency of  $\text{Ca}^{2+}$  through them:

$$P(U \rightarrow A)_a(t_k) = \begin{cases} \frac{\Delta t}{\tau_A}, & \text{if } \gamma_a(t_k) > \theta_a(n_a) \\ 0, & \text{otherwise} \end{cases} \quad (5.9)$$

The detailed description of the activation propensity  $\gamma_a(t_k)$  and the threshold  $\theta_a(n_a)$  can be found in Lenk et al., 2020. The transitions between active to refractory,  $A \rightarrow R$ , and refractory to dormant,  $R \rightarrow U$ , are spontaneous and dependent on their time scale  $\tau_R$  and  $\tau_U$ .

$$P(A \rightarrow R)_a(t_k) = \frac{\Delta t}{\tau_R} \quad (5.10)$$

$$P(R \rightarrow U)_a(t_k) = \frac{\Delta t}{\tau_U} \quad (5.11)$$

In silico modeling of gap junction coupling using the INEXA model

Since several experiments report that a loss of astrocytic gap junctions increases the susceptibility to seizures, in **Publication I**, in order to study how the different astrocytic gap junction coupling conditions affected the neuronal activity, I modified the connection probability function for the astrocyte-astrocyte connections.

The connection probability for the astrocyte-astrocyte connections was modified from a step function to a Gaussian probability function dependent on the inter-soma distance  $d$ .

$$P_{AA}(d) = e^{-\frac{d^2 - \mu_A}{2\sigma_A^2}} \quad (5.12)$$

To force the different connectivity levels of the astrocytes I varied the standard deviation for the Gaussian distribution ( $\sigma_A$ ). The mean for the Gaussian distribution ( $\mu_A$ ) was instead kept fixed at zero.

In **Publication I**, we simulated three different astrocyte connectivity levels, for this thesis the work was extended simulating four coupling conditions. The fully uncoupled gap junctions condition was simulated forcing a standard deviation for the Gaussian distribution smaller than the minimum connection distance allowed for the astrocytes. The standard deviation was in this case  $\sigma_A = 10 \mu\text{m}$ ; in this way, no astrocytes could be found for the connections. To simulate the low connectivity condition it was chosen a standard deviation equal to the minimum connection distance allowed ( $\sigma_A = 30 \mu\text{m}$ ); this led to an average of about one gap junction for each astrocyte. The medium connectivity condition was simulated with a standard deviation  $\sigma_A = 50 \mu\text{m}$ , and for the high gap junction connectivity condition, the standard deviation was chosen to be  $\sigma_A = 80 \mu\text{m}$ . All the higher values of standard deviation always led to the same connectivity level of about four gap junctions on average for each astrocyte in the network. Table 5.1 summarizes the parameters used.

For this study, the neuronal network comprised 250 neurons, of which 200 were excitatory and 50 inhibitory. The average number of excitatory synapses was 10,000. The number of astrocytes in the network was set to 107, leading to a neuron-astrocyte network where 70% of the total cells were neurons and 30% were astrocytes. Each astrocyte was then connected to an average of 90 excitatory synapses.

As background network activity three different input noise levels were used to simulate the case of low, high, and hyper-activity. The noise level for the high activity was set to three times the noise level for the low activity, and the hyperactivity noise level was eight times the low noise value.

The simulated time for these simulations was 180 s, with a time step of 5 ms. Each combination of conditions (coupling-noise) was simulated ten times. Each network was created from scratch at the beginning of each of the ten simulation runs; and with the same network, the three different noise levels were then simulated.



**Table 5.1** Parameters used to force the coupling conditions in the simulations.

Coupling	$\sigma_A$	Avg gap junctions
Uncoupled	10 $\mu\text{m}$	$0.002 \pm 0.006$
Low	30 $\mu\text{m}$	$1.03 \pm 0.08$
Medium	50 $\mu\text{m}$	$2.94 \pm 0.21$
High	80 $\mu\text{m}$	$3.90 \pm 0.18$

### Implementation of the 3D network topology in the INEXA model

The majority of the applications and cultures utilizing MEAs are with planar cultures; however, the structure of the brain is tridimensional. To investigate the differences between the planar and the 3D network structure, in **Publication II**, the computational neuron-astrocyte model INEXA, previously described in Section 5.1.1, was extended into a 3D network structure.

To translate the culture area from planar to 3D, the total volume was kept constant and the original planar virtual culture area,  $750 \times 750 \times 10 \mu\text{m}^3$ , was modified in  $180 \times 180 \times 180 \mu\text{m}^3$ . The neuron-astrocyte network comprised 250 neurons, of which 80% excitatory and 20% inhibitory, and 63 astrocytes. In this study, first, we compared the network features and the activity of the planar and the 3D network. In this case, the maximum astrocytic gap junction distance was  $d = 100 \mu\text{m}$  for both configurations. Then, we varied the distance ranges between two coupled astrocytes according to Lallouette et al., 2014, from 70 to 120  $\mu\text{m}$ , and compared the neuronal activity in those networks. The parameters used for the simulations are summarized in Table 5.2.

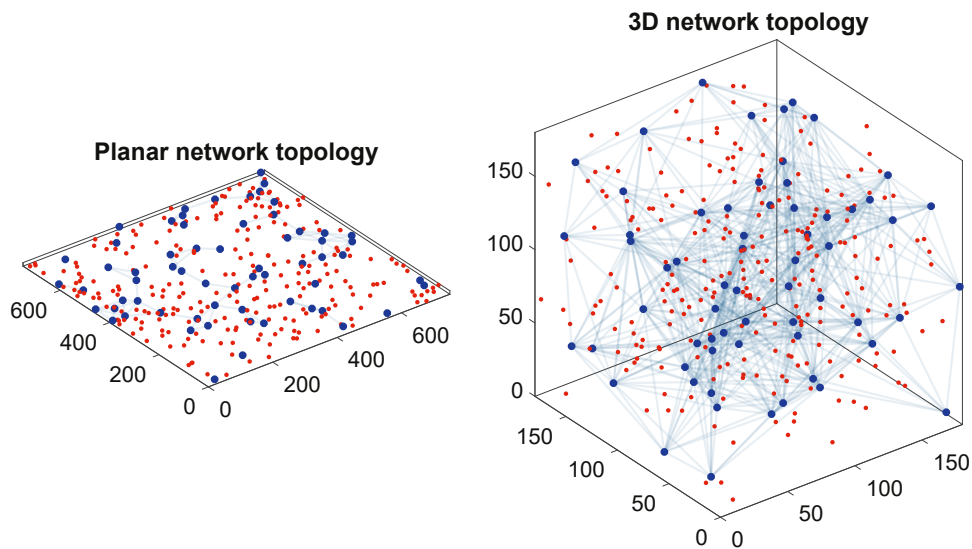


**Figure 5.3** Comparison between the planar (left) and the 3D (right) network structures in the neuron-astrocyte computational model INEXA. Neurons are in red and astrocytes are shown in blue, together with their connections. Figure reproduced with permission from **Publication II**.

**Table 5.2** Comparison of the characteristics of the planar and the 3D networks. Table modified with permission from **Publication II**.

Characteristics	Planar network	3D network
Dimensions [ $\mu\text{m}^3$ ]	750x750x10	180x180x180
Cell numbers	250 neurons, 63 astrocytes	250 neurons, 63 astrocytes
Noise	0.02	0.02
Synaptic strength	$\pm 0.7$	$\pm 0.7$
Max gap junction distance [m]	100	(a) 100, (b) 70 - 120

### 5.1.2 Data acquisition

#### Cell culturing and MEA preparation

Rat primary cortical neurons (A1084001; Thermo Fisher Scientific) and rat primary cortical astrocytes (N7745100; Thermo Fisher Scientific) were combined at various ratios to create cultures with different compositions. The desired ratios for

the cultures were: *NS*, containing only neurons and no added astrocytes; *90/10*, consisting of 90% neurons and 10% added astrocytes; *80/20*, with 80% neurons and 20% added astrocytes; and *70/30*, with 70% neurons and 30% added astrocytes. The number of neurons plated was kept constant at approximately 80,000 per MEA, and the number of astrocytes was adjusted accordingly to achieve the desired ratio. The cells were plated on either standard or thin 60-electrode MEAs (60MEA200/30iR; Multi Channel System MCS GmbH, Reutlingen, Germany). Details of the cell plating and MEA preparation are provided in Section 6.1.1 and in Lenk et al., 2021.

## MEA recording

Recordings of the cells were carried out at 28 days in vitro (DIV) with a sampling frequency of 25,000 Hz for 5 minutes. The raw signals were then subjected to filtering using a second-order bandpass filter (300-3000 Hz) and sorted using Wave Clus, a MATLAB tool (Chaure et al., 2018). To detect spikes, a signal threshold of  $\pm 5\sigma$  was used, where  $\sigma$  represents the standard deviation of the filtered signal.

### 5.1.3 Data analysis

#### Activity analysis

Both the simulated spike trains (**Publication I-III**) and the sorted MEA recordings (**Publication III**) were analyzed using a network-wide CMA algorithm to extract bursts (Välkki et al., 2017). Spike rate (SR; spikes per minute) and burst rate (BR; bursts per minute) were extracted. The single-channel SR and BR of the MEAs were averaged for each MEA. In **Publication III** to reproduce the recording of signals on the MEA plate, the activity of 60 simulated neurons was randomly selected. Each neuron was selected from the surrounding of each one of the virtual electrodes. From the simulated data of **Publication I-III**, we also extracted how many times each astrocyte in the networks entered the active state during the 5 minutes of simulation time. The active state was defined as in Section 5.1.1.

## Correlation analysis

In **Publication III**, we analyzed the correlation between SR and BR and the degree of the nodes in the different experimental cultures. We used both a Pearson's correlation analysis and a linear regression analysis. Lastly, we pairwise cross-correlated the binary spike trains of each experimental MEA channel data and the simulated spike train as well. We obtained cross-correlation matrices, and to further analyze these, we thresholded for correlation values higher than 0.65, to consider only channel pairs with high positive correlation.

## Graph analysis

In **Publication II**, to analyze the network structure I conducted a graph analysis of the 3D astrocyte network. The total number of cell bodies was defined as vertices,  $V_{astro}$ , while the gap junctions between the astrocytes were defined as links,  $E_{astro}$ . From the graphs created, I calculated the mean degree  $k$ , such as the mean number of links for each node, i.e. average gap junctions per astrocyte. The shortest path,  $L$ , was also calculated; this parameter describes the minimum amount of links needed to be crossed to connect two nodes. In this analysis, astrocytes were defined as *hub astrocytes* if they were connected to more than 75% of the neighbors. Moreover, I determined the number of active astrocytes,  $N_{act}$ , as the number of astrocytes that were in the active state at least once during the time course of the simulation.

In **Publication III**, from the spike cross-correlation matrices we constructed undirected graphs. We evaluated the number of nodes, the number of edges, the mean degree of the networks, and the mean shortest path. In this analysis, nodes were those channels or simulated neurons with at least one connection to another one; edges were defined as the connections with cross-correlation values higher than 0.65, the mean degree is the mean number of connection for the channels and the mean shortest path is the minimum amount of connections needed to be crossed to connect any pair of nodes. A similar graph analysis was conducted for the astrocytic network in the case of the simulated data. In this case, the edges were the simulated gap junctions, and thus the mean degree was the average number of gap junctions for each astrocyte. For the simulated data, we combined then the two graph analyses of neuronal activity and astrocyte network with the activity analysis, such as SR. The code with the implementation of the graph analysis and the data from Publi-

tion II is publicly available online on GitHub at [https://github.com/barbara-ge/INEXA\\_IEEETransMolBiolMulti-ScaleCommun2020-1](https://github.com/barbara-ge/INEXA_IEEETransMolBiolMulti-ScaleCommun2020-1); while the repository with the full code and the data from Publication III is available at <https://github.com/barbara-ge/ACM-NanoCom2021>.

## 5.2 Results

### 5.2.1 Gap junction uncoupling increases spike and burst rate

With the above-mentioned connectivity parameters (Sec. 5.1.1), we obtained four different levels of connectivity in the networks (Table 5.1, Fig. 5.4A). In the uncoupled case, the astrocytes had on average about 0 gap junctions (Fig. 5.4B); the low connectivity case resulted in an average of about one gap junction for each astrocyte (Fig. 5.4B), and the astrocyte network presented small subnetworks of coupled astrocytes, but still several uncoupled astrocytes (Fig. 5.4A). The medium connectivity resulted, instead in a mostly connected astrocyte network, with few small networks on the side of the simulated culture area. The high connectivity case resulted in an almost fully coupled network, with an average of four gap junctions for each astrocyte (Fig. 5.4A-B). Increasing the astrocyte connectivity, the astrocyte-synapses connectivity decreased slightly (Fig. 5.4C). The differences were not statistically meaningful, but a trend could be noticed.

The simulations show that the low noise condition elicited a general low SR, moreover, a very small number of activated astrocytes was observed (Table 5.3, Fig. 5.5). Bursting was mostly not present in the simulated networks, and the few present bursts had a comparable small duration and about three spikes/burst. Increasing the noise level increased the SR, BR and BD in all the coupling, as expected. While the SR increased, also the number of activated astrocytes was higher, making visible a decreasing trend in the SR and BR when increasing the coupling (Table 5.3, Fig. 5.5). The differences however were not statistically significant for the SR, and were significant only in the case of high noise high connectivity vs. uncoupled for the BR ( $p = 0.03$ ). On the other hand, the BD and the spikes/bursts seem to have an increasing trend for more connected astrocytes, at all noise levels. Higher astrocyte connectivity led to a visible decrease in astrocyte activation, especially in the high-noise case.

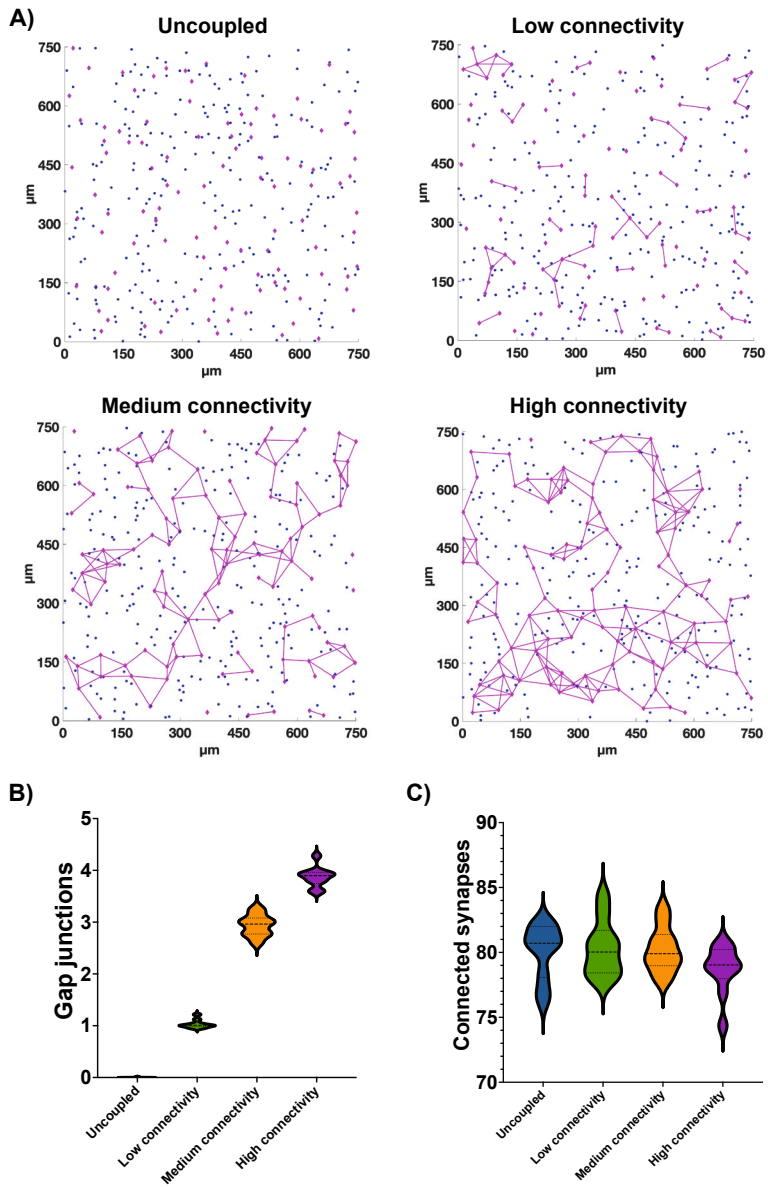


**Figure 5.4** Astrocyte networks couplings in neuron-astrocyte networks. A) Graphic representation of one of the ten networks created for each coupling level, from fully uncoupled to high connectivity. Astrocytes are displayed as diamonds in magenta, with their connections also shown in magenta. Neurons are represented by blue dots. Neuronal connections are not displayed for image clarity. B) Average gap junctions of each astrocyte for each of the ten runs for each coupling condition. C) Number of connected synapses on average to each of the astrocytes in the different coupling conditions.

**Table 5.3** Numerical results for the three simulated noise levels. For each noise level are shown: SR, spike rate (spikes/minute); BR, burst rate (bursts/minute); BD, burst duration (ms); spikes/burst, and astrocyte activation. The results are expressed as mean  $\pm$  standard deviation.

	Characteristics	Uncoupled	Low connectivity	Medium connectivity	High connectivity
Low noise	SR (spikes/minute)	25.7 $\pm$ 1.2	26.4 $\pm$ 1.2	26.3 $\pm$ 1.9	25.4 $\pm$ 1.2
	BR (burst/minute)	0.34 $\pm$ 0.01	0.37 $\pm$ 0.03	0.36 $\pm$ 0.02	0.36 $\pm$ 0.03
	BD (ms)	28.0 $\pm$ 4.2	25.1 $\pm$ 6.1	26.0 $\pm$ 4.8	27.4 $\pm$ 5.1
	Spikes/Burst	3.10 $\pm$ 0.05	3.10 $\pm$ 0.08	3.09 $\pm$ 0.06	3.07 $\pm$ 0.06
	Astrocyte activation	1.7 $\pm$ 0.8	3.7 $\pm$ 2.98	1.0 $\pm$ 1.6	0.5 $\pm$ 0.5
Medium noise	SR (spikes/minute)	93.0 $\pm$ 5.7	96.8 $\pm$ 7.7	96.2 $\pm$ 10.7	91.9 $\pm$ 5.2
	BR (burst/minute)	1.0 $\pm$ 0.2	1.1 $\pm$ 0.2	1.1 $\pm$ 0.3	1.0 $\pm$ 0.3
	BD (ms)	191.8 $\pm$ 56.1	155.1 $\pm$ 29.4	174.4 $\pm$ 46.2	175.9 $\pm$ 27.7
	Spikes/Burst	4.0 $\pm$ 0.2	3.9 $\pm$ 0.1	3.9 $\pm$ 0.1	3.9 $\pm$ 0.1
	Astrocyte activation	4.7 $\pm$ 2.2	8.5 $\pm$ 3.7	3.1 $\pm$ 2.3	3.5 $\pm$ 1.6
High noise	SR (spikes/minute)	224.3 $\pm$ 6.9	220.9 $\pm$ 6.0	219.5 $\pm$ 8.2	217.2 $\pm$ 6.3
	BR (burst/minute)	10.8 $\pm$ 1.9	9.5 $\pm$ 1.8	9.6 $\pm$ 2.4	8.7 $\pm$ 1.6
	BD (ms)	271.9 $\pm$ 22.6	262.3 $\pm$ 34.3	264.1 $\pm$ 36.4	277.5 $\pm$ 31.8
	Spikes/Burst	4.7 $\pm$ 0.1	4.7 $\pm$ 0.1	4.7 $\pm$ 0.1	4.8 $\pm$ 0.1
	Astrocyte activation	73.2 $\pm$ 13.1	70.6 $\pm$ 12.9	65.9 $\pm$ 19.1	49.0 $\pm$ 17.0

## 5.2.2 Network topology comparison between the planar and the 3D networks

When looking at the two different configurations, the planar and the 3D network, for the neuronal network, our results highlighted that the neuronal network connectivity was similar, 26.72% for the planar and 27.83% for the 3D configuration. The maximum amount of possible neuron-neuron connections was, for both, 62250 connections, such as the case of a fully coupled network where all the 250 neurons were connected to all the other 249 neurons. However, the average number of neuron-neuron connections was 66.52% for the planar network and 69.31% for the 3D configuration. The number of two-directional connections between neurons was 4924 in the planar network and 2719 connections in the 3D network. Since the side length of the 3D culture area was shorter (180 m, and 750 m in the planar culture area), this resulted in a shorter average neuron connection length in the 3D network. These lengths were 101.55 m for the 3D network and 209.67 m for the planar network.

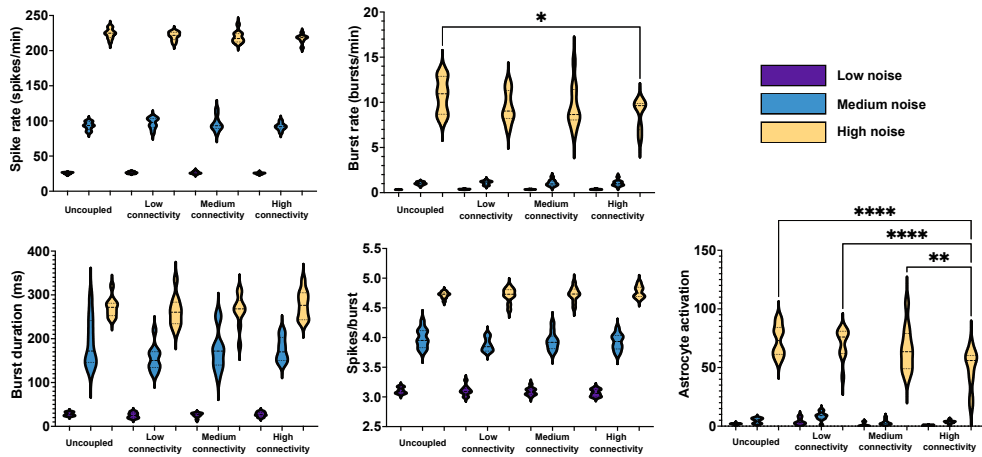


**Figure 5.5** Gap junction coupling activity analysis. The figure shows the spike rate (spikes/minute), burst rate (bursts/minute), burst duration (ms), spikes/burst, and astrocyte activation for the three simulated noise levels. The results for the low noise case are displayed in violet, for the medium noise in blue, and for the high noise in yellow. \*  $p < 0.05$ , \*\*  $p < 0.01$ ; \*\*\*  $p < 0.001$ ; \*\*\*\*  $p < 0.0001$ .

The astrocyte networks presented considerably more differences in the two configurations. Starting from the average gap junction connections each astrocyte had, was 2.70 for the planar network, while for the 3D network configuration was considerably higher (19.61 for each astrocyte). The highest amount of gap junction in the planar network was 7, while the minimum was 0; in the 3D network, the maximum gap junction amount was 35, and the minimum was 7. Even if the network was considerably more connected in the 3D network, the average distance between connected astrocytes did not decrease. It was 66.82 m in the planar network and 72.05 m in the 3D network. Higher connectivity was found in the 3D network also for neuron-astrocyte connections, which were 169.91 in the planar network versus 220.85 for the 3D network. Also, in the 3D network, no not astrocyte-controlled excitatory synapses were found, while in the planar network, the free excitatory synapses were 2500, resulting in 18.93% of all the excitatory synapses. The results here described are summarized in Table 5.4.

*Graph analysis comparison between the planar and the 3D network configurations.* As anticipated in the previous section, the 3D network presented higher astrocyte-astrocyte connectivity, resulting in an average mean degree  $k$  of  $19.61 \pm 7.30$ , versus the planar network in which it was  $2.70 \pm 1.53$ . As a reminder, the mean degree



**Table 5.4** Topological features of the two network configurations, planar and 3D. The features are subdivided into those of the neuronal network in the first section (N-N network); those of the astrocyte network in the middle section (A-A network); and, those for the neuron-astrocyte network in the last section (A-N network). Table modified from **Publication II**.

	Characteristics	Planar network	3D network
N-N network	Max. amount of NN connections	62250	62250
	Average neuron connections to other neurons	66.52	69.31
	Network connectivity [%]	26.72	27.83
	Average neurons connection length [ $\mu\text{m}$ ]	209.67	101.55
	Two directional connections between neurons	4924	2719
A-A network	Average gap junction connections	2.70	19.61
	Highest / lowest gap junction amount	7 / 0	35 / 7
	Average distance between connected astrocytes [ $\mu\text{m}$ ]	66.82	72.05
A-N network	Average number of astrocyte-neuron connections	169.91	220.85
	Excitatory synapses without an astrocyte	2500	0
	% of not astrocyte-controlled excitatory synapses	18.93	0.00

has here the meaning of the average number of gap junction connections for each astrocyte in the network. With the fixed maximum gap junction connection length set at 100  $\mu\text{m}$ , the planar network resulted in a not fully connected network and presented three subnetworks. These subnetworks had different dimensions, and they showed variable shortest path lengths  $L$ : (a)  $4.57 \pm 2.37$ , (b)  $3.89 \pm 2.20$ , (c)  $1.33 \pm 0.49$ . The 3D network instead was fully connected and presented a shortest path  $L$  of  $1.82 \pm 0.65$ . Even though the 3D network had higher connectivity the number of activated cells  $N_{act}$  was lower compared to the planar network ( $4.20 \pm 0.91$  for the 3D configuration versus  $8.00 \pm 3.20$  for the planar one). The results for the mean degree  $k$  and the shortest path  $L$  are averaged over all the 63 astrocytes in the network, while the number of activated astrocytes  $N_{act}$  over the ten simulation runs. The results are summarized in Table 5.5.

*Activity analysis in the planar and the 3D network configurations.* The spike rate and burst rate in the 3D network were considerably higher than in the planar net-

**Table 5.5** Graph analysis comparison for the planar and the 3D networks.  $k$  and  $L$  are displayed with mean and standard deviation over all astrocytes.  $N_{act}$  has the mean and standard deviation calculated over all the ten simulation runs. Table modified from **Publication II**.

Characteristics	Planar network	3D network
Mean degree $k$	$2.70 \pm 1.53$	$19.61 \pm 7.30$
Shortest path $L$	(a) $4.57 \pm 2.37$ , (b) $3.89 \pm 2.20$ , (c) $1.33 \pm 0.49$	$1.82 \pm 0.65$
Number of activated cells $N_{act}$	$8.00 \pm 3.20$	$4.20 \pm 0.91$

work. The average SR was  $301.47 \pm 37.79$  spikes/min for the 3D network, and  $69.18 \pm 3.17$  spikes/min. The average BR was  $26.80 \pm 4.05$  for the 3D network and  $1.08 \pm 0.17$  for the planar. When looking at the coefficient of variation (CV; standard deviation/mean) of the spike rate it can be noted that the 3D neuronal network had a higher spike variability, and had a percent CV of 12.5%; while the planar network had a percent CV of 4.6%. The burst rate instead was much more consistent in its variability, it presented a percent CV of 15.7% for the planar network and 15.1% for the 3D network. Together with an increase in the burst rate, the 3D network showed also longer bursts, with an average burst duration of  $193.89 \pm 46.93$  ms. The planar network presented bursts lasting on average for  $36.22 \pm 2.76$ . Also, for what concerns the burst duration in the network, the 3D presented a much higher inner variability between the neurons; the percent CV of the burst duration was 24.2% for the 3D network and 7.6% for the planar network. Since the number of neurons and the connectivity in the two N-N networks were comparable, these differences in the activity in the 3D network are probably to be attributed to the different astrocytic network topology and the lower number of active astrocytes, not inhibiting the neuronal activity. The results are shown summarized in Table 5.6.

**Table 5.6** Activity comparison between the planar and the 3D networks. Spike rate, burst rate, and burst duration are displayed with mean and standard deviation over the ten simulation runs. Table modified from **Publication II**.

Characteristics	Planar network	3D network
Spike rate [spikes/min]	$69.18 \pm 3.17$	$301.47 \pm 37.79$
Burst rate [bursts/min]	$1.08 \pm 0.17$	$26.80 \pm 4.05$
Burst duration [ms]	$36.22 \pm 2.76$	$193.89 \pm 46.93$

*Alteration of the connection radius of astrocyte in the 3D networks.* In the second part of the study, as previously described we varied the max reach distance  $d$  between astrocytes in the networks. The results of this second part showed that the astrocytic mean degree  $k$  increased with increasing the distance  $d$ , while the shortest path  $L$  and the number of activated astrocytes  $N_{act}$  decreased with increasing the max reach distance  $d$  (Figure 5.6). These results are analogous to those obtained in the comparison between the planar and the 3D networks, where an increased  $k$  is followed by a decreased  $L$  and  $N_{act}$ . The neuronal SR and BR increased when increasing the distance until  $d = 100$  m, and then it remains more or less constant for  $d = 110$  m and  $d = 120$  m (Figure 5.6). The burst duration also increased from  $d = 70$  m to  $d = 100$  m, and then decreased maintaining a high variability (Figure 5.6). Again analogously to the results obtained in the previous section, SR and BR were higher in the presence of higher astrocytic mean degree  $k$  and lower  $N_{act}$ . In Figure 5.7, the two network topologies for  $d = 70$  m and  $d = 120$  m are displayed. The node dimension and color represent the degree of the node, ranging from 2 to 16 for  $d = 70$  m, and from 10 to 51 for  $d = 120$  m. As expected, the nodes with the higher degree were located in the center of the network in both configurations. When analyzing the hub astrocytes, such as those connected to more than 75% of the neighboring astrocytes, we obtained that for  $d = 70$  m none was found, while for  $d = 120$  m there were four hub astrocytes (indicated in Figure 5.7 by black arrows). Figure 5.8 shows the spike rate for the neurons for the six different astrocytic maximum connection distances  $d$ . The neuronal network was kept constant so that the differences in spike rate were to be attributed only to the astrocyte network topologies. The neuronal spike rate, however, was already commented while referring to Figure 5.6. Here, instead, it can be noted that the neurons in the center were presenting a higher spike rate compared to the others in the network for all the distances; this most probably reflects the higher number of connections for the synapses in the center of the topology, increasing the stimuli eliciting the neuronal activity.

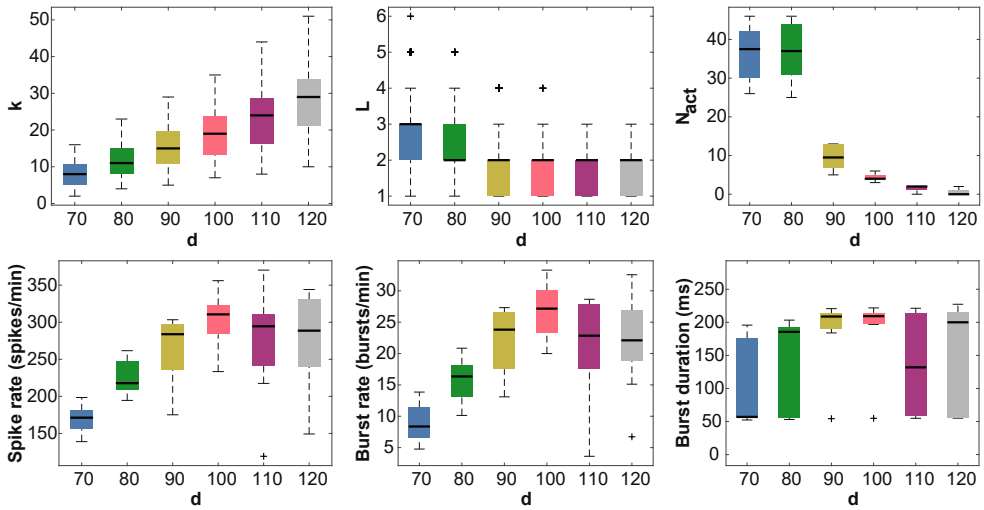


**Figure 5.6** Comparison between the graph analysis conducted on the astrocytic networks and the neuronal activity features for the different astrocytic link distances  $d$  simulated.  $k$  represent the astrocytic mean degree,  $L$  describes the mean shortest path Figure reproduced with permission from **Publication II**.

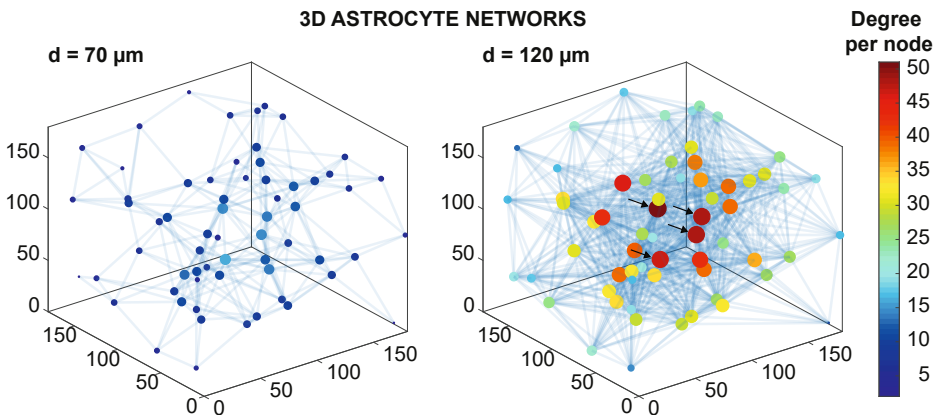


**Figure 5.7** Network topologies with mean degree  $k$  for the two distances  $d = 70 \text{ m}$  and  $d = 120 \text{ m}$ . The degree of the node is represented by the dimension and the color of the node itself. Light blue bars between the nodes represent the links. The black arrows in  $d = 120 \text{ m}$  represent the hub astrocytes. Figure reproduced with permission from **Publication II**.

### 5.2.3 Comparison between the activity and the topology of in vitro and in silico neuron-astrocyte networks

The neuronal and neuron-astrocyte computational networks here used were simulated with the previously described model INEXA (Section 5.1.1)(Lenk et al.,

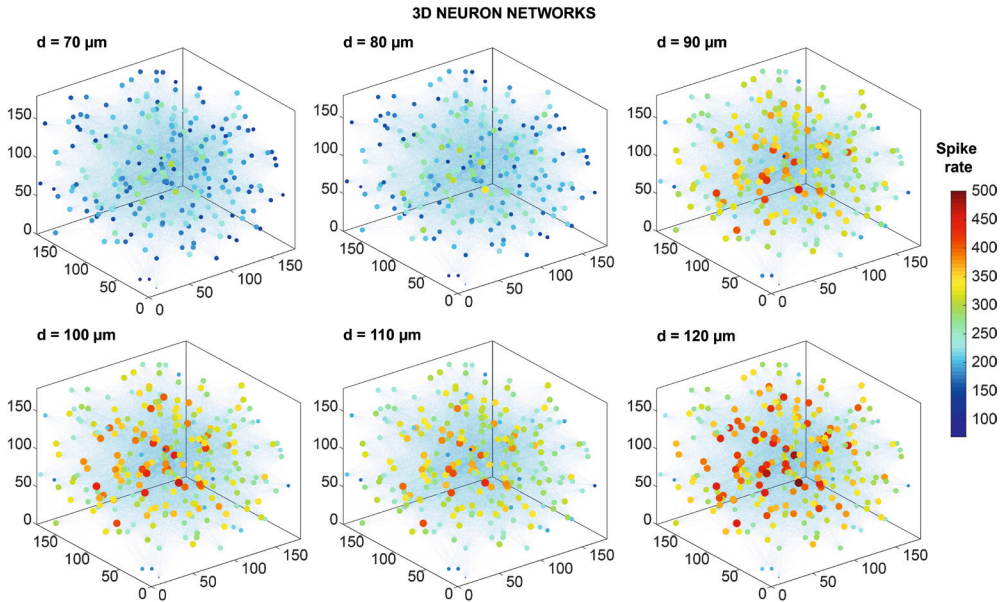


**Figure 5.8** Spike rate graph for the neuronal network for the six different max astrocyte connection distances. The neuronal topology here shown was kept constant. The nodes represent the neurons, and their color and dimension are the spike rate expressed in spikes/min. Axes are in  $\mu\text{m}$ . Figure modified with permission from **Publication II**.

2020), in its planar configuration. This better resembles the plating configuration of standard MEAs, described in Section 5.1.2. Similarly to the experimental setup, we simulated four different networks. *NS* comprised 250 neurons, of which 200 were excitatory and 50 inhibitory; the co-cultures were simulated adding to the neuronal network different amounts of astrocytes: 28 for the 90/10, 62 for the 80/20 and 107 for the 70/30. We simulated 5 minutes of activity and we ran each simulation 10 times.

*Co-cultures showed lower spike rate and burst rate.* In Publication III (Lenk et al., 2021) we analyzed and compared experimental data and simulated data of co-cultures with similar shares of neurons and astrocytes in the culture. Both the experimental and simulated data presented a higher SR and BR for the *NS* cultures (Fig. 5.9). Experimental data and simulated data showed comparable data for all the co-cultures, even though the BR of 80/20 was significantly different ( $p = 0.045$ ). The simulated data was not able to replicate the high inner variability obtained from the *NS* cultures, which resulted in a much higher standard deviation for the experimental data.

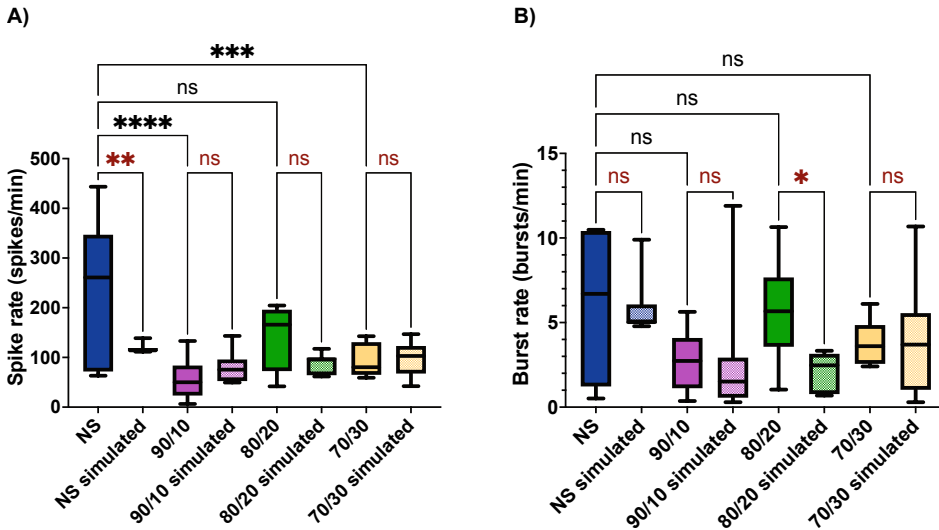


**Figure 5.9** Comparison between experimental data and simulated data. A) Spike rate (spikes/min), and B) burst rate (bursts/min) for NS and the co-cultures. Experimental data is shown in solid colors, while simulated data is shown with the square patterned filling. Statistical comparisons between the experimental cultures are shown in black, while the comparisons between experimental and simulated data are in red. *ns*  $p > 0.05$ ; \*  $p < 0.05$ ; \*\*  $p < 0.01$ ; \*\*\*  $p < 0.001$ ; \*\*\*\*  $p < 0.0001$ .

*Graph analysis of the neuronal activity.* The graph analysis was created for the experimental data from the correlation matrix between the spike trains of the electrodes of each MEA. This analysis showed for the experimental data a higher number of nodes in NS compared to the co-cultures (Fig. 5.10 A). As a reminder, we defined nodes as those electrodes with at least one connection to another electrode with a weight higher than 0.65. Simulated data did not show differences between the different conditions. When comparing the experimental data and the simulated data we can notice that NS and 80/20 were comparable, while in the experimental data, the nodes for 90/10 and 70/30 were lower, even though the SR were comparable (Fig. 5.10 A). The mean degree in the NS culture of the experimental data showed very high inner variability, which was not found in the simulated data (Fig. 5.10 B). The experimental data showed a much lower mean degree for the co-cultures compared to NS; this was visible also in the simulated data but with a less important difference, which was not statistically significant (Fig. 5.10 B). The mean degrees in the simulated data and the experimental data proved to be always comparable and no statistically meaningful differences were noticed. The mean shortest path for the



precise information on the connections and their weights. As expected for networks with more astrocytes more connections, and thus a higher mean degree, were found (Fig. 5.12 A); also the mean shortest path was higher for simulated co-cultures with more astrocytes (Fig. 5.12 B). The increase in connections did not correlate with an increase in the astrocytes activation, which was comparable in all the simulated cultures (Fig. 5.12 C).

*Activity response to the astrocyte network topology.* For the simulated data, we combined the graph analysis from the astrocyte topologies with the relative SR and correlation analysis of the 60 electrodes of the simulated MEAs. In Figure 5.13, the mean SR of the electrodes ranges from blue to green; each electrode is represented by a dot and its color reflects the SR, while the dot dimension reflects the degree. Only the links, the blue lines, with weights higher than 0.65 have been plotted. The astrocytes are here represented by diamonds in which the color, ranging from red to yellow, represents how many times the astrocyte got activated during the simulated time; the diamond dimension instead represents the degree. From Figure 5.13 can be noted that neurons with higher SR are not always those with a higher degree. Electrodes with fewer astrocytes in the neighboring showed higher SR. The astro-

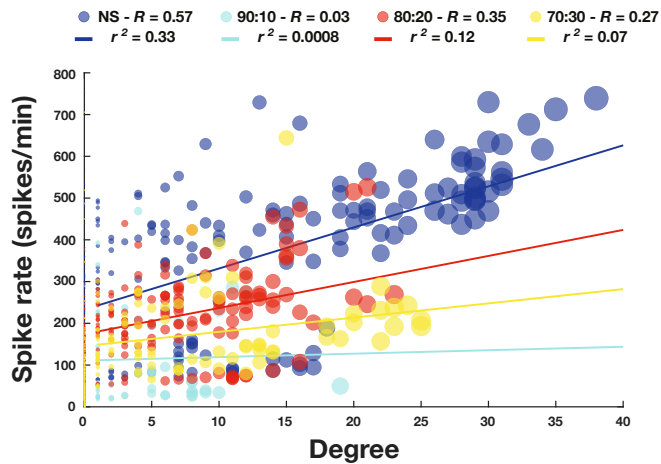


**Figure 5.11** Pearson's correlation analysis  $R$  in the experimental data to determine the relationship between the spike rate and the degree of the electrodes. Each electrode on the MEAs is represented by a circle, where the size of the circle represents the node centrality based on the cross-correlation values of the edges of the node. Linear regression models with the relative  $r^2$  are depicted by solid lines. Figure reproduced with permission from **Publication III**.



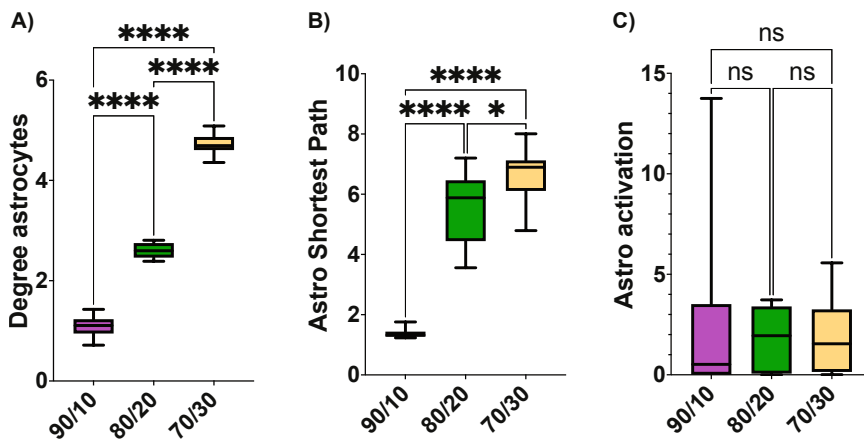


**Figure 5.12** Astrocyte network topology graph analysis. A) Mean degree (i.e., the gap junctions), B) the mean shortest path, and C) the mean number of times in which an astrocyte entered the active state. <sup>ns</sup>  $p > 0.05$ ; \*  $p < 0.05$ ; \*\*  $p < 0.01$ ; \*\*\*  $p < 0.001$ ; \*\*\*\*  $p < 0.0001$ . Figure reproduced with permission from **Publication III**.

cyte activation clearly depends on the activity of the neighboring neurons, rather than on the astrocyte degree, as seen already from Figure 5.12 C.

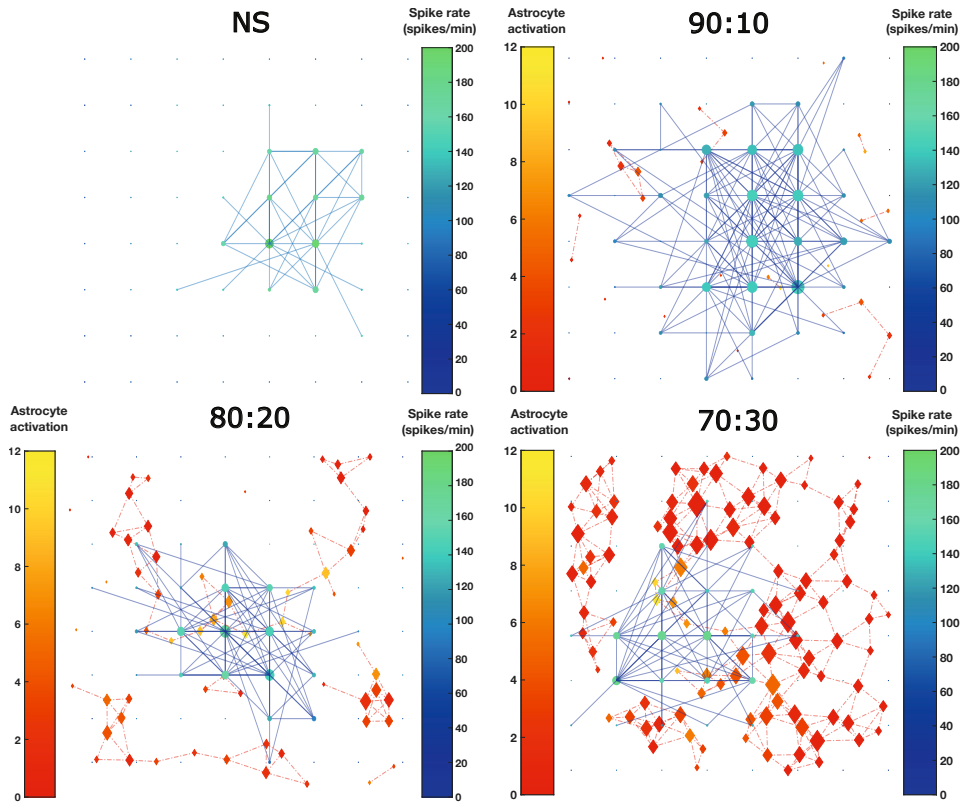


**Figure 5.13** Activity response to the astrocyte network topology. The figure displays the response of activity to the topology of the astrocyte network. It depicts 60 selected neurons as dots, with solid blue lines indicating the neuronal connections based on cross-correlation (edge weight > 0.65). The dot diameter indicates the mean degree of the neuron, while the dot color represents the spike rate expressed in spikes/min and ranges from blue (low) to green (high). The astrocytes are shown in a diamond shape, and their gap junctions are represented by dot-dashed red lines. The color of the diamond reflects the astrocyte activation, defined as the number of times the particular astrocyte was activated and ranges from red (low) to yellow (high). The size of the diamond indicates the degree of the astrocyte. Figure reproduced with permission from **Publication III**.

## 6 AIM 2: EXPERIMENTAL STUDY OF THE ASTROCYTIC IONIC CLEARANCE AND ITS EFFECTS ON NEURONAL SPIKING

### 6.1 Methods

#### 6.1.1 Experimental data acquisition

##### MEA and Coverslip Preparation

In **Publication IV** we used 60-electrode standard MEAs (60MEA200/30iR-Ti and -ITO, purchased from Multichannel Systems MCS GmbH, Reutlingen, Germany). We coated the sterilized MEAs and the glass coverslips with Poly-D-Lysine (PDL) and successively with laminin. The protocol details can be found in **Publication IV**. For the recordings, we used 40 MEAs, 8 per each neuron-astrocyte ratio plated. For **Publication V** we coated the MEAs and the coverslips with the same protocol. We used 18 standard MEAs (60MEA200/30iR-Ti, Multichannel Systems MCS GmbH, Reutlingen, Germany), and 6 glass coverslips.

##### Cell Culture

For **Publication IV** and **Publication V**, we used rat primary cortical astrocytes (N7745100, Thermo Fisher Scientific, Waltham, MA, USA) and E18 primary rat cortex neurons (A1084001, Thermo Fisher Scientific, Waltham, MA, USA). The astrocyte culture was expanded from a plating density of  $20 \times 10^4$  cells/cm<sup>2</sup> and allowed to reach confluency in four days. To prevent further proliferation, the confluent astrocytes were treated with Cytosine b-D-arabinofuranoside (ara-C) for five days. At DIV9, they were ready for co-culture plating. The neurons and ara-C

treated astrocytes were separately centrifuged at 250×g for 5 minutes, resuspended in their respective media, and counted using the Countess Automated Cell Counter (Thermo Fisher Scientific, Waltham, MA, USA) after trypan blue staining to assess cell count and viability. In order to obtain various ratios of neuron-astrocyte co-culture, the number of neurons remained constant at 80,000 per MEA (40,000 per coverslip), while the number of astrocytes was varied. Both co-cultures and NS were plated on coverslips for immunocytochemistry (ICC) and live/dead assays. Following seeding, the MEAs and coverslips were incubated for approximately one hour before adding 1 ml of medium to each MEA and 500 l to each coverslip. For **Publication IV**, the co-culture ratios of neurons to astrocytes were 90/10, 80/20, 70/30, and 50/50 percent, where the first number specifies the proportion of neurons and the second number represents the proportion of astrocytes. Additionally, cultures comprising only neurons without separately added astrocytes were also plated, which are denoted as NS cultures. For **Publication V**, we employed the culture ratios of only NS, 80/20, and 50/50. The medium was refreshed every 2-3 days by replacing half of its volume, and after the recordings, the medium was completely replaced after the chemical stimulation. All cell cultures were maintained at +37 °C in a 5% CO<sub>2</sub> atmosphere.

### Immunofluorescence and imaging

Every week, coverslips from both the co-cultures and the NS were fixed for ICC. The fixing and permeabilization protocol has been described in detail in both **Publication IV** and **Publication V**. In **Publication IV**, the cells were stained for primary antibodies, including Microtubule Associated Protein 2 (MAP2) and Glial Fibrillary Acidic Protein (GFAP) from Sigma Aldrich (St. Louis, MO, USA) and then incubated with species-specific Alexa Fluor conjugated secondary antibodies. In **Publication V**, the primary antibodies used were MAP2 (chicken) from Thermo Fisher Scientific (Waltham, MA, USA) and GFAP (rabbit) from Sigma Aldrich (St. Louis, MO, USA).

After washing the coverslips thrice with a wash buffer containing 0.1% Triton X-100 in PBS, the cells were incubated with species-specific Alexa Fluor conjugated secondary antibodies. Secondary antibodies used were Alexa fluor 488 (anti-mouse) and Alexa fluor 555 (anti-rabbit) from Thermo Fisher Scientific (Waltham, MA, USA). The coverslips were further washed with the wash buffer, and then 4',6-

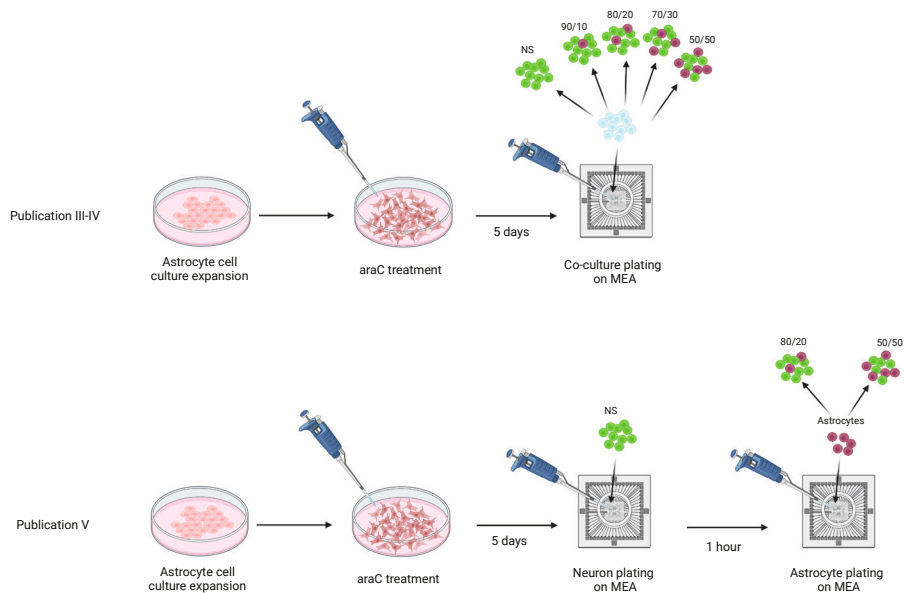


**Figure 6.1** Graphical description of the cell plating protocols used in **Publication III-V**. Astrocytes were plated and left in the incubator until confluent. When they reached confluency astrocytes were treated with ara-C for 5 days. At this point in **Publication III-IV** astrocytes and neurons were mixed together based on the desired cell proportions and then plated. In **Publication V** the neurons were plated first and left settling for 1 hour and then the different amounts of astrocytes were plated based on the desired final neuron-astrocyte ratio. Figure created with BioRender.com.

diamidino-2-phenylindole (DAPI) was added, followed by rinsing with PBS. Finally, the coverslips were mounted onto microscope glasses with ProLong Gold Antifade Mountant (Thermo Fisher Scientific, Waltham, MA, USA) and cured for 24 hours in the dark at RT. The coverslips were stored at +4 °C and imaged using an Olympus IX51 Fluorescence Microscope with an Olympus DP30BW camera (Olympus Corporation, Hamburg, Germany). The images were processed using Fiji (ImageJ) software and an in-house MATLAB (MathWorks, Inc., Natick, MA, USA) tool.

## Chemical stimulated hyperactivity with 4-AP and gabazine

In **Publication IV**, at DIV28, we applied 75 M 4-Aminopyridine (4-AP; 0940; Tocris, Bristol, UK) or 30 M SR-95531 hydrobromide (gabazine; 1262; Tocris, Bristol, UK) to the co-cultures and NS on MEAs to elicit hyperactivity through ion-dependent pathways (4-AP) or through transmitter-dependent pathways (gabazine).

For the recording protocol, we first recorded spontaneous neuronal activity for five minutes. Then, we pipetted appropriate volumes of previously prepared stock solutions of the drugs (4-AP: 10 mM; gabazine: 25 mM; both diluted in ultra-pure water) into the MEA wells to achieve final drug concentrations. The cell cultures were immediately recorded for ten minutes. After 24 hours (DIV29), we recorded MEAs for 5 minutes after the 5-minute settling period. The used and here explained protocol is presented for clearness in Figure 6.2.

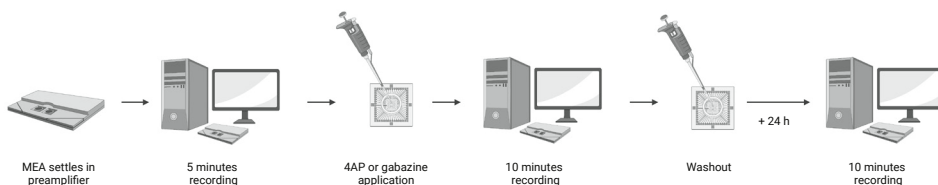


**Figure 6.2** Graphical description of the used protocol to stimulate the MEAs and register the drug-induced activity.

## MEA Recordings

Weekly recordings of the electrical activity of the co-cultures and the NS cultures on the MEAs were conducted using the Multichannel Experimenter software (Multichannel Systems MCS GmbH, Reutlingen, Germany) and a MEA2100-System. The cultures on the MEAs were allowed to settle in the MEA preamplifier for five minutes before recording spontaneous neuronal activity for five minutes. Raw signals were sampled at 25 kHz.

## 6.1.2 Data analysis

### Cell counter from immunolabeled images

In **Publication IV** and **Publication V**, we used fixed coverslips to ensure that the ratios of neuron and astrocyte cell populations were consistent. The cultures were stained with DAPI, which labels all the nuclei in the culture, and with MAP2 and GFAP, which specifically label neurons and astrocytes, respectively. We analyzed several regions of interest (ROIs) from the immunolabeled images taken at DIV14 (**Publication IV**) and DIV29 (**Publication V**). To count the cells, we created a semi-automated tool using MATLAB (MathWorks, Inc., Natick, MA, USA), and the cell counting script can be found in <https://github.com/barbara-ge/NeuronAstrocyteCounter>. A flow chart of the image analysis used in the cell counting script is shown in Figure 6.3.

The script first generates a segmented black-and-white (BW) mask of the DAPI-stained nuclei and removes debris with radii smaller than a predefined threshold. This method also separates cells that are clustered together. Then, the BW-masked nuclei are counted.

Next, the cleaned nuclei mask is merged with the corresponding MAP2 mask, which combines the neurons with their nuclei. A nucleus is considered to belong to a neuron if more than a predefined fraction of its border is within the MAP2 mask. The threshold is selected based on image brightness and visual control to optimize neuronal detection and minimize false classifications.

All remaining non-categorized nuclei are then merged with the GFAP-stained BW mask of the astrocytes. If the non-categorized nuclei borders are contained in the GFAP mask, the cells are counted as astrocytes. The threshold selection for the GFAP mask is similar to the one for the MAP2 mask. An example of nuclei selection is shown in Figure 6.6 b-c.

### Spiking and Bursting Analysis

In **Publication IV**, the raw signals underwent the same sorting and filtering procedures as in **Publication III** (described in Section 5.1.3). Using the resulting timestamps, we analyzed several parameters at different time points (7, 14, 21, 28, and 29 DIV), including SRs (spikes per minute), BRs (bursts per minute), the percentage

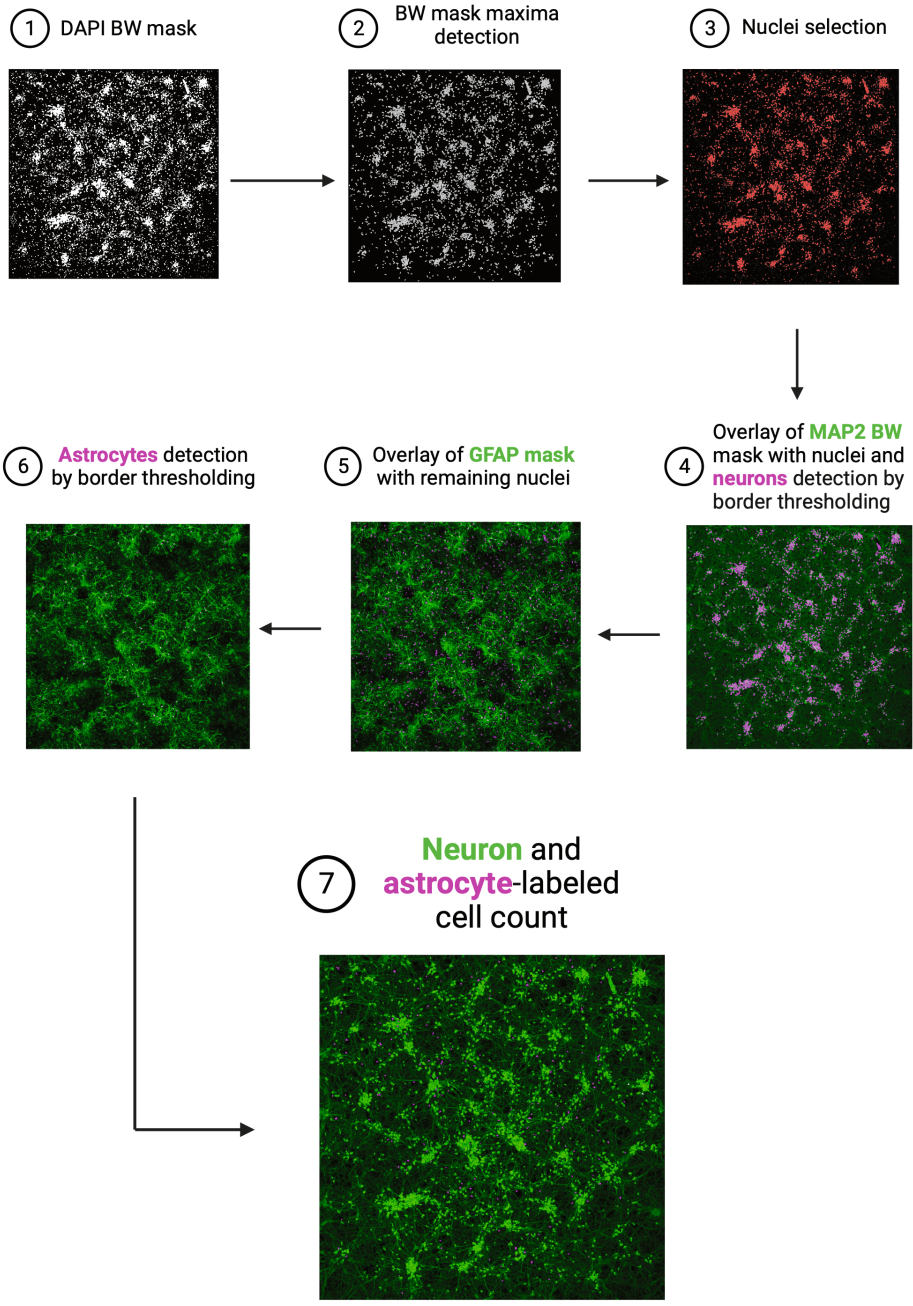


**Figure 6.3** Image analysis steps used for the cell labeling and neuron and astrocyte detection. Figure created with BioRender.com



of spikes contained in bursts (spikes in bursts/total spikes), and inter-burst intervals (IBIs) (measured as the time in milliseconds from the end of a burst to the start of the subsequent burst). We calculated these parameters for each channel of the MEA and then obtained an average value for the entire chip.

In **Publication V**, we calculated the spike rate (SR; Hz), burst rate (BR; Hz), burst duration (BD; in ms), the percentage of spikes contained in bursts (% spikes in burst), the inter-spikes intervals (ISI; in ms), and the inter-bursts intervals (IBI; in ms) at 14, 19, and 28 DIV. For this study, the aforementioned analysis has been conducted in a time window of 100 seconds, between 100 seconds and 200 seconds of the total recording time, to match the analysis time window used in the analysis of the entropy and complexity of the signals which will be later explained.

#### Network Synchronicity by Channel Inter-Correlation Analysis

In **Publication IV**, we assessed network synchronicity by examining the correlations of time-varying spectral entropies between MEA channels, following the method presented by Kapucu et al., 2016. We computed the pairwise inter-channel correlations and connections, with high correlation weights indicating high synchronization between the networks near the considered microelectrodes.

We then compared the connection weights between the different co-cultures and between the chemically stimulated cultures and their respective baseline measurements for each channel pair. Our analysis involved reporting all the correlation weights of each channel pair for each MEA, without averaging them.

#### Network Synchronicity by Binned Activity Analysis

In **Publication IV**, we used an alternative approach to assess network synchronicity based on spiking activity. First, we transformed the spike trains into binary time series with a time bin of 5 ms for each MEA channel, where a value of 1 indicated the presence of a spike, and 0 indicated the absence. We then summed the values across all MEA channels per bin and identified all local maxima in the resulting time series. The higher peaks corresponded to spikes and bursts that occurred in the same time bin and involved a larger network.

To avoid double-counting bursts in the summed signal, we only counted peaks that were separated by at least the minimum inter-burst interval identified in the

MEA during the previous burst analysis. This step ensured that we only counted the peaks that corresponded to distinct bursts. Next, we counted all remaining detected peaks that involved more than ten channels and defined these as network bursts (NBs).

#### Delay in the Response Times of the Convulsants

In **Publication IV**, we observed a delay in the response times following the application of 4-AP and gabazine, which was evident in the raster plots of the signals. Consequently, we developed an algorithm to identify the initial burst before the drug-induced alteration in the bursting pattern.

Following gabazine exposure, the network response produced a distinct, highly precise series of bursts that spanned the entire network. We also noted that the final NBs encompassed over half of the electrodes in our cultures and that the bursting patterns of all our gabazine-stimulated cultures changed towards the end of the recordings.

To compare the differences in the bursting activity, we computed the mean inter-burst interval (meanIBI) and the standard deviation of the IBIs (stdIBI) for the last 20 NBs in the recording. We selected the last 20 NBs to ensure that the drug had enough time to affect the activity. If there were fewer than 20 NBs in the recording, we excluded the MEAs from the analysis.

From the meanIBI and stdIBI, we derived the normal distribution of the IBIs. To find the bursts in the induced repetitive burst series, we used the following rule, which is also graphically described in Figure 6.4.

$$\begin{cases} |IBI_i(j) - meanIBI_i| < stdIBI_i, & NB_i(j) \in \text{repetitive series} \\ |IBI_i(j) - meanIBI_i| > stdIBI_i, & NB_i(j) \notin \text{repetitive series} \end{cases}$$

In this rule,  $i$  defines the MEA index,  $j$  the NB index, and  $stdIBI_i$  is the standard deviation of the last 20 IBIs of the  $i^{th}$  MEA recording. If the absolute value of the difference between the IBI of an NB and the mean IBI of the corresponding MEA was smaller than  $stdIBI_i$ , then the NB belonged to the repetitive burst series; otherwise, it did not belong to it.

To finally evaluate the duration it took for the convulsant to show its effects on the neuronal activity, we calculated the time from the drug application and the time

point at which the first burst of the repetitive series occurred.

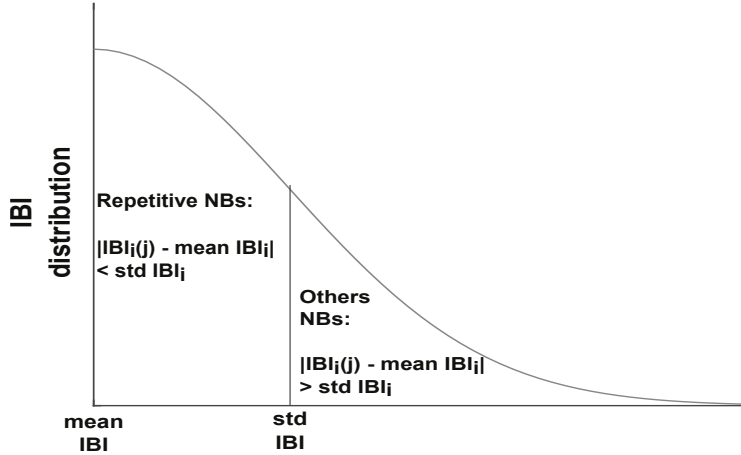


**Figure 6.4** Graphical representation of the selection rule for the repetitive NBs. Figure modified from **Publication IV**.

#### Complexity and entropy analysis

In **Publication V**, to study the activity pattern development in the days in vitro and between the different cultures, we used complexity-entropy (C-E) causality planes (Rosso et al., 2007; Rosso et al., 2012; Subramaniam et al., 2015). These metrics allow for the discrimination of chaotic signals from patterned ones. This analysis employs the Bandt and Pompe approach (Bandt and Pompe, 2002) to define the normalized Shannon entropic measure  $H_s[P]$  (Shannon, 1948), which characterizes the degree of regularity in the signal, and the statistical complexity measure  $C_{js}[P]$ , which characterizes the physical structure in a signal (Lamberti et al., 2004; Martin et al., 2003).

Given a single-channel time series  $X = \{x_t\}_{t=1}^T$ , based on the approach by Bandt and Pompe (Bandt and Pompe, 2002), we can define ordinal patterns of dimension  $M$  for each time point  $u$  as follows:

$$(u) \rightarrow (x_{u-(M-1)\tau}, x_{u-(M-2)\tau}, \dots, x_{u-\tau}, x_u). \quad (6.1)$$

The  $M$ -dimensional vector  $(x_{u-(M-1)\tau}, x_{u-(M-2)\tau}, \dots, x_{u-\tau}, x_u)$  assigned to each time  $u$  is obtained using Taken's embedding theorem, and qualitatively represents the

embedding vector at time-point  $u$  for a given lag  $\tau$  and dimension  $M$ . A sequence of integers  $(s_0, s_1, \dots, s_{M-1})$  is defined such that it describes the rank order of the components of the embedding vector (with 0 indicating the smallest value) and is a unique permutation of the set  $\{0, 1, \dots, M-1\}$  satisfying Rosso et al., 2012

$$x_{u-s(M-1)\tau} \leq x_{u-s(M-2)\tau} \leq \dots \leq x_{u-s_1\tau} \leq x_{u-s_0\tau} \quad (6.2)$$

and

$$s_l < s_{l-1} \quad \text{if} \quad x_{u-s_{l-1}} = x_{u-s_l}. \quad (6.3)$$

Note that there exist  $M!$  different possible ordinal patterns when a time series is embedded in  $M$  dimensions, and we denote these patterns by  $\pi_1, \pi_2, \dots, \pi_{M!}$ .

For all  $M!$  possible permutations, the associated relative frequencies for pattern  $\pi_i$  can be computed as Rosso et al., 2012,

$$p(\pi_i) = \frac{\#\{u | u \leq T - (M-1)\tau; (u) \text{ has type } \pi_i\}}{T - (M-1)\tau} \quad (6.4)$$

where  $\#$  stands for the number of occurrences. We can now define the normalized entropy measure  $\mathcal{H}_s[P]$  as

$$\mathcal{H}_s[P] = \frac{S[P]}{\log M!} \quad (6.5)$$

with

$$S[P] = - \sum_{i=1}^{M!} p(\pi_i) \log p(\pi_i) \quad (6.6)$$

and the complexity measure  $C_{js}[P]$  as Rosso et al., 2012

$$C_{js}[P] = \mathcal{Q}[P, P_e] \mathcal{H}_s[P], \quad (6.7)$$

where  $P_e$  represents the uniform probability distribution, i.e.,  $P_e = \{1/M, \dots, 1/M\}$  and  $\mathcal{Q}[P, P_e]$  represents the disequilibrium in terms of the Jensen-Shannon divergence  $\mathcal{F}_e$  and is given as

$$\mathcal{Q}[P, P_e] = \mathcal{Q}_0 \mathcal{F}_e \quad (6.8)$$

with,

$$\mathcal{F}_e = S[(P + P_e)] - S[P]/2 - S[P_e]/2 \quad (6.9)$$

where  $S[\cdot]$  is the Shannon entropy measure defined in Equation 6.6.

For the C-E analysis, we used a time window of 100 seconds, between 100 seconds and 200 seconds of the total recording time, as mentioned above. Furthermore, we used an embedding dimension  $M = 5$  and optimal time lag  $\tau = 100$ . The signal was low-pass filtered at 40 Hz to denoise the signal and then down-sampled to 1 kHz.

After preprocessing the signals, we obtained the ordinal pattern distributions used to estimate entropy and complexity as given in Equations 6.5 and 6.7.

The null hypothesis to be tested in this analysis is that the underlying dynamics of the time series is a stationary, linear, stochastic, and correlated process which is measured by a static, monotonic, and possibly nonlinear observation function (Puthanmadam Subramaniam and Hyttinen, 2014; Schreiber and Schmitz, 1996). To test that, we used the iterative amplitude adjusted Fourier transform (iAAFT) scheme (Schreiber and Schmitz, 1996), which employs an iterative approach to produce surrogates that have the same power spectra and values as the original data at hand to generate surrogates. For each single channel signal of the MEAs, we generated 49 iAAFT surrogates and then applied the same preprocessing and C-E analysis. From both the 60 original signals for each MEA, and the 2940 generated iAAFT surrogates (49 iAAFT surrogates for 60 channels), we measured the complexity and entropy, and we generated the empirical cumulative distribution function (empirical CDF) of the measures.

The empirical CDF is a step function that shows for any point of the series its probability of observation. The empirical CDFs generated from the complexity and entropy measures in the iAAFT surrogates of all the MEAs of each culture were then treated as "control" in the statistical analysis.

The used script is publicly available at <https://github.com/narayanps/NolinearTimeSeriesAnalysis>.

## Analysis of the spike waveforms

In **Publication V**, we analyzed how the astrocytes affect and interfere, if they do, with the recorded signals. We obtained and analyzed several features, such as the amplitude or the peaks, of the raw signals, and from those differentiated different spike waveforms in the cell cultures, and at the different developmental stages.

The Wave Clus sorting algorithm (Chaure et al., 2018) differentiates all the spike waveforms found in the recordings and clusters them based on the similarity of the

waveforms. The waveforms were saved in time windows of a total of 3 ms divided into 60 time points, each every 0.04 ms; 19 time points were recorded before the spike (for a total of 1 ms) and 40 time points after the spike (for a total of 2 ms), with the spike being at the 20<sup>th</sup> time point.

All the spike wavelets comprised in the same cluster were then averaged (Fig. 6.5B, black line) to obtain one single waveform for each cluster. Then the waveform was categorized into five possible classes: regular spiking (RS), fast-spiking (FS), triphasic spiking (TS), compound spiking (CS), and positive spiking (PS) (Fig. 6.5C). We defined the waveforms based on the previous work from S. H. Sun et al., 2021.

The features used to categorize and analyze the wavelets were: the spike amplitude (in V), as the amplitude between the baseline and the peak amplitude; the 1<sup>st</sup> peak-through ratio, such as the absolute value of the ratio between the amplitude of the 1<sup>st</sup> peak before the spike and the actual spike peak amplitude; the amplitude slope calculated as  $(\text{Spike peak amplitude} - 1^{\text{st}} \text{ peak amplitude}) / (\text{Spike time point} - 1^{\text{st}} \text{ peak time point})$ ; the peak-to-peak time (in ms), as the time between the 1<sup>st</sup> peak before the spike and the 1<sup>st</sup> peak after the spike (defined as 2<sup>nd</sup> peak); the spike duration (in ms), as the time between the spike peak and the 2<sup>nd</sup> peak. The baseline was calculated as the mean between the voltage at the first time step and the voltage at the 60<sup>th</sup> time point. A representative image of the waveform features is shown in Fig. 6.5A.

For the waveform selection, first of all, we discriminated the positive spikes (PS), if the spike amplitude was positive, otherwise, the spikes were categorized as negative spiking (NegS). All the negative spikes were then further divided into:

- Triphasic-spiking (TS): if the 1<sup>st</sup> peak-through ratio was higher than 0.1;
- Compound-spiking (CS): if the 1<sup>st</sup> peak-through ratio was higher than 0.1 and the peak-to-peak time was larger than 1 ms;
- Fast-spiking (FS): if the 1<sup>st</sup> peak-through ratio was lower than 0.1 and the spike duration was smaller than 0.3 ms;
- Regular-spiking (RS): if the 1<sup>st</sup> peak-through ratio was lower than 0.1 but the spike duration was bigger than 0.3 ms;

The decision tree for the waveform selection is shown in Fig. 6.5B, and the MATLAB code used for the waveform analysis is publicly available on GitHub at <https://github.com/barbara-ge/WaveformAnalysis>.

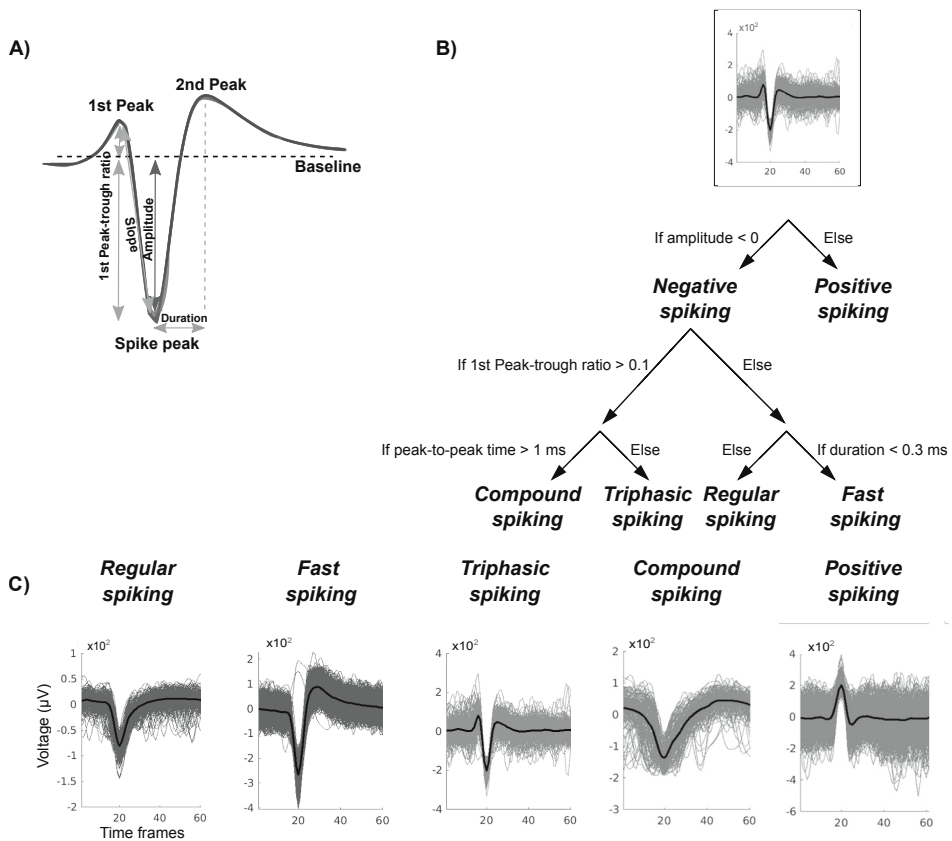


**Figure 6.5 Waveform selection and features.** A) Waveform features used for the waveform analysis (modified from S. H. Sun et al., 2021); B) decision tree of the algorithm used for the waveform detection; C) Examples of the five possible waveforms: regular spiking, fast-spiking, triphasic spiking, compound spiking, and positive spiking.

## Statistical analysis

The statistical analysis of the studies in **Publication IV**, and **Publication V**, was conducted in GraphPad Prism (v.9). In **Publication IV**, the data was not normally distributed, thus the Mann–Whitney U test was used to evaluate differences between culture groups. A p-value under 0.05 was considered significant.

In the case of the statistical comparisons between the correlation weights of the stimulated MEAs and their baseline, we used all the single channel signals, leading to a large number of data points. Due to the large datasets involved, statistical tests can often be affected (Fagerland, 2012). In our cultures, even small differences in

the distributions led to p-values that quickly approached zero. As a result, we supplemented the significance tests with an effect size analysis (Lin et al., 2013), which used Glass's delta (Smith and Glass, 1977), to compare the two groups. The control in our data was the baseline weights. The Glass's delta value indicates the number of standard deviations that the mean value of the data is greater than the control's mean. A positive delta value indicates that the data's mean is higher than the control's mean, while a negative delta value means that the mean of the control group is higher. We used a published MATLAB toolbox (Hentschke and Stüttgen, 2011) to compute the Glass's delta.

The dataset analyzed in **Publication V** exhibited a normal distribution, and to compare the various co-cultures, we employed ordinary one-way ANOVA. The criterion for significance was set at  $p < 0.05$ , where  $p$  represents the probability of obtaining results in the distribution's tail.

The empirical CDF generated from the iAAFT surrogates and from the original signals were compared to test their distribution differences with a two-sample Kolmogorov-Smirnov test. The test rejects the null hypothesis,  $b = 1$ , of having the data from the same distribution if  $p < 0.05$ ; otherwise,  $b = 0$ .

## 6.2 Results

### 6.2.1 Astrocyte response to chemically induced hyperactivity

*Neuron-astrocyte ratios remained as plated.* At 14DIV we counted the cells with the script mentioned in Section 6.1.2; we controlled that the plated cell ratios remained similar to those we plated and that no cell death, detachment or further replication happened in the cultures. The obtained neurons ratios were, on average, 92.2, 80.2, 77.1, 73.3, and 58.2% for the NS, 90/10, 80/20, 70/30, and 50/50 cultures, respectively (Fig. 6.6A). Differences between cultures in the neurons counts were always statistically insignificant ( $p > 0.05$ ), confirming that no visible differences were present in the numbers of neurons in the cultures and thus that a uniform neuronal culture density was maintained. The detected number of astrocytes at DIV14 were, on average, 7.8, 19.9, 22.9, 26.7, and 41.8% for the NS, 90/10, 80/20, 70/30, and 50/50 co-cultures, respectively (Fig. 6.6A). Note that a small percentage of astrocytes already existed in the commercially obtained neuronal cell stock in the NS



cultures.

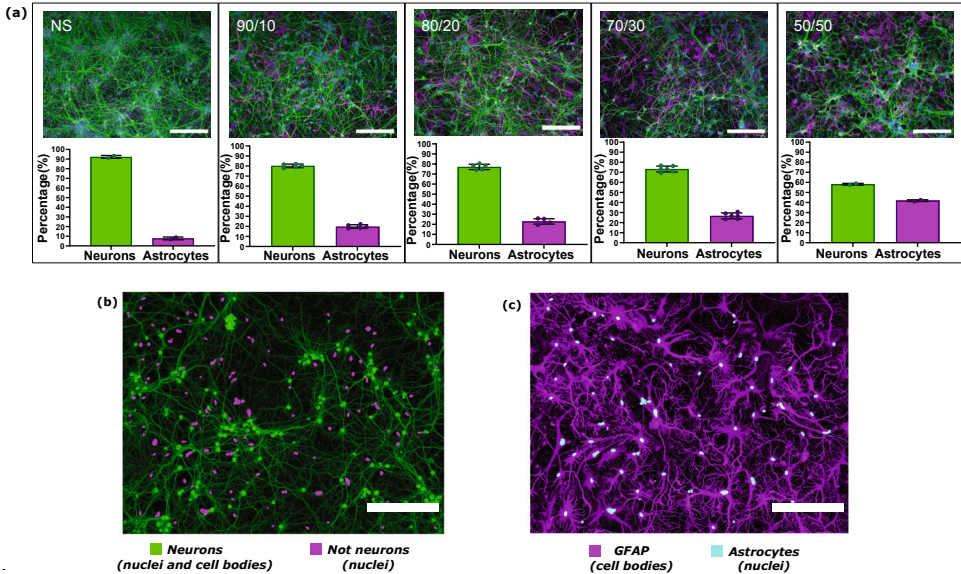


**Figure 6.6** Cell detection and count from immunolabeled images. a) relative ratios of neurons (in green), and astrocytes (in magenta) in the plated co-cultures. b) representative image of the neuronal detection (in green), where the non labeled nuclei are left in magenta. c) representative image of the astrocyte detection (in cyan), from the non labeled nuclei left from image b.

*Activity response to chemical stimulation with 4-AP and gabazine.* At 28DIV the cultures all presented spiking and bursting. Figure 6.7a displays the rasterplots of a subgroup of 10 electrodes from representative MEAs at baseline (on the left), and the same electrodes after the injection of either 4-AP or gabazine. In the rasterplots each spike in the electrodes (*y axes*) is represented by a black dot. In the *x axes* the recording time is expressed.

From Fig. 6.7a it is visible how 4AP increased the spiking more visibly for the NS, but less impactfully for the other cultures; while gabazine increased the spiking for all the shown recordings. With different time courses, gabazine induced a precise repetitivity in the synchronized spiking, which are represented in the rasterplots on the right bottom by the vertical lines.

In general, at baseline NS showed higher SR and BR, and higher variability (Fig. 6.7b-c), the co-cultures all showed lower SR and BR. After the drug injections, the MEAs in the NS, 90/10 and 80/20 cultures elicited with 4-AP showed a slightly

higher SR and BR, while those from the 70/30 and 50/50 showed a decrease, especially in the BR. Gabazine induced a visible higher SR and BR in all the co-cultures.

Moreover, when looking at the synchronization, the addition of 4-AP decreased the percentage of spikes in bursts in all the cultures (Fig. 6.7d). The IBIs, after 4-AP injection, increased or remained similar (Fig. 6.7e).

Gabazine in the co-cultures highly increased the percentage of spikes in bursts, in the NS cultures the value remained almost unchanged (Fig. 6.7d). The IBIs, after gabazine injection, visibly decreased to very small values in all the cultures (Fig. 6.7e); the precise repetivity seen in Figure 6.7a, can be here noticed in the very small standard deviation of the IBIs.

Furthermore, we tested the possible cytotoxic effects of 4-AP and gabazine with a live/dead assay (**Publication IV**, Supplementary Figure S2A,B); phenotypic impacts have been studied with immunocytochemistry (ICC) (**Publication IV**, Supplementary Figure S2A,B). The live/dead assay confirmed that neither 4-AP nor gabazine affected astrocyte viability after 24 h from the exposure compared to unstimulated control cultures (**Publication IV**, Figure 2E,F).

*Gabazine increased neuronal network synchronization.* Synchronization was analyzed accounting for the spectral entropies between MEA channels, as described in Section 6.1.2.

When looking at the correlation weights between the channels at baseline, in Figure 6.8a, we can notice that by increasing the astrocyte ratio the median correlation weight shifted toward lower levels.

After adding the drugs, we noticed two different responses in the MEAs stimulated with 4-AP and with gabazine. The correlation weights of the MEAs elicited with 4-AP slightly changed at the single channel-pair level, as can be seen in the representative heatmap of one MEA from the 80/20 coculture (Figure 6.8b); here each square represents a channel pair at baseline (lower left triangle) and after 4-AP injection (upper right triangle). The square color represents the correlation weight and spans from 0, in deep blue, to 1, in dark red. Figure 6.8b shows how at the single channel-pair level the correlation in many pairs appears decreased; however, when looking at the more general level, Figure 6.8d, shows that the median of the differences between the correlation values of the channel pairs after 4-AP stimulation and at baseline always lies around 0. While looking at the effect of gabazine we can see from both Figure 6.8c and d, that the correlation weights increased, and the

effect was more visible for co-cultures with more astrocytes, i.e. 80/20, 70/30, and 50/50.

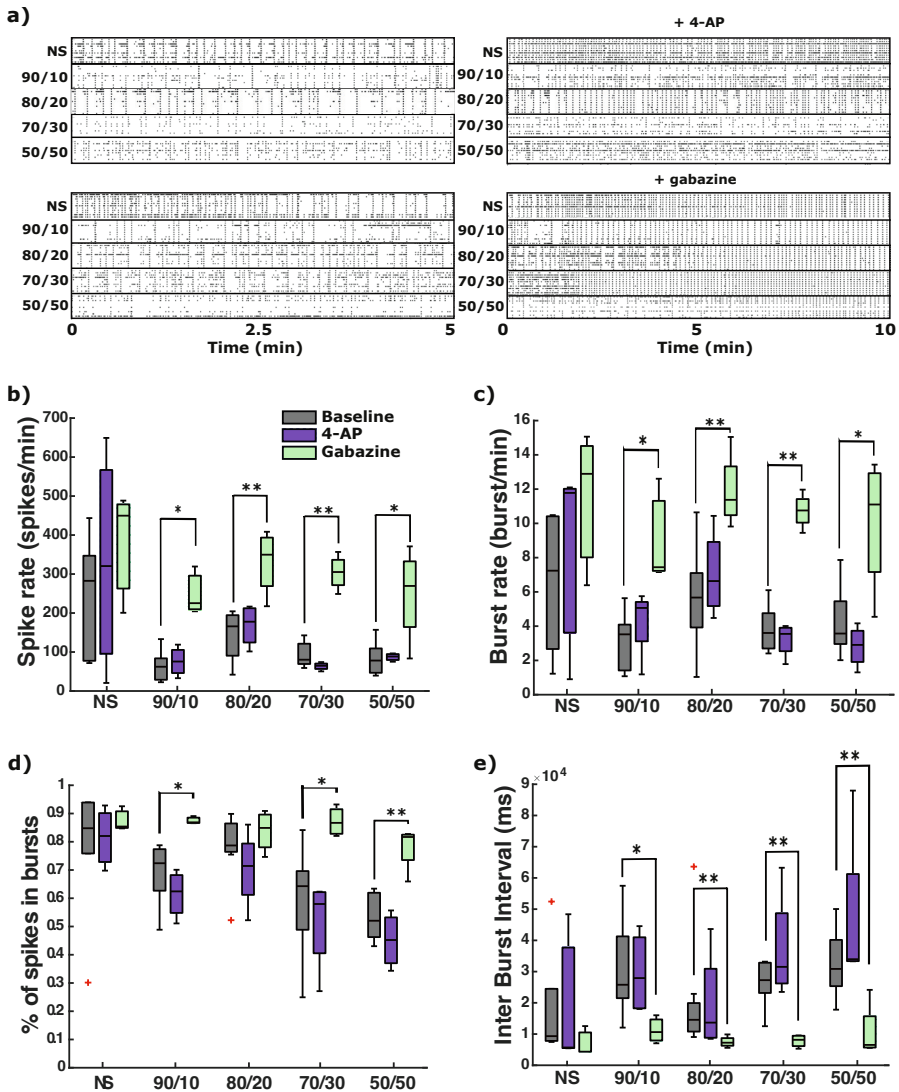


**Figure 6.7** Activity response to the injection of 4-AP and gabazine. a) Representative raster plots of 10 electrodes of two MEAs per culture condition, at baseline (left) and after the drug application (4-AP top right, gabazine bottom right). b) SR (spikes/minute), c) BR (bursts/minute), d) the percentage of spikes in bursts, and e) IBI (ms), of the MEAs for NS, 90/10, 80/20, 70/30, and 50/50 at baseline (in grey), after 4-AP injection (in purple), and after gabazine injection (in green). \* p<0.05; \*\* p<0.01. Red crosses represent the population outliers.

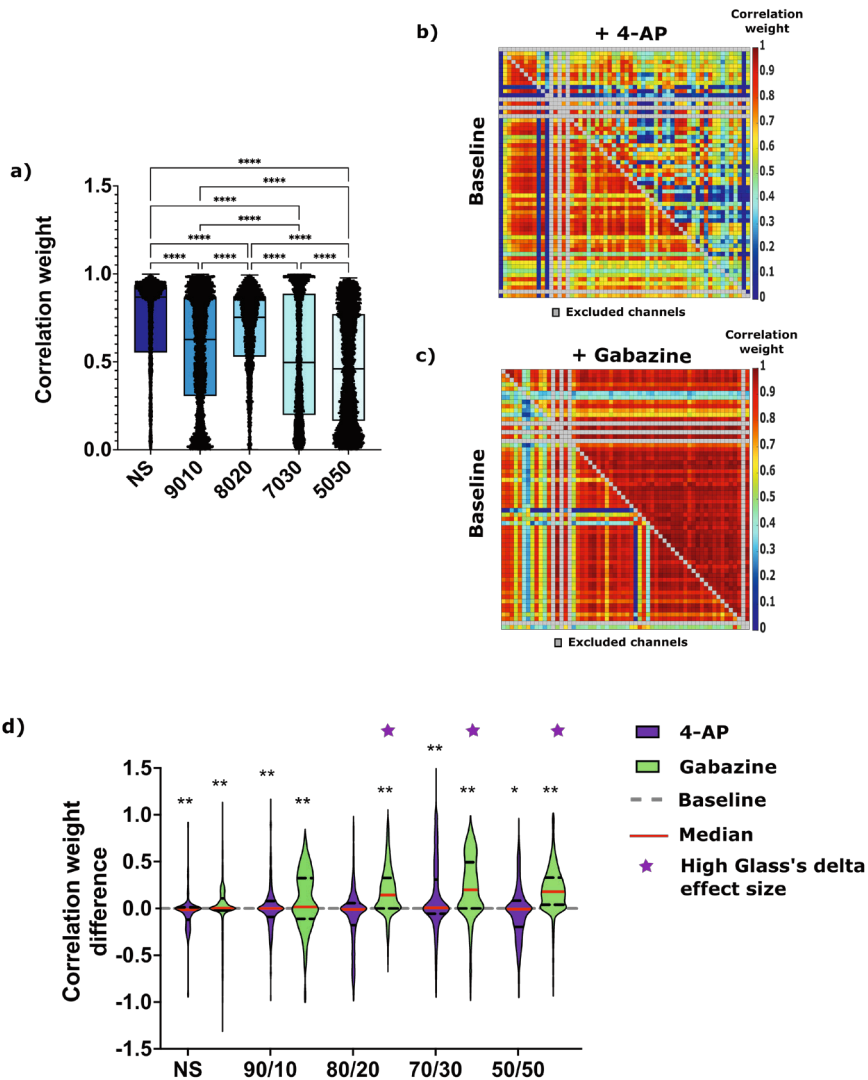


**Figure 6.8** Neuronal network synchronization at baseline and after chemical stimulation. a) Correlation weights of the different cultures at baseline. b) representative correlation heatmap of one MEA from the 80/20 co-culture at baseline (bottom left half), and after 4-AP stimulation (upper right half). c) representative correlation heatmap of one MEA from the 80/20 co-culture at baseline (bottom left half), and after gabazine stimulation (upper right half). The heatmaps squares represent the correlation weight of the channel pairs; the weights span from 0 (deep blue) to 1 (dark red). Excluded channels are shown in grey. d) violin plots of the differences between the stimulated correlation weight of each channel pair and its baseline value; MEAs stimulated with 4-AP are shown in purple, and those stimulated with gabazine in green. The pink stars represent those groups with high Glass' delta effect size. \*  $p < 0.05$ ; \*\*  $p < 0.01$ ; \*\*\*\*  $p < 0.0001$ .

*Gabazine-induced synchronization was delayed in co-cultures.* The stimulations with 4-AP and gabazine sorted very different responses. Notably, gabazine induced a very clear spike synchronization, while 4-AP induced a similar synchronization only in NS cultures. Figures 6.9 a, and b, display the different responses of two representative MEAs for each culture ratio one stimulated with 4-AP and the other with gabazine. From these figures we can notice how the NBs decrease from NS to the 50/50 co-cultures stimulated with 4-AP; while for gabazine there is a decrease from NS to the co-cultures but not between the co-cultures.

Also, gabazine induced a synchronization that appears delayed in cultures with more astrocytes. We quantified this delay with the analysis described in Section 6.1.2. Figure 6.9c shows that the average time at which the first NB of the synchronous series appears increases from the NS cultures to the 50/50 co-cultures.

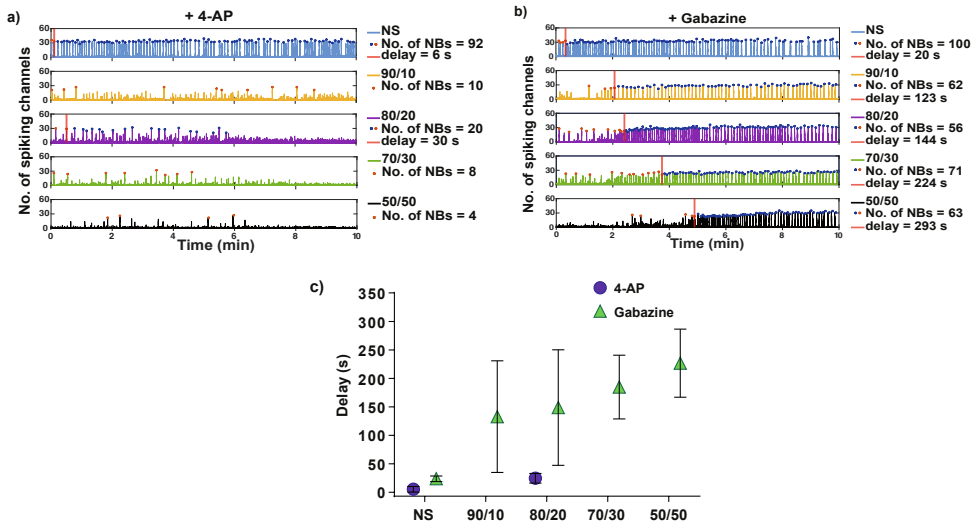


**Figure 6.9** Gabazine-induced delayed effects on the synchronization. a) Summed spiking activity of the channels of representative MEAs in NS (blue), 90/10 (yellow), 80/20 (purple), 70/30 (green), and 50/50 (black) stimulated with 4-AP, and b) with gabazine. The network bursts (NBs) are displayed in orange or in blue. Blue dots represent highly repetitive NBs, the orange dots represent the others. When both are present the NB in the legend shows the sums of the two. The red vertical lines represent the time point at which the first NB was found. c) Shows the delays for the cell culture types in the appearance of the first NB of the highly repetitive series for the gabazine (in green), and for 4-AP (in purple), when the NB series was present.

## 6.2.2 Neuronal signal development and control in co-cultures

*Spiking activity development in neuron-astrocyte networks.* To analyze the activity development we analyzed the SR and BR at 14, 19, and 28 DIV. The SR and BR developed and increased over the recording weeks (Fig. 6.10A-B). NS showed higher SR levels compared to 80/20, and 50/50 starting from 19 DIV. At 14 DIV the SR for NS was lower than 80/20 but higher than 50/50, and no clear pattern was noticeable. From 19 DIV a lower SR was noticeable for the co-cultures and almost linearly with the number of astrocytes in the culture. BR followed similar patterns.

The BD at 14 DIV was longer for the bursts in the 50/50 co-culture and there seemed to be an increase for co-cultures (Fig. 6.10C). At 19 and 28 DIV even though the BD seemed lower for co-cultures and especially the 50/50 co-culture, the differences between NS, 80/20, and 50/50 were not statistically significant (Fig. 6.10C).

To check the network synchronization we calculated the percentage of spikes contained in bursts to the whole amount of spikes in the recording window. For the NS and the 50/50, there was an increase in synchronization over the recording weeks, while for 80/20 this was not appearing from this analysis and the spikes were already almost all contained in bursts at 14 DIV (Fig. 6.10D). The 50/50 coculture showed lower synchronization compared to the other two.

The ISI analysis shows that the ISI decreased over the DIV recordings, and the 50/50 co-cultures showed higher ISI compared to NS and 80/20 (Fig. 6.10E). Similar behavior was noticeable for the IBI as well (Fig. 6.10F).

*Signal patterning analysis with complexity-entropy planes.* Complexity and entropy planes have been used to study the signal structure and patterning of the single channels of the MEAs.

On all days in vitro, the NS culture presented higher complexity levels and lower entropy levels, followed by the 80/20 co-culture and then the 50/50. Looking at Fig. 6.11A-B and C, it is possible to notice how the points representing the single channels of the MEAs shift toward lower levels of entropies and higher levels of complexity when the days in vitro increase, showing a progressive increase in the signal patterning. The 50/50 co-culture throughout all the DIVs showed very high values of entropy and low values of complexity showing an almost completely unpatterned and random signal.

The empirical CDFs of the complexity and entropy measures from the generated

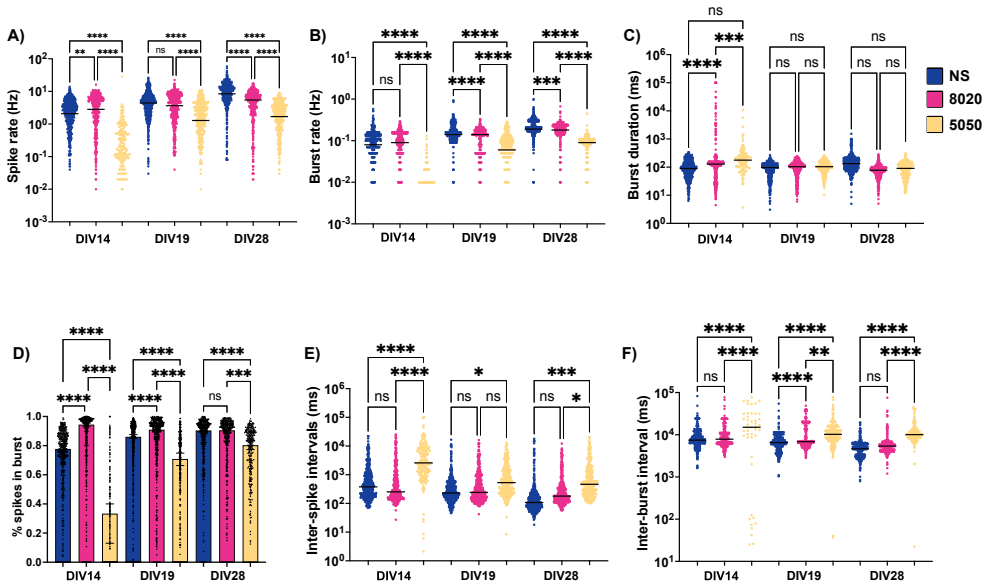


**Figure 6.10** Activity development analysis. A) spike rate (Hz), B) burst rate (Hz), C) burst duration in ms, D) % spikes in bursts, E) inter-spikes intervals in ms, and F) inter-bursts intervals in ms for NS (in blue), 80/20 (in magenta) and 50/50 (in yellow) co-cultures for 14, 19 and 28 DIV. Subfigures C, E, and F are centered where the majority of the results were located, leaving some outliers outside the figure. *ns* - non significant; \* < 0.05; \*\* < 0.01; \*\*\* < 0.001, \*\*\*\* < 0.0001.

iAAFT surrogates at DIV 14 presented fewer differences from those of the original signals (Fig. 6.11A1-A2). From DIV 19 to DIV 28, the empirical CDFs of the complexity measure from the original signals in the NS culture and the 80/20 co-culture shifted towards higher values, showing a higher probability in the distribution to find higher complexity values, thus a more patterned signal (Fig. 6.11B1-C1). On the other hand, the empirical CDF of the entropy measures from the original signals in the NS culture and the 80/20 co-culture, showed an increase in the probability of lower values of entropy (Fig. 6.11B2-C2). The NS culture showed a more visible change in the distributions of the complexity and entropy, compared to the 80/20 co-culture, showing also from the E-C planes (Fig. 6.11B-C) a higher signal patterning. For the 50/50 co-culture, the empirical CDFs of both the complexity and the entropy measures in the original signals always present higher probability at lower



values compared to the ones from the iAAFT surrogates; showing how the signals were completely not patterned for the 50/50 co-culture (Fig. 6.11A1 to C2).

The empirical CDFs were proved different between those obtained from the measures from the original signals and the iAAFT surrogates in all the cultures and at all DIVs with the use of a two-sample Kolmogorov-Smirnov test, which resulted  $h=1$  in all the cases.

*Spike waveform analysis in neuron-astrocytes co-cultures.* The waveform analysis conducted on the spike cutouts saved from Waveclus tool (Chaure et al., 2018) showed in general a prevalence of regular spiking in all our cultures. At 14 DIV NS and 80/20 co-cultures presented more RS than the 50/50, which presented instead more CS and TS, compared to NS and 80/20 (Fig. 6.12A). At 19 DIV the trend in RS switched and the 50/50 co-cultures showed a prevalence compared to the others in RS (Fig. 6.12B); a trend that was then clear at 28 DIV (Fig. 6.12C). CS remained more prevalent in 50/50 compared to the other cultures at 19 DIV and 28 DIV, even though the differences were not statistically significant (Fig. 6.12B-C). However, CS was rare in general on all days in vitro. PS prevalence increased from 14 DIV to 28 DIV for the 50/50 co-culture but remained mostly constant for NS and 80/20. At 28 DIV no statistically significant differences were however noticeable for the different co-cultures for the PS prevalence. FS and TS followed an inverse trend compared to RS, at 14 DIV were slightly higher for the co-cultures, and then reversed at 28 DIV. This trend is the consequence of the shift in spike duration we can notice from 14 DIV to 28 DIV (Fig. 6.12F). The spike duration remained mostly constant for the 50/50 co-culture but shifted from longer duration to shorter most noticeably for the NS and for the 80/20 co-culture as well. The differences in the spike duration between the co-cultures were also comparable to the differences in the positive and negative slopes, such as how fast the negative or positive spike peak, respectively, was reached from the 1<sup>st</sup> peak. At 14 DIV the differences in the positive slopes were not statistically significant, proceeding in the days in vitro the slopes increased for NS and 80/20, while decreased for the 50/50 co-culture (Fig. 6.12G). Leading to a faster spike reach for the NS and for the 80/20 co-cultures, and a slower reach for the 50/50 co-culture. The trend was similar also for the negative spikes, were however the differences between the two co-culture ratios, 80/20 and 50/50, were not statistically significant (Fig. 6.12H). The spike amplitude of the negative spikes seemed to be lower for the 80/20 and 50/50 co-culture on 14 and 19 DIV,



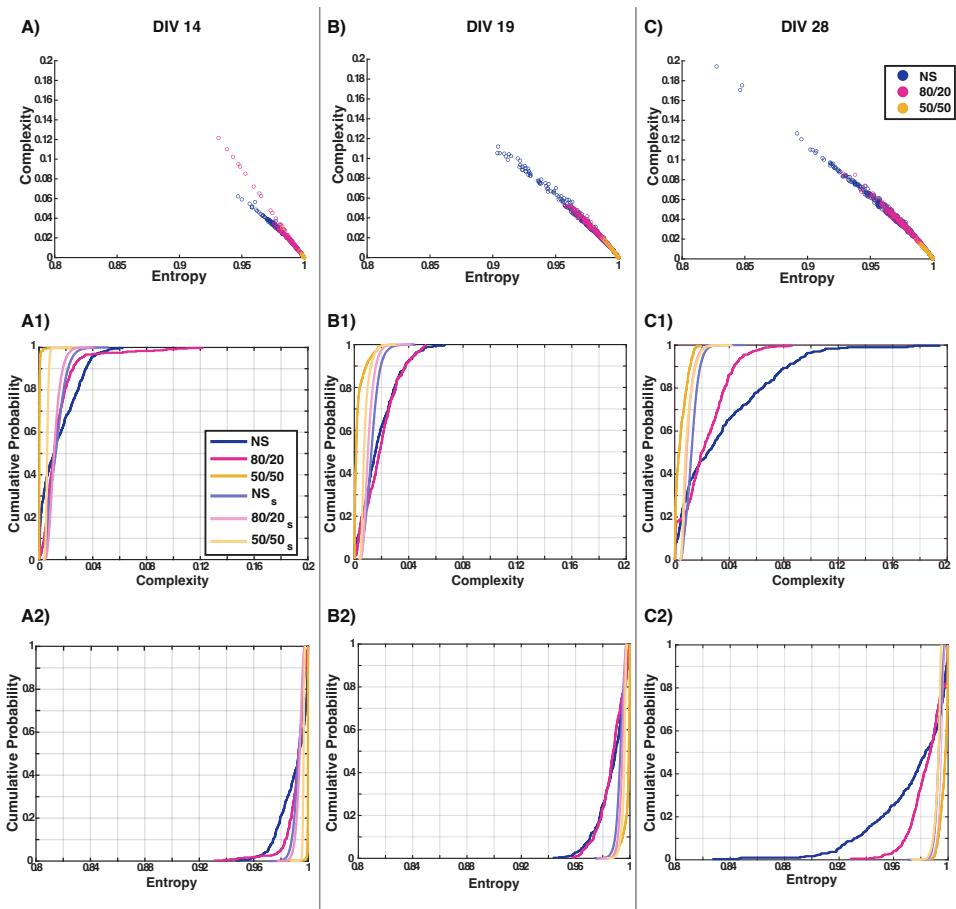


**Figure 6.11** Complexity-Entropy planes and surrogates analysis. A, B, and C) show the complexity-entropy values of the single channels in the cultures at DIV 14, DIV 19, and DIV 28, respectively. NS are shown in blue, 80/20 in magenta, and 50/50 in yellow. A1, B1, and C1) present the empirical CDF of the complexity values of the cultures on each measurement day in vitro, compared to the empirical CDF of the complexity levels of the relative generated surrogates (subscript  $s$  in the labels). The NS $_s$  are shown in light blue, the 80/20 $_s$  in pink, and the 50/50 $_s$  in light yellow. A2, B2, and C2) show the empirical CDF of the entropy measures of the cultures on each day in vitro, compared to the empirical CDF of the entropies of the relative generated iAAFT surrogates. The original complexity and entropy values from the C-E planes, and the entropy and complexity empirical CDFs were compared at each DIV with a two-sample Kolmogorov-Smirnov test.

but then at 28 DIV all the amplitudes were similar (Fig. 6.12D). The amplitude of the positive spikes remained instead more or less constant throughout all the days in vitro (Fig. 6.12E).

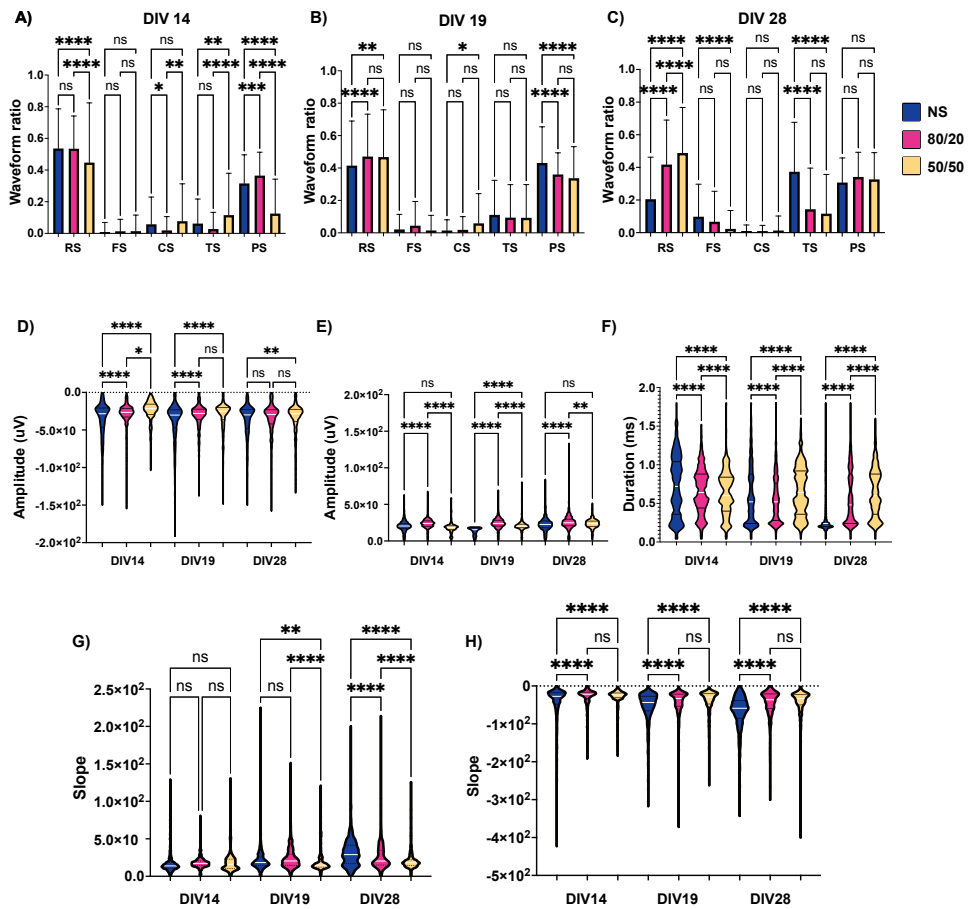


**Figure 6.12** Spike waveform analysis. A, B, and C) Prevalence of the spike waveforms in the NS, 80/20, and 50/50 co-cultures (blue, magenta, and yellow) at 14, 19, and 28 DIV, respectively. RS - regular spiking, FS - fast-spiking, CS - compound spiking, TS - triphasic spiking, and PS - positive spiking. D and E) Spike amplitude in V at 14, 19, and 28 DIV for the negative and positive spikes, respectively. F) Spike duration in ms, counted as the time from the spike peak to the 2<sup>nd</sup> peak (or to the end of the time window in absence of the 2<sup>nd</sup> peak). G and H) Positive and negative slopes, respectively, to reach the spike peak for the NS, 80/20 and 50/50 co-cultures at 14, 19, and 28 DIV. *ns* - non significant; \* <0.05; \*\* <0.01; \*\*\* <0.001; \*\*\*\* <0.0001.

## 7 DISCUSSION

### 7.1 Higher astrocyte presence reduces astrocytic activation

Chapter 5 (**Publication I-III**) aimed at showing the computational work done to study how the astrocyte topology controls and affects neuronal activity.

The first step was to simulate the gap junction uncoupling (**Publication I**). Cx43 and Cx30, two specific families of connexins highly abundant in astrocytes, proved to have implications in epileptogenesis (Walrave et al., 2020). Wallraff and colleagues showed that a loss of astrocytic gap junctions, obtained in a Cx30/Cx43 double knock-out mouse model, seemed to facilitate seizure susceptibility (Wallraff, 2006).

Our results showed a decreasing tendency for the spike rate and the burst rate in more connected astrocyte networks (Fig. 5.5). However, our results were not statistically significant when looking at the comparisons between coupling conditions. The reason for these small differences might lie in the small difference between the obtained number of gap junctions for the different coupling cases. Also, it can be noted that their activation decreases when the astrocytic coupling increases. This happens because of a redistribution of  $IP_3$  through the connected astrocytes, reducing their activation probability. Thus, a reduced astrocytic activation might lead to reduced control of the neuronal spiking activity. It must be noted, also, that the INEXA model does not include  $K^+$  pathways, which are mainly connected to the gap junction uncoupling-dependent seizure susceptibility.

A similar tendency was also seen in **Publication II**, where when increasing the maximum connectivity distance for the astrocytes, we obtained more gap junctions for each astrocyte, and this returned a lower astrocytic activation and thus a higher spike rate.

In **Publication III**, we combine *in vitro* recordings with *in silico* modeling. From the *in silico* data, while mapping the neuronal activity in response to the astrocytic activation, we can indeed notice that the most active astrocytes were those located

near highly active neurons, rather than those with a higher degree (i.e., a higher number of gap junctions). However, in the same figure (Fig. 5.13), we can notice that the network with more astrocytes (70/30, 70% neurons, and 30% astrocytes), and with more connections, presented a lower amount of neuronal connections with a high cross-correlation. Thus, this means that higher astrocytic connectivity was still able to counteract the neuronal activity and its synchronization. In this study the downregulation effect might have been more visible because increasing the number of astrocytes in the simulated co-culture, counteracted the decrease in astrocytic activation, thus resulting similar for the three different co-cultures (90/10, 80/20, and 70/30; where the first number is the percentage of neurons in the culture and the second one is the percentage of astrocytes in the culture) (Fig. 5.12).

In the same work, we showed that for the NS in *in vitro* cultures, the spike rate was highly correlated to the connection degree of the electrodes. The co-cultures showed a lower to no correlation between the spike rate and the electrode degree (Fig. 5.11). This shows that astrocytes desynchronize neuronal activity.

## 7.2 Astrocytes and the plating conditions affect the network topology

The use of computational models allows to change, study and evaluate all the network structural features, which are not possible or are difficult to obtain *in vitro* or *in vivo*, and also to combine these with their local effects on neuronal activity. **Publication III** highlights that in most of the cases, the simulations were able to reproduce the features of the neuronal activity that we obtained *in vitro* with MEA recordings of neuronal cultures (NS) and co-cultures (90/10, 80/20, and 70/30).

The only cultures which were less accurately simulated were the NS cultures, which presented a much more inner variability and a generally higher mean spike rate. The average burst rate was instead comparable also for NS. The higher variability in real cultures might depend on the lower maturation stages in these cultures, compared to the co-cultures. It has been shown that astrocytes control neuronal maturation and neurite growth (Taga et al., 2019; van den Pol and Spencer, 1999). Taga and colleagues observed that neuron-astrocyte co-cultures presented a higher expression of AMPA, GABA, and glycine receptors compared to monocultures (Taga et al., 2019). van den Pol and Spencer observed that neurons cultured with rat and human astrocytes presented longer neurites (van den Pol and Spencer, 1999).

Extending the planar topology of the INEXA model toward a 3D topology (**Publication II**), allowed us to simulate neuron-astrocyte networks in more physiological conditions. The results we obtained from the comparison between the planar and the 3D topology, were comparable to those obtained from Frega, 2016, where she observed an increase in spontaneous neuronal activity.

Our topology analysis highlighted that the final neuronal network connectivity was comparable for the planar and the 3D network, while the number of synapses contacted by an astrocyte was higher in the 3D configuration. The increase in the spike rate, also in this study most probably depends on the decrease in the number of active astrocytes, which was smaller in the 3D network.

### 7.3 Astrocytes prevent neuronal hyperactivity induced by extracellular $K^+$

In **Publication IV**, and **Publication V**, we aimed at unraveling the effects that ionic and gliotransmitter clearance from the astrocytes have on neuronal network activity *in vitro*.

It is known that astrocytes clear  $K^+$  from the extracellular space (Wallraff, 2006). It is also known that the GJ coupling is tightly connected to the clearance of  $K^+$  and glutamate (Djukic et al., 2007; Seifert et al., 2009). As shown in **Publication II-III** increasing the number of astrocytes in the network increases the number of GJ, as expected; on the other side, this increased connectivity corresponds to a decreased astrocyte activation (**Publication I**).

In **Publication IV** we aimed at modeling *in vitro* cultures with different shares of neurons and astrocytes, to study how these different cultures responded to hyperactivity. The hyperactivity was induced with two drugs, 4-AP and gabazine, which interfere with two different pathways. 4-AP, a voltage-gated  $K^+$  channel blocker, when applied to the neuronal cultures induces synchronized  $Ca^{2+}$  transients, which trigger glutamate release (Kasatkina, 2016). Gabazine, instead, is a  $GABA_A$  receptor antagonist, which is reported to block GABAergic signaling, increasing spike rate, burst rate, and synchronization (Bradley et al., 2018; Hyvärinen et al., 2019). Voltage-gated  $K^+$  channels and  $GABA_A$  receptors are expressed in both neurons and astrocytes, thus we expect the drugs to affect both cell types.

In **Publication IV**, gabazine induced a hypersynchronous spiking activity, which

appeared delayed in co-cultures. As said before, more astrocytes in the cultures mean more GJ between these cells, so a faster exchange of ions and neuroactive substances in response to the stimulation. Also, the more astrocytes we have in the culture the more GABA<sub>A</sub> the drug needs to block, which might cause a delayed response. Blocking GABA<sub>A</sub> receptors reduces Ca<sup>2+</sup> transients (Meier et al., 2008). Inhibitory gliotransmitters release, e.g. D-serine, from the astrocytes, depends on Ca<sup>2+</sup> elevation (Halassa et al., 2007b), we hypothesize that reduced intracellular Ca<sup>2+</sup> levels lead to a failure in the control of neuronal activity and increased spike and burst rates.

4-AP, instead, in our experiments failed to induce any statistically significant increase in spiking or bursting activity. However, the effect on NS cultures was much more effective than on co-cultures. We think that astrocyte networks with more astrocytes and more GJ (**Publication III**) more effectively cleared the accumulating K<sup>+</sup> resulting from the blockade of voltage-gated K<sup>+</sup> channels, thus leading to better control of the neuronal activity.

## 7.4 Astrocytes increase chaotic behaviors in neuronal spiking

In **Publication V**, we used unconventional analysis for MEA recordings to deeply analyze the signals and their patterning over time and in cultures with different neuron-astrocyte ratios.

Our results suggest that astrocytes decreased the spike and burst rates and decreased their synchronicity and repetitivity, as seen in **Publication IV**. The decrease was more significant for the 50/50 co-culture compared to the 80/20 co-culture, suggesting that the decline directly depends on the number of astrocytes in the culture.

Our results from **Publication IV**, and **Publication V**, indicate that astrocytes desynchronized the activity of the neurons. The percentage of spikes in bursts was lower for the 50/50 co-culture.

To further study the patterning of the signals, in **Publication V**, we analyzed the entropy and complexity of the signals. These parameters are not commonly used in signals from MEA recordings. Complexity and entropy measures to study neural activity patterns have been adopted in EEG signals (Abou-Abbas et al., 2022; Angulo-Ruiz et al., 2022; Shen et al., 2021; Subramaniam et al., 2015). Multiscale

entropy, in particular, has been used to discriminate between different neurological disorders, and between patients with generalized seizures from those with focal seizures Shen et al., 2021.

Our complexity-entropy analysis showed that the complexity of the signals increased more prominently in the NS cultures during development. This measure indicates patterning, and thus, a more repetitive and synchronous activity. The co-cultures, instead, presented less repetitive and patterned activity in general when developed. However, the 80/20 cultures presented more patterning already at 14 DIV compared to NS.

The entropy measure discriminates stochastic activity with low entropy levels from chaotic activity with high entropy levels (Rosso et al., 2007; Rosso et al., 2012; Subramaniam et al., 2015).

Our results showed that entropy decreased during development. The NS cultures showed less chaotic behaviors, meaning lower entropy, compared to co-cultures. While high entropy values indicate a random activity of the network, it does not mean that said activity is truly random.

Interestingly, a recent study on classifiers to discriminate EEG data from epileptic patients and seizure-free patients found that the Shannon entropy was lower in epileptic patients compared to seizure-free individuals (Abou-Abbas et al., 2022). This suggests that an increase in overall neuronal activity with over-synchronicity can be well characterized by information measures with real impact on signal processing tools for diagnostics. Thus understanding real entropy variations considering information/complexity measures can produce predictors of neural states, associating areas of the brain with their structural configuration.

## 7.5 Astrocytes regulate neuronal depolarization and repolarization

In **Publication V**, we expanded our research and looked at how astrocytes interfere with neuronal spike development and shape, and we classified the shapes of the spike signal cutouts and their features. The waveform analysis demonstrated that co-cultures presented more regular spiking and less fast spiking, along with a slower reach of the spike peak, shown by smaller slope values, and with a longer interval between the spike peak and the second peak. Our results suggest that in co-cultures, astrocytes slow down the reaching of necessary differences in the membrane poten-

tial by clearing the extracellular space from excessive ions. As described in Section 2.1, the concentration of  $\text{Na}^+$  and  $\text{K}^+$  ions in the extracellular and intracellular space, respectively, creates a negative membrane potential before the generation of an action potential. During an action potential,  $\text{Na}^+$  ions flow inside the cell, reversing the membrane potential to a positive value, and during repolarization,  $\text{K}^+$  ions are extruded from the cell, restoring the negative membrane potential (Hodgkin and Huxley, 1952). Astrocytes clear  $\text{K}^+$  ions from the extracellular space using  $\text{Na}^+/\text{K}^+$ -ATPase, Kir4.1, and  $\text{Na}^+/\text{K}^+/\text{2Cl}^-$  cotransporter (NKCC) channels (Bellot-Saez et al., 2021; Butt and Kalsi, 2006; Larsen et al., 2014; Wallraff, 2006). During an action potential, the astrocyte extrude  $\text{Na}^+$  ions, which results in a slower inversion of the relative charge between the intracellular and extracellular space. As a result, the spike peak is reached slower when more astrocytes are present near a neuron, as shown by our results. During the repolarization phase, astrocytes slow down the reach of a higher positive charge of the extracellular space by uptaking  $\text{K}^+$  ions. This explains the longer duration from the spike peak to the second peak observed in our results. The refractory period prevents the initiation of new spikes during depolarization, repolarization, and part of the hyperpolarization phase, and co-cultures presented longer depolarization and repolarization phases, leading to fewer spikes initiated and lower spike rates.

In **Publication V**, co-cultures presented longer depolarization and repolarization phases, preventing more spikes to be elicited, and thus the neurons presented a lower spike rate. Another interesting result we obtained from **Publication V**, was the quantification of the positive spikes. In MEAs, the amplitude and the polarity of the signal depend on the distance between the neuron and the electrode (Obien et al., 2015); with the action potentials reaching the higher amplitude very near the electrode and then decreasing up to becoming positive for longer distances. In our recordings, the amplitude of the signals was comparable between the co-culture and the NS culture, as well as the percentual amount of positive spikes. This suggests that the presence of the astrocytes affects the generation of the spikes locally, but does not interfere with the extracellular action potential diffusion. Otherwise, in the case of an insulating effect from the astrocytes, we would have seen a decrease in the amplitude for co-cultures and especially for the 50/50 co-culture, as well as a decrease of positive spikes.

Both **Publication IV** and **Publication V** shed light on the crucial role of astro-



cytes in regulating neuronal activity and maintaining homeostasis, offering novel insights into the impact of  $K^+$  clearance on neuronal spiking. Additionally, our findings underscore the significance of accounting for varying cell proportions in drug testing and co-culture experiments.



## 8 CONCLUSIONS

This thesis aimed to study how astrocytes control and shape neuronal spiking, with particular attention to astrocytic ionic clearance. To this regard, we first evaluated computationally the effects of changes in the astrocytic network topology on neuronal activity, and experimentally, and computationally, how different ratios of astrocytes in the networks affect the signaling and the responses to hyperactivity. The conclusions drawn by each study comprised in this thesis were:

- In our *in silico* studies, the astrocyte activation strongly depends on the basal noise, and networks with the gap junctions uncoupled showed less efficacy in downregulating neuronal activity compared to the fully connected networks (**Publication I**). In the extension of the study for this thesis, I observed that the astrocytic activation was also inversely proportional to the gap junction coupling. Thus, the fully connected networks presented a lower astrocyte activation, which might counteract the activity inhibition.
- In the 3D network topology, compared to the planar topology, we found more synaptic connections for the astrocytes, which were accompanied by a lower astrocytic activation due to a higher redistribution of neurotransmitters. This resulted in higher neuronal spiking. Moreover, shorter astrocytic connection distances are accompanied by fewer gap junction connections and higher astrocytic activation, while longer connection radiuses centralized the information propagation in the astrocytes leading to more connected astrocytes in the center of the network (**Publication II**).
- *In silico* co-cultures well replicated the activity and features of the *in vitro* co-cultures. While simulated neuron cultures failed to replicate the inner variability shown by the experimental "pure" neuronal cultures. The simulations on the astrocyte networks with different relative ratios of neurons and astrocytes showed that astrocyte activation was mainly dependent on the spike rate of the neighboring neurons rather than from their gap junction coupling. However,

we noticed that in areas of our virtual co-cultures with highly connected astrocytes, the neuronal activity was lower and the correlation between electrodes was also inferior to the areas with less connected astrocytes (**Publication III**).

- Astrocytes counteracted 4-AP-induced hyperactivity in our cultures on MEAs, while failing in controlling gabazine-induced hyperactivity and synchronization. These results suggest that extracellular  $K^+$  clearance from the astrocytes effectively removed excessive  $K^+$  from the ECS, leading to an unaffected neuronal activity. Blocking  $GABA_A$  receptors instead resulted in hyperactivity and hyper synchronicity most probably due to failed release of inhibiting transmitters from the astrocytes, e.g. D-serine (**Publication IV**).
- Astrocytes decreased the signal spike slope and increased the spike duration, such as slowing both the depolarization and repolarization phases of the action potentials. The longer time spent by the neurons in the refractory phase resulted in a lower spike rate in co-cultures. Moreover, astrocytes increased chaotic behaviors decreasing the signal patterning (**Publication V**).

In summary, this thesis highlights the importance of using computational studies to overcome experimental limitations, such as in the analysis of the correlation between the neuronal and astrocytic network topologies and the neuronal spiking activity. This thesis stresses also the importance of adopting interdisciplinary analysis techniques to go beyond standard spike and bursts analyses to deepen the knowledge of the astrocytic processes that regulate neuronal signaling. Moreover, considering the active role of astrocytes in shaping and regulating the signal in neuronal networks, we want to emphasize the need to consider the proportion of astrocytes in both neuron-astrocyte co-cultures *in vitro* and neuron-astrocyte network simulations *in silico*. An illustration of the significance of investigating various ratios of neurons and astrocytes and cellular distribution is evident in the unequal neuron-astrocyte ratios observed in different brain regions, which may ultimately account for differences in susceptibility to epileptic seizures.

## REFERENCES

- Abou-Abbas, L., Jemal, I., Henni, K., Ouakrim, Y., Mitiche, A., & Mezghani, N. (2022). Eeg oscillatory power and complexity for epileptic seizure detection. *Applied Sciences*, 12(9). <https://doi.org/10.3390/app12094181>
- Agulhon, C., Petravicz, J., McMullen, A. B., Sweger, E. J., Minton, S. K., Taves, S. R., Casper, K. B., Fiacco, T. A., & McCarthy, K. D. (2008). What is the role of astrocyte calcium in neurophysiology? *Neuron*, 59(6), 932–946. <https://doi.org/https://doi.org/10.1016/j.neuron.2008.09.004>
- Angulo-Ruiz, B. Y., Munoz, V., Rodríguez-Martínez, E. I., Cabello-Navarro, C., & Gomez, C. M. (2022). Multiscale entropy of adhd children during resting state condition. *Cognitive Neurodynamics*, 1–23.
- Araque, A., Carmignoto, G., Haydon, P. G., Oliet, S. H. R., Robitaille, R., & Volterra, A. (2014). Gliotransmitters travel in time and space. *Neuron*, 81(4), 728–39. <https://doi.org/10.1016/j.neuron.2014.02.007>
- Araque, A., Parpura, V., Sanzgiri, R. P., & Haydon, P. G. (1999). Tripartite synapses: Glia, the unacknowledged partner. *Trends in Neurosciences*, 22(5), 208–215. [https://doi.org/10.1016/S0166-2236\(98\)01349-6](https://doi.org/10.1016/S0166-2236(98)01349-6)
- Armbruster, M., Naskar, S., Garcia, J. P., Sommer, M., Kim, E., Adam, Y., Haydon, P. G., Boyden, E. S., Cohen, A. E., & Dulla, C. G. (2022). Neuronal activity drives pathway-specific depolarization of peripheral astrocyte processes. *Nature Neuroscience*, 25(5), 607–616.
- Attwell, D., Buchan, A. M., Charpak, S., Lauritzen, M., Macvicar, B. A., & Newman, E. A. (2010). Glial and neuronal control of brain blood flow. *Nature*, 468(7321), 232–43. <https://doi.org/10.1038/nature09613>
- Bandt, C., & Pompe, B. (2002). Permutation entropy: A natural complexity measure for time series. *Phys. Rev. Lett.*, 88, 174102. <https://doi.org/10.1103/PhysRevLett.88.174102>

- Bazargani, N., & Attwell, D. (2016a). Astrocyte calcium signaling: the third wave. *Nature Neuroscience*, 19(2), 182–189. <https://doi.org/10.1038/nn.4201>
- Bazargani, N., & Attwell, D. (2016b). Astrocyte calcium signaling: the third wave. *Nature neuroscience*, 19(2). <https://doi.org/10.1038/nn.4201>
- Bedner, P., Dupper, A., Hüttmann, K., Müller, J., Herde, M. K., Dublin, P., Deshpande, T., Schramm, J., Häussler, U., Haas, C. A., Henneberger, C., Theis, M., & Steinhäuser, C. (2015a). Astrocyte uncoupling as a cause of human temporal lobe epilepsy. *Brain*, 138(5), 1208–1222. <https://doi.org/10.1093/brain/awv067>
- Bedner, P., Dupper, A., Hüttmann, K., Müller, J., Herde, M. K., Dublin, P., Deshpande, T., Schramm, J., Häussler, U., Haas, C. A., Henneberger, C., Theis, M., & Steinhäuser, C. (2015b). Astrocyte uncoupling as a cause of human temporal lobe epilepsy. *Brain*, 138(5), 1208–1222. <https://doi.org/10.1093/brain/awv067>
- Bellot-Saez, A., Kékesi, O., Morley, J. W., & Buskila, Y. (2017). Astrocytic modulation of neuronal excitability through K<sup>+</sup>spatial buffering. *Neuroscience and Biobehavioral Reviews*, 77, 87–97. <https://doi.org/10.1016/j.neubiorev.2017.03.002>
- Bellot-Saez, A., Stevenson, R., Kékesi, O., Samokhina, E., Ben-Abu, Y., Morley, J. W., & Buskila, Y. (2021). Neuromodulation of astrocytic k<sup>+</sup> clearance. *International Journal of Molecular Sciences*, 22(5). <https://doi.org/10.3390/ijms22052520>
- Bordey, A., & Sontheimer, H. (1998). Properties of human glial cells associated with epileptic seizure foci. *Epilepsy Research*, 32(1-2), 286–303. [https://doi.org/10.1016/S0920-1211\(98\)00059-X](https://doi.org/10.1016/S0920-1211(98)00059-X)
- Bradley, J. A., Luithardt, H. H., Metea, M. R., & Strock, C. J. (2018). In Vitro Screening for Seizure Liability Using Microelectrode Array Technology [eprint: <https://academic.oup.com/toxsci/article-pdf/163/1/240/24688804/kfy029.pdf>]. *Toxicological Sciences*, 163(1), 240–253. <https://doi.org/10.1093/toxsci/kfy029>
- Brodal, P. (2016). *The central nervous system* (5th ed.). Oxford University Press.
- Butt, A. M., & Kalsi, A. (2006). Inwardly rectifying potassium channels (kir) in central nervous system glia: A special role for kir4.1 in glial functions. *Jour-*

- nal of Cellular and Molecular Medicine*, 10(1), 33–44. <https://doi.org/https://doi.org/10.1111/j.1582-4934.2006.tb00289.x>
- Buzsáki, G., Anastassiou, C. A., & Koch, C. (2012). The origin of extracellular fields and currents—eeg, ecog, lfp and spikes. *Nature reviews neuroscience*, 13(6), 407–420.
- Cerina, M., Piastra, M. C., & Frega, M. (2023). The potential of in vitro neuronal networks cultured on micro electrode arrays for biomedical research. *Progress in Biomedical Engineering*. <http://iopscience.iop.org/article/10.1088/2516-1091/acce12>
- Chan, S.-C., Mok, S.-Y., Ng, D. W.-K., & Goh, S.-Y. (2017). The role of neuron-glia interactions in the emergence of ultra-slow oscillations. *Biological cybernetics*, 111(5), 459–472.
- Charles, A. C., Merrill, J. E., Dirksen, E. R., & Sanderson, M. J. (1991). Intercellular signaling in glial cells: calcium waves and oscillations in response to mechanical stimulation and glutamate. *Neuron*, 6(6), 983–92. <http://www.ncbi.nlm.nih.gov/pubmed/1675864>
- Charlesworth, P., Cotterill, E., Morton, A., Grant, S. G. N., & Eglen, S. J. (2015). Quantitative differences in developmental profiles of spontaneous activity in cortical and hippocampal cultures. *Neural development*, 10, 1. <https://doi.org/10.1186/s13064-014-0028-0>
- Chatton, J.-Y., Pellerin, L., & Magistretti, P. J. (2003). Gaba uptake into astrocytes is not associated with significant metabolic cost: Implications for brain imaging of inhibitory transmission. *Proceedings of the National Academy of Sciences*, 100(21), 12456–12461. <https://doi.org/10.1073/pnas.2132096100>
- Chaure, F. J., Rey, H. G., & Quian Quiroga, R. (2018). A novel and fully automatic spike sorting implementation with variable number of features. *Journal of Neurophysiology*, 120(4), 1859–1871. <https://doi.org/10.1152/jn.00339.2018>
- Chiappalone, M., Bove, M., Vato, A., Tedesco, M., & Martinoia, S. (2006). Dissociated cortical networks show spontaneously correlated activity patterns during in vitro development. *Brain Research*, 1093(1), 41–53. <https://doi.org/https://doi.org/10.1016/j.brainres.2006.03.049>
- Cho, C.-H. (2013). New mechanism for glutamate hypothesis in epilepsy. *Frontiers in cellular neuroscience*, 7, 127. <https://doi.org/10.3389/fncel.2013.00127>

- Clausen, M. V., Hilbers, F., & Poulsen, H. (2017). The structure and function of the Na,K-ATPase isoforms in health and disease. *Frontiers in Physiology*, 8. <https://doi.org/10.3389/fphys.2017.00371>
- Coons, A. H., Creech, H. J., & Jones, R. N. (1941). Immunological properties of an antibody containing a fluorescent group. *Proceedings of the Society for Experimental Biology and Medicine*, 47(2), 200–202. <https://doi.org/10.3181/00379727-47-13084P>
- Cornell-Bell, A., Finkbeiner, S., Cooper, M., & Smith, S. (1990). Glutamate induces calcium waves in cultured astrocytes: long-range glial signaling. *Science*, 247(4941), 470–473. <https://doi.org/10.1126/science.1967852>
- Cornell-Bell, A., & Finkbeiner, S. (1991). Ca<sup>2+</sup> waves in astrocytes. *Cell Calcium*, 12(2-3), 185–204. [https://doi.org/10.1016/0143-4160\(91\)90020-F](https://doi.org/10.1016/0143-4160(91)90020-F)
- Cotterill, E., Charlesworth, P., Thomas, C. W., Paulsen, O., & Egle, S. J. (2016). A comparison of computational methods for detecting bursts in neuronal spike trains and their application to human stem cell-derived neuronal networks [PMID: 27098024]. *Journal of Neurophysiology*, 116(2), 306–321. <https://doi.org/10.1152/jn.00093.2016>
- Coulter, D. A., & Steinhäuser, C. (2015). Role of astrocytes in epilepsy. *Cold Spring Harbor perspectives in medicine*, 5(3), a022434. <https://doi.org/10.1101/cshperspect.a022434>
- Dallérac, G., Zapata, J., & Rouach, N. (2018). Versatile control of synaptic circuits by astrocytes: Where, when and how? *Nature Reviews Neuroscience*, 19, 726–743. <https://doi.org/10.1038/s41583-018-0080-6>
- Dani, J. W., Chernjavsky, A., & Smith, S. J. (1992). Neuronal activity triggers calcium waves in hippocampal astrocyte networks. *Neuron*, 8(3), 429–440. [https://doi.org/10.1016/0896-6273\(92\)90271-E](https://doi.org/10.1016/0896-6273(92)90271-E)
- De Pittà, M., & Berry, H. (2019). *Computational glioscience*. Springer.
- De Pittà, M., Volman, V., Berry, H., & Ben-Jacob, E. (2011). A tale of two stories: Astrocyte regulation of synaptic depression and facilitation. *PLoS Computational Biology*, 7(12). <https://doi.org/10.1371/journal.pcbi.1002293>
- De Pittà, M., Volman, V., Berry, H., Parpura, V., Volterra, A., & Ben-Jacob, E. (2012). Computational quest for understanding the role of astrocyte signaling in synaptic transmission and plasticity. *Frontiers in computational neuroscience*, 6, 98.



- Debanne, D., Campanac, E., Bialowas, A., Carlier, E., & Alcaraz, G. (2011). Axon physiology. *Physiological Reviews*, *91*(2), 555–602. <https://doi.org/10.1152/physrev.00048.2009>
- Dekker, P. (2002). *Epilepsy - A manual for Medical and Clinical Officers In Africa* (World Health Organization, Ed.). World Health Organization.
- de Melo Reis, R. A., Freitas, H. R., & de Mello, F. G. (2020). Cell calcium imaging as a reliable method to study neuron–glial circuits. *Frontiers in Neuroscience*, *14*. <https://doi.org/10.3389/fnins.2020.569361>
- Devinsky, O., Vezzani, A., Najjar, S., De Lanerolle, N. C., & Rogawski, M. A. (2013). Glia and epilepsy: Excitability and inflammation. <https://doi.org/10.1016/j.tins.2012.11.008>
- Djukic, B., Casper, K. B., Philpot, B. D., Chin, L.-S., & McCarthy, K. D. (2007). Conditional Knock-Out of Kir4.1 Leads to Glial Membrane Depolarization, Inhibition of Potassium and Glutamate Uptake, and Enhanced Short-Term Synaptic Potentiation. *Journal of Neuroscience*, *27*(42), 11354–11365. <https://doi.org/10.1523/JNEUROSCI.0723-07.2007>
- Doengi, M., Hirnet, D., Coulon, P., Pape, H.-C., Deitmer, J. W., & Lohr, C. (2009a). Gaba uptake-dependent  $Ca^{2+}$  signaling in developing olfactory bulb astrocytes. *Proceedings of the National Academy of Sciences*, *106*(41), 17570–17575. <https://doi.org/10.1073/pnas.0809513106>
- Doengi, M., Hirnet, D., Coulon, P., Pape, H.-C., Deitmer, J. W., & Lohr, C. (2009b). Gaba uptake-dependent  $Ca^{2+}$  signaling in developing olfactory bulb astrocytes. *Proceedings of the National Academy of Sciences*, *106*(41), 17570–17575. <https://doi.org/10.1073/pnas.0809513106>
- Dossi, E., Vasile, F., & Rouach, N. (2018). Human astrocytes in the diseased brain [Molecular mechanisms of astrocyte–neuron signalling]. *Brain Research Bulletin*, *136*, 139–156. <https://doi.org/10.1016/j.brainresbull.2017.02.001>
- Eid, T., Behar, K., Dhaher, R., Bumanglag, A. V., & Lee, T.-S. W. (2012). Roles of glutamine synthetase inhibition in epilepsy. *Neurochemical research*, *37*(11), 2339–50. <https://doi.org/10.1007/s11064-012-0766-5>
- Eid, T., Gruenbaum, S. E., Dhaher, R., Lee, T.-S. W., Zhou, Y., & Danbolt, N. C. (2016). The Glutamate–Glutamine Cycle in Epilepsy. *Advances in neurobiology* (pp. 351–400). [https://doi.org/10.1007/978-3-319-45096-4\\_14](https://doi.org/10.1007/978-3-319-45096-4_14)

- Fagerland, M. W. (2012). T-tests, non-parametric tests, and large studies—a paradox of statistical practice? *BMC medical research methodology*, 12(1), 1–7.
- Fahrner, A., Kann, G., Flubacher, A., Heinrich, C., Freiman, T. M., Zentner, J., Frotscher, M., & Haas, C. A. (2007). Granule cell dispersion is not accompanied by enhanced neurogenesis in temporal lobe epilepsy patients. *Experimental Neurology*, 203(2), 320–332. <https://doi.org/10.1016/j.expneurol.2006.08.023>
- Fellin, T., & Haydon, P. G. (2005). Do astrocytes contribute to excitation underlying seizures? *Trends in Molecular Medicine*, 11(12), 530–533. <https://doi.org/https://doi.org/10.1016/j.molmed.2005.10.007>
- Forsgren, L., Beghi, E., Oun, A., & Sillanpaa, M. (2005). The epidemiology of epilepsy in Europe - a systematic review. *European Journal of Neurology*, 12(4), 245–253. <https://doi.org/10.1111/j.1468-1331.2004.00992.x>
- Frega, M. (2016). *Neuronal Network Dynamics in 2D and 3D in vitro Neuroengineered Systems* (Vol. 53). <https://doi.org/10.1007/978-3-642-35133-4>
- Fujii, Y., Maekawa, S., & Morita, M. (2017). Astrocyte calcium waves propagate proximally by gap junction and distally by extracellular diffusion of atp released from volume-regulated anion channels. *Scientific Report*, 7. <https://doi.org/https://doi.org/10.1038/s41598-017-13243-0>
- Glass, M., & Dragunow, M. (1995). Neurochemical and morphological changes associated with human epilepsy. *Brain Research Reviews*, 21(1), 29–41. [https://doi.org/10.1016/0165-0173\(95\)00005-N](https://doi.org/10.1016/0165-0173(95)00005-N)
- Gordleeva, S. Y., Tsybina, Y. A., Krivonosov, M. I., Ivanchenko, M. V., Zaikin, A. A., Kazantsev, V. B., & Gorban, A. N. (2021). Modeling working memory in a spiking neuron network accompanied by astrocytes. *Frontiers in Cellular Neuroscience*, 15. <https://doi.org/10.3389/fncel.2021.631485>
- Guerra-Gomes, S., Sousa, N., Pinto, L., & Oliveira, J. F. (2018). Functional roles of astrocyte calcium elevations: From synapses to behavior. *Frontiers in Cellular Neuroscience*, 11. <https://doi.org/10.3389/fncel.2017.00427>
- Halassa, M. M., Fellin, T., & Haydon, P. G. (2007a). The tripartite synapse: Roles for gliotransmission in health and disease. *Trends in Molecular Medicine*, 13(2), 54–63. <https://doi.org/https://doi.org/10.1016/j.molmed.2006.12.005>

- Halassa, M. M., Fellin, T., & Haydon, P. G. (2007b). The tripartite synapse: Roles for gliotransmission in health and disease. *Trends in molecular medicine*, *13*(2), 54–63.
- Harris, J. J., Jolivet, R., & Attwell, D. (2012). Synaptic energy use and supply. *Neuron*, *75*(5), 762–77. <https://doi.org/10.1016/j.neuron.2012.08.019>
- Haydon, P. G. (2001). Glia: Listening and talking to the synapse. *Nature Reviews Neuroscience*, *2*(3), 185–193. <https://doi.org/10.1038/35058528>
- Hebb, D. O. (1949). *The Organization of Behavior*. <https://doi.org/10.2307/1418888>
- Heinemann, U., & Lux, H. (1977). Ceiling of stimulus induced rises in extracellular potassium concentration in the cerebral cortex of cat. *Brain Research*, *120*(2), 231–249. [https://doi.org/10.1016/0006-8993\(77\)90903-9](https://doi.org/10.1016/0006-8993(77)90903-9)
- Hentschke, H., & Stüttgen, M. C. (2011). Computation of measures of effect size for neuroscience data sets. *European Journal of Neuroscience*, *34*(12), 1887–1894.
- Herculano-Houzel, S. (2009). The human brain in numbers: a linearly scaled-up primate brain. *Frontiers in human neuroscience*, *3*, 31. <https://doi.org/10.3389/neuro.09.031.2009>
- Heuser, K., Nagelhus, E. A., Taubøll, E., Indahl, U., Berg, P. R., Lien, S., Nakken, S., Gjerstad, L., & Ottersen, O. P. (2010). Variants of the genes encoding AQP4 and Kir4.1 are associated with subgroups of patients with temporal lobe epilepsy. *Epilepsy Research*, *88*(1), 55–64. <https://doi.org/10.1016/j.eplepsyres.2009.09.023>
- Hinterkeuser, S., Schröder, W., Hager, G., Seifert, G., Blümcke, I., Elger, C. E., Schramm, J., & Steinhäuser, C. (2000). Astrocytes in the hippocampus of patients with temporal lobe epilepsy display changes in potassium conductances. *European Journal of Neuroscience*, *12*(6), 2087–2096. <https://doi.org/10.1046/j.1460-9568.2000.00104.x>
- Hodgkin, A. L., & Huxley, A. F. (1952). A quantitative description of membrane current and its application to conduction and excitation in nerve. *The Journal of Physiology*, *117*(4), 500–544. <https://doi.org/https://doi.org/10.1113/jphysiol.1952.sp004764>
- Hyvärinen, T., Hyysalo, A., Kapucu, F. E., Aarnos, L., Vinogradov, A., Eglen, S. J., Ylä-Outinen, L., & Narkilahti, S. (2019). Functional characterization

- of human pluripotent stem cell-derived cortical networks differentiated on laminin-521 substrate: Comparison to rat cortical cultures. *Scientific Reports*, 9.
- Ito, S., Yeh, F.-C., Hiolski, E., Rydygier, P., Gunning, D. E., Hottowy, P., Timme, N., Litke, A. M., & Beggs, J. M. (2014). Large-scale, high-resolution multielectrode-array recording depicts functional network differences of cortical and hippocampal cultures. *PLOS ONE*, 9(8), 1–16. <https://doi.org/10.1371/journal.pone.0105324>
- Jackson, M. B. (2006). Action potentials. *Molecular and cellular biophysics* (pp. 434–469). Cambridge University Press. <https://doi.org/10.1017/CBO9780511754869.017>
- Jourdain, P., Bergersen, L. H., Bhaukaurally, K., Bezzi, P., Santello, M., Domercq, M., Matute, C., Tonello, F., Gundersen, V., & Volterra, A. (2007). Glutamate exocytosis from astrocytes controls synaptic strength. *Nature Neuroscience*, 10(3), 331–339. <https://doi.org/10.1038/nn1849>
- Kang, J., Jiang, L., Goldman, S. A., & Nedergaard, M. (1998). Astrocyte-mediated potentiation of inhibitory synaptic transmission. *Nature Neuroscience*, 1(8), 683–692. <https://doi.org/10.1038/3684>
- Kapucu, F. E., Välkki, I., Mikkonen, J. E., Leone, C., Lenk, K., Tanskanen, J. M. A., & Hyttinen, J. A. K. (2016). Spectral entropy based neuronal network synchronization analysis based on microelectrode array measurements. *Frontiers in Computational Neuroscience*, 10. <https://doi.org/10.3389/fncom.2016.00112>
- Kasatkina, L. A. (2016). 4-aminopyridine sequesters intracellular ca<sup>2+</sup> which triggers exocytosis in excitable and non-excitable cells. *Scientific Reports*, 6.
- Kim, W. T., Rioult, M. G., & Cornell-Bell, A. H. (1994). Glutamate-induced calcium signaling in astrocytes. *Glia*, 11(2), 173–184. <https://doi.org/10.1002/glia.440110211>
- Lallouette, J., De Pittà, M., Ben-Jacob, E., & Berry, H. (2014). Sparse short-distance connections enhance calcium wave propagation in a 3D model of astrocyte networks. *Frontiers in Computational Neuroscience*, 8(April), 1–18. <https://doi.org/10.3389/fncom.2014.00045>
- Lallouette, J., Pittà, M. D., & Berry, H. (2018). Astrocyte networks and intercellular calcium propagation. *bioRxiv*. <https://doi.org/10.1101/248989>

- Lamberti, P., Martin, M., Plastino, A., & Rosso, O. (2004). Intensive entropic non-triviality measure. *Physica A: Statistical Mechanics and its Applications*, 334(1), 119–131. <https://doi.org/https://doi.org/10.1016/j.physa.2003.11.005>
- Larsen, B. R., Assentoft, M., Cotrina, M. L., Hua, S. Z., Nedergaard, M., Kaila, K., Voipio, J., & MacAulay, N. (2014). Contributions of the na<sup>+</sup>/k<sup>+</sup>-atpase, nkcc1, and kir4.1 to hippocampal k<sup>+</sup> clearance and volume responses. *Glia*, 62(4), 608–622. <https://doi.org/https://doi.org/10.1002/glia.22629>
- Lenk, K. (2011). A Simple Phenomenological Neuronal Model with Inhibitory and Excitatory Synapses. *BMC Neuroscience*, 12(Suppl 1), P260. <https://doi.org/10.1186/1471-2202-12-S1-P260>
- Lenk, K., Satuvuori, E., Lallouette, J., Ladrón-de-Guevara, A., Berry, H., & Hyttinen, J. A. K. (2020). A computational model of interactions between neuronal and astrocytic networks: The role of astrocytes in the stability of the neuronal firing rate. *Frontiers in Computational Neuroscience*, 13. <https://doi.org/10.3389/fncom.2019.00092>
- Lewis, R., Asplin, K. E., Bruce, G., Dart, C., Mobasheri, A., & Barrett-Jolley, R. (2011). The role of the membrane potential in chondrocyte volume regulation. *Journal of Cellular Physiology*, 226(11), 2979–2986. <https://doi.org/https://doi.org/10.1002/jcp.22646>
- Li, L., Zhou, J., Sun, H., Liu, J., Wang, H., Xiuling, L., & Wang, C. (2020). A computational model to investigate gaba-activated astrocyte modulation of neuronal excitation. *Computational and Mathematical Methods in Medicine*, 2020, 1–13. <https://doi.org/10.1155/2020/8750167>
- Li, Q., Li, Q.-Q., Jia, J.-N., Liu, Z.-Q., Zhou, H.-H., & Mao, X.-Y. (2019). Targeting gap junction in epilepsy: Perspectives and challenges. *Biomedicine & Pharmacotherapy*, 109, 57–65. <https://doi.org/https://doi.org/10.1016/j.biopha.2018.10.068>
- Lin, M., Lucas Jr, H. C., & Shmueli, G. (2013). Research commentary—too big to fail: Large samples and the p-value problem. *Information Systems Research*, 24(4), 906–917.
- Ma, B., Buckalew, R., Du, Y., Kiyoshi, C. M., Alford, C. C., Wang, W., McTigue, D. M., Enyeart, J. J., Terman, D., & Zhou, M. (2016). Gap junction cou-

- pling confers isopotentiality on astrocyte syncytium. *Glia*, 64(2), 214–226. <https://doi.org/https://doi.org/10.1002/glia.22924>
- Manninen, T., Havela, R., & Linne, M.-L. (2018). Computational models for calcium-mediated astrocyte functions. *Frontiers in Computational Neuroscience*, 12. <https://doi.org/10.3389/fncom.2018.00014>
- Martin, M., Plastino, A., & Rosso, O. (2003). Statistical complexity and disequilibrium. *Physics Letters A*, 311(2), 126–132. [https://doi.org/https://doi.org/10.1016/S0375-9601\(03\)00491-2](https://doi.org/https://doi.org/10.1016/S0375-9601(03)00491-2)
- Martinian, L., Boer, K., Middeldorp, J., Hol, E., Sisodiya, S., Squier, W., Aronica, E., & Thom, M. (2009). Expression patterns of glial fibrillary acidic protein (gfap)-delta in epilepsy-associated lesional pathologies. *Neuropathology and Applied Neurobiology*, 35(4), 394–405. <https://doi.org/10.1111/j.1365-2990.2008.00996.x>
- Mathern, G. W., Mendoza, D., Lozada, A., Pretorius, J. K., Dehnes, Y., Danbolt, N. C., Nelson, N., Leite, J. P., Chimelli, L., Born, D. E., Sakamoto, A. C., Assirati, J. A., Fried, I., Peacock, W. J., Ojemann, G. A., & Adelson, P. D. (1999). Hippocampal GABA and glutamate transporter immunoreactivity in patients with temporal lobe epilepsy. *Neurology*, 52(3), 453–72. <https://doi.org/10.1212/01.wnl.0000149636.44660.99>
- Meier, S. D., Kafitz, K. W., & Rose, C. R. (2008). Developmental profile and mechanisms of gaba-induced calcium signaling in hippocampal astrocytes. *Glia*, 56(10), 1127–1137. <https://doi.org/https://doi.org/10.1002/glia.20684>
- Mennerick, S., & Zorumski, C. (1994). Glial contributions to excitatory neurotransmission in cultured hippocampal cells. *Nature*, 19.
- Min, R., & Nevian, T. (2012). Astrocyte signaling controls spike timing-dependent depression at neocortical synapses. *Nature Neuroscience*, 15(5), 746–753. <https://doi.org/10.1038/nn.3075>
- Navarrete, M., Perea, G., de Sevilla, D. F., Gómez-Gonzalo, M., Núñez, A., Martín, E. D., & Araque, A. (2012). Astrocytes Mediate In Vivo Cholinergic-Induced Synaptic Plasticity (P. Scheiffele, Ed.). *PLoS Biology*, 10(2), e1001259. <https://doi.org/10.1371/journal.pbio.1001259>
- Nedergaard, M. (1994). Direct signaling from astrocytes to neurons in cultures of mammalian brain cells. *Science*, 263(5154), 1768–1771. <https://doi.org/10.1126/science.8134839>

- Nett, W. J., Oloff, S. H., & McCarthy, K. D. (2002). Hippocampal astrocytes in situ exhibit calcium oscillations that occur independent of neuronal activity [PMID: 11784768]. *Journal of Neurophysiology*, 87(1), 528–537. <https://doi.org/10.1152/jn.00268.2001>
- Newman, E., & Reichenbach, A. (1996). The Müller cell: a functional element of the retina. *Trends in neurosciences*, 19(8), 307–12. <http://www.ncbi.nlm.nih.gov/pubmed/8843598>
- Oberheim, N. A., Takano, T., Han, X., He, W., Lin, J. H. C., Wang, F., Xu, Q., Wyatt, J. D., Pilcher, W., Ojemann, J. G., Ransom, B. R., Goldman, S. A., & Nedergaard, M. (2009a). Uniquely hominid features of adult human astrocytes. *The Journal of neuroscience: the official journal of the Society for Neuroscience*, 29(10), 3276–87. <https://doi.org/10.1523/JNEUROSCI.4707-08.2009>
- Oberheim, N. A., Takano, T., Han, X., He, W., Lin, J. H. C., Wang, F., Xu, Q., Wyatt, J. D., Pilcher, W., Ojemann, J. G., Ransom, B. R., Goldman, S. A., & Nedergaard, M. (2009b). Uniquely hominid features of adult human astrocytes. *The Journal of neuroscience : the official journal of the Society for Neuroscience*, 29(10), 3276–87. <https://doi.org/10.1523/JNEUROSCI.4707-08.2009>
- Obien, M. E. J., Deligkaris, K., Bullmann, T., Bakkum, D. J., & Frey, U. (2015). Revealing neuronal function through microelectrode array recordings. *Frontiers in Neuroscience*, 8. <https://doi.org/10.3389/fnins.2014.00423>
- Oliveira, J. F., & Araque, A. (2022). Astrocyte regulation of neural circuit activity and network states. *Glia*, 70(8), 1455–1466. <https://doi.org/https://doi.org/10.1002/glia.24178>
- O'Rourke, N. A., Weiler, N. C., Micheva, K. D., & Smith, S. J. (2012). Deep molecular diversity of mammalian synapses: Why it matters and how to measure it. *Nature Reviews Neuroscience*, 13(6), 365–379.
- Oschmann, F., Berry, H., Obermayer, K., & Lenk, K. (2018). From in silico astrocyte cell models to neuron-astrocyte network models: A review [Molecular mechanisms of astrocyte-neuron signalling]. *Brain Research Bulletin*, 136, 76–84. <https://doi.org/https://doi.org/10.1016/j.brainresbull.2017.01.027>

- Pachitariu, M., Steinmetz, N., Kadir, S., Carandini, M., & Kenneth D., H. (2016). Kilosort: Realtime spike-sorting for extracellular electrophysiology with hundreds of channels. *bioRxiv*. <https://doi.org/10.1101/061481>
- Parpura, V., Basarsky, T. A., Liu, F., Jęftinija, K., Jęftinija, S., & Haydon, P. G. (1994). Glutamate-mediated astrocyte–neuron signalling. *Nature*, *369*(6483), 744–747. <https://doi.org/10.1038/369744a0>
- Perea, G., & Araque, A. (2007). Astrocytes Potentiate Transmitter Release at Single Hippocampal Synapses. *Science*, *317*(5841), 1083–1086. <https://doi.org/10.1126/science.1144640>
- Perea, G., & Araque, A. (2005). Properties of synaptically evoked astrocyte calcium signal reveal synaptic information processing by astrocytes. *Journal of Neuroscience*, *25*(9), 2192–2203. <https://doi.org/10.1523/JNEUROSCI.3965-04.2005>
- Perez-Catalan, N., Doe, C., & Ackerman, S. (2021). The role of astrocyte-mediated plasticity in neural circuit development and function. *Neural Development*, *16*. <https://doi.org/10.1186/s13064-020-00151-9>
- Postnov, D. E., Koreshkov, R., Brazhe, N. A., Brazhe, A. R., & Sosnovtseva, O. V. (2009). Dynamical patterns of calcium signaling in a functional model of neuron–astrocyte networks. *Journal of biological physics*, *35*(4), 425–445.
- Puthanmadam Subramaniam, N., & Hyttinen, J. (2014). Characterization of dynamical systems under noise using recurrence networks: Application to simulated and eeg data. *Physics Letters A*, *378*(46), 3464–3474. <https://doi.org/https://doi.org/10.1016/j.physleta.2014.10.005>
- Quian Quiroga, R. (2009). What is the real shape of extracellular spikes? *Journal of Neuroscience Methods*, *177*(1), 194–198. <https://doi.org/https://doi.org/10.1016/j.jneumeth.2008.09.033>
- Quiroga, R. Q., Nadasdy, Z., & Ben-Shaul, Y. (2004). Unsupervised spike detection and sorting with wavelets and superparamagnetic clustering. *Neural computation*, *16*(8), 1661–1687.
- Quiroga, R. Q., Reddy, L., Koch, C., & Fried, I. (2007). Decoding visual inputs from multiple neurons in the human temporal lobe. *Journal of Neurophysiology*, *98*(4), 1997–2007. <https://doi.org/10.1152/jn.00125.2007>
- Ramón y Cajal, S. (1911). Histologie du système nerveux de l’homme et des vertébrés. *Paris: Maloine*. <https://doi.org/http://dx.doi.org/10.5962/bhl.title.48637>



- Rose, C. R., & Ransom, B. R. (1997). Gap junctions equalize intracellular  $\text{Na}^+$  concentration in astrocytes. *GLIA*, 20(4), 299–307. [https://doi.org/10.1002/\(SICI\)1098-1136\(199708\)20:4<299::AID-GLIA3>3.0.CO;2-1](https://doi.org/10.1002/(SICI)1098-1136(199708)20:4<299::AID-GLIA3>3.0.CO;2-1)
- Rossi, D., & Volterra, A. (2009). Astrocytic dysfunction: Insights on the role in neurodegeneration. *Brain Research Bulletin*, 80(4-5), 224–232. <https://doi.org/10.1016/j.brainresbull.2009.07.012>
- Rosso, O. A., Larrondo, H. A., Martin, M. T., Plastino, A., & Fuentes, M. A. (2007). Distinguishing noise from chaos. *Phys. Rev. Lett.*, 99, 154102. <https://doi.org/10.1103/PhysRevLett.99.154102>
- Rosso, O. A., Carpi, L. C., Saco, P. M., Gómez Ravetti, M., Plastino, A., & Larrondo, H. A. (2012). Causality and the entropy–complexity plane: Robustness and missing ordinal patterns. *Physica A: Statistical Mechanics and its Applications*, 391(1), 42–55. <https://doi.org/https://doi.org/10.1016/j.physa.2011.07.030>
- Savtchenko, L. P., & Rusakov, D. A. (2014). Regulation of rhythm genesis by volume-limited, astroglia-like signals in neural networks. *Philosophical Transactions of the Royal Society B: Biological Sciences*, 369(1654), 20130614. <https://doi.org/10.1098/rstb.2013.0614>
- Schreiber, T., & Schmitz, A. (1996). Improved surrogate data for nonlinearity tests. *Phys. Rev. Lett.*, 77, 635–638. <https://doi.org/10.1103/PhysRevLett.77.635>
- Seifert, G., Huttmann, K., Binder, D. K., Hartmann, C., Wyczynski, A., Neusch, C., & Steinhauser, C. (2009). Analysis of Astroglial  $\text{K}^+$  Channel Expression in the Developing Hippocampus Reveals a Predominant Role of the Kir4.1 Subunit. *Journal of Neuroscience*, 29(23), 7474–7488. <https://doi.org/10.1523/JNEUROSCI.3790-08.2009>
- Seifert, G. (2010). Astrocyte dysfunction in temporal lobe epilepsy. *Epilepsia*, 51(SUPPL. 5), 54. <https://doi.org/10.1111/j.1528-1167.2010.02840.x>
- Seifert, G., Schilling, K., & Steinhauser, C. (2006). Astrocyte dysfunction in neurological disorders: a molecular perspective. *Nature reviews. Neuroscience*, 7(3), 194–206. <https://doi.org/10.1038/nrn1870>
- Sejnowski, T. J., Koch, C., & Churchland, P. S. (1988). Computational neuroscience. *Science*, 241(4871), 1299–1306. <https://doi.org/10.1126/science.3045969>

- Shannon, C. E. (1948). A mathematical theory of communication. *The Bell System Technical Journal*, 27(3), 379–423. <https://doi.org/10.1002/j.1538-7305.1948.tb01338.x>
- Shen, K., McFadden, A., & McIntosh, A. R. (2021). Signal complexity indicators of health status in clinical eeg. *Scientific Reports*, 11(1), 20192.
- Smith, M. L., & Glass, G. V. (1977). Meta-analysis of psychotherapy outcome studies. *American psychologist*, 32(9), 752.
- Sofroniew, M. V., & Vinters, H. V. (2010). Astrocytes: Biology and pathology. *Acta Neuropathologica*, 119(1), 7–35. <https://doi.org/10.1007/s00401-009-0619-8>
- Srinivasan, R., Huang, B. S., Venugopal, S., Johnston, A. D., Chai, H., Zeng, H., Golshani, P., & Khakh, B. S. (2015). Ca<sup>2+</sup> signaling in astrocytes from ip3r2<sup>-/-</sup> mice in brain slices and during startle responses in vivo. *Nature neuroscience*, 18(5), 708–717.
- Stafstrom, C. E., & Carmant, L. (2015). Seizures and epilepsy: an overview for neuroscientists. *Cold Spring Harbor perspectives in medicine*, 5(6). <https://doi.org/10.1101/cshperspect.a022426>
- Steinhäuser, C., & Seifert, G. (2002). Glial membrane channels and receptors in epilepsy: impact for generation and spread of seizure activity. *European Journal of Pharmacology*, 447(2-3), 227–237. [https://doi.org/10.1016/S0014-2999\(02\)01846-0](https://doi.org/10.1016/S0014-2999(02)01846-0)
- Steinhäuser, C., Seifert, G., & Bedner, P. (2012). Astrocyte dysfunction in temporal lobe epilepsy: K<sup>+</sup> channels and gap junction coupling. *Glia*, 60(8), 1192–1202. <https://doi.org/10.1002/glia.22313>
- Stockert, J. C., & Blazquez-Castro, A. (2017). *Fluorescence microscopy in life sciences*. Bentham Science Publisher. <https://doi.org/10.2174/97816810851801170101>
- Subramaniam, N. P., Donges, J. F., & Hyttinen, J. (2015). Signatures of chaotic and stochastic dynamics uncovered with  $\varepsilon$ -recurrence networks. *Proceedings of the Royal Society A: Mathematical, Physical and Engineering Sciences*, 471(2183), 20150349. <https://doi.org/10.1098/rspa.2015.0349>
- Sun, J.-J., Kilb, W., & Luhmann, H. J. (2010). Self-organization of repetitive spike patterns in developing neuronal networks in vitro. *European Journal of Neu-*

- rosience*, 32(8), 1289–1299. <https://doi.org/https://doi.org/10.1111/j.1460-9568.2010.07383.x>
- Sun, S. H., Almasi, A., Yunzab, M., Zehra, S., Hicks, D. G., Kameneva, T., Ibbotson, M. R., & Meffin, H. (2021). Analysis of extracellular spike waveforms and associated receptive fields of neurons in cat primary visual cortex. *The Journal of Physiology*, 599(8), 2211–2238. <https://doi.org/https://doi.org/10.1113/JP280844>
- Taga, A., Dastgheyb, R., Habela, C., Joseph, J., Richard, J.-P., Gross, S. K., Lauria, G., Lee, G., Haughey, N., & Maragakis, N. J. (2019). Role of human-induced pluripotent stem cell-derived spinal cord astrocytes in the functional maturation of motor neurons in a multielectrode array system. *Stem cells translational medicine*, 8(12), 1272–1285.
- Tan, C. X., Burrus Lane, C. J., & Eroglu, C. (2021). Chapter nine - role of astrocytes in synapse formation and maturation. In G. J. Bashaw (Ed.), *Molecular mechanisms of neural development and insights into disease* (pp. 371–407). Academic Press. <https://doi.org/https://doi.org/10.1016/bs.ctdb.2020.12.010>
- Thom, M. (2014). Review: Hippocampal sclerosis in epilepsy: A neuropathology review. *Neuropathology and Applied Neurobiology*, 40(5), 520–543. <https://doi.org/10.1111/nan.12150>
- Tian, G.-F., Azmi, H., Takano, T., Xu, Q., Peng, W., Lin, J., Oberheim, N., Lou, N., Wang, X., Zielke, H. R., Kang, J., & Nedergaard, M. (2005). An astrocytic basis of epilepsy. *Nature Medicine*, 11(9), 973–981. <https://doi.org/10.1038/nm1277>
- Tsodyks, M., Pawelzik, K., & Markram, H. (1998). Neural networks with dynamic synapses. *Neural Computation*, Volume 10(Issue 4), 821–835. <http://www.mitpressjournals.org/doi/abs/10.1162/089976698300017502>
- Välkki, I. A., Lenk, K., Mikkonen, J. E., Kapucu, F. E., & Hyttinen, J. A. K. (2017). Network-Wide Adaptive Burst Detection Depicts Neuronal Activity with Improved Accuracy. *Frontiers in Computational Neuroscience*, 11(May), 1–14. <https://doi.org/10.3389/fncom.2017.00040>
- van den Pol, A., & Spencer, D. (1999). Differential neurite growth on astrocyte substrates: Interspecies facilitation in green fluorescent protein-transfected

- rat and human neurons. *Neuroscience*, 95(2), 603–616. [https://doi.org/https://doi.org/10.1016/S0306-4522\(99\)00430-3](https://doi.org/https://doi.org/10.1016/S0306-4522(99)00430-3)
- Verkhratsky, A., & Kettenmann, H. (1996). Calcium signalling in glial cells. *Trends in neurosciences*, 19(8), 346–52. [https://doi.org/10.1016/0166-2236\(96\)10048-5](https://doi.org/10.1016/0166-2236(96)10048-5)
- Verkhratsky, A., & Nedergaard, M. (2018). Physiology of Astroglia. *Physiological Reviews*, 98(1), 239–389. <https://doi.org/10.1152/physrev.00042.2016>
- Verkhratsky, A., Untiet, V., & Rose, C. R. (2020). Ionic signalling in astroglia beyond calcium. *The Journal of Physiology*, 598(9), 1655–1670. <https://doi.org/https://doi.org/10.1113/JP277478>
- Verkhratsky, A., Orkand, R. K., & Kettenmann, H. (1998). Glial Calcium: Homeostasis and Signaling Function. *Physiological Reviews*, 78(1), 99–141. <https://doi.org/10.1152/physrev.1998.78.1.99>
- Volterra, A., Liaudet, N., & Savtchouk, I. (2014). Astrocyte ca<sup>2+</sup> signalling: An unexpected complexity. *Nature Reviews Neuroscience*, 15(5), 327–335.
- von Bartheld, C. S., Bahney, J., & Herculano-Houzel, S. (2016). The search for true numbers of neurons and glial cells in the human brain: A review of 150 years of cell counting. *Journal of Comparative Neurology*, 524(18), 3865–3895. <https://doi.org/10.1002/cne.24040>
- Wallraff, A. (2006). The Impact of Astrocytic Gap Junctional Coupling on Potassium Buffering in the Hippocampus. *Journal of Neuroscience*, 26(20), 5438–5447. <https://doi.org/10.1523/JNEUROSCI.0037-06.2006>
- Walrave, L., Vinken, M., Leybaert, L., & Smolders, I. (2020). Astrocytic connexin43 channels as candidate targets in epilepsy treatment. *Biomolecules*, 10(11). <https://doi.org/10.3390/biom10111578>
- World Health Organization. (2018). Epilepsy - Fact sheet. <http://www.who.int/mediacentre/factsheets/fs999/en/>
- Yger, P., Spampinato, G. L., Esposito, E., Lefebvre, B., Deny, S., Gardella, C., Stimberg, M., Jetter, F., Zeck, G., Picaud, S., Duebel, J., & Marre, O. (2018). A spike sorting toolbox for up to thousands of electrodes validated with ground truth recordings in vitro and in vivo (D. Kleinfeld, Ed.). *eLife*, 7, e34518. <https://doi.org/10.7554/eLife.34518>

## PUBLICATIONS



# PUBLICATION

I

**Influence of astrocytic gap junction coupling on in silico neuronal network activity**

**Genocchi, B., Lenk, K., and Hyttinen, J.**

*Mediterranean Conference on Medical and Biological Engineering and Computing, 480–487*




**Publication reprinted with the permission of the copyright holders.**







# Influence of Astrocytic Gap Junction Coupling on *in Silico* Neuronal Network Activity

Barbara Genocchi<sup>(✉)</sup> , Kerstin Lenk , and Jari Hyttinen 

Faculty of Medicine and Health Technology, BioMediTech,  
Tampere University, Tampere, Finland  
barbara.genocchi@tuni.fi

**Abstract.** Astrocytes cover a plethora of roles supporting neurons in their maturation and regulating the concentrations of several ions and neurotransmitters. Moreover, astrocytes dysfunctions are, nowadays, suspected to have important implication in several brain diseases, as for example in epilepsy and Alzheimer's disease. The astrocytes themselves are forming a network mediated by gap junctions. A loss of gap junctions between astrocytes has been connected with epilepsy. The aim of this study is to computationally test the influence of astrocytes connectivity in regulating activity in the neuronal network. To conduct the study, it has been used an *in silico* neuron-astrocyte model developed in our group. The model simulates the processes governing the communications between an astrocyte and a pre- and a postsynaptic neuron in the tripartite synapse, as well as between astrocytes through gap junction coupling. The modeled network comprises 250 neurons and 107 astrocytes. Three different astrocytic connectivity levels have been studied – representing 0, 2 and 4 gap junctions on average per astrocyte. Additionally, three different noise levels have been applied to the presynaptic terminal to simulate low, high and hyperactivity. Since the activation of astrocytes is driven by the activity of the neuronal network, the results showed that in case of low activity astrocytes were not activated and did not regulate neuronal activity. In case of high neuronal activity and hyperactivity, astrocytes showed an increased capability of downregulating neuronal activity when increasing the astrocytic connectivity. These results are in accordance with several *in vivo* experiments from different laboratories.

**Keywords:** Astrocytes · Epilepsy · Simulation · Gap junctions · Connectivity

## 1 Introduction

Since early 1990s and with the introduction of the concept of the tripartite synapse [1–3], several roles have been acknowledged to astrocytes. Nowadays, astrocytes are known to promote synapse formation, maturation and elimination, and to help in long-distance communication and information integration. They also provide maintenance of ionic and neurotransmitters homeostasis, in order to preserve spatial and temporal encoding of synaptic transmission and to avoid excitotoxicity [4]. Several reviews have focused on astrocyte calcium signaling [5, 6], which can be triggered by neuronal activity and stimulates gliotransmitters release from astrocytes to neurons. Therefore, calcium signaling can in turn modulate the neuronal activity [7]. During the last years,

© Springer Nature Switzerland AG 2020

J. Henriques et al. (Eds.): MEDICON 2019, IFMBE Proceedings 76, pp. 480–487, 2020.

[https://doi.org/10.1007/978-3-030-31635-8\\_58](https://doi.org/10.1007/978-3-030-31635-8_58)

barbara.genocchi@tuni.fi

it has become clear that particular abnormal functionalities in glial cells and astrocytes can be correlated with central nervous system (CNS) diseases [8, 9]. The main astrocytic dysfunctions thought to be related with epilepsy are impaired potassium buffering, abnormalities in astrocytic gap junctions (GJs) and abnormal uptake of glutamate. In particular from *in vivo* experiments, researchers reported spontaneous epileptiform activity in the CNS due to a loss of Cx30 and Cx43. Those two connexins are fundamentals specifically for the formation of astrocytic GJs [10].

During the last decade, the increasing quest for understanding the roles of astrocytes in health and brain diseases together with the large amount of data from *in vitro* and *in vivo* research has stimulated the use of computational tools and models at several scales: from single astrocytes to astrocytes networks towards neuron-astrocytes *in silico* models [11].

The aim of this study is to computationally investigate the role of astrocytic network connectivity in the regulation of neuronal activity. In order to evaluate the influence of astrocytic GJs connectivity, our custom neuron-astrocyte network model has been used with different amounts of GJs between astrocytes [11, 12]. To the best of our knowledge, the role of GJs have not been studied before in biophysically plausible computational models comprising larger networks as well as external stimuli as input. Amiri et al. [13] and Naeem et al. [14] presented network models with neuron and astrocytes as well as GJs between neighboring astrocytes, but lacking a proper network topology; in fact, in both cases the astrocytes were distributed in lines and the cells contacted only the two neighboring astrocytes.

## 2 Methods

The astrocyte–neuronal network model used in this study is based on a tripartite synapse model [12]. It is a modified version of Tsodyks–Markram presynaptic model [15], used as described by De Pittà et al. [16] and combined with astrocytic effects as described in the latter paper. To simulate the neuronal activity, we used a spiking neuronal network, called INEX model [17], which comprises excitatory and inhibitory neurons connected by synapses and includes a noise term. The neuronal activity is created with Poisson processes. The above mentioned Tsodyks–Markram model simulates the glutamate release from the presynaptic terminal. It assumes that at the time in which a spike arrives only part of the neurotransmitter is ready to be released, and only a small amount of these releasable resources are de facto released.

The astrocyte  $IP_3$  and calcium dynamics are also included in the model as described in De Pittà et al. [16], where intracellular calcium release from the stores follows the  $IP_3$  release. Astrocytes, when active, release glutamate and signal back to the synapses that are connected to them. Calcium release stimulates a wave propagation between neighboring astrocytes through GJs. In our present model, the propagation is implemented according to the model introduced by Lallouette et al. [18].

The model simulates 180 s and the time step used is 5 ms. These two parameters are a satisfactory compromise to consider both, the fast dynamics of neurons and the slower astrocytic response, keeping the simulation time on the computer cluster as reasonable as possible. We simulated each of the below described conditions three times.

The neuronal network, comprising 200 excitatory neurons and 50 inhibitory neurons, was randomly created once and the connections between neurons were created following a Gaussian distribution based on the distance between two neurons. The simulations produced networks with roughly 10,000 excitatory synapses.

Astrocytes cover non-overlapping domains and the average radius of a rodent protoplasmic astrocyte is  $\sim 30 \mu\text{m}$ , considering the soma and the primary processes [19]. Hence, in our model if the distance between astrocytes is shorter than this value the connection is not created. The neuronal network was then combined with three different astrocytic networks, all of them counting 107 astrocytes. On average each astrocyte in the network is connected to 90 nearby excitatory synapses. By varying the parameters of the Gaussian distribution of the astrocyte connections, the chosen average number of GJs for each astrocyte was respectively 0, 2 and 4 (Fig. 1A, B, and C).

To elicit the activation of astrocytes, three different noise levels have been applied to the presynaptic terminals in the neurons. These simulated the three conditions of low, high and hyperactivity. The last one could be considered as an epileptic form. The high noise was three times the noise value used for low activity and the hyperactivity was 8 times the low noise value.

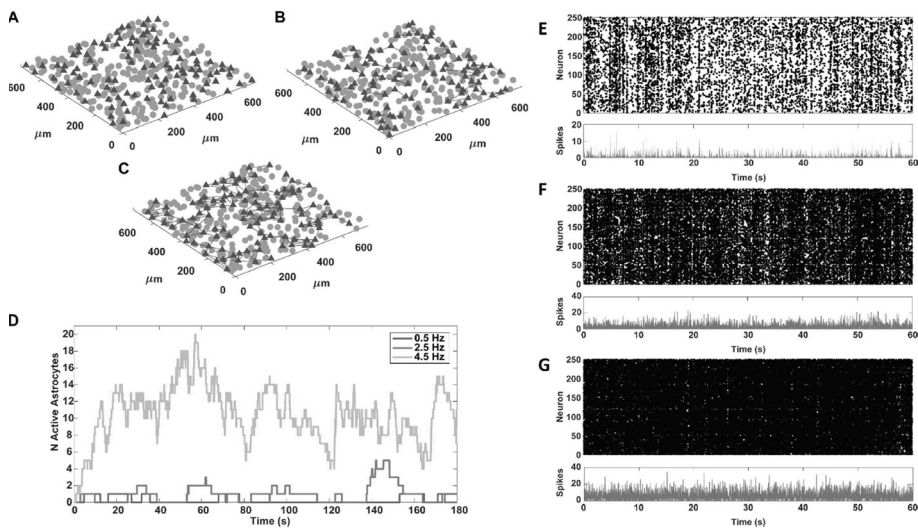


**Fig. 1.** 2D graphical representation of the three different networks configurations used in the simulations: (A) No gap junction coupling, (B) two GJs, and (C) four GJs per astrocyte on average. Green dots represent excitatory and inhibitory neurons and red triangles represent astrocytes. The red lines represent connections including GJs between astrocytic processes. (D) Comparison between astrocytic activation in the case of low (blue), high (red) neuronal activity and hyperactivity (orange) for the network with no GJs between astrocytes. The plot shows the number of active cells at each time step (5 ms). On the right are shown examples of a raster plot from a simulation with low activity (E), high activity (F) and hyperactivity (G). In the upper part of each subplot, black dots represent spikes occurring in the neurons for the first 60 s of the simulation. In the lower part of each subplot is shown the number of spikes binned to 5 ms.

To conduct neuronal burst analysis, a modified version of an algorithm by Kapucu et al. [20] was used. This tool calculates intrinsic bursting using the cumulative moving average and the skewness of the interspike interval histogram.

### 3 Results

#### 3.1 Low Noise Condition

To simulate low neuronal activity, a weak noise input was applied to the neurons, resulting in an average presynaptic frequency of 0.5 Hz. The consequent number of active astrocytes is shown in Fig. 1D (in blue).

Since the astrocytic activation is correlated with the presynaptic activity, the average number of active astrocytes was very low. A raster plot and the number of spikes binned per 5 ms of the first 60 s of the simulation for postsynaptic neurons in case of no gap junction coupling between astrocytes is shown as an example in Fig. 1E.

The spike rate, calculated in spikes/min, varied in similar intervals of values for all three configurations (Table 1). In fact, the notches, such as the triangular cuts on the boxes sides, in the box plots in Fig. 2A overlap. This means that the three medians represented by red lines in the plot, cannot be considered statistically different.

In these low activity simulations, bursting is mainly not present in neurons. In Fig. 2A, the medians of the burst rate are all around very low values (Table 1). However, a few neurons presented some bursting, shown by the red pluses. Pluses show data points beyond the whiskers. This probably occurred in neurons with more synaptic connections, enhancing their own activity. Due to this high variability in the bursts rate, the standard deviation appears to be higher than the value itself.

**Table 1.** Spike rate (spikes/min) and burst rate (burst/min) with 0, 2 and 4 GJs per astrocyte for the simulated low activity.

N of GJs	Avg. spike rate $\pm$ std	Avg. burst rate $\pm$ std
0	32.05 $\pm$ 9.65	0.07 $\pm$ 0.16
2	35.54 $\pm$ 10.88	0.06 $\pm$ 0.16
4	34.75 $\pm$ 10.92	0.09 $\pm$ 0.20

#### 3.2 High Noise Condition

To simulate diffused high activity in the neuronal network, a noise input was applied to the presynaptic terminal. The noise input was three times larger than the one used for low activity and resulted in a presynaptic activity with a frequency of 2.5 Hz (Fig. 1F). This led to a stronger activation of the astrocytes as can be seen from the red curve in Fig. 1D.

The results show that when increasing the number of GJs, the postsynaptic spike and burst rate were decreased (Table 2, Fig. 2B). The spike rate decrease is clearer, when comparing the no gap junction case to 2 and 4 GJs on average. Between 2 and 4 GJs on average, it is still possible to notice a small increase in the downregulation of the activity.

In addition, the burst rate decreased with increasing number of GJs, but also in this case the high variability of bursting amongst all the 250 neurons resulted in a high standard deviation. Since the notches of the boxes for spike and burst rate of the no gap junction condition and respectively the 2 and 4 GJs do not overlap, we can conclude that the two distributions are statistically different with 95% confidence from the first one.

**Table 2.** Spike rate (spikes/min) and burst rate (burst/min) with 0, 2 and 4 GJs per astrocyte for the simulated high activity.

N of GJs	Avg. spike rate $\pm$ std	Avg. burst rate $\pm$ std
0	140.52 $\pm$ 42.81	2.46 $\pm$ 2.03
2	126.81 $\pm$ 37.54	1.74 $\pm$ 1.54
4	120.23 $\pm$ 34.62	1.59 $\pm$ 1.35

### 3.3 Hyperactivity Condition

To simulate diffused hyperactivity in the neuronal network, a noise input 8 times larger than the one used for low activity was applied to the presynaptic terminal. This resulted in a presynaptic activity with a frequency of 4.5 Hz (Fig. 1G). The stronger activation of the astrocytes can be seen in the orange curve in Fig. 1D. The active astrocytes overexcite the synapses connected to them by releasing glutamate in the extrasynaptic space. In turn, the inhibitory neurons are not anymore capable to downregulate the system.

In order to evaluate, if the spike and burst rate was decreasing when increasing the GJs coupling, it was conducted a paired-sample Student's t-test. For both spike rate (SR) and burst rate (BR) (Table 3, Fig. 2C), the 2 and 4 GJs distributions were significantly decreased in respect to the no gap junction distribution (SR:  $p = 0.012$  and  $p = 0.002$ , respectively. BR:  $p = 0.003$  and  $p = 4.67e-04$ , respectively).

**Table 3.** Spike rate (spikes/min) and burst rate (burst/min) with 0, 2 and 4 GJs per astrocyte for the simulated hyperactivity.

N of GJs	Avg. spike rate $\pm$ std	Avg. burst rate $\pm$ std
0	280.49 $\pm$ 78.21	13.53 $\pm$ 8.37
2	272.71 $\pm$ 69.65	12.51 $\pm$ 7.17
4	271.79 $\pm$ 83.97	12.57 $\pm$ 8.50

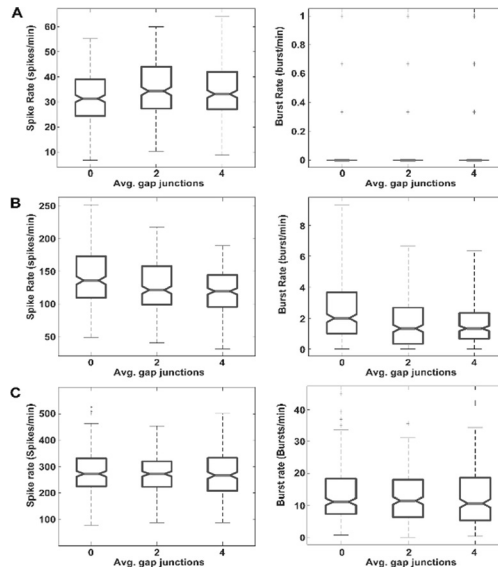


**Fig. 2.** Box plots of spike rate (spikes/min; left) and burst rate (bursts/min; right) for low activity (A), high activity (B) and hyperactivity (C). The red lines represent the medians of the data distributions. The notches indicate the 95% confidence interval of the median.

## 4 Conclusions

During the last decade, researchers have investigated whether dysfunctions in astrocytes can cause or partially cause CNS disorders. Several *in vivo* experiments seem to confirm that hypothesis [8–10].

This study aim was to computationally evaluate the role of astrocytic connectivity on the capability to downregulate high activity in an astrocyte-neuron network. Astrocytic connectivity was expressed in terms of average number of GJs per astrocyte. Three different astrocyte network connectivity levels were investigated: 0, 2 and 4 GJs on average per astrocyte in the network.

The activation of astrocytes is triggered by the neuronal network activity. Neuronal activity, in turn, is modulated by the astrocytes controlling the amount of available resources at the synapses through local calcium activity and subsequent glutamate release.

In the low noise condition, as expected, it was not possible to observe any regulatory functions related to the number of GJs (Table 1, Fig. 2A). The input noise resulted in a low number of active astrocytes in the network. In high and hyperactivity, instead, the number of active astrocytes was higher, producing increased modulatory response thus decreasing the spike and burst rates (Fig. 2B and C).

These results demonstrate that the capability of the astrocytic network in down-regulating the hyperactivity depends on the number of GJs and thus on the astrocyte network connectivity. These results are in accordance to the experiments in which the

deletion of Cx43 and Cx30, resulting in a cell-specific loss of GJs, stimulated the generation of spontaneous epileptiform activity [10].

Our simulation results highlight the possible role of astrocytes in the neuronal regulation that could also affect the susceptibility of the neuronal system to epileptic events. Astrocytes may thus also offer a new drug target for treating neural diseases.

**Acknowledgment.** This research has received funding from the European Union’s Horizon 2020 research and innovation programme under the Marie Skłodowska-Curie grant agreement No. 713645. K. L. is funded by the Academy of Finland (decision no. 314647).

**Conflict of Interest.** The authors declare that they have no conflict of interest.

## References

1. Nedergaard, M.: Direct signaling from astrocytes to neurons in cultures of mammalian brain cells. *Science* **263**, 1768–1771 (1994)
2. Parpura, V., Basarsky, T.A., Liu, F., et al.: Glutamate-mediated astrocyte–neuron signaling. *Nature* **369**, 744–747 (1994)
3. Araque, A., Parpura, V., Sanzgiri, R.P., et al.: Tripartite synapses: glia, the unacknowledged partner. *Trends Neurosci.* **22**, 208–215 (1999)
4. Vasile, F., Dossi, E., Rouach, N.: Human astrocytes: structure and functions in the healthy brain. *Brain struct. funct.* **222**, 2017–2029 (2017)
5. Bazargani, N., Attwell, D.: Astrocyte calcium signaling: the third wave. *Nat. Neurosci.* **19**, 182–189 (2016)
6. Perea, G., Navarrete, M., Araque, A.: Tripartite synapses: astrocytes process and control synaptic information. *Trends Neurosci.* **32**, 421–431 (2009)
7. Savtchouk, I., Volterra, A.: Gliotransmission: beyond black-and-white. *J. Neurosci.* **38**, 14–25 (2018)
8. Seifert, G., Schilling, K., Steinhäuser, C.: Astrocyte dysfunction in neurological disorders: a molecular perspective. *Nat. Rev. Neurosci.* **7**, 194–206 (2006)
9. Dossi, E., Vasile, F., Rouach, N.: Human astrocytes in the diseased brain. *Brain Res. Bull.* **136**, 140–147 (2018)
10. Seifert, G., Carmignoto, G., Steinhäuser, C.: Astrocyte dysfunction in epilepsy. *Brain Res. Rev.* **63**, 212–221 (2010)
11. Oschmann, F., Berry, H., Obermayer, K., et al.: From in silico astrocyte cell models to neuron-astrocyte network models: a review. *Brain Res. Bull.* **136**, 76–84 (2018)
12. Lenk, K., Raisanen, E., Hyttinen, J.A.K.: Understanding the role of astrocytic GABA in simulated neural networks. In: *Conference Proceedings of the IEEE Engineering in Medicine and Biology Society*, pp. 6121–6124 (2016)
13. Amiri, M., Hosseinmardi, N., Bahrami, F., et al.: Astrocyte–neuron interaction as a mechanism responsible for generation of neural synchrony: a study based on modeling and experiments. *J. Comput. Neurosci.* **34**, 489 (2013)
14. Naeem, M., McDaid, L.J., Harkin, J., et al.: On the role of astroglial syncytia in self-repairing spiking neural networks. *IEEE Trans. Neural Netw. Learn. Syst.* **26**(10), 2370–2380 (2015)
15. Tsodyks, M.V., Markram, H.: The neural code between neocortical pyramidal neurons depends on neurotransmitter release probability. *PNAS* **94**, 719–723 (1997)

16. De Pittà, M., Volman, V., Berry, H., et al.: A tale of two stories: Astrocyte regulation of synaptic depression and facilitation. *PLoS Comput. Biol.* **7**, e1002293 (2011)
17. Lenk, K.: A simple phenomenological neuronal model with inhibitory and excitatory synapses. In: Conference Proceedings of NOLISP 2011. *LNAI*, vol. 7015 (2011)
18. Lallouette, J., De Pittà, M., Ben-Jacob, E., et al.: Sparse short-distance connections enhance calcium wave propagation in a 3D model of astrocyte networks. *Front. Comput. Neurosci.* **8**, 1–18 (2014)
19. Oberheim, N.A., Takano, T., Hanet, X., et al.: Uniquely hominid features of adult human astrocytes. *J. Neurosci.* **29**(10), 3276–3287 (2009)
20. Kapucu, F., Tanskanen, J., Mikkonen, J.E., et al.: Burst analysis tool for developing neuronal networks exhibiting highly varying action potential dynamics. *Front. Comput. Neurosci.* **6**, 1–14 (2012)



## PUBLICATION

### II

**Larger connection radius increases hub astrocyte number in a 3-d  
neuron-astrocyte network model**

Lenk, K., Genocchi, B., Barros, M. T., and Hyttinen, J. A.

*IEEE Transactions on Molecular, Biological and Multi-Scale Communications*, 7(2), 83–88

**Publication reprinted with the permission of the copyright holders.**



# Larger Connection Radius Increases Hub Astrocyte Number in a 3-D Neuron–Astrocyte Network Model

Kerstin Lenk<sup>1</sup>, Barbara Genocchi<sup>2</sup>, Michael Taynnan Barros<sup>3</sup>, *Member, IEEE*, and Jari A. K. Hyttinen<sup>1</sup>

**Abstract**—Astrocytes - a prominent glial cell type in the brain - form networks that tightly interact with the brain's neuronal circuits. Thus, it is essential to study the modes of such interaction if we aim to understand how neural circuits process information. Thereby, calcium elevations, the primary signal in astrocytes, propagate to the adjacent neighboring cells and directly regulate neuronal communication. It is mostly unknown how the astrocyte network topology influences neuronal activity. Here, we used a computational model to simulate planar and 3D neuron-astrocyte networks with varying topologies. We investigated the number of active nodes, the shortest path, and the mean degree. Furthermore, we applied a graph coloring analysis that highlights the network organization between different network structures. With the increase of the maximum distance between two connected astrocytes, the information flow is more centralized to the most connected cells. Our results suggest that activity-dependent plasticity and the topology of brain areas might alter the amount of astrocyte controlled synapses.

**Index Terms**—Simulation, astrocytes, gap junctions, neurons, network topology.

## I. INTRODUCTION

THE PROPAGATION of information inside the brain is historically considered to be based on the communication between neurons. However, recent experimental studies show that astrocytes actively modulate neuronal activity. They are tightly linked to neurons via the so-called tripartite synapse [1] forming the neuron-astrocyte molecular communication system. The primary signaling mediator evoked by the synaptic communication in astrocytes is calcium [2]–[4]. Calcium propagates inside the complex astrocytic branch trees and from cell to cell through gap junction coupling (GJC) [3], [5]. Thereby, astrocytes form non-overlapping domains coupled only to the nearest neighbors [6]. Mainly

unknown is how the astrocyte network topology influences the neuronal activity.

Different types of computational models are used to investigate the intra- and intercellular pathways of astrocytes and the communication with neurons (reviewed in [7], [8]). Lallouette *et al.* simulated five different 3D topologies of only-astrocyte networks [9], [10], of which some included long-distance connections and hubs. The propagation range of calcium in astrocytes was mostly given by the absence of long-distance GJC and independent of the presence of hubs. The correct functioning of this network could easily be perturbed under the effect of diseases, for example, with the increase of the overall network complexity. Barros *et al.* investigated the impact of calcium propagation in astrocyte network topologies in a model with altered intracellular dynamics to mimic Alzheimer's disease [11]. They concluded that calcium transmission was differently affected in healthy or disease states - intracellularly and in the network propagation patterns. However, this theoretical study did not include experimental data, and the signaling was only implemented from the neurons towards the astrocytes but not vice versa. Neuronal networks have also been studied using computational models, such as [12], where they analyze the activity and noise of neuronal networks under small-world topologies.

Recently, we implemented a combined neuron-astrocyte network model called INEXA [13], [14]. Therewith, we investigated the astrocyte's influence on the neuronal network stability. The simulations resembled *in vitro* experiments with planar multielectrode arrays (MEAs). In the INEXA model, the astrocytes and neurons communicated through the tripartite synapse by exchanging activating and depressing transmitters [13]. In the model, each astrocyte was connected to several hundreds of synapses. In Genocchi *et al.* [14], we varied the number of astrocytic GJCs and the noise levels applied to the presynaptic terminals to simulate low, high, and hyperactivity. The astrocytes increasingly downregulated high and hyperactivity with increased astrocytic GJCs.

Here, we extend our previous studies with the overall objective of investigating the importance of the astrocyte network topology and the role of the most active astrocytes in regulating the network activity. Therefore, we analyze the astrocyte network organization, where nodes are classified from most influencing nodes to the least. Since network nodes with higher degrees exist, an astrocyte connected to more than 75% of its neighbors is defined as a hub astrocyte, which presents the strongest influence in the overall network activity [9], [15]. First, we create planar and 3D neuron-astrocyte networks using

Manuscript received June 23, 2020; revised October 14, 2020; accepted December 16, 2020. Date of publication January 27, 2021; date of current version June 29, 2021. The work of Kerstin Lenk was supported by the Academy of Finland under Grant 314647 and Grant 326452. The work of Barbara Genocchi and Michael Taynnan Barros was supported by the European Union's Horizon 2020 Research and Innovation Programme through the Marie Skłodowska-Curie Grant under Agreement 713645 and Agreement 839553. The associate editor coordinating the review of this article and approving it for publication was G. Jun. (*Corresponding author: Kerstin Lenk.*)

Kerstin Lenk, Barbara Genocchi, and Jari A. K. Hyttinen are with the BioMediTech, Faculty of Medicine and Health Technology, Tampere University, 33520 Tampere, Finland (e-mail: lenk.kerstin@gmail.com).

Michael Taynnan Barros is with the BioMediTech, Faculty of Medicine and Health Technology, Tampere University, 33520 Tampere, Finland, and also with the School of Computer Science and Electronic Engineering, University of Essex, Colchester CO4 3SQ, U.K.

Digital Object Identifier 10.1109/TMBMC.2021.3054890

This work is licensed under a Creative Commons Attribution 4.0 License. For more information, see <https://creativecommons.org/licenses/by/4.0/>

the previously-mentioned INEXA model [13] and compare their characteristics. Second, we vary the distance range within which two astrocytes are coupled to each other in the 3D network. According to Lallouette *et al.* [9], we choose the link radius, which seems to reflect the biological network topology the closest. Subsequently, we quantify the resulting neuronal network activity and topological measures of the astrocytic network. Third, to link network structure to network organization, we use a graph coloring algorithm to analyze the node organization over different distance values. We show that the organization and node structure are interlinked with the astrocyte activity levels regarding distance to neighboring astrocytes and the cell's position in the network.

## II. METHODS

### A. Neuron-Astrocyte Network Model

In the discrete-time model INEXA [13], the neuronal firing rate  $\lambda_i$  of a postsynaptic neuron  $i$  is calculated for each time slice  $t_k$  of 5 ms as follows:

$$\lambda_i(t_k) = \max \left( 0, c_i + \sum_j y_{ij} \cdot s_j(t_{k-1}) - \sum_j y_{Astro} \cdot A_{ija}(t_{k-1}) \right), \quad (1)$$

where  $c_i$  denotes the noise of neuron  $i$ , which is sampled from a triangular distribution between 0 and an upper bound value,  $C_{max}$ . In the original model,  $c$  was implemented to study several noise levels of neurons. The term  $y_{ij}$  is the synaptic strength between the presynaptic neuron  $j$  to postsynaptic neuron  $i$ , which can vary over time. Thereby, the synapse can be either excitatory ( $y_{ij}$  between 0 and 1) or inhibitory ( $y_{ij}$  between  $-1$  and 0). The parameter  $s_j$  is a binary parameter that indicates whether a spike has been emitted by neuron  $j$  in the previous time step  $t_{k-1}$  ( $s_j = 1$  if a spike has been emitted, else  $s_j = 0$ ). The second part in the equation denotes the depressing effect exerted by the astrocytes.  $A_{ija}$  is a binary term that describes whether the synapse  $ij$  is wrapped by astrocyte “a” and if astrocyte “a” was in the active state at the previous time step. Otherwise  $A_{ija}$  is equal to zero, removing the astrocytic effect on the neuronal firing rate. If an active astrocyte wraps the synapse  $ij$ , the astrocyte applies a depressing effect,  $y_{Astro}$ , on the synapse.

The second governing equation is the one for the intracellular calcium dynamics  $[Ca^{2+}]_{ija}$  in an astrocyte “a” that wraps synapse  $ij$ :

$$\begin{aligned} [Ca^{2+}]_{ija}(t_k) &= [Ca^{2+}]_{ija}(t_{k-1}) + \Omega_{acc} \\ &\times \left( [IP3]_{ija}(t_k) - [Ca^{2+}]_{ija}(t_{k-1}) \right). \end{aligned} \quad (2)$$

The calcium concentration is a sum of the calcium concentration remained from the last time slice ( $[Ca^{2+}]_{ija}(t_{k-1})$ ), of the IP<sub>3</sub>-mediated  $Ca^{2+}$ -induced  $Ca^{2+}$ -release from the endoplasmic reticulum (ER) stores, and of the uptake of  $Ca^{2+}$  back

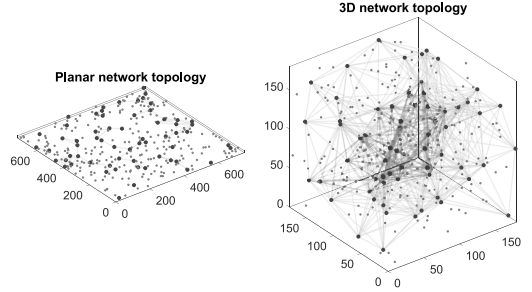


Fig. 1. Topologies for the planar (left) and 3D (right) neuron-astrocyte network. Note, both networks have the same total volume. Astrocytes and their connections are shown in blue and neurons in red. Axes are in  $\mu\text{m}$ .

to the ER by the SERCA pumps. The ER regulation of  $Ca^{2+}$  concentration is modeled in the second part of the equation. To reflect the slow dynamics of the calcium release (up to seconds) we multiplied the ER term by the time scale  $\Omega_{acc}$ .

We extended the INEXA model [13] with the following modifications: To change from a planar to a 3D topology, we kept a similar volume as described in this letter (Figure 1). The network space from planar dimensions ( $750 \times 750 \times 10 \mu\text{m}^3$ , which resembles the culture area of a planar MEA) was altered to  $180 \times 180 \times 180 \mu\text{m}^3$  in 3D. We used 250 neurons with 80% excitatory and 20% inhibitory, and 63 astrocytes for all simulations. The neuron-neuron and astrocyte-neuron connections, as well as the GJC, was modeled as described in Lenk *et al.* [13].

In the first step, the astrocytes were connected based on the spatially-constrained link radius topology model [9], where all astrocytes in the distance  $d$  equal to  $100 \mu\text{m}$  were connected in the planar dimension and 3D. In the second step, we concentrated solely on 3D and ranged  $d$  between 70 to  $120 \mu\text{m}$ . For each distance  $d$ , the simulation was run ten times with the same topology, each with a simulated time of five minutes.

Initially, we fixed the upper boundary for the neuronal noise level  $C_{max}$  to 0.02 and the upper boundary for synaptic weights to 0.7 and  $-0.7$  for excitatory and inhibitory neurons, respectively [13]. Keeping the rules for creating the topologies for the planar and 3D networks resulted in very high connectivity in 3D ( $>80\%$ ). Thus, we reduced the probability that two neurons connect with each other, which resulted in similar connection numbers (Table I). We then obtained the neuronal activity as spikes (i.e., Dirac function of action potentials) per cell over time.

### B. Graph Theory Analysis

We developed a graph of the 3D astrocyte network  $G_{astro} = (V_{astro}, E_{astro})$ , where  $V_{astro}$  was the set of vertices (cell bodies) and  $E_{astro}$  the set of nodes (connection between two cells). We collected  $V_{astro}$  and  $E_{astro}$  based on the topology of the INEXA model. For each simulation, we determined the total number of astrocytes activated at least once during a simulation,  $N_{act}$ . We calculated the mean degree  $k$ , which quantifies the number of connected cell pairs (number of GJCs). Furthermore, the number of hub cells, i.e., nodes

TABLE I  
COMPARISON OF THE CHARACTERISTICS OF THE PLANAR AND THE 3D NETWORKS. SPIKE RATE, BURST RATE, AND BURST DURATION ARE FEATURES OF THE NEURONAL NETWORK ACTIVITY AND DISPLAYED WITH MEAN AND STANDARD DEVIATION OVER THE TEN SIMULATION RUNS. MEAN DEGREE  $k$ , SHORTEST PATH  $L$  AND NUMBER OF ACTIVE CELLS  $N_{act}$  ARE FEATURES OF THE ASTROCYTE NETWORK TOPOLOGY.  $k$  AND  $L$  ARE DISPLAYED WITH MEAN AND STANDARD DEVIATION OVER ALL NODES.  $N_{act}$  HAS THE MEAN AND STANDARD DEVIATION OVER ALL SIMULATION RUNS

Characteristics	Planar network	3D network
Dimensions [ $\mu m^3$ ]	750x750x10	180x180x180
Cell numbers	250 neurons, 63 astrocytes	250 neurons, 63 astrocytes
Noise and synaptic strength	$c = 0.02, y = \pm 0.7$	$c = 0.02, y = \pm 0.7$
Spike rate [spikes/min]	$69.18 \pm 3.17$	$301.47 \pm 37.79$
Burst rate [bursts/min]	$1.08 \pm 0.17$	$26.80 \pm 4.05$
Burst duration [ms]	$36.22 \pm 2.76$	$193.89 \pm 46.93$
Max. amount of NN connections	62250	62250
Average neuron connections to other neurons	66.52	69.31
Network connectivity [%]	26.72	27.83
Average neurons connection length [ $\mu m$ ]	209.67	101.55
Two directional connections between neurons	4924	2719
Average gap junction connections	2.70	19.61
Highest / lowest gap junction amount	7 / 0	35 / 7
Average distance between connected astrocytes [ $\mu m$ ]	66.82	72.05
Average number of astrocyte-neuron connections	169.91	220.85
Excitatory synapses without an astrocyte	2500	0
% of not astrocyte controlled excitatory synapses	18.93	0.00
Mean degree $k$	$2.70 \pm 1.53$	$19.61 \pm 7.30$
Shortest path $L$	[(a) $4.57 \pm 2.37$ , (b) $3.89 \pm 2.20$ , (c) $1.33 \pm 0.49$ ]	$1.82 \pm 0.65$
Number of activated cells $N_{act}$	$8.00 \pm 3.20$	$4.20 \pm 0.91$

which are coupled to more than 75% of the neighbors, was determined. The shortest path  $L$  denoted the minimal number of GJCs one must cross to connect the two astrocytes. Finally, we employed a graph coloring algorithm based on greedy coloring, i.e., on a coloring spectrum with the maximum amount of colors equal to the maximum number of degree. Our greedy coloring scheme is close to a Welsh-Powell algorithm [15], but with fewer colors available since we adjusted that number to match the number of degrees we got from the 3D astrocyte topologies.

### C. Quantification of the Neuronal Activity

For all simulations in the planar dimension and 3D, we analyzed the spontaneous activity inside the neuronal network. From the activity-temporal series of each neuron, we calculated the features of spike rate, burst rate, and burst duration, according to [16]. We averaged each feature over all neuronal cells in each simulation and over the number of simulation runs per distance  $d$ .

## III. RESULTS

### A. Comparison of Planar and 3D Networks

As we kept the cell number the same and the percent of connectivity between the cells similar, it resulted in shorter neuronal connections in 3D than in the planar networks (Table I). However, the average distance between astrocytes increased from planar to 3D. Less bidirectional connections between a pair of neurons were counted. As there were more neighbors in a certain distance in 3D, the number of gap junctions between astrocytes and the average number of neuron-astrocyte connections was increased. In 3D, all excitatory synapses were occupied by an astrocyte branch, unlike in the planar network.

Measuring the neuronal activity showed a five-fold higher spike rate in 3D (Table I). Also, the burst rate and duration significantly increased when changing from a planar to a 3D neuron-astrocyte network. The graph theory analysis revealed that the mean degree  $k$  increased from planar (2.70 on average) to 3D (19.51 on average). In the planar networks, the network was divided into three subnetworks (Table I, (a)-(c) for parameter  $L$ ). The number of active astrocytes,  $N_{act}$ , decreased with higher dimensionality.

### B. Alteration of the Link Radius of Astrocytes in 3D Networks

The graph analysis for the astrocytes networks showed that the mean degree  $k$  increased when increasing the distance  $d$  between astrocytes (Figure 2). The shortest path  $L$  instead decreased since the increase in connections available for each node of the network allows cells to reach other cells with fewer node hops. The number of active astrocytes  $N_{act}$  varied significantly over the ten simulations ran for each distance (Figure 2), especially in the simulations with short distances ( $d = 70 \mu m$  and  $80 \mu m$ ). Also,  $N_{act}$  showed a decreasing tendency when increasing the distance. In Figure 3, the network organization for astrocytes with link distances of 70 and  $120 \mu m$  is displayed. The color and size of the node varied with the number of connections per node ranging from 2 to 16 for  $d = 70 \mu m$  and 10 to 51 for  $d = 120 \mu m$ . In the case of  $d = 120 \mu m$ , we counted four hub astrocytes (indicated by an arrow in Figure 3) and none for the other distances. This indicates that extending the distance  $d$  increases the network connectivity. Hence, the nodes with the highest degrees were found in the center of the topology.

The neuronal activity describing features spike rate, burst rate, and burst duration increased from  $d = 70 \mu m$  to

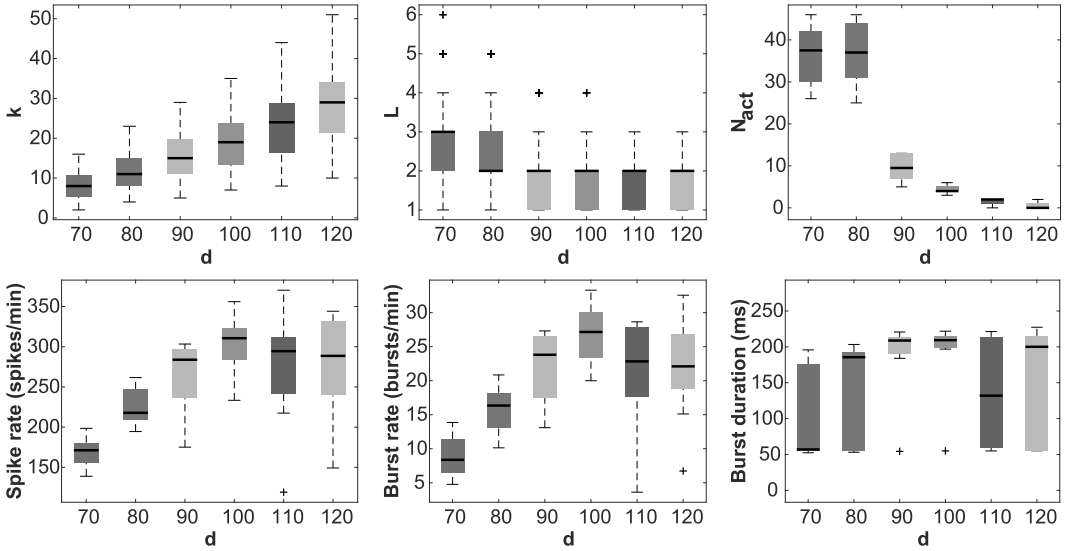


Fig. 2. Astrocytic network features, such as mean degree  $k$ , shortest path  $L$  and number of active astrocytes  $N_{act}$ , for each link radius  $d$  are shown in the upper row. Neuronal features, such as spike rate (spikes/minute), burst rate (bursts/minute), and burst duration (ms) are displayed in the lower row. The bold lines in the box plots represent the median and the crosses represent the outliers. The lower and upper whiskers represent the 25th and 75th percentiles of the data distribution, respectively.

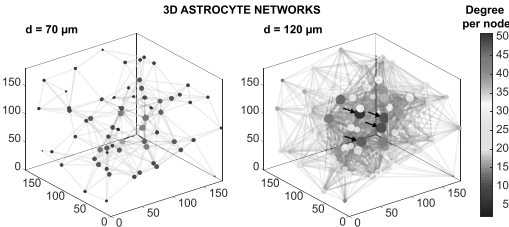


Fig. 3. Colored graphs for the astrocyte networks build with distance  $d = 70 \mu\text{m}$  (left) and  $d = 120 \mu\text{m}$  (right) indicating the degree per node using the greedy coloring scheme. Arrows indicate the hub astrocytes (connected to more than 75% of their neighbors). Axes are in  $\mu\text{m}$ .

$d = 100 \mu\text{m}$ . For  $d = 110 \mu\text{m}$  and  $d = 120 \mu\text{m}$ , they decreased again (Figure 2). Figure 4 displays the spike rate per neuron for each link radius  $d$  of the astrocytic network, respectively. Here, an example of how the spike rates were distributed in the neuronal network. The figure was reconstructed with data obtained from just one of the ten simulation runs per  $d$ . Since the neuronal network topology was fixed for all  $d$ , the spike rate variability across the six subfigures was a reflection of the astrocytic  $N_{act}$ .

#### IV. DISCUSSION AND CONCLUSION

In the last two decades, *in vitro* MEA experiments moved from planar to 3D in terms of the electrode shape [17], [18] and/ or scaffolds (e.g., by using hydrogels or microbeads) [19]–[21]. In 3D networks, Vogel [21] measured similar neuron projections ranging from 80 to 120  $\mu\text{m}$  as we simulated in this study. In addition, when shifting from planar to 3D networks, she observed an increase of spontaneous

neuronal activity [21]. Noteworthy, our comparison between the planar and 3D network topologies shows that the astrocytes fully control the neuronal network in 3D. This increase in synaptic coverage is accompanied by a decreased astrocytic activation leading to a higher neuronal activity, which again highlights the astrocytic effect on controlling the neuronal activity as already shown in Lenk *et al.* [13] and Genocchi *et al.* [14]. This observation is relevant since the number of synapses ensheathed by astrocytes seem to vary between and within brain areas [22]. Our results suggest that activity-dependent plasticity, i.e., potentiation or depression of neurotransmitter release, and the topology of brain areas might alter the amount of astrocyte controlled synapses. The results from our graph analysis in the 3D network show that a shorter distance  $d$  between two astrocytes is followed by a larger number of active astrocytes  $N_{act}$  and shortest paths  $L$ , as well as a lower mean degree  $k$ , which is in accordance with Lallouette *et al.* [9], [10]. To summarize, longer distances between astrocytes seem to centralize the information propagation in astrocytes.

We will evaluate how structure and activity will be interlinked with network organization and information propagation in the next step. This quantification will help to understand the neuron-astrocyte dynamics and how the brain structure is plastic based on the cell molecular communications properties and patterns.

#### SOFTWARE AND DATA AVAILABILITY

The code and the resulting data used in this study can be found at [https://github.com/kerstinlenk/INEXA\\_IIEEETransMolBiolMulti-ScaleCommun2020](https://github.com/kerstinlenk/INEXA_IIEEETransMolBiolMulti-ScaleCommun2020). The MATLAB code for the published INEXA model [13] is available in a

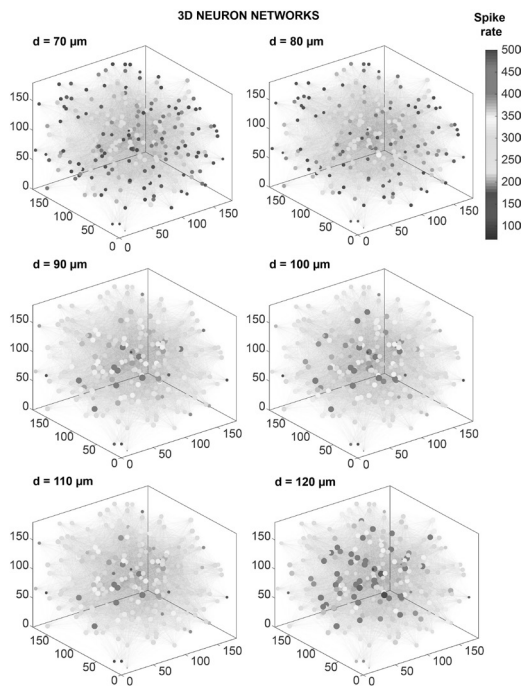


Fig. 4. Colored graphs for the neuronal networks, indicating the spike rate (spikes/min) per node using the greedy coloring scheme. Note that the neuronal network topology and the connections between neurons is the same for all the six subplots. The distances  $d$ , from  $d = 70 \mu\text{m}$  to  $d = 120 \mu\text{m}$ , represent the link radii for the astrocyte network. Axes are in  $\mu\text{m}$ .

publicly accessible repository: [https://github.com/kerstinlenk/INEXA\\_FrontCompNeurosci2020](https://github.com/kerstinlenk/INEXA_FrontCompNeurosci2020). The code for the burst analysis tool is stored at <https://doi.org/10.5281/zenodo.3883622>.

## REFERENCES

- [1] A. Araque, V. Parpura, R. P. Sanzgiri, and P. G. Haydon, "Tripartite synapses: Glia, the unacknowledged partner," *Trends Neurosci.*, vol. 22, no. 5, pp. 208–215, 1999.
- [2] A. Semyanov, C. Henneberger, and A. Agarwal, "Making sense of astrocytic calcium signals—From acquisition to interpretation," *Nat. Rev. Neurosci.*, vol. 21, pp. 551–564, Sep. 2020. [Online]. Available: [www.nature.com/nrn](http://www.nature.com/nrn)
- [3] A. Verkhratsky and M. Nedergaard, "Physiology of astroglia," *Physiol. Rev.*, vol. 98, no. 1, pp. 239–389, 2017.
- [4] D. Rusakov, K. Zheng, and C. Henneberger, "Astrocytes as regulators of synaptic function: A quest for the  $\text{Ca}^{2+}$  master key," *Neuroscientist*, vol. 17, no. 5, pp. 513–523, 2011. [Online]. Available: <http://discovery.ucl.ac.uk/1305349/>
- [5] G. Perea and A. Araque, "Glial calcium signaling and neuron-glia communication," *Cell Calcium*, vol. 38, nos. 3–4, pp. 375–382, 2005.
- [6] M. Barthélemy, "Spatial networks," *Phys. Rep.*, vol. 499, nos. 1–3, pp. 1–101, 2011. [Online]. Available: <http://dx.doi.org/10.1016/j.physrep.2010.11.002>
- [7] F. Oschmann, H. Berry, K. Obermayer, and K. Lenk, "From in silico astrocyte cell models to neuron-astrocyte network models: A review," *Brain Res. Bull.*, vol. 136, pp. 76–84, Jan. 2018. [Online]. Available: <https://linkinghub.elsevier.com/retrieve/pii/S0361923017300540>
- [8] M. De Pittà, *Neuron-Glia Interactions*. New York, NY, USA: Springer, 2020, pp. 1–30. [Online]. Available: [https://doi.org/10.1007/978-1-4614-7320-6\\_100691-1](https://doi.org/10.1007/978-1-4614-7320-6_100691-1)
- [9] J. Lallouette, M. De Pittà, E. Ben-Jacob, and H. Berry, "Sparse short-distance connections enhance calcium wave propagation in a 3D model of astrocyte networks," *Front. Comput. Neurosci.*, vol. 8, pp. 1–18, Apr. 2014. [Online]. Available: <http://www.pubmedcentral.nih.gov/articlerender.fcgi?artid=3997029&tool=pmcentrez&rendertype=abstract>
- [10] J. Lallouette, M. De Pittà, and H. Berry, *Astrocyte Networks and Intercellular Calcium Propagation*. Cham, Switzerland: Springer, 2019, ch. 7, pp. 177–210. [Online]. Available: [https://doi.org/10.1007/978-3-030-00817-8\\_7](https://doi.org/10.1007/978-3-030-00817-8_7)
- [11] M. T. Barros, W. Silva, and C. D. M. Regis, "The multi-scale impact of the Alzheimer's disease on the topology diversity of astrocytes molecular communications nanonetworks," *IEEE Access*, vol. 6, pp. 78904–78917, 2018. [Online]. Available: <https://ieeexplore.ieee.org/document/8573759/>
- [12] J. Tang, J. Zhang, J. Ma, and J. Luo, "Noise and delay sustained chimera state in small world neuronal network," *Sci. China Technol. Sci.*, vol. 62, no. 7, pp. 1134–1140, 2019.
- [13] K. Lenk, E. Satu vuori, J. Lallouette, A. Ladrón-de-Guevara, H. Berry, and J. A. K. Hyttinen, "A computational model of interactions between neuronal and astrocytic networks: The role of astrocytes in the stability of the neuronal firing rate," *Front. Comput. Neurosci.*, vol. 13, p. 92, Jan. 2020.
- [14] B. Genocchi, K. Lenk, and J. Hyttinen, "Influence of astrocytic gap junction coupling on in silico neuronal network activity," in *Proc. Mediterr. Conf. Med. Biol. Eng. Comput.*, 2020, pp. 480–487. [Online]. Available: [http://dx.doi.org/10.1007/978-3-030-31635-8\\_58](http://dx.doi.org/10.1007/978-3-030-31635-8_58)
- [15] D. J. A. Welsh and M. B. Powell, "An upper bound for the chromatic number of a graph and its application to timetabling problems," *Comput. J.*, vol. 10, no. 1, pp. 85–86, Jan. 1967. [Online]. Available: <https://academic.oup.com/comjnl/article/10/1/85/376064>
- [16] I. A. Välikki, K. Lenk, J. E. Mikkonen, F. E. Kapucu, and J. A. K. Hyttinen, "Network-wide adaptive burst detection depicts neuronal activity with improved accuracy," *Front. Comput. Neurosci.*, vol. 11, pp. 1–14, May 2017. [Online]. Available: <http://journal.frontiersin.org/article/10.3389/fncom.2017.00040/full>
- [17] M. O. Heuschkel, M. Fejt, M. Raggenbass, D. Bertrand, and P. Renaud, "A three-dimensional multi-electrode array for multi-site stimulation and recording in acute brain slices," *J. Neurosci. Methods*, vol. 114, no. 2, pp. 135–148, 2002.
- [18] H.-Y. Chu, T.-Y. Kuo, B. Chang, S.-W. Lu, C.-C. Chiao, and W. Fang, "Design and fabrication of novel three-dimensional multi-electrode array using SOI wafer," *Sens. Actuat. A, Phys.*, vols. 130–131, pp. 254–261, Aug. 2006.
- [19] G. Palazzolo, N. Brogiere, O. Cenciarelli, H. Dermutz, and M. Zenobi-Wong, "Ultrasoft alginate hydrogels support long-term three-dimensional functional neuronal networks," *Tissue Eng. A*, vol. 21, nos. 15–16, pp. 2177–2185, 2015.
- [20] N. Antill-O'Brien, J. Bourke, and C. D. O'Connell, "Layer-by-layer: The case for 3D bioprinting neurons to create patient-specific epilepsy models," *Materials*, vol. 12, no. 19, p. 3218, 2019.
- [21] M. Frega, *Neuronal Network Dynamics in 2D and 3D in vitro Neuroengineered Systems*, vol. 53, no. 9, 2016. [Online]. Available: <https://doi.org/10.1007/978-3-319-30237-9>
- [22] I. Farhy-Tselnicker and N. J. Allen, "Astrocytes, neurons, synapses: A tripartite view on cortical circuit development," *Neural Develop.*, vol. 13, no. 1, pp. 1–12, 2018.



**Kerstin Lenk** received the Diploma (Dipl.-Inf.[FH]) degree in computer science from the Lausitz University of Applied Sciences, Germany, in 2009, and the Ph.D. degree in computer science from the Clausthal University of Technology, Germany, in 2016.

She is currently an Academy of Finland Postdoctoral Researcher with Jari Hyttinen's Laboratory, Faculty of Medicine and Health Technology, Tampere University, Finland. Her research interests include modeling the interactions between neurons and astrocytes in health and diseases like epilepsy, Alzheimer's, and schizophrenia. She is a Reviewer for journals including *Scientific Reports*, *Journal of Computational Neuroscience*, *Cognitive Computation*, and *PLOS Computational Biology*. She has organized several international conferences and workshops.



**Barbara Genocchi** received the B.Sc. degree in physics and the M.Sc. degree in nuclear, subnuclear and biomedical physics from the Università degli Studi di Torino, Italy. She is currently pursuing the Ph.D. degree with the Faculty of Medicine and Health Technology, Jari Hyttinen's Group Computational Biophysics and Imaging Group, Tampere University. Her work is currently part of the BioMEP Doctoral Programme, which has received funding from the European Union's Horizon 2020 Research and Innovation Programme under the

Marie Skłodowska-Curie Grant. Her research interests include the role of astrocytes in neural networks, focused on epilepsy, especially using computational methods.



**Michael Taynnan Barros** (Member, IEEE) received the B.Tech. degree in telematics from the Federal Institute of Education, Science and Technology of Paraíba in 2011, the M.Sc. degree in computer science from the Federal University of Campina Grande in 2012, and the Ph.D. degree in telecommunication software from the Waterford Institute of Technology in 2016.

He is currently the recipient of the Marie Skłodowska Curie Individual Fellowship (MSCA-IF) from the BioMediTech Institute, Tampere University, Finland, and an Assistant Professor (Lecturer) with the School of Computer Science and Electronic Engineering, University of Essex, U.K. He has authored or coauthored over 60 research papers in various international flagship journals and conferences in the areas of wireless communications, molecular and nanoscale communications as well as bionanoscience. His research interests include Internet of BioNanoThings, molecular communications, bionanoscience, and 6G communications. He received the CONNECT Prof. Tom Brazil Excellence in Research Award in 2020. He is also a reviewer for many journals and participated as technical program committee and reviewer for various international conferences.



**Jari A. K. Hyttinen** received the M.Sc. and Ph.D. degrees from the Tampere University of Technology in 1986 and 1994, respectively. He is a Full Professor, and the Head of the BioMediTech Unit, Faculty of Medicine and Health Technology (MET), Tampere University. He has been a Visiting Researcher with the University of Pennsylvania, University of Tasmania, Duke University and a Visiting Professor with the University of Wollongong, Australia, in 2017, and ETH Zürich, Switzerland, in 2018. His laboratory,

the Computational Biophysics and Imaging Group, develops novel computer simulations (in-silico) on cellular biophysics, body-on-chip technologies and *in-vitro* 3-D imaging methods for future personalized medicine. He has graduated over 110 M.Sc. and 18 Ph.D.s. He has coauthored more than 380 scientific refereed articles, including over 170 referee journal papers, some patents and he is a Co-Founder of the company Injeq. He has served in many positions of trust, including Chair of the Finnish Society of Medical Physics and Biomedical Engineering from 2001 to 2004, the President of the European Alliance on Medical and Biological Engineering Sciences (EAMBES) from 2015 to 2017. He is also a EAMBES Fellow, and the Chair of the EAMBES Fellows Division from 2017 to 2020.



# PUBLICATION

## III

**Astrocytic control in in vitro and simulated neuron-astrocyte networks**

**Genocchi, B., Ahtiainen, A., Barros, M. T., Tanskanen, J. M., Hyttinen, J., and  
Lenk, K.**

*Proceedings of the Eight Annual ACM International Conference on Nanoscale Computing and  
Communication, 1-7*

**Publication reprinted with the permission of the copyright holders.**



# Astrocytic control in *in vitro* and simulated neuron-astrocyte networks

Barbara Genocchi

barbara.genocchi@tuni.fi

Faculty of Medicine and Health  
Technology, Tampere University  
Tampere, Finland

Annika Ahtiainen

annika.ahtiainen@tuni.fi

Faculty of Medicine and Health  
Technology, Tampere University  
Tampere, Finland

Michael T. Barros

michael.barros@tuni.fi

School of Computer Science and  
Electronic Engineering, University of  
Essex  
Colchester, Essex, UK

Jarno M.A. Tanskanen

jarno.tanskanen@tuni.fi

Faculty of Medicine and Health  
Technology, Tampere University  
Tampere, Finland

Jari Hyttinen

jari.hyttinen@tuni.fi

Faculty of Medicine and Health  
Technology, Tampere University  
Tampere, Finland

Kerstin Lenk

kerstin.lenk@tugraz.at

Institute of Neural Engineering, Graz  
University of Technology  
Graz, Austria

## ABSTRACT

Astrocytes are involved in the information propagation in the brain by interacting with neurons. Computational modeling helps to study the underlying mechanisms for this communication deeply. In this work, we aimed to analyze how the number of astrocytes and the resulting astrocytic network structure affects neuronal activity. Therefore, we conducted *in vitro* experiments with microelectrode arrays and simulations with our previously published computational neuron-astrocyte network model side-by-side. In those, we included neuronal cultures without supplemented astrocytes and three conditions with co-cultures where different amounts of astrocytes were added. We then conducted a cross-correlation analysis between the single-channel spike trains and a graph analysis, which included the mean degree, mean shortest path, and the number of nodes, based on the highly correlated channels. Furthermore, we combined the cross-correlation network analysis of the simulated data and the structure of the astrocyte topology. Our experimental results showed that the spike rate was very variable and higher in cultures without added astrocytes than overall in co-cultures. In the co-cultures, the activity was elevated with an increasing number of astrocytes. Additionally, the spike rate was correlated with the mean degree of the neuronal network. This correlation was smaller with larger numbers of astrocytes in the culture. The simulations showed that the most active neurons were localized in the center of the network, which were, however, not always the most connected ones. The astrocytic activation was mainly driven by the vicinity to highly active neurons rather than from the activation through gap junctions. To conclude, the co-cultures with added astrocytes showed stabilization of neuronal activity. Furthermore, increasing the number of astrocytes led to a higher

neuronal activity, indicating a feedback excitation loop between astrocytes and neurons.

## KEYWORDS

neurons, astrocytes, simulations, *in vitro* microelectrode arrays, graph analysis

### ACM Reference Format:

Barbara Genocchi, Annika Ahtiainen, Michael T. Barros, Jarno M.A. Tanskanen, Jari Hyttinen, and Kerstin Lenk. 2021. Astrocytic control in *in vitro* and simulated neuron-astrocyte networks. In *The Eight Annual ACM International Conference on Nanoscale Computing and Communication (NANOCOM '21)*, September 7–9, 2021, Virtual Event, Italy. ACM, New York, NY, USA, 7 pages. <https://doi.org/10.1145/3477206.3477458>

## 1 INTRODUCTION

In the field of *Molecular Communications*, biophysical interactions between cells are modelled as a communication system [10, 17, 18]. In the brain, astrocytes and neurons form tight networks and exchange information. Neurons and astrocytes communicate in a close feedback loop, which serves as a mechanism for synaptic activity regulation. Astrocytes play an essential role in controlling neuronal activity, and their impairment can lead to neurological diseases. For example, astrocyte dysfunctions have been found in epilepsy, Alzheimer's disease, brain tumors, major depressive disorder, and Down syndrome [5].

Computational models are used to understand biophysical pathways and to support experiments. Various types of astrocyte models with different levels of details – from subcellular to network level – have been developed to study intra- and intercellular mechanisms of astrocytes and their communication to neurons [reviewed in 12]. For example, Amiri et al. [1] introduced a model including 50 pyramidal neurons, 50 interneurons and 50 astrocytes. Inhibitory and excitatory neurons were linked in pairs to their neighbors and one astrocyte. The latter also was connected with one neighboring astrocyte via gap junctions (GJs). With the model, the authors demonstrated that increasing the astrocytic coupling strength to the excitatory and inhibitory neurons resulted in decreased synchronized neuronal oscillations.

In this work, we explored how astrocytes affect neuronal network activity using a multi-modal analysis comprised of both *in vitro* and computational modeling. For that, we recorded neuronal activity from neuronal cultures without added astrocytes as well as neuron-astrocytes co-cultures plated on microelectrode arrays (MEAs). The co-cultures were composed of different neuron-astrocyte ratios to study how the amount of astrocytes affects neuronal activity. Moreover, we aimed to study how the astrocytic network topology influences the activity. For this, we used a mathematical neuron-astrocyte network model developed by Lenk et al. [10, 11] and Genocchi et al. [7]. To understand the role of neuron-astrocyte connection in both experimental and simulation data, we performed a graph analysis based on the correlations between the spike trains from selected neurons as well as on the simulated astrocytic topology. *Molecular Communications* seek efforts that unite the analysis of intercellular communication mechanisms. Our model that analyzes different brain cell types within the same graph analysis on network structure and activity contributes to that work.

## 2 BACKGROUND AND RELATED WORK

**Biological relevance.** The intercommunication between neuronal networks and astrocytes regulates cognitive functions [14]. A pre- and a postsynaptic neuron can be enwrapped by an astrocyte and build together the so-called tripartite synapse (Fig. 1) [2]. Triggered by incoming action potentials, the presynaptic neuron releases neurotransmitters like glutamate to the synaptic cleft. Glutamate binds to the metabotropic glutamate receptors (mGluR) at the astrocyte's cell membrane. Consequently, inositol 1,4,5-trisphosphate (IP<sub>3</sub>) is released from the endoplasmic reticulum followed by calcium (Ca<sup>2+</sup>) elevations in the cytosol. The increasing Ca<sup>2+</sup> levels trigger the opening of further IP<sub>3</sub> channels leading to a Ca<sup>2+</sup>-induced Ca<sup>2+</sup> release (CICR). Linked with the Ca<sup>2+</sup> elevations is a release of gliotransmitters like glutamate, D-serine, or adenosine triphosphate (ATP) [3, 13]. Astrocytes diffuse gliotransmitters and IP<sub>3</sub> with a short-distance communication through GJs [14]. Thus, astrocytic network connectivity is crucial for activity control and network synchronization.

**Computational network model.** Recently, we have published a neuron-astrocyte network model called INEXA [7, 10, 11], which represents a computational equivalent of *in vitro* neuron-astrocyte co-cultures on MEAs. The neurons can be either excitatory or inhibitory. The astrocytes are connected to the excitatory synapses and to neighboring astrocytes by GJs. In this framework, astrocytes control the neuronal activity of the connected synapse through local calcium dynamics and the uptake and release of excitatory and inhibitory gliotransmitters. Local astrocytic calcium dynamics are summed into global calcium dynamics, simulating the calcium wave propagation through GJs. The novelty of the INEXA model was the simulation of the communication between astrocytes and neurons in a biophysically plausible network topology. In Lenk et al. [11], we investigated the influence of different ratios of astrocytes on neuronal network activity. The results showed that astrocytes stabilize neuronal activity with a delicate balance between excitation and inhibition. In Genocchi et al. [7], we further explored the role of GJ coupling on this balancing effect. Our simulation results indicated that a highly coupled astrocytic network was more

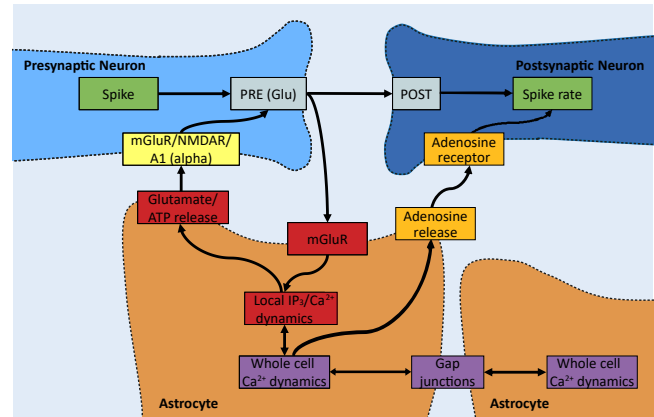


**Figure 1: Schematic of a pre- and a postsynaptic neuron and an adjacent astrocyte. Figure adapted from Lenk et al. [11].**

effective in decreasing the spike rate of the neurons compared to the networks with fewer GJs on average. In Lenk et al. [10], we extended the network from a planar topology to a 3D network model and simulated different astrocytic network topologies modifying the maximum distance between astrocytes. The results from the analysis of the 3D network revealed that larger connection distances between astrocytes centralized the information flow in the astrocytic network.

**Molecular communications in neuron-astrocyte networks.** An effort to describe the communication pathways between neurons and astrocytes from the viewpoint of *Molecular Communications* has also been made. In Valenza et al. [18], the authors implemented a network communication model between artificial spiking neurons and astrocytes. The tripartite synapse was described as a nonlinear transistor-like model. Their model showed that the presence of astrocytes in the network created subgroups of neurons with polychronic activity. This particular pattern of activity is considered to be the basis of the network memory. In Taynnan Barros et al. [17], communication in different types of cells has been studied. The authors considered excitable cells (smooth muscle cells), non-excitable cells (epithelial cells), and hybrid cells (astrocytes). The communication in this model happens through Ca<sup>2+</sup> signaling through GJs. Their results highlight that the complex intracellular behavior as well as the size and structure of connections between the cells (i.e., GJ coupling) can impact the communication performance in the different models.

## 3 METHODS

**Cell culturing.** Co-cultures were established by combining rat primary cortical astrocytes (N7745100; Thermo Fisher Scientific) and primary rat cortex neurons (A1084001; Thermo Fisher Scientific) at specified ratios. Astrocytes, before MEA plating, were cultured until confluency and subsequently treated with Cytosine b-D-arabinofuranoside (ara-c; C1768; 2.5 μM; Sigma-Aldrich) for five days to terminate further astrocyte proliferation. On the day of MEA plating, neurons and astrocytes were centrifuged and counted as stated in the Thermo Fisher Scientific protocols. The number of neurons was always kept constant (80,000 neurons per MEA). The

number of astrocytes per MEA was adjusted to achieve different neuron-astrocyte co-culture ratios. The co-culture ratios used were 90:10, 80:20, and 70:30 percent, where the first number represents the percentage of plated neurons and the second number percentage of plated astrocytes. In addition to co-cultures, cultures with only neurons (NS) were prepared without any separately added astrocytes. Half the volume of the medium was refreshed every 2-3 days and always completely refreshed after MEA recordings (see next paragraph). Neuron-astrocyte co-cultures were cultured in neurobasal plus medium supplemented with 2% B-12 Plus supplement, 1% P/S, 1% GlutaMAX, and 1% sodium pyruvate. NS cultures were cultured in the cell culture media as suggested in the Thermo Fisher Scientific protocols.

*MEA preparation and recording.* The day before cell plating, all sterilized MEAs ( $n=28$ ) were coated with Poly-D-Lysine (0.1 mg/ml; Thermo Fisher Scientific) for 1 hour. The MEAs were washed three times with ultrapure water, dried, and incubated with laminin (L2020; 20  $\mu\text{g/ml}$ ; Sigma-Aldrich) overnight at +4 °C. The following day, laminin was aspirated just before the plating. MEAs used in this study were either standard or thin 60-electrode MEAs (60MEA200/30iR; Multi Channel Systems MCS GmbH, Reutlingen, Germany). Raw signals were recorded at 28 days *in vitro* (DIV) at a sampling rate of 25 kHz for 5 minutes using a MEA2100-System and the Multi Channel Experimenter software. The raw signals were filtered and sorted with a tool called Wave Clus for MATLAB (R2009b or higher) [4]. We used a second-order bandpass elliptic filter in the range of 300 - 3000 Hz. Positive and negative spikes were detected when they exceeded the threshold of  $\pm 5\sigma$ , where  $\sigma$  is the standard deviation of the filtered signal.

*Neuronal and neuron-astrocyte network simulations.* Planar neuronal and neuron-astrocyte networks were simulated using the INEXA model [11]. The use of a planar network topology better resembles the *in vitro* cell distribution on a MEA. To reproduce the experimental setup, we simulated topologies with 250 neurons (200 excitatory and 50 inhibitory) without any astrocytes and with different numbers of astrocytes to reflect the plated ratios (i.e., ratio 90:10, 28 astrocytes; 80:20, 62 astrocytes; 70:30, 107 astrocytes). For each simulated culture, we ran 10 simulations. The simulated time was 5 minutes.

*Neuronal and astrocytic activity analysis.* The sorted signals and the simulated spike trains were further analyzed with a MATLAB tool [19] that uses a network-wide cumulative moving average (CMA) algorithm [9]. We analyzed the spike rate (SR; spikes per minute) and burst rate (BR; bursts per minute) of the recorded and simulated signals. Single-channel SR and BR of the experimental data were then averaged for each MEA. To simulate the capturing of the neuronal activity on an MEA, we randomly selected 64 neurons in the surroundings of the virtual electrode positions. SR and BR of the selected neurons were then determined for the simulated MEA channels. Additionally, we calculated how many times each astrocyte entered the active state during the 5 minutes simulated time. The astrocytes are considered active when the astrocytic intracellular  $\text{Ca}^{2+}$  overcome a certain threshold and elicit the release of gliotransmitters.

*Statistical analysis.* Statistical analysis was conducted either in MATLAB or GraphPad Prism (v.9). Firstly, to compare the different experimental and simulated co-cultures, we used a Mann-Whitney  $u$  test, and the test was considered significant for  $p < 0.05$ , where  $p$  is the probability to obtain results in the tail of the results distribution. A small  $p$ -value rejects the null-hypothesis. Secondly, to analyze the correlation between SR or BR and the features from the graph analysis in the experimental data (see paragraph Graph analysis), we used Pearson's correlation coefficient  $R$ . To further test the linear dependence between SR and the degree, we conducted a linear regression analysis (`fitlm`-function in MATLAB). The regression parameter  $r^2$  represents the fraction of data in accordance with the applied regression model. The statistical significance of the regression analysis was tested with a Student's  $t$ -test, and the test was considered significant for  $p < 0.05$ .

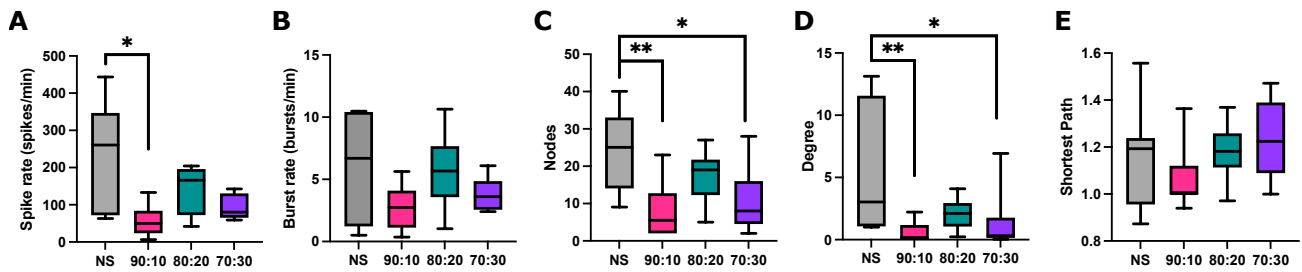
Thirdly, to analyze the underlying network structure of the cultures on the MEAs, we conducted a pairwise cross-correlation analysis in MATLAB between binary encoded spike trains of each MEA channel. We created a correlation matrix based on the pairwise correlation values and normalized the matrix by the maximum of all correlation values. We then thresholded the correlation at a value of  $> 0.65$  to consider only the channel pairs with a high positive correlation. We applied the same approach to the selected simulated neuronal spike trains (see paragraph Neuronal and astrocytic activity analysis).

*Graph analysis.* To analyze the structure of the experimental and simulated networks, we conducted an undirected graph analysis on the binary encoded spike trains in MATLAB to measure the network structure of the culture. For this, we evaluated the mean degree of the network, the number of nodes in the network, and the mean shortest path. The edges in this analysis are defined as the connections between the channels (in the experiments) or neurons (in the simulations) with cross-correlation value  $> 0.65$ . Nodes were defined as those channels or neurons with at least one edge to another channel or neuron. For the simulated network, we also analyzed the astrocytic structural network by calculating the mean degree and the mean shortest path based on the astrocytic network topology. In this context, the edges were the simulated GJs between astrocytes. Furthermore, we combined the graph analysis from the astrocytic and neuronal networks for the simulated data with the activity analysis (i.e., spike rate).

## 4 RESULTS

*Lower spike rate (SR) and burst rate (BR) in co-cultures.* The experimental data showed a higher SR in the NS cultures compared to the co-cultures. Even though only the pairwise comparison between NS and 90:10 was statistically significant ( $p = 0.028$ ), the lower mean SR for the MEAs with astrocytes was noticeable (Fig. 2A). Simulated data of NS also showed a higher SR compared to the simulations with astrocytes comprised in the network (Fig. 2F). In this case, the pairwise differences in SR were significant for NS vs. 90:10 ( $p = 0.003$ ) and NS vs. 80:20 ( $p = 0.0015$ ). Pairwise  $t$ -tests between the experimental and simulated data resulted in no statistical difference (NS,  $p = 0.67$ ; 90:10,  $p = 0.17$ ; 80:20,  $p = 0.08$ ; 70:30,  $p = 0.83$ ).

## Experimental data



## Simulated data

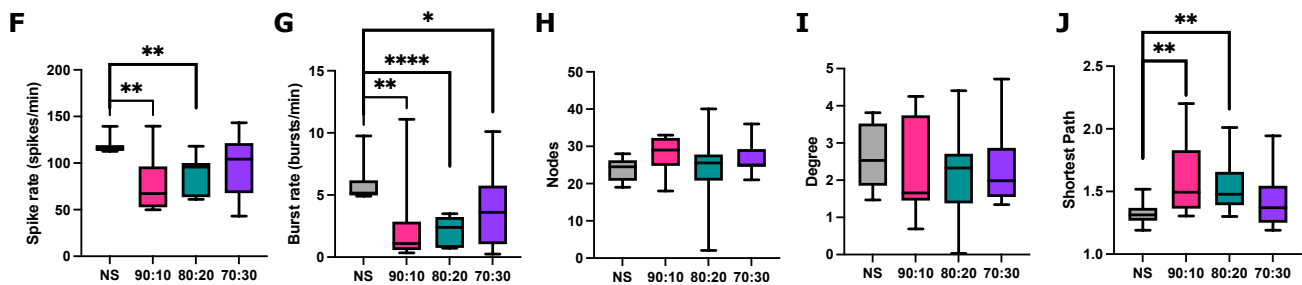


**Figure 2: Analysis of the neuronal data. Spike rate (A,F) and burst rate (B,G) as well as the number of nodes (C,H), the mean degree (D,I) and the mean shortest path (E,J) of the experimental data (top panel) and simulated data (bottom panel) for the four culture ratios. Statistical significance: \*  $p < 0.05$ ; \*\*  $p < 0.01$ ; \*\*\*\*  $p < 0.0001$ .**

The mean BR was decreased for all co-cultures compared to NS (Fig. 2B and G). However, those differences were not statistically significant for the experimental data, while they were significant for the simulated data (NS vs. 90:10,  $p = 0.0027$ ; NS vs. 80:20,  $p < 0.0001$ ; NS vs. 70:30,  $p = 0.027$ ). In general, the NS population exhibited very high variability in the experimental data (Fig. 2A and B). In the simulated data, the addition of astrocytes in the network increased the variability of the SR and BR (Fig. 2F and G). The results from the experimental data and the simulations were in similar ranges – the pairwise t-tests gave statistical difference only for the culture ratio 80:20 (NS,  $p = 0.96$ ; 90:10,  $p = 0.31$ ; 80:20,  $p = 0.003$ ; 70:30,  $p = 0.70$ ).

*Graph analysis of the neuronal activity.* The graph analysis on the experimental data showed that the NS networks created from the binary encoded spike trains have a higher number of nodes compared to the co-cultures (NS vs. 90:10,  $p = 0.005$ ; NS vs. 80:20,  $p = 0.19$ ; NS vs. 70:30,  $p = 0.03$ ) (Fig. 2C). The number of nodes in the simulated data did not exhibit differences between the culture ratios (Fig. 2H). The simulations reproduced the experimental results for NS but not for the co-cultures. In fact, pairwise comparison between the number of nodes was statistically different for 90:10 and 70:30 (NS,  $p = 0.94$ ; 90:10,  $p < 0.0001$ ; 80:20,  $p = 0.08$ ; 70:30,  $p = 0.002$ ).

The mean degree was lower in the co-cultures compared to NS in the experimental data (NS vs. 90:10,  $p = 0.006$ ; NS vs. 80:20,  $p = 0.28$ ; NS vs. 70:30,  $p = 0.03$ ) (Fig. 2D). The experimental data

indicated more variability in the mean degree of the NS than in the co-cultures. The simulated data did not show significant differences between the cultures (Fig. 2I). The degree values were in the same ranges for the experimental and simulated data for NS and 80:20 but were, however, statistically different for 90:10 and 70:30 (NS,  $p = 0.65$ ; 90:10,  $p = 0.0003$ ; 80:20,  $p = 0.99$ ; 70:30,  $p = 0.03$ ).

The mean shortest path for the experimental data was in the same range for NS and the co-cultures, with a tendency to increase with an increasing number of astrocytes in the culture (Fig. 2E). In the simulated data, a decrease in the mean shortest path for the simulated co-cultures was observable (Fig. 2J). Overall, the mean shortest path of the simulated data was slightly higher than the experimental results, and it was statistically different in all the culture ratios except 70:30 (NS,  $p = 0.03$ ; 90:10,  $p = 0.0002$ ; 80:20,  $p = 0.0002$ ; 70:30,  $p = 0.08$ ).

*SR and BR correlation with the graph analysis features of the experimental data.* The Pearson's correlation  $R$  between the SR and the mean degree was  $R = 0.57$  for the NS,  $R = 0.03$  for the 90:10,  $R = 0.35$  for the 80:20, and  $R = 0.27$  for the 70:30 cultures (Fig. 3). The circle diameter represents the degree importance calculated based on the cross-correlation values of the incoming connections. In addition, the linear regression analysis showed that a good agreement between the linear regression and the data was found only for NS, while for the co-cultures the  $r^2$  returned very low values (NS:

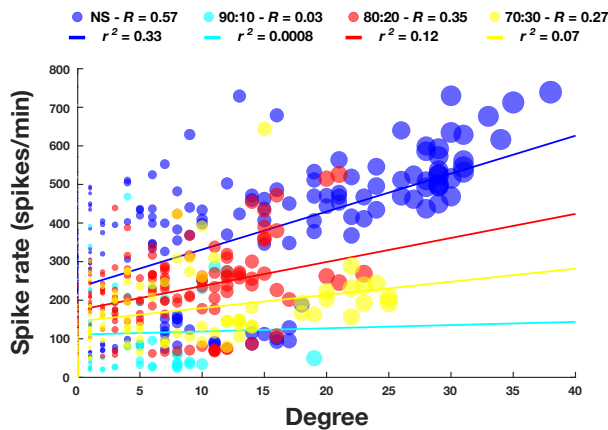


**Figure 3: Pearson’s correlation analysis  $R$  between the spike rate and the degree for the four different cultures. Each circle represents one channel of an MEA. The circle diameter represents the node centrality based on cross-correlation values of the incoming edges of the node. The solid lines represent the linear regression models for the experimental data for the different cultures with the relative  $r^2$  parameter.**

$r^2 = 0.38$ ,  $p < 0.0001$ ; 90:10:  $r^2 = 0.0008$ ,  $p = 0.829$ ; 80:20:  $r^2 = 0.12$ ,  $p < 0.0001$ ; 70:30:  $r^2 = 0.07$ ,  $p = 0.012$ ).

*Graph analysis of the astrocyte topology.* For the simulations, we conducted a graph analysis based on the topology of the astrocytes to combine these results with the graph analysis based on the cross-correlation analysis of the simulated neuronal networks. The mean degree and mean shortest path of the astrocytes increased with the number of astrocytes in the network (Fig. 4A and B). All the pairwise differences between the simulated co-cultures were statistically significant ( $p < 0.0001$ ). The astrocytic activation, expressed as how many times an astrocyte entered the active state during the time of the simulation, instead did not show any differences between the three different simulated co-cultures (Fig. 4C).

*Network response to astrocyte influence.* For the simulated data, we plotted the structural network based on the graph analysis for the neuronal data with the relative SR of each of the 64 selected neurons indicated by the color bar ranging from blue to green (Fig. 5). The neurons with higher SR are not always those with a higher amount of connections but more centered in the network. The radius of the dot represents the degree of the neurons. The connections here are not the synapses between the neurons but the connections based on the cross-correlation analysis.

To analyze the effect of the astrocytes, we combined the topology network of the astrocytes with the connections determined by the cross-correlation of the binary encoded neuronal activity (Fig. 5). The diamonds represent the astrocytes with their connections, i.e., GJs, and the color of the diamond indicates how many times the astrocyte has been in the active state during the simulation. The dimension of the diamonds reflects the degree of the astrocyte.

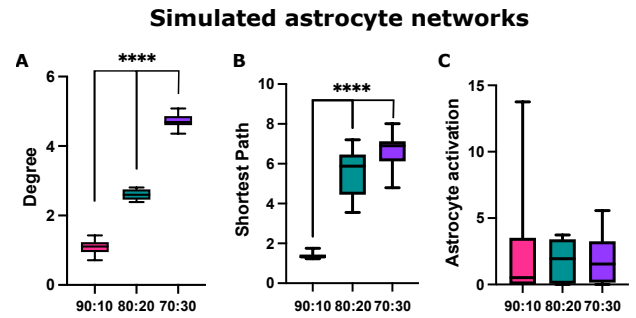


**Figure 4: Astrocyte network graph analysis. (A) the mean degree (i.e., gap junctions), (B) the mean shortest path, and (C) the mean number of times an astrocyte entered the active state. The results show the average of the features for the astrocytes in the simulated network. The simulations were repeated ten times for each co-culture. \*\*\*\*  $p < 0.0001$ .**

## 5 DISCUSSION AND CONCLUSION

Astrocytes have proved to communicate with the neurons and to control the neuronal activity [1–3]. Computational models of astrocytes and neurons can help to highlight the pathway through which this communication happens [12]. Previously, we developed a computational neuron-astrocyte network model called INEXA [11].

In the present work, we aim to analyze how the number of astrocytes and the resulting astrocytic network topology affect neuronal network activity. In the brain, individual areas contain different ratios of neurons and astrocytes [8] and varying numbers of synapses ensheathed by astrocytes [6]. To validate the aim, we ran *in vitro* experiments with MEAs and simulations with the INEXA model side-by-side. We included neuronal cultures without supplemented astrocytes and co-cultures added with different amounts of astrocytes in both setups. Our results from the experimental data show that NS cultures exhibited a high variability which might be due to different maturation stages within those cultures [15, 16]. Compared to the NS cultures, the neuron-astrocyte co-cultures exhibit a lower SR and BR. With our simulations, we can replicate similar SR and BR. Also, the nodes and degree analysis based on the neuronal cross-correlation analysis shows a lower amount of nodes and a lower mean degree for the co-cultures than NS cultures. During the spike sorting of the MEA recordings, we realized that the cultures containing more astrocytes have smaller amplitudes of the action potentials. This might have led to underestimating the spike number (which is beyond the scope of this paper). It is an interesting feature to be investigated in the future.

The Pearson’s correlation and linear regression analysis of the experimental data reveals that the SR is correlated with the mean degree for NS and that the correlation coefficient  $R$  decreased for the co-cultures. These results indicate that the number of astrocytes in the network affects neuronal activity. Since it is very challenging to experimentally study the effect of the astrocytic topology and activation on neuronal network activity, we used our computational model to overcome this limitation. Our results from the graph analysis of the astrocytic network topology show that the mean degree, which represents the number of GJs, and the mean shortest



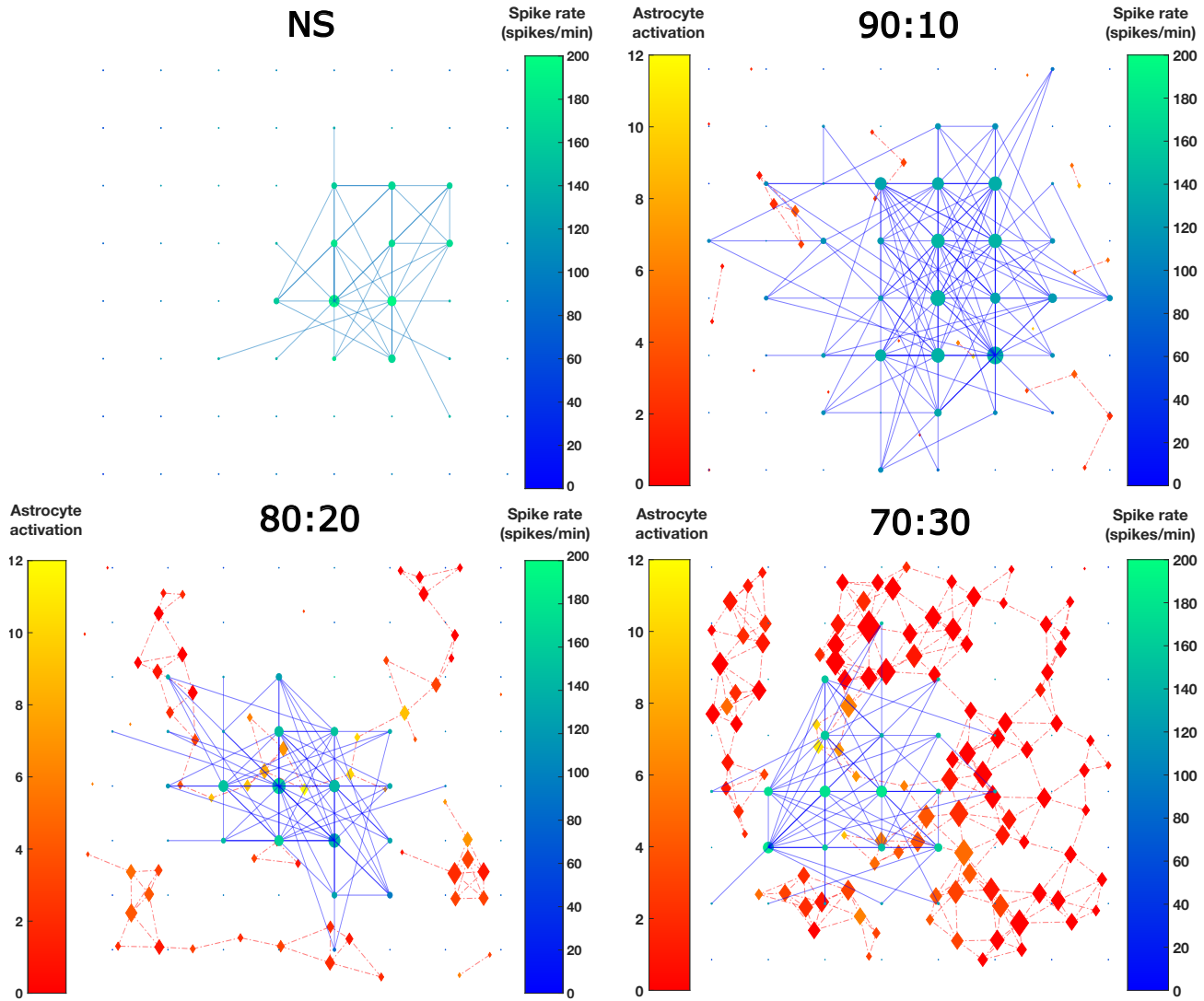


**Figure 5: Combination of astrocytic network effect and the neuronal activity network for the simulated data. The 64 selected neurons are shown as dots. The neuronal connections based on the cross-correlation are shown in solid blue lines (edge weight > 0.65). The diameter of the dot reflects the degree of the neuron. The color bar for the SR values (spikes/min) ranges from blue (low) to green (high). The astrocytes are shown in diamond shape and their gap junctions as dot-dashed red lines. The astrocyte activation defines how many times that particular astrocyte got activated; the color bar ranges from red (low) to yellow (high). The dimension of the diamonds reflects the degree of the astrocyte.**

path increased when increasing the number of astrocytes in the network. Instead, the astrocytic activation does not differ between the simulated co-cultures showing that the activation through GJs had a low effect. The astrocytes redistribute the resources (i.e., glutamate and IP<sub>3</sub>) through the GJs, and they get activated based on these resources. Thus, the more GJs an astrocyte has, the less the distribution has activating effect on the connected astrocytes. This behavior might be indicated by the higher variability in the activation for 90:10. Instead, the variability in the astrocyte activation of the 70:30 culture can be explained by a higher input from the neurons.

To study how the astrocytes locally affect neuronal activity, we combine the cross-correlation-based graph analysis with the astrocyte topology and activation. Highly spiking neurons in our simulated networks are localized in the network center and only slightly depend on the degree. These results from the simulations are following the results from the correlation analysis of the experimental data. The activation of the astrocytes was mainly co-localized with the highly spiking neurons but not dependent on the astrocyte mean degree. However, the increase of neuronal SR with higher numbers of astrocytes seems to depend on the astrocyte mean degree. These results are in accordance with [10] and [7]. In previous



publications, we found that hub astrocytes with a high number of GJs lead to higher SR [7] and centralize the neuronal activity [10]. Also, our results show a feedback communication with neurons and a preferential inhibition in less connected networks.

## SOFTWARE AND DATA AVAILABILITY

The code and the resulting data used in this study can be found at <https://github.com/barbara-ge/ACM-NanoCom2021>. The MATLAB code for the published INEXA model [11] is available in a publicly accessible repository: [https://github.com/kerstinlenk/INEXA\\_FrontCompNeurosci2020](https://github.com/kerstinlenk/INEXA_FrontCompNeurosci2020). The code for the burst analysis tool is stored at <https://doi.org/10.5281/zenodo.3883622>.

## ACKNOWLEDGEMENT

The authors acknowledge the TUNI TCSC Narvi computing cluster for the computational resources. The work of B.G. and M.T.B. is funded by the European Union's Horizon 2020 Research and Innovation Programme under the Marie Skłodowska-Curie grant agreement No. 713645 and No. 839553. The works of A.A. and J.M.A.T. have been supported by funding from the European Union's Horizon 2020 Research and Innovation Programme under grant agreement No. 824164, project "Hybrid Enhanced Regenerative Medicine Systems". K.L. received funding from the Academy of Finland (decision nos. 314647, 326452).

## REFERENCES

- [1] Mahmood Amiri, Narges Hosseinmardi, Fariba Bahrami, and Mahyar Janahmadi. 2013. Astrocyte-neuron interaction as a mechanism responsible for generation of neural synchrony: a study based on modeling and experiments. *Journal of Computational Neuroscience* 34, 3 (2013), 489–504. <https://doi.org/10.1007/s10827-012-0432-6>
- [2] Alfonso Araque, Vladimir Parpura, RP Sanzgiri, and PG Haydon. 1999. Tripartite synapses: glia, the unacknowledged partner. *Trends in Neurosciences* 22, 5 (1999), 208–215. [https://doi.org/10.1016/s0166-2236\(98\)01349-6](https://doi.org/10.1016/s0166-2236(98)01349-6)
- [3] Paola Bezzi, Giorgio Carmignoto, Lucia Pasti, Sabino Vesce, Daniela Rossi, Barbara Lodi Rizzini, Tullio Pozzant, and Andrea Volterra. 1998. Prostaglandins stimulate calcium-dependent glutamate release in astrocytes. *Nature* 391, 6664 (1998), 281–285. <https://doi.org/10.1038/34651>
- [4] Fernando J. Chauré, Hernan G. Rey, and Rodrigo Quiñero. 2018. A novel and fully automatic spike-sorting implementation with variable number of features. *Journal of Neurophysiology* 120, 4 (2018), 1859–1871. <https://doi.org/10.1152/jn.00339.2018> PMID: 29995603.
- [5] Elena Dossi, Flora Vasile, and Nathalie Rouach. 2018. Human astrocytes in the diseased brain. *Brain Research Bulletin* 136 (2018), 139–156. <https://doi.org/10.1016/j.brainresbull.2017.02.001> Molecular mechanisms of astrocyte-neuron signalling.
- [6] Isabella Farhy-Tselnicker and Nicola J. Allen. 2018. Astrocytes, neurons, synapses: A tripartite view on cortical circuit development. *Neural Development* 13, 1 (2018), 1–12. <https://doi.org/10.1186/s13064-018-0104-y>
- [7] Barbara Genocchi, Kerstin Lenk, and Jari Hyttinen. 2020. Influence of Astrocytic Gap Junction Coupling on *in Silico* Neuronal Network Activity. In *MEDICON 2019, IFMBE Proceedings*. Springer Nature Switzerland AG 2020, 480–487. <https://doi.org/10.1007/978-3-030-31635-8>
- [8] Suzana Herculano-Houzel. 2014. The glia/neuron ratio: How it varies uniformly across brain structures and species and what that means for brain physiology and evolution. *Glia* 62, 9 (2014), 1377–1391. <https://doi.org/10.1002/glia.22683>
- [9] Fikret Emre Kapucu, Jarno Tanskanen, Jarno Mikkonen, Laura Ylä-Outinen, Susanna Narkilahti, and Jari Hyttinen. 2012. Burst analysis tool for developing neuronal networks exhibiting highly varying action potential dynamics. *Frontiers in Computational Neuroscience* 6 (2012), 38. <https://doi.org/10.3389/fncom.2012.00038>
- [10] Kerstin Lenk, Barbara Genocchi, Michael T Barros, and Jari A.K. Hyttinen. 2021. Larger Connection Radius Increases Hub Astrocyte Number in a 3D Neuron-Astrocyte Network Model. *IEEE Transactions on Molecular, Biological and Multi-Scale Communications* (2021), 1–5. <https://doi.org/10.1109/TMBMC.2021.3054890>
- [11] Kerstin Lenk, Eero Satu vuori, Jules Lallouette, Antonio Ladrón-de Guevara, Hugues Berry, and Jari A. K. Hyttinen. 2020. A Computational Model of Interactions Between Neuronal and Astrocytic Networks: The Role of Astrocytes in the Stability of the Neuronal Firing Rate. *Frontiers in Computational Neuroscience* 13, January (2020), 92. <https://doi.org/10.3389/fncom.2019.00092>
- [12] Franziska Oschmann, Hugues Berry, Klaus Obermayer, and Kerstin Lenk. 2017. From *in silico* astrocyte cell models to neuron-astrocyte network models: A review. *Brain Research Bulletin* 136 (2017), 1–9. <https://doi.org/10.1016/j.brainresbull.2017.01.027>
- [13] Gertrudis Perea and Alfonso Araque. 2007. Astrocytes potentiate transmitter release at single hippocampal synapses. *Science (New York, N.Y.)* 317, 5841 (2007), 1083–6. <https://doi.org/10.1126/science.1144640>
- [14] Mirko Santello, Nicolas Toni, and Andrea Volterra. 2019. Astrocyte function from information processing to cognition and cognitive impairment. *Nature Neuroscience* 22, 2 (2019), 154–166. <https://doi.org/10.1038/s41593-018-0325-8>
- [15] George M. Smith, Urs Rutishauser, Jerry Silver, and Robert H. Miller. 1990. Maturation of astrocytes *in vitro* alters the extent and molecular basis of neurite outgrowth. *Developmental Biology* 138, 2 (1990), 377–390. [https://doi.org/10.1016/0012-1606\(90\)90204-V](https://doi.org/10.1016/0012-1606(90)90204-V)
- [16] Arens Taga, Raha Dastgheyb, Christa Habela, Jessica Joseph, Jean-Philippe Richard, Sarah K. Gross, Giuseppe Lauria, Gabsang Lee, Norman Haughey, and Nicholas J. Maragakis. 2019. Role of Human-Induced Pluripotent Stem Cell-Derived Spinal Cord Astrocytes in the Functional Maturation of Motor Neurons in a Multielectrode Array System. *STEM CELLS Translational Medicine* 8, 12 (dec 2019), 1272–1285. <https://doi.org/10.1002/sctm.19-0147>
- [17] Michael Taynnan Barros, Sasitharan Balasubramaniam, and Brendan Jennings. 2015. Comparative End-to-End Analysis of Ca<sup>2+</sup>-Signaling-Based Molecular Communication in Biological Tissues. *IEEE Transactions on Communications* 63, 12 (2015), 5128–5142. <https://doi.org/10.1109/TCOMM.2015.2487349>
- [18] Gaetano Valenza, Luciano Tedesco, Antonio Lanata, Danilo De Rossi, and Enzo P asquale Scilingo. 2013. Novel Spiking Neuron-Astrocyte Networks based on nonlinear transistor-like models of tripartite synapses. *Conference Proceedings of the Annual International Conference of the IEEE EMBS* (2013), 6559–6562. <https://doi.org/10.1109/EMBC.2013.6611058>
- [19] Inkeri A. Välikki, Kerstin Lenk, Jarno E. Mikkonen, Fikret E. Kapucu, and Jari A. K. Hyttinen. 2017. Network-Wide Adaptive Burst Detection Depicts Neuronal Activity with Improved Accuracy. *Frontiers in Computational Neuroscience* 11 (2017), 40. <https://doi.org/10.3389/fncom.2017.00040>

# PUBLICATION

## IV

**Astrocytes exhibit a protective role in neuronal firing patterns under  
chemically induced seizures in neuron-astrocyte co-cultures**

Ahtiainen \*, A., Genocchi \*, B., Tanskanen, J. M., Barros, M. T.,  
Hyttinen, J. A., and Lenk, K.

*International Journal of Molecular Sciences*, 22(23), 12770. \* these authors contributed  
equally to the manuscript.

**Publication reprinted with the permission of the copyright holders.**





Article

# Astrocytes Exhibit a Protective Role in Neuronal Firing Patterns under Chemically Induced Seizures in Neuron–Astrocyte Co-Cultures

Annika Ahtiainen <sup>1,\*</sup>, Barbara Genocchi <sup>1,\*</sup>, Jarno M. A. Tanskanen <sup>1</sup>, Michael T. Barros <sup>1,2</sup>, Jari A. K. Hyttinen <sup>1</sup> and Kerstin Lenk <sup>1,3,4</sup>

<sup>1</sup> Faculty of Medicine and Health Technology, Tampere University, 33520 Tampere, Finland; jarno.tanskanen@tuni.fi (J.M.A.T.); michael.barros@tuni.fi (M.T.B.); jari.hyttinen@tuni.fi (J.A.K.H.); kerstin.lenk@tugraz.at (K.L.)

<sup>2</sup> School of Computer Science and Electronic Engineering, University of Essex, Colchester CO4 3SQ, UK

<sup>3</sup> Institute of Neural Engineering, Graz University of Technology, 8010 Graz, Austria

<sup>4</sup> BioTechMed, 8010 Graz, Austria

\* Correspondence: annika.ahtiainen@tuni.fi (A.A.); barbara.genocchi@tuni.fi (B.G.)

† These two authors contributed equally to the study.



**Citation:** Ahtiainen, A.; Genocchi, B.; Tanskanen, J.M.A.; Barros, M.T.; Hyttinen, J.A.K.; Lenk, K. Astrocytes Exhibit a Protective Role in Neuronal Firing Patterns under Chemically Induced Seizures in Neuron–Astrocyte Co-Cultures. *Int. J. Mol. Sci.* **2021**, *22*, 12770. <https://doi.org/10.3390/ijms222312770>

Academic Editor: Timo T. Myöhänen

Received: 29 October 2021

Accepted: 22 November 2021

Published: 25 November 2021

**Publisher's Note:** MDPI stays neutral with regard to jurisdictional claims in published maps and institutional affiliations.



**Copyright:** © 2021 by the authors. Licensee MDPI, Basel, Switzerland. This article is an open access article distributed under the terms and conditions of the Creative Commons Attribution (CC BY) license (<https://creativecommons.org/licenses/by/4.0/>).

**Abstract:** Astrocytes and neurons respond to each other by releasing transmitters, such as  $\gamma$ -aminobutyric acid (GABA) and glutamate, that modulate the synaptic transmission and electrochemical behavior of both cell types. Astrocytes also maintain neuronal homeostasis by clearing neurotransmitters from the extracellular space. These astrocytic actions are altered in diseases involving malfunction of neurons, e.g., in epilepsy, Alzheimer's disease, and Parkinson's disease. Convulsant drugs such as 4-aminopyridine (4-AP) and gabazine are commonly used to study epilepsy in vitro. In this study, we aim to assess the modulatory roles of astrocytes during epileptic-like conditions and in compensating drug-elicited hyperactivity. We plated rat cortical neurons and astrocytes with different ratios on microelectrode arrays, induced seizures with 4-AP and gabazine, and recorded the evoked neuronal activity. Our results indicated that astrocytes effectively counteracted the effect of 4-AP during stimulation. Gabazine, instead, induced neuronal hyperactivity and synchronicity in all cultures. Furthermore, our results showed that the response time to the drugs increased with an increasing number of astrocytes in the co-cultures. To the best of our knowledge, our study is the first that shows the critical modulatory role of astrocytes in 4-AP and gabazine-induced discharges and highlights the importance of considering different proportions of cells in the cultures.

**Keywords:** 4-AP; gabazine; epilepsy; astrocytes; MEA; co-cultures

## 1. Introduction

Astrocytes are glial cells that control and sustain homeostasis in the central nervous system (CNS). In this study, we aim to investigate the role of astrocytes in the homeostasis of neuronal activity after the application of commonly used chemicals to induce epileptiform behavior. Adjacent astrocytes are connected via gap junctions (GJs) that mainly comprise connexins. GJs maintain brain functions, e.g., by channeling the propagation of adjoining astrocytic calcium ( $\text{Ca}^{2+}$ ) waves and regulating ion flow, neuronal activity, and behavior [1]. Astrocytes and neurons are in constant bidirectional feedback-like communication with each other. The interconnected group of a pre- and post-synaptic neuron and the astrocyte is referred to as tripartite synapse [2]. Neuronal firing induces the release of neurotransmitters like glutamate and  $\gamma$ -aminobutyric acid (GABA) from the pre-synaptic neurons [3,4]. When glutamate binds to the metabotropic glutamate receptors (mGluRs) at the astrocytic cell membrane, a cascade of chemical reactions elicits inositol trisphosphate ( $\text{IP}_3$ ) production, which triggers intracellular  $[\text{Ca}^{2+}]_i$  transients [5]. Astrocytes also possess  $\text{GABA}_A$  receptors, which are structurally comparable to those of the neurons [6]. However, the role of  $\text{GABA}_A$

in astrocytes is still unclear; previous research reported that GABA<sub>A</sub> receptor (GABA<sub>A</sub>R) activation depolarizes the astrocyte's membrane and activates voltage-gated Ca<sup>2+</sup> channels and evokes astrocytic [Ca<sup>2+</sup>]<sub>i</sub> transients [7,8]. The GABA uptake activates GABA:Na<sup>+</sup> co-transport by GAT-3, resulting in an accumulation of intracellular Na<sup>+</sup>. Astrocyte [Ca<sup>2+</sup>]<sub>i</sub> transients are elicited by the Na<sup>+</sup>/Ca<sup>2+</sup> exchanger and the relative Ca<sup>2+</sup>-induced Ca<sup>2+</sup> release from the endoplasmic reticulum [9].

The rise in [Ca<sup>2+</sup>]<sub>i</sub>, elicited by glutamate or GABA uptake, may result in the release of gliotransmitters that regulate the synaptic transmission and synaptic plasticity of neurons [2]. Released glutamate, together with ATP, D-serine, and adenosine, activates pre- and post-synaptic neuronal receptors, modulating the synaptic transmission and enhancing long- and short-term synaptic plasticity [10]. GABA released by the astrocytes induces slow outward currents (SOCs) in the neighboring neurons. The SOCs are inhibitory currents and are elicited by the activation of GABA<sub>A</sub>Rs [11]. Thus, the complex interactions between neurons and these types of glial cells regulates and maintains homeostasis in the brain, e.g., by modulating GABA and glutamate levels [12,13].

Dysfunctions in astrocytes have been connected to several CNS diseases, including epilepsy, Alzheimer's disease, and Parkinson's disease [14–17]. Epilepsy is a chronic disease characterized by seizures that can sometimes appear as involuntary body movements. Seizures can initiate in various parts of the brain and are characterized by excessive electrical discharges in groups of neurons [18]. Epilepsy is a family of complex heterogeneous disorders with multiple possible underlying causes, such as different channelopathies; or trauma, such as traumatic brain injury [19]. Due to the progression of the disease and the increased severity of the symptoms with time, as well as the increased cognitive and physical impairments in patients, epilepsy is often associated with neurodegenerative disorders [20]. In addition, a recent population-based study confirmed that epilepsy was more often diagnosed in patients affected by Alzheimer's disease or Parkinson's disease [21].

The central astrocytic dysfunctions linked to epilepsy concern the impaired extracellular potassium (K<sup>+</sup>) buffering and the excessive neurotransmitters in the extracellular space (ECS) [16]. Increased levels of K<sup>+</sup> can impair ionic homeostasis in the ECS, affecting the regular ionic exchanges through the membranes. Furthermore, elevated levels of glutamate stimulates excessive IP<sub>3</sub> production, thus affecting the astrocytic [Ca<sup>2+</sup>]<sub>i</sub> transients. Moreover, GABA has a central role in epilepsy, and disturbances in the glutamine–glutamate–GABA metabolic pathways may lead to seizures. Such GABA-mediated faults include, for example, the loss of GABAergic interneurons, the overproduction of GABA by reactive astrocytes, and occurring GABA<sub>A</sub>R-mediated tonic inhibition [22].

Epilepsy has been widely studied *in vitro* by reproducing the specific characteristics of epileptic seizures. These features are commonly investigated using, e.g., brain slices or cultures of primary rodent cells, as well as human induced pluripotent stem cells. Therefore, the neuronal extracellular activity is often recorded with microelectrode array (MEA) measurements [23–25]. MEA electrodes record extracellular potentials of neurons or neuronal populations in the vicinity of the electrodes. MEA recordings can be analyzed to study, for example, spiking and bursting activity patterns and action potential waveforms across the whole MEA area or at a subset of electrodes [26].

The brain exhibits an inhomogeneous distribution of neurons and astrocytes throughout the different brain areas [27]. In the human cortex, the relative amount of astrocytes amongst all the glial cells is approximately 50% [28]. In some studies with MEAs, electrophysiological recordings of cultures with only neurons, and co-cultures of neurons and astrocytes, were compared [29,30]. However, the numbers of plated astrocytes and neuronal cells are often fixed, i.e., the studies do not consider the possible effects of the neuron–astrocyte ratio. In previous studies, neuronal cultures supported with astrocytes have shown increased neuronal viability [31], earlier neuronal network formation and maturation [29], and differing firing rates [29,30] compared to 'pure' neuronal cultures, where no astrocytes were explicitly added. However, to our knowledge, there have been

no studies where the implications of the neuron–astrocyte ratio on neuronal activity have been investigated in a systematic manner.

Two convulsant drugs, 4-aminopyridine (4-AP) and SR-95531 hydrobromide (gabazine), are often used to induce and study epilepsy in *in vitro* models. However, the role of astrocytes in neuronal dynamics under the influence of these convulsants remains uncertain. 4-AP is a non-selective voltage-gated  $K^+$  channel blocker that has been reported to cause synchronous neuronal firing, increase action potential duration, and increase neuronal excitability by affecting the repolarization of the neuronal cell membrane after the depolarization phase of an action potential [32,33]. 4-AP induces epileptiform activity in neurons and results in synchronized  $[Ca^{2+}]_i$  transients modulated by GABA and glutamate receptors [34–37]. 4-AP likely affects the behavior of astrocytes since 4-AP-mediated stimulation induces an  $[Ca^{2+}]_i$  rise, and at high concentrations, a sequestration of  $[Ca^{2+}]_i$  of both excitable and non-excitable cells [35,38].

Gabazine is a competitive  $GABA_A$ R antagonist that is reported to increase spike rates, induce changes in neuronal firing patterns to more synchronized bursts, and cease slow negative potentials [39,40]. It allosterically inhibits the chloride ion ( $Cl^-$ ) influx and therefore reduces GABA-mediated synaptic inhibition. Thus, gabazine causes epileptiform activity in neurons by inhibiting neuronal hyperpolarization [41,42]. Therefore, mutations in extrasynaptic  $GABA_A$ R subunits are linked to epilepsy [43].

While researchers have studied the effects of 4-AP and gabazine on neurons, the role of astrocytes in these networks still needs further investigation. Hence, our study aims to explore how the neuronal responses to these drugs vary depending on the astrocyte numbers in the culture.

In this study, we investigated the modulatory effects of astrocytes on neuronal function during pharmacologically induced epileptiform discharges. We thus plated rat-derived neuron–astrocyte co-cultures and compared them with neuron cultures without added astrocytes. To differentiate between ion-elicited and transmitter-elicited epileptic-like activity, we induced hyperactivity in our cultures using 4-AP and gabazine, respectively, at 28 days *in vitro* (DIV). We hypothesized that a larger share of astrocytes in the culture would influence neuronal network development and the ionic and neurotransmitter homeostases, which would affect the responses to gabazine and 4-AP. To this end, we examined the effects of the astrocytic control on drug-induced epileptiform activity in cultures with different relative numbers of astrocytes and neurons. We quantified the differences in the activities of the baseline and the drug-induced cultures in terms of the spike rate, burst rate, and the number of active channels during the development (from DIV7 to DIV28). We studied the bursting patterns more deeply before, during, and after the epileptiform activity induction. Furthermore, the effects of these two chemicals on neuron and astrocyte viability were tested after 24 h of stimulation with a live/dead assay. In general, we investigated in our study the effects of the general epileptiform inducers 4-AP and gabazine on the modulatory effects of astrocytes on network activity, and the importance and effects of the neuron–astrocyte cell count ratio on drug responses. With this work, we aimed to elucidate the important role of astrocytes in neuronal function and homeostasis in health and disease.

## 2. Results

The following sections present the results obtained by live/dead assays, the cell counting of the different cell cultures, the spike rate (SR) and burst rate (BR) analyses of the baseline activities due to AP and gabazine stimulation, and the analysis of the synchronization based on cross-correlations and the binned spiking activity. Table 1 summarizes the methods and overall results.

**Table 1.** Summary table of the methods and results. (NS: a cell culture without explicitly added astrocytes; 90/10, 80/20, 70/30, 50/50: percentages of plated neurons/astrocytes for each cell culture type; NB: network-wide burst; ICC: immunocytochemistry).

Cell Culture Platform	Cell Culture Type	n	Experiment/Analysis	Methods Section	Stimulation (4-AP 75 $\mu$ M or Gabazine 30 $\mu$ M)	Results Section	Results
<b>MEAs</b>	NS, 90/10, 80/20, 70/30, and 50/50	8 MEAs per cell culture type (total n = 40)	Spontaneous baseline activity recording	4.6	None (control)	2.2 and 2.3	NS cultures experienced more robust development at the later stages of culture (DIV21–28) compared to co-cultures. Development of electrical activity was more robust for co-cultures with higher ratios of astrocytes (70/30 and 50/50) at early stages of culture (DIV7–DIV14). Co-cultures with higher astrocyte numbers had lower spike and burst rates and a lower percentage of spikes in bursts. IBI increased with increasing neuron–astrocyte ratio.
			Acute stimulation recording	4.7	4-AP	2.3	Slight increase in SRs and BRs for NS, 90/10, and 80/20, whereas with 70/30 and 50/50 SRs remained mostly unchanged, and the BRs slightly decreased. The percentage of spikes in bursts was reduced in all the cultures, and the IBI and its variability were slightly increased.
	NS, 90/10, 80/20, 70/30, and 50/50	8 MEAs per cell culture type (total n = 40)	Washout followed by recording after 24 h	4.7	Gabazine	2.3	SRs and BRs increased in all cultures. IBI values decreased for all cultures, and the percentage of spikes in bursts increased, synchronizing the network activity.
			Cross-correlation	4.7.3	4-AP	2.4	SRs were generally lower than at baseline except for NS and 70/30. BRs were higher than at baseline for NS and all the co-cultures except 80/20.
			NBs	4.7.4	Gabazine	2.4 and 2.5	SRs and BRs were generally lower for all cultures, except in the case of BRs in 90/10. Either no change or a small decrease in the numbers of channels with synchronized activity and the correlation weights of the connections.
<b>Coverslips</b>	NS, 90/10, 80/20, 70/30, and 50/50	3–4 per staining	Convulsant response delay	4.7.5	4-AP	2.5	Increased connection weights in all co-cultures which shifted the weight difference distribution towards positive values.
			ICC	4.3	Gabazine	2.1	The number of network-wide bursts decreased.
			ICC	4.3	4-AP	2.5	Repetitive synchronous NBs spanned over a constant number of channels (~40 channels).
<b>Coverslips</b>	NS	3–4	Live/dead assay	4.4	Control/4-AP/Gabazine	2.3	No noticeable delays in the NB synchronization.
			Live/dead assay	4.4	Control/4-AP/Gabazine	2.3	Increasing the relative numbers of astrocytes drastically delayed the effects of gabazine on neuronal firing (approximate delays were NS: 25 s; 90/10: 130 s; 80/20: 130 s; 70/30: 180 s; 50/50: 230 s).
<b>24-Well Plates</b>	Astrocytes	2–3	Live/dead assay	4.4	Control/4-AP/Gabazine	2.3	Neuron–astrocyte ratios were coherent after DIV14 with plating densities, and neuron counts were homogeneous through all the coverslips counted.
			Live/dead assay	4.4	Control/4-AP/Gabazine	2.3	4-AP slightly increased the neuronal viability. Neither 4-AP nor gabazine were toxic to neurons and did not decrease cell viability or affect their appearance.
							No differences in cell viability or appearance.

### 2.1. Neuron–Astrocyte Culture Ratios Corresponded Well to the Cell Plating Ratios

We plated neuron cultures without any added astrocytes (NS), as well as neuron–astrocyte co-cultures with cell count ratios of 90/10, 80/20, 70/30, and 50/50. In Figure 1A, representative immunofluorescent images used in cell counting at DIV14 of MAP2-positive neurons and GFAP-positive astrocytes for the NS and co-cultures are shown, along with the percentages of detected neurons and astrocytes. The percentages of neurons were, on average, 92.2, 80.2, 77.1, 73.3, and 58.2% for the NS, 90/10, 80/20, 70/30, and 50/50 cultures, respectively. The standard deviation of MAP2-positive cell counts from the total number of cells was only approximately 4.9% within the cultures, confirming near equal neuronal numbers and densities in all the cultures. The pairwise differences in the neuron counts between cultures were always statistically insignificant ( $p > 0.05$ ), confirming uniform neuronal culture density. The number of astrocytes at DIV14 corresponded to the seeded cell numbers: we detected, on average, 7.8, 19.9, 22.9, 26.7, and 41.8% of astrocytes in the NS, 90/10, 80/20, 70/30, and 50/50 cultures, respectively (Figure 1A). Note that a small percentage of astrocytes already existed in the commercially obtained neuronal cell stock in the NS cultures. Representative images of the masks created by the in-house semi-automated MATLAB tool are shown in Figure 1B,C.

### 2.2. The Development of Neuronal Baseline Activity in NS vs. Neuron–Astrocyte Co-Cultures

Spontaneous baseline electrical activity gradually increased in all cultures in a typical manner (Figure 1D–F) from DIV7 onward until the chemical stimulation was applied at DIV28. At DIV7, all cultures on the MEAs were active, but spiking and bursting activities were low. Co-cultures containing more astrocytes exhibited enhanced early-stage development and maturation of the neuronal networks, evaluated by their spike and burst rates (SRs and BRs), and numbers of active channels. In the earlier stages of the culture (DIV7 and DIV14), the SRs and BRs of the co-cultures developed faster, the numbers of active electrodes were higher, and, overall, the variability of the electrical activity across the MEA channels of the co-cultures were lower than for the NS (Figure 1D–F). Co-cultures with 50/50 and 70/30 ratios had more active electrodes than co-cultures containing less astrocytes. For instance, for the 90/10 ratio at DIV7, there was less than one active electrode on average, whereas the values for the 70/30 and 50/50 ratios were about six ( $p = 0.005$ ; Mann–Whitney U test) and nine ( $p = 0.005$ ), respectively. Between DIV14 and DIV21, neuronal electrical activity increased in all cultures and reached its peak around DIV28 (Figure 1D–F). At DIV14, co-cultures containing a higher astrocyte ratio exhibited more bursting than the 90/10 ratio and NS cultures. In fact, at DIV14, the average burst rate for the 80/20 ratio was almost two times higher, the 70/30 ratio almost three times higher, and the 50/50 ratio almost four times higher compared to the 90/10 ratio ( $p = 0.003$ ,  $p = 0.0006$ , and  $p = 0.01$  for the 80/20, 70/30, and 50/50 ratio co-cultures, respectively). At DIV21, both SRs and BRs were higher for co-cultures compared to the NS cultures. Both the 80/20 and 70/30 ratio co-cultures had twice more spikes on average than the NS cultures ( $p = 0.05$  for both), and the 70/30 ratio had over 2.3 times more bursts than the NS ( $p = 0.02$ ). At DIV28, there were slightly more active electrodes for the NS cultures compared to the 70/30 ( $p = 0.04$ ) and 50/50 ratio ( $p = 0.04$ ) co-cultures. Moreover, the NS cultures had more spiking activity on average compared to the 90/10 ratio culture ( $p = 0.03$ ). The 80/20 ratio co-culture had both more spikes ( $p = 0.01$ ) and bursts ( $p = 0.04$ ) per minute on average compared to the 90/10 ratio co-culture. Moreover, the 80/20 ratio co-culture had 144 spikes per minute on average, whereas the 50/50 ratio co-culture had 83 spikes per minute ( $p = 0.05$ ).

The NS and co-cultures experienced maturation at different rates. Heat maps in Figure 1G–I present the fold change of the SR, BR, and the number of active electrodes of each culture at different weeks in vitro compared to DIV7. Representative images of one 50/50 neuron–astrocyte co-culture on the MEA are presented in Figure 1J, showing the stage of the same network at DIV7 and DIV21.



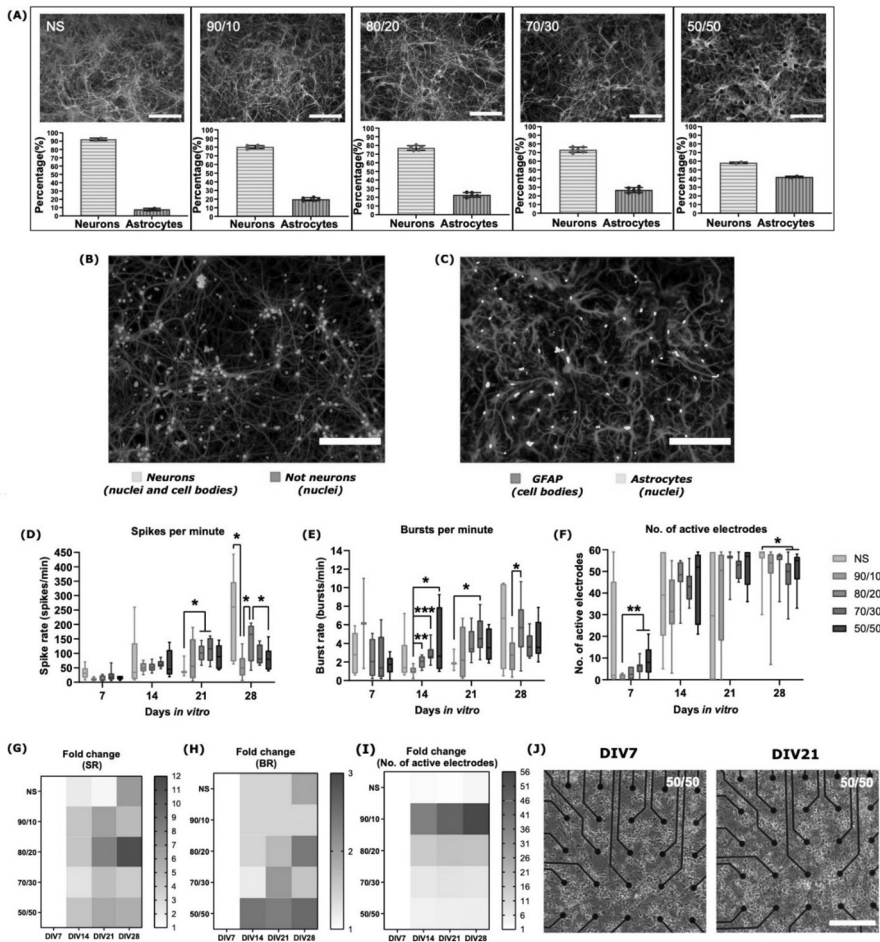


**Figure 1.** The number of astrocytes in the culture affects (co)-culture structure and neuronal electrical activity and its development. **(A)** ICC images of MAP2-positive neurons (green) and GFAP-positive astrocytes (magenta) of NS and neuron–astrocyte co-cultures, along with the percentages of neurons and astrocytes, which were calculated for each culture. The bar height represents the average percentage of cells, the whiskers the standard deviations, and the dots the individual values for each culture’s region of interest (ROI). Nucleus staining with DAPI is indicated in blue. **(B)** A representative image for counting MAP2-positive neurons and their nuclei (green) and the nuclei of non-neuronal cells (magenta). **(C)** A representative image for counting GFAP- and DAPI-positive astrocyte nuclei (cyan) and the cell bodies of the GFAP-positive astrocytes (magenta). The development of **(D)** neuronal spiking activity, **(E)** bursting activity, and **(F)** number of active electrodes for each culture over 28 days in vitro. In the box plots, the darker blue bar in the middle of each box represents the median, and the attached whiskers range from the smallest value to the largest. \*  $p < 0.05$ ; \*\*  $p < 0.01$ ; \*\*\*  $p < 0.001$ . In general, co-cultures with higher ratios of astrocytes (70/30 and 50/50) had more spiking, bursting, and active electrodes at earlier stages of culture (DIV7–DIV14). However, towards DIV28, the activity of co-cultures stabilized compared to the previous week, but the activity of NS continued to increase. Fold change of **(G)** spike rate, **(H)** burst rate, and **(I)** number of active electrodes after DIV7. Spike rates increased from DIV7 for all the cultures until DIV28, except that the spike rates for 90/10, 70/30, and 50/50 decreased slightly from DIV21 to DIV28. Burst rates developed faster for 80/20, 70/30, and 50/50 from DIV7 to DIV21, whereas NS and 90/10 lagged behind in burst rate development (decreasing fold change depicted in grey). The number of active electrodes exploded from DIV7 to DIV14 for all the cultures but remained relatively steady after that. **(J)** Representative images of DIV7 (left) and DIV21 (right) of the same 50/50 co-culture on MEA. The development of neuronal networks was visually observable with a microscope. Scale bar 200 μm in all images.

From DIV7 to DIV14, the NS cultures experienced the slowest increase in the spike rate (114% and a 2-fold increase) compared to neuron–astrocyte co-cultures with over 300% and a 4-fold increase in their spike rates, except for the 70/30 ratio co-culture (Figure 1G). Moreover, the number of active electrodes drastically increased from DIV7 to DIV14 and rose from 7 to 41 electrodes on average for all cultures (Figure 1I). At DIV7, the 90/10 ratio co-culture had only one active electrode, whereas at DIV14, there were 33 active electrodes, resulting in higher change compared to other cultures (Figure 1I). However, the average SRs and BRs remained lower for the 90/10 ratio co-culture at DIV14 compared to other co-cultures with more astrocytes (Figure 1D,E). Therefore, the 90/10 ratio co-cultures lagged in maturation despite the high increase in the fold change of the active electrodes. Furthermore, only the 70/30 and 50/50 co-cultures with a higher ratio of astrocytes experienced an increase in BRs (20% and a 1.2-fold increase for the 70/30 ratio co-culture and 146% and 2.5-fold increase for the 50/50 ratio co-culture), whereas BRs slightly decreased for other cultures from DIV7 to DIV14 (Figure 1H, where the decrease is depicted in a grey color). At DIV21, all co-cultures had above a 1-fold change in SRs, BRs, the number of active electrodes compared to DIV7, and a percentage increase from DIV14 values, except for the 50/50 ratio co-culture that had 4% less bursting compared to DIV14, and the 90/10 ratio co-culture that had lower BR compared to DIV7. At DIV28, SRs for all cultures increased compared to DIV7, but percentage-wise there was a decrease from DIV21 for the 90/10, 80/20, and 50/50 ratio co-cultures (−25%, −17%, and −5%, respectively). Therefore, co-cultures with higher ratios of astrocytes, the 70/30 and 50/50 ratio co-cultures in particular, experienced relatively earlier maturation in terms of fold changes in SRs, BRs, and the number of active electrodes, which was evaluated by a more robust increase in their activity at the early stage of culture (from DIV7 to DIV14). However, the activity of co-cultures stabilized towards 28 days in the culture, whereas the NS cultures experienced a continued increase in activity at the later stages of culture (from DIV21 to DIV28) after a relatively slow start.

### 2.3. 4-AP and Gabazine Affected Neuronal Activity but Did Not Decrease Cell Viability

The MEA recordings and the chemical stimulation workflow are presented in Figure 2A and are described in the Method Sections 4.5 and 4.6.

The possible cytotoxic effects and phenotypic impacts of 4-AP and gabazine were tested with a live/dead assay (Supplementary Figure S2A,B) and immunocytochemistry (ICC) (Supplementary Figure S2A,B). The live/dead assay confirmed that neither 4-AP nor gabazine affected astrocyte viability after 24 h from the exposure compared to unstimulated control cultures (Figure 2E,F). Moreover, for the NS cultures, 4-AP increased neuronal viability by approximately 10% ( $p = 0.04$ ; Mann–Whitney U test) compared to unstimulated cultures, whereas gabazine did not cause significant changes (Figure 2D).

The effects of the chemicals were also observed using ICC, which confirmed no visible changes in the neuron (Figure 2G) or astrocyte (Figure 2H) morphology, which was evaluated from the expressions of neuron- and astrocyte-specific markers, i.e., GFAP, S100 $\beta$ , and vimentin (VIM) for astrocytes (Figure 2H), and MAP2 and  $\beta$ 3-tubulin (b3tub) for neurons. Hence, neuron and astrocyte cultures had their typical ICC marker expression without any apparent signs of phenotypic alterations after 4-AP or gabazine exposure. Moreover, almost all MEAs still presented spiking and bursting activity after 24 h from the exposure to the drugs (Supplementary Figure S1A–D).

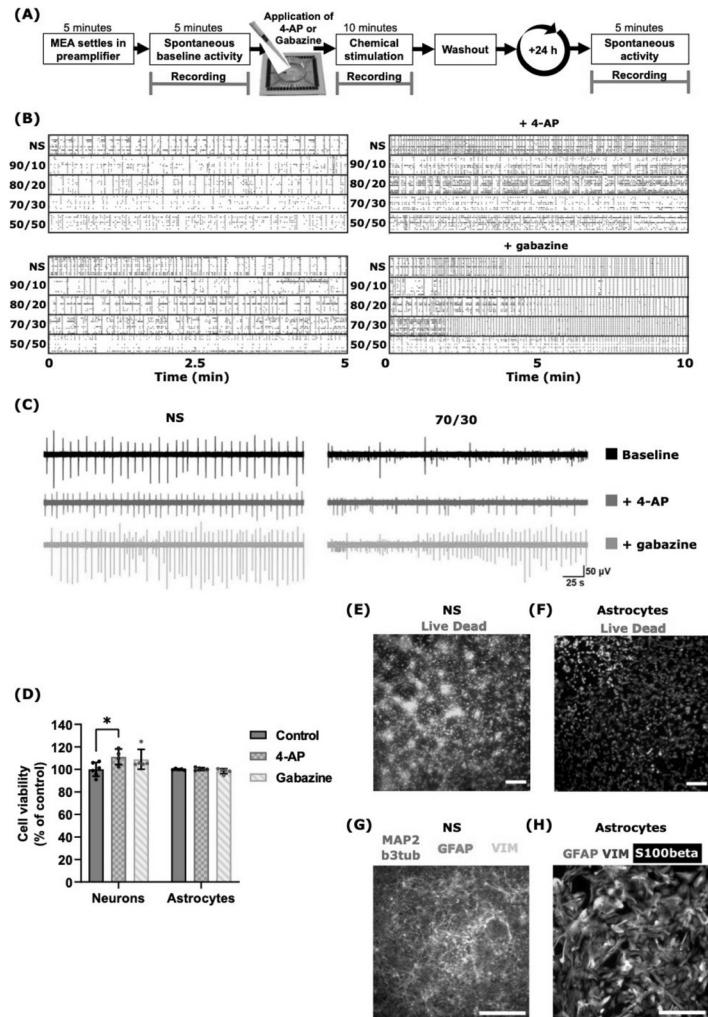


**Figure 2.** Functional and morphological assessments of primary neuron and astrocyte cultures. (A) Measurement protocol for cultures on MEAs: all MEAs were left to settle for 5 min before recording the spontaneous (baseline) activity. Neurons and co-cultures were directly stimulated on MEAs by either 75  $\mu$ M 4-AP or 30  $\mu$ M gabazine, followed by a 10-min recording right after stimulation. Convulsants were washed out, and the cell culture medium was replaced. The next day, spontaneous activity and culture recovery were evaluated with a 5-min spontaneous recording. (B) Raster plots show different cultures' baseline activity before (left panels) and after 4-AP or gabazine exposure (right panels). (C) Representative neuronal spiking activity after 4-AP (violet) or gabazine (green) stimulation and at baseline (black) for NS (left traces) and 70/30 cultures (right traces). (D) Neuron and astrocyte viability assessment results indicated that neither 4-AP nor gabazine caused cell death. In fact, 24-h 4-AP exposure increased the viability of NS cultures ( $p = 0.038$ ). (E,F) Representative live/dead images of rat cortical neurons and astrocytes. Live cells are shown in green and dead cells in red. (G,H) Representative, untreated, untreated, ICC images of rat cortical neurons and astrocytes. Astrocytes uniformly expressed astrocyte-specific markers GFAP (G) violet, (H) green), S100 $\beta$  (white), and vimentin (G) yellow (H) violet) as well as neuronal proteins such as  $\beta$ 3-tubulin and MAP2 (G) both in green). Nucleus (DAPI) is indicated in blue. Scale bar 200  $\mu$ m in all images.

The representative acute effects of 4-AP and gabazine on the neuronal spike activity are shown in Figure 2B. The left panels show the raster plots of the spontaneous activities of the different NS and co-cultures before the chemical stimulation; the activity of the corresponding MEAs after 4-AP or gabazine exposure is shown in the raster plots in the right panels. The convulsant 4-AP increased the SRs and slightly decreased burst synchronization (Figure 2B, upper right), while gabazine induced hyper-synchronized activity in the networks (Figure 2B, lower right). A deeper analysis of burst synchronization is shown in Section 2.4. Figure 2C illustrates the changes in the neuronal activity of the NS and 70/30 ratio co-cultures before and after chemical stimulation: 4-AP did not cause any visible changes in neuronal spiking, whereas gabazine affected both the NS and 70/30 ratio co-cultures by increasing the neuronal activity and spiking intensity.

All cultures on the MEAs exhibited bursting at DIV28 (Figure 3). In general, before the stimulation, the co-cultures with higher numbers of astrocytes showed lower spike and burst rates (Figure 3A,B). Moreover, the percentage of spikes in bursts decreased with the increasing number of astrocytes in the cultures, whereas inter-burst intervals (IBIs), i.e., the time between the end of the previous burst and the start of the next one, increased (Figure 3C,D).

Interestingly, 4-AP seemed to have a varying effect on the cultures depending on the neuron–astrocyte ratios. Cultures with higher numbers of astrocytes exhibited minor effects of 4-AP: 4-AP slightly increased or left almost unchanged the SRs and BRs for the NS, 90/10 ratio, and 80/20 ratio co-cultures. The SRs decreased for the 70/30 ratio co-culture and slightly increased for the 50/50 ratio co-culture, and the BRs decreased for the 50/50 ratio co-culture and remained almost unchanged for the 70/30 ratio co-culture (Figure 3A,B,E,F). However, none of the co-cultures with astrocytes reached a SR comparable with seizure-like hyperactivity. Moreover, the stimulation with 4-AP reduced the percentage of spikes in bursts in all the cultures and slightly increased the IBI and its variability in the co-cultures (Figure 3C,D). These differences, however, were not statistically significant.

Gabazine stimulation had a much greater effect on neuronal activity than 4-AP stimulation. Gabazine increased the SRs and BRs in all the cultures (Figure 3A,B;  $p = 0.02$  SRs and BRs for the 90/10 ratio co-culture;  $p = 0.004$  SRs/0.008 BRs for the 80/20 ratio co-culture;  $p = 0.004$  SRs and BRs for the 70/30 ratio co-culture;  $p = 0.03$  SRs/0.02 BRs for the 50/50 ratio co-culture; Mann–Whitney U test). The SR and BR fold change for the NS was lower than for the co-cultures (Figure 3E,F). Gabazine also decreased the IBI values for all the cultures (with an overall average fold change of 0.4;  $p = 0.03$  for the 90/10 ratio co-culture;  $p = 0.008$  for the 80/20 ratio co-culture;  $p = 0.004$  for the 70/30 ratio co-culture; and  $p = 0.008$  for the 50/50 ratio co-culture) and increased the percentage of spikes in bursts (with an overall average fold change of 1.3), synchronizing the network activity (Figure 3C,D). Moreover, the relative changes in the percentage of spikes in bursts and IBIs were more notable in co-cultures containing more astrocytes (the 70/30 and 50/50 ratio co-cultures). In all co-cultures, gabazine caused an over 2-fold increase in spike and burst rates ( $p = 0.03$ , except for the 90/10 and NS cultures), whereas in the NS, the fold change remained under two (Figure 3E,F).

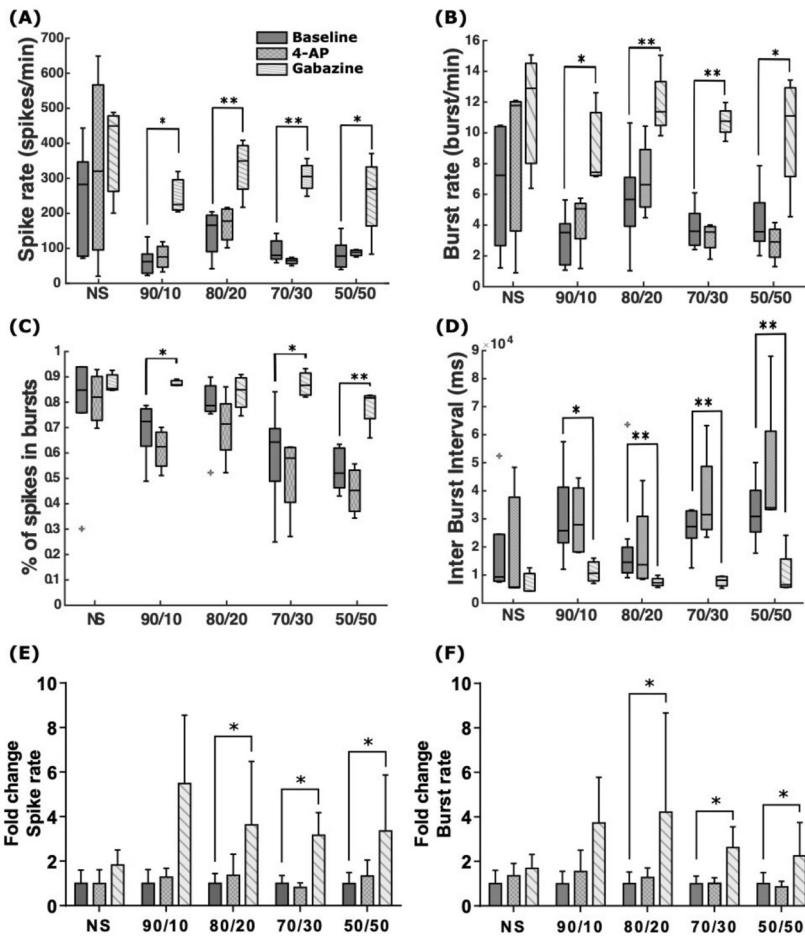


**Figure 3.** Responses of NS and neuron–astrocyte co-cultures to 75  $\mu\text{M}$  4-AP and 30  $\mu\text{M}$  gabazine at DIV28. (A) SR and (B) BR. 4-AP slightly increased the SRs and BRs in NS, 90/10, and 80/20 co-cultures but had hardly any effect in the co-cultures with higher numbers of astrocytes. Gabazine increased the SRs and BRs in all cultures. (C) The percentages of spikes contained in bursts decreased after 4-AP application in all cultures. However, gabazine induced an increase in the percentage of spikes in bursts in all the cultures. (D) The IBIs remained the same or slightly rose after the 4-AP application. Gabazine induced a decrease in IBI, and the decrease was greater in co-cultures with more astrocytes. (E,F) The fold change in the SRs and BRs compared to the corresponding baseline values before stimulation. \*  $p < 0.05$ ; \*\*  $p < 0.01$ . In the box plots, the data points for each subplot are the respective MEA averages between the channels; the black bar in the middle of the box represents the median, and the box edges represent the 25th and 75th percentiles, respectively. The whiskers extend to the most extreme data points that are not considered outliers. Red crosses represent outlier cultures. In the fold changes, the bar height represents the population mean, and the whiskers represent the population's standard deviation.

#### 2.4. 4-AP and Gabazine Had Different Effects on Neuronal Network Synchronization

The application of 4-AP and gabazine had different effects at the network level. We analyzed the correlations of time-varying spectral entropies between MEA channels (CorSE analysis, Section 4.7.3). 4-AP caused a slight decrease in the number of channels with synchronized activity and in the inter-channel correlation weights of the connections (Figure 4A,B). The inter-channel correlation weights represent the level of synchronicity, expressed as a value from 0 to 1, between a selected pair of channels in the MEA. Figure 4A

shows a heatmap of the correlation weights between the 60 channels of the MEA; in the heatmap, the correlation weights at baseline are shown in the lower left half, and in the upper right half, the weights for the same channel pairs after the stimulation with 4-AP in a representative 80/20 ratio culture MEA are represented. It appears clear that certain connections were maintained while others were weakened. This is reflected in the channel connectivity map (Figure 4B), where only the channels with correlation weights higher than 0.75 are shown for clarity (for the same MEA as in Figure 4A). The black lines represent the links between the synchronized channels; the thickness of a line reflects the correlation weight of the connection. The stimulation of 80/20 ratio co-cultures with gabazine shows a clear increase in all correlation weights (Figure 4C, Supplementary Table S1). Thus, there is an overall average of a 1.55-fold increase in the number of channels linked with a correlation weight higher than 0.75 (Figure 4D). However, the changes for both 4-AP and gabazine were not statistically significant culture-wise, even though they are visually noticeable.

The violin plots in Figure 4E show that in the case of 4-AP stimulation, the median of the connection weight differences between the baseline measurements and measurements after stimulation, as well as the whole weight difference distribution, were centered around zero, where the stimulation showed almost no effect on the connectivity. However, the gabazine stimulation increased the connection weights in all the co-cultures with astrocytes and shifted the weight difference distribution towards positive values. Here, we analyzed all the connections weights (approximately 3000) between the channels of each MEA (four per culture group), and, due to the large  $n$  of the connection weights ( $n$  was approximately 10,000) in each culture group, the Student's  $t$ -test gave a  $p$ -Value well below  $p < 0.01$  for the pairwise analysis of the weights after 4-AP and at baseline ( $p < 0.0001$  for all cultures, except where  $p = 0.1$  for the 80/20 ratio co-culture and  $p < 0.05$  for the 50/50 ratio co-culture). The effect size analysis showed a low to medium effect (Glass's delta  $\leq 0.6$ ) of the stimulation with 4-AP. In contrast, in the case of gabazine stimulation, the effect size analysis showed a low effect for the NS (Glass's delta = 0.15), a medium effect for the 90/10 ratio co-cultures (Glass's delta = 0.7), and a high effect for the co-cultures with more astrocytes (Glass's delta  $\geq 0.9$ ) ( $p < 0.0001$  for all cultures). All the Glass's deltas resulted in positive values, depicting an increase in the stimulated weights, except in the stimulation with 4-AP in the 80/20 ratio cultures. The Glass's delta and its confidence intervals for all the comparisons between the stimulated effects and the baseline are shown in Supplementary Table S1.

The network effects of 4-AP and gabazine were also observable in the numbers of network-wide bursts (NBs). Gabazine synchronized the bursting of all the networks in all the cultures; this effect was more pronounced in neuron–astrocyte co-cultures containing higher numbers of astrocytes (Supplementary Figure S1F;  $p = 0.03$  for both the 80/20 and 70/30 ratio co-cultures). The increasing number of NBs for gabazine stimulation was directly related to the neuron–astrocyte ratio (1.1, 2.4, 3.8, 12.1, and 7.8-fold changes for the NS, 90/10, 80/20 70/30, and 50/50 ratio co-cultures, respectively). There was no change in the number of NBs in 4-AP stimulation of the cultures (Supplementary Figure S1E). However, 24 h after stimulation, cultures exposed to drugs showed fewer NBs than the day before, except for the NS ( $p = 0.03$ ; Mann–Whitney U test).

### 2.5. Gabazine Induced Synchronization and Neuron–Astrocyte Ratio Effects on Gabazine's Delay in Response Time

Interestingly, the effect of gabazine on neuronal activity was delayed in the co-cultures with higher numbers of astrocytes. The NBs in the MEAs stimulated with 4-AP spanned fewer channels (around 20 channels on average) than in the gabazine stimulated NBs (approximately 30 channels on average) (Figure 5A). Moreover, the bursting activity of the stimulated MEAs was not repetitive and did not show any noticeable differences between cultures. The repetitive synchronous NBs in MEAs stimulated with gabazine spanned a constant number of channels, which slightly decreased with the increasing number of astrocytes (Figure 5B).

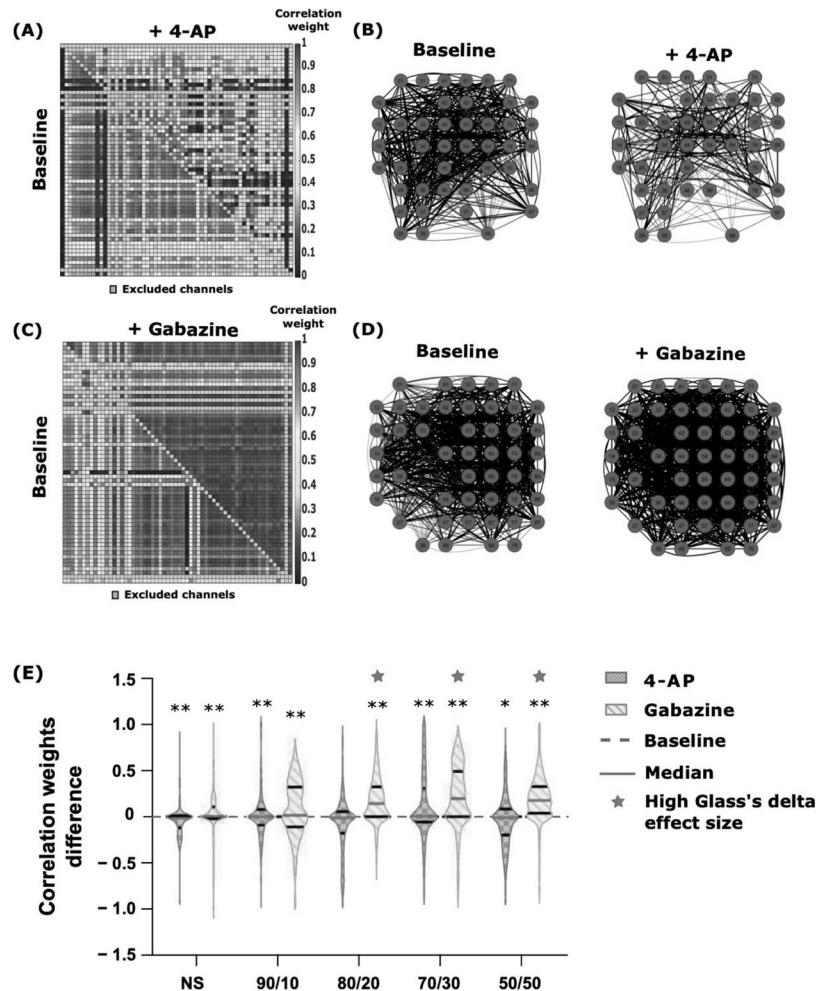


**Figure 4.** The effects of 75  $\mu\text{M}$  4-AP and 30  $\mu\text{M}$  gabazine on network connectivity and activity. (A,C) show the pairwise channel correlation weight heatmaps at baseline (lower-left halves) and after the stimulation (upper-right halves) with 4-AP (A) and gabazine (C) from a representative 80/20 co-culture on one MEA for each chemical stimulation protocol. Correlation weights span between 0 (blue) and 1 (red). The noisy channel pairs excluded from the analysis and the diagonal points not calculated are shown in grey. (B,D) show the pairwise channel connectivity maps for the same MEAs and chemical stimulations as in (A,C), respectively. The red circles represent the MEA channels, and the black lines represent the connections found between the channels. Only the connections with weights larger than 0.75 are shown for clarity. The line thickness represents the correlation weight. (E) displays the correlation weight differences after stimulation with 4-AP or gabazine compared to baseline for each channel pair. 4-AP slightly decreased channel correlation weights or left them unchanged, whereas gabazine increased them in all the cultures except NS. The effect was more pronounced for higher numbers of astrocytes. The exact numerical values of the Glass's delta effect size analysis can be seen in Supplementary Table S1. The grey dashed line represents the weight difference if there are no changes between baseline and chemical stimulation; the solid red lines are the median, the solid black lines are the quartiles, and the magenta stars represent the populations with higher Glass's delta effect sizes. \*  $p < 0.05$ , \*\*  $p < 0.01$ .

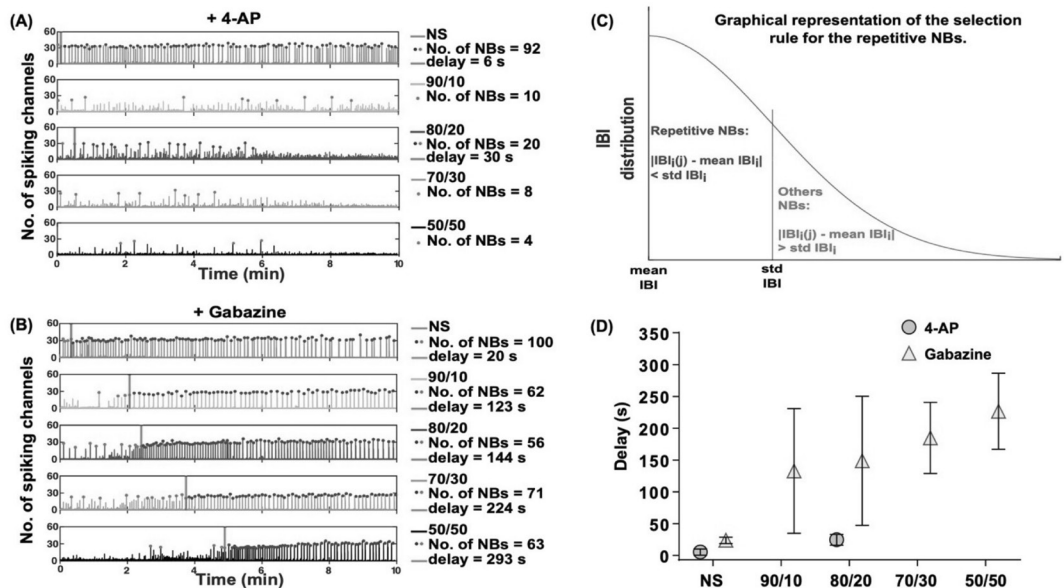


**Figure 5.** (A,B) Channel spiking activity summed in 5 ms time bins for five cultures (NS in blue, 90/10 in yellow, 80/20 in violet, 70/30 in green, and 50/50 in black) and the detected NBs (orange dots and blue dots) over the 10-min recordings after stimulation with 75  $\mu\text{M}$  4-AP and 30  $\mu\text{M}$  gabazine, respectively. The blue dots represent the repetitive NBs, and the orange dots represent the other NBs. When both are presented, the number of NBs is defined as the sum between the two. The  $y$ -axis of each subplot shows the number of channels participating in an NB. The red lines represent the delays defined as the time points of the first bursts belonging to the repetitive burst series (blue dots). (C) shows a graphical representation of the rule we used to select the bursts belonging to the repetitive burst series (blue dots); (i) is the MEA index, and (j) is the NB index in the series. (D) shows the delays due to the gabazine (in green) and 4-AP (in lilac) effects on the network activities for each cell culture type.

Lowering the neuron–astrocyte ratio (i.e., increasing the relative numbers of astrocytes) drastically delayed the effects of gabazine on neuronal firing. For the NS, the delay was, on average, around 25 s, whereas it was approximately 130 s for the 90/10 ratio co-cultures, 150 s for the 80/20 ratio co-cultures, 180 s for the 70/30 ratio co-cultures, and approximately 230 s for the 50/50 ratio co-cultures (Figure 5D). Figure 5D shows the delays in all the MEAs for the NS and co-cultures and indicates an increasing delay of gabazine effects with the increasing numbers of astrocytes. The 90/10 and 80/20 ratio co-cultures exhibited a higher inter-culture variability. No delayed effects or changes in the NB synchronization were noticeable for 4-AP (Figure 5A,D).

### 3. Discussion

In our study, we aimed to investigate the role of astrocytes in balancing drug-elicited epileptic activity. We investigated the effects of the numbers of astrocytes, with respect to the number of neurons, on neuronal firing, bursting, and network behavior with and without 4-AP and gabazine application. We anticipated that astrocytic control, determined by the number of astrocytes in the cultures, might enhance early neuronal network development compared to cultures with less astrocytes.

Our study showed that the addition of astrocytes to the neuronal network led to the earlier development and maturation of the cultures based on their electrical activity characterizations, confirming previous findings on primary co-cultures [29]. It has been shown that astrocytes are crucial for the synaptogenesis of neurons, and that they also contribute to neuronal branching and the formation of functional networks with circuits [44]. Therefore,



the astrocytic regulation of nascent synapse formation, neuronal network development, and maturation, especially in the early stages of culture (DIV7 to DIV14), are likely to enhance the maturation of the co-cultures containing more astrocytes. Moreover, astrocytes have a significant role in regulating synapse maintenance and elimination that defines the structure of the network. This might explain the lower activity variance across the cultures and the stabilization in neuronal activity of the higher astrocyte-ratio co-cultures towards DIV28 as the neurons and astrocytes begin to show mature morphology.

4-AP and gabazine are two convulsant drugs commonly used in *in vitro* experiments to induce epileptic seizures in brain tissues [32,33,45]. 4-AP is a voltage-gated  $K^+$  channel blocker, and gabazine is a  $GABA_A$  receptor antagonist. 4-AP application results in synchronized  $[Ca^{2+}]_i$  transients, which trigger the release of glutamate [35]. Both neurons and astrocytes express voltage-gated  $K^+$  channels and  $GABA_A$  receptors. Therefore, these drugs are expected to affect both cell types.

Gabazine has been shown to block GABAergic signaling in both rat and hPSC-derived networks, leading to increased spike rates, burst rates, and synchronization [39,46,47]. In our study, gabazine induced seizure-like hyperactivity in all our cultures, increasing SRs and BRs, which indicates that our cultures had functional inhibitory systems.

Interestingly, for gabazine stimulation, we noticed that the hypersynchronous bursts appeared delayed for the co-cultures, compared to the neuronal cultures, without added astrocytes. This suggests that the maturational stage, which depends on the astrocyte number in the culture, may also affect the modulational effects of the drug. Furthermore, co-cultures with higher numbers of astrocytes have more neuron–astrocyte interconnections with GJs, that allows for a quick exchange of ions, metabolites, and neuroactive substances that are released by neurons and astrocytes during pharmacological stimulation. More astrocytes in the culture also means more  $GABA_A$ Rs, which likely causes differential responses between the cultures. Astrocytes exhibit a high density of  $GABA_A$ Rs, which are functionally and structurally similar to the neuronal ones [6]. In a study conducted on subventricular zone astrocytes,  $GABA_A$ R activation induced a  $Ca^{2+}$  increase through the activation of voltage-gated  $Ca^{2+}$  channels [48]. Thus, the blockade of the  $GABA_A$ Rs reduces  $[Ca^{2+}]_i$  transients [8]. Since the inhibitory gliotransmitters release, e.g., D-serine from the astrocytes, which depends on  $Ca^{2+}$  elevation [49], we hypothesize that reduced intracellular  $Ca^{2+}$  levels lead to a failure in the control of neuronal activity and increased SRs and BRs. Corroborating our hypothesis, a reduction in neuronal  $[Ca^{2+}]_i$  transients, and a relative abnormal neurotransmission, was also noticed in acute models of epileptiform activity *in vitro* on *Sip1* deficient mice [50], and in ischemia-like conditions in hippocampal neurons and astrocytes during oxygen-glucose deprivation/reoxygenation [51]. We noticed that increasing the number of astrocytes, and therefore most probably the amount of  $GABA_A$ Rs, increased the time needed for the drug to block most of these receptors. Hence, gabazine-elicited synchronization was delayed in the co-cultures with higher percentages of astrocytes in the culture, but it led to epileptic-like hyperactivity in all cultures despite the astrocyte numbers.

In our experiments, 4-AP, instead, failed to show any statistically significant increase in SRs or BRs in our cultures. However, our findings indicate that low concentrations (75  $\mu$ M) of 4-AP increases neuronal viability, which supports the previous findings about the neuroprotective effects of 4-AP on different neuronal types [52–56]. Moreover, 4-AP seems to prevent glutamate-induced cell death [56]. We also demonstrated that the co-cultures with higher percentages of astrocytes more effectively counteracted the effect of 4-AP on neuronal activity. This might result from a more extended astrocytic network which includes an elevated number of GJs that contribute to the clearing of accumulating  $K^+$  and  $[Ca^{2+}]_i$ . Furthermore, our results for the 4-AP stimulation are in line with a previous study by Tukker et al. [57]. They showed that rat cortical cultures containing 45% astrocytes and human induced pluripotent stem cell derived co-cultures with 10–15% astrocytes remained relatively unaffected by 100  $\mu$ M 4-AP exposure. They also showed that the 4-AP-induced possible excitability is dependent on the cell source and the proportions of different cell

types in the culture. However, the drug-induced effects vary between the models and depend on the cell seeding density, neuronal maturation (DIV), and the different ratios of inhibitory and excitatory cell types in the cultures [45,57]. In addition, a study by Bradley et al. tested multiple pharmacological agents with rat primary cortical neurons (without added astrocytes) [47]. They demonstrated a rise in neuronal activity in 4-AP-treated NS cultures. Both 100  $\mu\text{M}$  4-AP and 10  $\mu\text{M}$  gabazine treatments caused a decrease in the IBI and an increase in the percentage of spikes in bursts. Although, in our study, 4-AP did not increase the percentage of spikes in bursts. Moreover, one of our studies on a computational neuron–astrocyte network model showed that in heightened hyperactivity, the network with more GJs controlled and downregulated the neuronal activity [58]. A previous study [59] conducted a graph analysis on neuronal cultures with no added astrocytes. The application of 4-AP induced hypersynchronization and increased functional connections. This led to decreased path lengths and increased clustering coefficients.

Astrocytes have been shown to clear  $\text{K}^+$  from the ECS with non-voltage-gated  $\text{K}^+$  channels, e.g., Kir channels,  $\text{Na}^+/\text{K}^+$ -ATPase, and  $\text{Na}^+/\text{K}^+/\text{2Cl}^-$  cotransporters [60]. Furthermore, they uptake the excessive glutamate through glutamate transporters [61]. The cleared  $\text{K}^+$  and glutamate are successfully buffered to distal areas through GJs [3,15,62]. The effect of the blockade of voltage-gated  $\text{K}^+$  channels by 4-AP is assumingly counteracted by the astrocytic  $\text{K}^+$  and glutamate buffering, which leads to statistically insignificant changes in our recorded activity features, such as SRs, BRs, IBIs, and burst durations. Here, we hypothesize that while the extracellular  $\text{K}^+$  and glutamate were increasing due to the effect of 4-AP on the neurons, the astrocytes may have kept clearing the excess  $\text{K}^+$  and glutamate via non-voltage-gated  $\text{K}^+$  channels and glutamate transporters. The protection was more visible in co-cultures with higher numbers of astrocytes, thus presenting a more significant amount of non-voltage-gated  $\text{K}^+$  channels and transporters.

The use of defined neuron–astrocyte co-cultures provides us with a method to assess the role of astrocytes in neuronal networks since combining neurons and varying numbers of astrocytes results in different network structures. In fact, our approach could be used to assess the effects of drugs in various brain regions, as they have distinct amounts of astrocytes [28]; this would provide additional information with more anatomical relevance about brain functions. Moreover, co-cultures, such as those used here, with predetermined neuron–astrocyte ratios and the relative results on the drug-elicited epileptic-like hyperactivity, can be used to study different brain areas' susceptibility to epilepsy. From epileptogenic studies, the hippocampus and the cortex, compared to other brain areas, presented a higher epileptogenic index [63], a parameter that describes the propensity of a brain area to generate rapid discharges. In temporal lobe epilepsy, the most frequently epileptogenic areas are the hippocampus, the amygdala, and the pyriform cortex [64]. A study conducted on African giant rats highlighted how the cortex presents a lower GFAP expression compared to other brain regions such as the cerebellum or the dentate gyrus [65]. Altogether, these studies suggest that brain regions with a lower presence of astrocytes might be more susceptible to seizures. Our results, showing the higher sensitivity of co-cultures with less astrocytes to epilepsy-inducing drugs, are in line with the aforementioned *ex vivo* and *in vivo* studies.

Therefore, our study further elucidates the important role of astrocytes in controlling neuronal activity and homeostasis and it provides new insights into the mechanisms of the action of 4-AP and gabazine on neurons and astrocytes. Our results also highlight the importance of considering different proportions of cells, or at least assessing the share of astrocytes in neuronal cultures in drug testing.

#### 4. Materials and Methods

The cell cultures and performed experiments, described in detail below, are summarized in Table 1, along with the main results.

#### 4.1. MEA and Coverslip Preparation

The day before cell plating, all sterilized MEAs ( $n = 40$ , 8 MEAs per each plating ratio) and 13 mm diameter glass coverslips were coated with Poly-D-Lysine (PDL, 0.1 mg/mL, Sigma-Aldrich, St. Louis, MO, USA) for one hour. MEAs and coverslips were washed three times with ultrapure water, dried, and incubated with laminin (L2020, 20  $\mu\text{g}/\text{mL}$ , Sigma-Aldrich, St. Louis, MO, USA) overnight at  $+4\text{ }^{\circ}\text{C}$ . The following day, laminin was aspirated just before the plating cells. MEAs used in this study (models: 60MEA200/30iR-Ti and -ITO and 60ThinMEA200/30iR-ITO, Multichannel Systems MCS GmbH, Reutlingen, Germany) had 60 microelectrodes with 30  $\mu\text{m}$  diameters and 200  $\mu\text{m}$  interelectrode distances in eight by eight layouts.

#### 4.2. Cell Culture

Rat primary cortical astrocytes (N7745100, Thermo Fisher Scientific, Waltham, MA, USA) were thawed and plated to a cell culture six-well plate (Nunclon; Sigma-Aldrich, St. Louis, MO, USA) at a density of  $20 \times 10^4$  cells/ $\text{cm}^2$ . Astrocytes were cultured for four days (until confluency) in DMEM/F-12 (with HEPES, L-Glutamine) supplemented with a 1% N-2 supplement, 1% Penicillin-Streptomycin (P/S), and 10% fetal bovine serum (all purchased from Thermo Fisher Scientific, Waltham, MA, USA). To prevent further astrocyte DNA replication and proliferation, confluent astrocytes were treated with Cytosine b-D-arabinofuranoside (ara-c, C1768, 2.5  $\mu\text{M}$ , Sigma-Aldrich, St. Louis, MO, USA) for five days, after which they were considered ready for co-culture plating. Cortical astrocytes were also separately plated on coverslips for immunocytochemical analysis (Section 4.3) and on a 24-well plate for live/dead assay after chemical stimulation (Section 4.4) using the same plating density.

Primary rat cortex neurons (A1084001, Thermo Fisher Scientific, Waltham, MA, USA) derived from E18 rat brains were rapidly thawed. Neurons and Ara-C treated astrocytes were separately centrifuged at  $250 \times g$  for 5 min, resuspended in their own media, and counted. The cell count and viability were determined with the trypan blue exclusion assay using the Countess Automated Cell Counter (Thermo Fisher Scientific, Waltham, MA, USA). To achieve different neuron-astrocyte co-culture ratios, the number of neurons was kept constant (80,000 neurons per MEA, 40,000 per coverslip), and the number of astrocytes was adjusted accordingly. The used neuron-astrocyte co-culture ratios were 90/10, 80/20, 70/30, and 50/50 percent (the first number indicates the percentage of neurons, and the second number indicates the percentage of astrocytes). The mixed co-cultures were then recentrifuged before plating. In addition, cultures were prepared with only neurons without separately added astrocytes. These cultures with no separately added astrocytes are referred to as the NS cultures. All used cell cultures for MEAs and coverslips were obtained from a single thaw of cells, i.e., the neuron and astrocyte stocks were from single lots. Neurons and astrocytes were thawed later for 24-h drug treatment characterization (L/D assay and ICC), but these cells had identical lot numbers to the neurons and astrocytes previously plated on MEAs and coverslips.

The NS were plated on coverslips for live/dead assays. In addition, the NS and the co-cultures were plated on the laminin-PDL-coated MEAs and coverslips (for immunocytochemistry (ICC)) in a small drop of medium, which was replenished after cell attachment with either the neuronal medium (NS) or the co-culture medium (co-cultures). The co-culture medium contained neurobasal plus medium with 2% B-12 Plus supplement, 1% P/S, 1% GlutaMAX supplement, and 1% sodium pyruvate. For NS, the same cell culture medium was used without sodium pyruvate and with a 0.25% GlutaMAX supplement. The cell culture medium and all the supplements were purchased from Thermo Fisher Scientific (Waltham, MA, USA). Half the volume of the medium was refreshed every 2–3 days and always after MEA recordings and chemical stimulation. All cell cultures were cultured inside a  $+37\text{ }^{\circ}\text{C}$  incubator in a 5%  $\text{CO}_2$  atmosphere.

#### 4.3. Immunofluorescence and Imaging

Three to four coverslips for each of the co-cultures and the NS were fixed for ICC weekly during the whole culture period and after chemical stimulation (Sections 4.4 and 4.5). Cells were rinsed with phosphate-buffered saline (D-PBS, Thermo Fisher Scientific, Waltham, MA, USA), and were fixed with 3.7% paraformaldehyde in PBS for 20 min at room temperature (RT). Coverslips were then rinsed with PBS and permeabilized with 0.3% Triton X-100 (Sigma-Aldrich, St. Louis, MO, USA) in PBS for 10 min at RT. After permeabilization, cells were blocked with 5% (*v/v*) goat serum (GS, Sigma-Aldrich, St. Louis, MO, USA) in PBS for 120 min at RT and incubated with primary antibodies diluted to 5% (*v/v*) GS-PBS overnight at +4 °C. The primary antibodies used were Microtubule Associated Protein 2 (MAP2, mouse, MAB3418, 1:1000) and Glial Fibrillary Acidic Protein (GFAP, rabbit, AB5804, 1:1000) from Sigma Aldrich (St. Louis, MO, USA). Moreover, GFAP (mouse; MA5-12023, 1:200), S100 $\beta$  (rabbit, PA5-78161, 1:500),  $\beta$ 3-tubulin ( $\beta$ 3tub, mouse, MA1-118, 1:1000), and Vimentin (VIM, chicken, PA1-10003, 1:1000) were used (Thermo Fisher Scientific, Waltham, MA, USA). The next day, coverslips were washed three times with a wash buffer (0.1% Triton X-100 in PBS) and incubated with species-specific Alexa Fluor conjugated secondary antibodies in the dark for one hour at RT. Secondary antibodies were Alexa fluor 488 (anti-mouse, A-11001, 1:500), Alexa fluor 555 (anti-rabbit, A-21428, 1:500), and Alexa fluor 647 (anti-chicken, A32933, 1:500) (all from Thermo Fisher Scientific, Waltham, MA, USA). Coverslips were washed with the wash buffer, after which 1:1000 4',6-diamidino-2-phenylindole (DAPI, 10  $\mu$ g/mL in PBS, Thermo Fisher Scientific, Waltham, MA, USA) was added. After 10 min at RT, the samples were rinsed with PBS, after which coverslips were mounted with a ProLong Gold Antifade Mountant (Thermo Fisher Scientific, Waltham, MA, USA) onto microscope glasses and cured for 24 h in the dark at RT. Coverslips were stored at +4 °C and imaged with an Olympus IX51 Fluorescence Microscope with an Olympus DP30BW camera (Olympus Corporation, Hamburg, Germany). Images were processed using Fiji (ImageJ) software and analyzed with an in-house MATLAB (MathWorks, Inc., Natick, MA, USA) tool (Section 4.7).

#### 4.4. Neuron and Astrocyte Viability

To determine the effect of 4-AP and gabazine on neuron (DIV14) and astrocyte (DIV3) viability, a live/dead Viability/Cytotoxicity Kit (L3224; Thermo Fisher Scientific, Waltham, MA, USA) containing 4  $\mu$ M ethidium homodimer-1 (EthD-1) and 2  $\mu$ M calcein-AM was used according to the manufacturer's instructions. Neurons and astrocytes previously separately plated on 24-well plates and coverslips were chemically stimulated (Section 4.5.) for approximately 24 h. Live/dead imaging of the control and chemically treated cells were captured with a Nikon Eclipse Ti2 (Nikon Instruments, Inc., Melville, NY, USA) fluorescent microscope with an ORCA-Fusion camera (model: C14440-20UP, Hamamatsu Photonics K. K., Hamamatsu City, Japan). The live/dead images were analyzed for cell viability using the particle size-based analysis (modified from [66]). An average of four to six ROIs in total were counted from two to four wells per NS/astrocytes in Fiji software (ImageJ). After chemical stimulation and live/dead assays, neurons and astrocytes on coverslips were fixed for ICC (Section 4.3).

#### 4.5. Chemical Stimulation

At DIV28, the co-cultures and the NS on MEAs were stimulated with 75  $\mu$ M 4-Aminopyridine (4-AP; 0940; Tocris, Bristol, UK) or 30  $\mu$ M SR-95531 hydrobromide (gabazine; 1262; Tocris, Bristol, UK). Before chemical stimulation, the cells on the MEAs were left to settle in the MEA2100-System preamplifier (Section 4.6) for five minutes to alleviate possible effects of mechanical disturbance from moving the MEAs from the incubator to the preamplifier. After that, spontaneous neuronal activity was recorded for five minutes. Subsequently, appropriate volumes of previously prepared stock solutions (4-AP: 10 mM; gabazine: 25 mM; both diluted in ultra-pure water) of the drugs were pipetted directly to the MEA wells to result in the final drug concentrations, and the cell cultures on the MEAs were immediately recorded for ten minutes. Finally, the whole medium reservoir was

replaced with a fresh prewarmed cell medium. The same chemical stimulation replacement was applied on the 24-well plates and coverslips that were stimulated for approximately 24 h inside an incubator (Section 4.4).

#### 4.6. MEA Recordings

The electrical activity of the co-cultures and the NS on the MEAs were recorded weekly using a MEA2100-System and the Multichannel Experimenter software (Multichannel Systems MCS GmbH, Reutlingen, Germany). The cultures on the MEAs were left to settle for five minutes in the MEA preamplifier, after which spontaneous neuronal activity was recorded for five minutes. At DIV28, the co-cultures and NS were also chemically stimulated with 75  $\mu$ M 4-AP or 30  $\mu$ M gabazine, as described in Section 4.5. Right after chemical stimulation, electrical activity was recorded for ten minutes. After the recordings, the whole medium reservoir was replaced with a fresh cell culture medium, and MEAs were put back into the incubator. After 24 h, MEAs were recorded for 5 min after the 5-min settling period. Raw signals were recorded at the sampling rate of 25 kHz and stored on a personal computer. The protocol to study the induction of epileptiform activity in the cultures is presented in Figure 2A.

#### 4.7. Data Analysis

##### 4.7.1. Cell Count

To verify that the relative amounts of neurons and astrocytes in all cultures remained after plating, we counted the cells on the coverslips that we fixed and immunostained with DAPI, MAP2, and GFAP at DIV14 (see Section 4.3). Several ROIs from a coverslip were selected for imaging spanning between the center of the culture and the less populated borders. To count the cells, we developed a semi-automated tool in MATLAB (MathWorks, Inc., Natick, MA, USA). The tool creates segmented black/white (BW) masks of the DAPI-stained nuclei of both cell types. Then, it selects the intensity peaks in the image and removes as debris all continuous regions with radiuses smaller than a predefined radius around the intensity peak. This method also separates the cells grouped in clusters. Thereafter, the revised nuclei are counted.

Then, the mask indicating the nuclei was merged with the mask created from the corresponding MAP2 image, indicating the neurons and their nuclei; if more than a predefined fraction of the nucleus border was contained within the MAP2 mask, the nucleus was considered to belong to a neuron. The threshold was chosen based on the image brightness and visual control to maximize the neuronal detection and minimize the false classification. All the nuclei that were not counted as neuronal were then merged with the GFAP-stained BW mask of the astrocytes. If the still non-categorized nuclei borders were contained in the GFAP mask, whose threshold selection was similar to the one for the MAP2 mask, the cells were counted as astrocytes.

##### 4.7.2. Spiking and Bursting Analysis

The raw MEA signals were filtered, neuronal action potentials detected, and spike waveform cut-outs were sorted with a widely used tool, Wave Clus for MATLAB [67]. The signal was filtered with a second-order bandpass (300–3000 Hz) elliptic filter to retain only the action potential peaks for further analysis. Positive and negative spikes were detected with a threshold of  $\pm 5\sigma$ , where  $\sigma = \text{median}(|x|)/0.6745$  and  $x$  is the bandpass filtered signal. The detector dead time was 1.5 ms after each spike.

The timestamps of the spikes obtained from the sorted signals were then further analyzed with a MATLAB tool developed in our group [68]. The tool uses a cumulative moving average-based algorithm [69] further adapted to calculate and unify the burst detection parameters for the whole network [68]. This method is able to overcome the intrinsic differences between networks leading to a more reliable comparison between the bursting activities.

From the timestamps, we analyzed the SRs (spikes per minute), BRs (bursts per minute), percentages of spikes contained in bursts (spikes in bursts/total spikes), and inter-burst intervals (IBIs) (time in milliseconds from the end of a burst to the start of the subsequent burst). All the above parameters were evaluated for each channel of a MEA and then averaged over the chip. The reported median in the box plots, instead, should be considered as a ratio.

To better visualize the effects of the used drugs on the network activities, we also calculated the fold change of the SRs and BRs. The values before and after stimulation were compared separately for each MEA by dividing the value after stimulation with the respective value at the baseline. We also evaluated the fold change for the baseline conditions by comparing each MEA-specific value to their respective average.

#### 4.7.3. Network Synchronicity by Channel Inter-Correlation Analysis

To evaluate the synchronicity in a network, we used a MATLAB tool called CorSE that analyses the correlations of time-varying spectral entropies between MEA channels [70]. From the tool, we extracted the pairwise inter-channel correlations and connections. Since the correlation is calculated for the channel spectral entropies at lag zero, a high correlation weight corresponds to high synchronization between the networks in the vicinities of the microelectrodes considered. We then analyzed the differences in the weights of the connections between the measurements from the chemically stimulated cultures and their respective baseline measurements for each channel pair. For this specific case, all the correlation weights of each channel pair of each MEA are reported in the results and were not averaged for each MEA.

#### 4.7.4. Network Synchronicity by Binned Activity Analysis

In addition to CorSE, network synchronicity was also assessed based on the spiking activity. We first binned the detected spikes (1 = when a spike was present, 0 = otherwise) that were non-overlapping into 5 ms bins for each MEA channel. After that, we summed the bin values across all MEA channels per bin. Then, we counted all the local maxima of the summed time series. The higher peaks in our summed time series corresponded with spikes and bursts occurring in the same time bin and spanning a larger network. In order to be sure to count the bursts from the summed signal only once, we counted only the peaks separated by at least the minimum IBI found in the MEA from the previous burst analysis. This passage assures us not to count the summed peaks in the same bursts repeatedly. After that, we counted all the remaining detected peaks that spanned more than ten channels, and we defined these as network bursts (NBs).

#### 4.7.5. Delay in the Response Times of the Convulsants

To evaluate the different delays in response times from the 4-AP and gabazine application to detectable responses, we developed an algorithm that is explained below to detect the first burst before the detectable change in bursting pattern. The response of the network to the gabazine exposure produced a visible, highly precise bursting series spanning across the network. Moreover, we visually noticed that the last NBs spanned over half of the electrodes in our cultures and that at the end of the recordings, all our cultures chemically stimulated with gabazine changed their bursting patterns. To assess the differences in the bursting activity before and after detectable drug responses (convulsant-induced bursting), we calculated the mean IBI (*meanIBI*) and the standard deviation of the IBIs (*stdIBI*) of the last 20 NBs in the recording. The choice of the last 20 NBs was made to be sure that the drug would have had time to produce effects on the activity. If there were less than 20 NBs in the recording, the MEAs were discarded for the present analysis. We obtained the normal distribution of the IBIs based on the *meanIBI* and the *stdIBI*. Then, we analyzed

the IBIs between the sequential NBs spanning over more than 20 channels. To find the bursts in the repetitive burst series, we used the following rule:

$$\begin{cases} |IBI_i(j) - \text{mean}IBI_i| < \text{std}IBI_i, & NB_i(j) \in \text{repetitive series} \\ |IBI_i(j) - \text{mean}IBI_i| > \text{std}IBI_i, & NB_i(j) \notin \text{repetitive series} \end{cases} \quad (1)$$

where  $i$  is MEA index,  $j$  is the NB index, and  $\text{std}IBI_i$  is the standard deviation of the last 20 IBIs of the MEA recording. If the absolute value of the differences between the IBI of an NB and the mean IBI of the corresponding MEA was smaller than  $\text{std}IBI_i$ , then the NB belonged to the repetitive burst series; otherwise, it did not belong to it. A graphical representation of the selection rule used is shown in Figure 5C.

To finally evaluate the duration it took for the convulsant to show its effects on the neuronal activity, we analyzed the time difference from the convulsant application time point to the time point at which the first burst of the repetitive series occurred and called the time difference a delay.

#### 4.7.6. Statistical Analysis

The raw MEA data were analyzed using MATLAB (v. 2020b), whereas the timestamps and the results were analyzed with SPSS Statistics software (IBM SPSS Statistics for Windows, Version 26.0. Armonk, NY: IBM Corp.), GraphPad Prism software (v. 9) (GraphPad Software, San Diego CA, USA), and MATLAB (v. 2020b). Due to the non-normal distribution of the data, the Mann–Whitney U test or the Wilcoxon rank sum test was used to evaluate differences between culture groups. A  $p$ -Value under 0.05 was considered significant. Since statistical tests are often affected by large datasets, and thus the  $p$ -Value quickly tended towards zero even for small differences in the distributions [71], we complemented the significance tests with an effect size analysis [72]. As an effect size measure, we used the Glass's delta [73] for the comparison between two groups.

In our analysis, the correlation weights at baseline have been used as control. The Glass's delta value should be interpreted as how many standard deviations the mean value of the chemically stimulated weights is larger than the control mean value; values above 0.8 are normally considered as a large effect size, between 0.2 and 0.8 as a medium effect size, and smaller than 0.2 as a small effect size [74]. The sign of delta indicates which of the two means is higher: a positive value indicates that the mean of the chemically stimulated group is higher than the control, and a negative Glass's delta means that the mean of the control group is higher. To compute the Glass's delta, we used the MATLAB toolbox that was made available [75].

## 5. Conclusions

In this study, we aimed to investigate how astrocytes may play a role in the regulation of neuronal activity during drug-induced epileptiform behavior. To do so, we compared the responses of neuron–astrocyte co-cultures with predetermined numbers of neurons and different numbers of astrocytes. We chemically stimulated the co-cultures with 4-AP or gabazine to assess the control of the astrocytes on neuronal behavior. The cultures were plated on MEAs to record the extracellular neuronal electrical activity. This is the first study investigating the effects with respect to different neuron–astrocyte ratios in co-cultures on MEAs and the first study to characterize the effects of 4-AP and gabazine on neuronal networks.

Our results showed that astrocytes effectively counteracted 4-AP-induced epileptic-like activity; in fact, no visible changes in the neuronal activity were noticeable after blocking the voltage-gated  $K^+$  channels by applying 4-AP. This effect was more detectable when we increased the number of astrocytes, which led to a lower spike rate than at baseline.

On the other hand, the astrocytes did not fully counteract the effect of gabazine, a  $GABA_A$  receptor ( $GABA_A R$ ) blocker. The neuronal activity increased and became synchronized due to gabazine in all cultures. However, this gabazine-induced synchronization was induced with a delay that noticeably extended with the increase of the number of astrocytes

in the co-cultures. Thus, the effects of the GABA<sub>A</sub>R blockade were directly connected to the number of astrocytes in the culture, the relative number of GABA<sub>A</sub>Rs, and the extent of the astrocytic network.

Our results further confirm that the astrocyte number in neuronal cultures affects neuronal network maturation and thus functions by enhancing the early development of the neuronal electrical activity. This, together with the astrocyte control of homeostasis, alters the responsiveness of the neurons to the pharmacological agents.

Our study highlights the significant regulatory role of astrocytes on neuron functionality in the brain and the importance of an in detail consideration of the ratio of astrocytes in neuronal cultures exposed to chemical stimulation. Brain regions exhibit inhomogeneous neuron–astrocyte ratios, and this different cellular distribution may reflect differences in epileptic seizure susceptibility. Hence, it is crucial to explore the impact of the drugs in co-cultures with different cellular ratios, as was done in this paper.

**Supplementary Materials:** The following are available online at <https://www.mdpi.com/article/10.3390/ijms222312770/s1>.

**Author Contributions:** Conceptualization, A.A., B.G., J.A.K.H. and K.L.; methodology, A.A. and B.G.; software, B.G.; validation, A.A. and B.G.; formal analysis, A.A. and B.G.; investigation, A.A. and B.G.; data curation, A.A. and B.G.; writing—original draft preparation, A.A. and B.G.; writing—review & editing, A.A., B.G., M.T.B., J.M.A.T., J.A.K.H. and K.L.; visualization, A.A. and B.G. All authors have read and agreed to the published version of the manuscript.

**Funding:** The works of A.A. and J.M.A.T. have been supported by funding from the European Union’s Horizon 2020 Research and Innovation Programme under grant agreement No. 824164, project “Hybrid Enhanced Regenerative Medicine Systems”. The work of B.G. and M.T.B. is funded by the European Union’s Horizon 2020 Research and Innovation Programme under the Marie Skłodowska-Curie grant agreement No. 713645 and No. 839553, respectively. K.L. was funded by the Academy of Finland (decision nos. 314647, 326452).

**Institutional Review Board Statement:** Not applicable.

**Data Availability Statement:** The code for the burst analysis is available at: The code for the correlated spectral entropy analysis (CorSE) is available in Matlab Central at: <https://www.mathworks.com/matlabcentral/fileexchange/59626-spectral-entropy-based-neuronal-network-synchronization-analysis-corse>, (accessed on 24 November 2021).

**Acknowledgments:** The authors acknowledge the Faculty of Medicine and Health Technology, Tampere University, and especially the Tampere Imaging Facility for their services.

**Conflicts of Interest:** The authors declare no conflict of interest.

## References

1. Takeuchi, H.; Suzumura, A. Gap junctions and hemichannels composed of connexins: Potential therapeutic targets for neurodegenerative diseases. *Front. Cell. Neurosci.* **2014**, *8*, 189. [CrossRef]
2. Araque, A.; Parpura, V.; Sanzgiri, R.P.; Haydon, P.G. Tripartite synapses: Glia, the unacknowledged partner. *Trends Neurosci.* **1999**, *22*, 208–215. [CrossRef]
3. Mayorquin, L.C.; Rodriguez, A.V.; Sutachan, J.-J.; Albarracín, S.L. Connexin-Mediated Functional and Metabolic Coupling Between Astrocytes and Neurons. *Front. Mol. Neurosci.* **2018**, *11*, 118. [CrossRef]
4. Verkhratsky, A.; Nedergaard, M. Physiology of Astroglia. *Physiol. Rev.* **2018**, *98*, 239–389. [CrossRef]
5. Bazargani, N.; Attwell, D. Astrocyte calcium signaling: The third wave. *Nat. Neurosci.* **2016**, *19*, 182–189. [CrossRef] [PubMed]
6. Fraser, D.D.; Mudrick-Donnon, L.A.; MacVicar, B. Astrocytic GABA receptors. *Glia* **1994**, *11*, 83–93. [CrossRef] [PubMed]
7. Boddum, K.; Jensen, T.; Magloire, V.; Kristiansen, U.; Rusakov, D.A.; Pavlov, I.; Walker, M.C. Astrocytic GABA transporter activity modulates excitatory neurotransmission. *Nat. Commun.* **2016**, *7*, 13572. [CrossRef]
8. Meier, S.D.; Kafitz, K.W.; Rose, C.R. Developmental profile and mechanisms of GABA-induced calcium signaling in hippocampal astrocytes. *Glia* **2008**, *56*, 1127–1137. [CrossRef]
9. Doengi, M.; Hirnet, D.; Coulon, P.; Pape, H.-C.; Deitmer, J.W.; Lohr, C. GABA uptake-dependent Ca<sup>2+</sup> signaling in developing olfactory bulb astrocytes. *Proc. Natl. Acad. Sci. USA* **2009**, *106*, 17570–17575. [CrossRef]
10. Mederos, S.; González-Arias, C.; Perea, G. Astrocyte–Neuron Networks: A Multilane Highway of Signaling for Homeostatic Brain Function. *Front. Synaptic Neurosci.* **2018**, *10*, 45. [CrossRef] [PubMed]



11. Le Meur, K.; Mendizabal-Zubiaga, J.; Grandes, P.; Audinat, E. GABA release by hippocampal astrocytes. *Front. Comput. Neurosci.* **2012**, *6*, 59. [CrossRef]
12. Rose, C.R.; Felix, L.; Zeug, A.; Dietrich, D.; Reiner, A.; Henneberger, C. Astroglial Glutamate Signaling and Uptake in the Hippocampus. *Front. Mol. Neurosci.* **2018**, *10*, 451. [CrossRef]
13. Lee, S.; Yoon, B.-E.; Berglund, K.; Oh, S.-J.; Park, H.; Shin, H.-S.; Augustine, G.J.; Lee, C.J. Channel-Mediated Tonic GABA Release from Glia. *Science* **2010**, *330*, 790–796. [CrossRef]
14. Dossi, E.; Vasile, F.; Rouach, N. Human astrocytes in the diseased brain. *Brain Res. Bull.* **2018**, *136*, 139–156. [CrossRef]
15. Bedner, P.; Steinhäuser, C. Altered Kir and gap junction channels in temporal lobe epilepsy. *Neurochem. Int.* **2013**, *63*, 682–687. [CrossRef] [PubMed]
16. Steinhäuser, C.; Grunnet, M.; Carmignoto, G. Crucial role of astrocytes in temporal lobe epilepsy. *Neuroscience* **2016**, *323*, 157–169. [CrossRef] [PubMed]
17. Walrave, L.; Vinken, M.; Leybaert, L.; Smolders, I. Astrocytic Connexin43 Channels as Candidate Targets in Epilepsy Treatment. *Biomolecules* **2020**, *10*, 1578. [CrossRef] [PubMed]
18. Shneker, B.F.; Fountain, N.B. Epilepsy. *Dis. Mon.* **2003**, *49*, 426–478. [CrossRef]
19. Bhalla, D.; Godet, B.; Druet-Cabanac, M.; Preux, P.-M. Etiologies of epilepsy: A comprehensive review. *Expert Rev. Neurother.* **2011**, *11*, 861–876. [CrossRef]
20. Ono, T.; Galanopoulou, A.S. Epilepsy and Epileptic Syndrome. In *Neurodegenerative Diseases*; Ahmad, S.I., Ed.; Advances in Experimental Medicine and Biology; Springer: New York, NY, USA, 2012; Volume 724, pp. 99–113. ISBN 978-1-4614-0652-5.
21. Blank, L.J.; Acton, E.K.; Thibault, D.; Willis, A.W. Neurodegenerative disease is associated with increased incidence of epilepsy: A population based study of older adults. *Age Ageing* **2021**, *50*, 205–212. [CrossRef] [PubMed]
22. Müller, J.; Timmermann, A.; Henning, L.; Müller, H.; Steinhäuser, C.; Bedner, P. Astrocytic GABA Accumulation in Experimental Temporal Lobe Epilepsy. *Front. Neurol.* **2020**, *11*, 614923. [CrossRef]
23. Tanskanen, J.M.; Ahtiainen, A.; Hyttinen, J.A. Toward Closed-Loop Electrical Stimulation of Neuronal Systems: A Review. *Bioelectricity* **2020**, *2*, 328–347. [CrossRef]
24. Keller, J.M.; Frega, M. Past, Present, and Future of Neuronal Models In Vitro. In *In Vitro Neuronal Networks*; Chiappalone, M., Pasquale, V., Frega, M., Eds.; Advances in Neurobiology; Springer International Publishing: Cham, Switzerland, 2019; Volume 22, pp. 3–17. ISBN 978-3-030-11134-2.
25. Thomas, C.A., Jr.; Springer, P.A.; Loeb, G.E.; Berwald-Netter, Y.; Okun, L.M. A miniature microelectrode array to monitor the bioelectric activity of cultured cells. *Exp. Cell Res.* **1972**, *74*, 61–66. [CrossRef]
26. Ylä-Outinen, L.; Tanskanen, J.M.A.; Kapucu, F.E.; Hyysalo, A.; Hyttinen, J.A.K.; Narkilahti, S. Advances in Human Stem Cell-Derived Neuronal Cell Culturing and Analysis. In *In Vitro Neuronal Networks*; Chiappalone, M., Pasquale, V., Frega, M., Eds.; Advances in Neurobiology; Springer International Publishing: Cham, Switzerland, 2019; Volume 22, pp. 299–329. [CrossRef]
27. Herculano-Houzel, S. The glia/neuron ratio: How it varies uniformly across brain structures and species and what that means for brain physiology and evolution. *Glia* **2014**, *62*, 1377–1391. [CrossRef] [PubMed]
28. Von Bartheld, C.S.; Bahney, J.; Herculano-Houzel, S. The search for true numbers of neurons and glial cells in the human brain: A review of 150 years of cell counting: Quantifying Neurons and Glia in Human Brain. *J. Comp. Neurol.* **2016**, *524*, 3865–3895. [CrossRef] [PubMed]
29. Enright, H.A.; Lam, D.; Sebastian, A.; Sales, A.P.; Cadena, J.; Hum, N.R.; Osburn, J.J.; Peters, S.K.G.; Petkus, B.; Soccia, D.A.; et al. Functional and transcriptional characterization of complex neuronal co-cultures. *Sci. Rep.* **2020**, *10*, 11007. [CrossRef] [PubMed]
30. Odawara, A.; Matsuda, N.; Ishibashi, Y.; Yokoi, R.; Suzuki, I. Toxicological evaluation of convulsant and anticonvulsant drugs in human induced pluripotent stem cell-derived cortical neuronal networks using an MEA system. *Sci. Rep.* **2018**, *8*, 10416. [CrossRef]
31. Aebersold, M.J.; Thompson-Steckel, G.; Joutang, A.; Schneider, M.; Burchert, C.; Forró, C.; Weydert, S.; Han, H.; Vörös, J. Simple and Inexpensive Paper-Based Astrocyte Co-culture to Improve Survival of Low-Density Neuronal Networks. *Front. Neurosci.* **2018**, *12*, 94. [CrossRef] [PubMed]
32. Myers, T.L.; González, O.; Stein, J.B.; Bazhenov, M. Characterizing Concentration-Dependent Neural Dynamics of 4-Aminopyridine-Induced Epileptiform Activity. *Epilepsy J.* **2018**, *4*, 128. [CrossRef]
33. Žiburkus, J.; Cressman, J.R.; Schiff, S.J. Seizures as imbalanced up states: Excitatory and inhibitory conductances during seizure-like events. *J. Neurophysiol.* **2013**, *109*, 1296–1306. [CrossRef]
34. Amakhin, D.; Soboleva, E.; Ergina, J.L.; Malkin, S.; Chizhov, A.; Zaitsev, A.V. Seizure-Induced Potentiation of AMPA Receptor-Mediated Synaptic Transmission in the Entorhinal Cortex. *Front. Cell. Neurosci.* **2018**, *12*, 486. [CrossRef] [PubMed]
35. Kasatkina, L.A. 4-Aminopyridine sequesters intracellular Ca<sup>2+</sup> which triggers exocytosis in excitable and non-excitable cells. *Sci. Rep.* **2016**, *6*, 34749. [CrossRef] [PubMed]
36. Hongo, Y.; Takasu, K.; Ikegaya, Y.; Hasegawa, M.; Sakaguchi, G.; Ogawa, K. Heterogeneous effects of antiepileptic drugs in an in vitro epilepsy model—A functional multineuron calcium imaging study. *Eur. J. Neurosci.* **2015**, *42*, 1818–1829. [CrossRef] [PubMed]
37. Pacico, N.; Mingorance-Le Meur, A. New In Vitro Phenotypic Assay for Epilepsy: Fluorescent Measurement of Synchronized Neuronal Calcium Oscillations. *PLoS ONE* **2014**, *9*, e84755. [CrossRef]

38. Wu, Z.-Z.; Li, D.-P.; Chen, S.-R.; Pan, H.-L. Aminopyridines Potentiate Synaptic and Neuromuscular Transmission by Targeting the Voltage-activated Calcium Channel  $\beta$  Subunit. *J. Biol. Chem.* **2009**, *284*, 36453–36461. [CrossRef]
39. Hyvärinen, T.; Hyysalo, A.; Kapucu, F.E.; Aarnos, L.; Vinogradov, A.; Eglen, S.J.; Ylä-Outinen, L.; Narkilahti, S. Functional characterization of human pluripotent stem cell-derived cortical networks differentiated on laminin-521 substrate: Comparison to rat cortical cultures. *Sci. Rep.* **2019**, *9*, 17125. [CrossRef]
40. Shmoel, N.; Rabieh, N.; Ojovan, S.M.; Erez, H.; Maydan, E.; Spira, M.E. Multisite electrophysiological recordings by self-assembled loose-patch-like junctions between cultured hippocampal neurons and mushroom-shaped microelectrodes. *Sci. Rep.* **2016**, *6*, 27110. [CrossRef]
41. Behrens, M.M.; Ali, S.S.; Dao, D.N.; Lucero, J.; Shekhtman, G.; Quick, K.L.; Dugan, L.L. Ketamine-Induced Loss of Phenotype of Fast-Spiking Interneurons Is Mediated by NADPH-Oxidase. *Science* **2007**, *318*, 1645–1647. [CrossRef]
42. Ueno, S.; Bracamontes, J.; Zorumski, C.; Weiss, D.S.; Steinbach, J.H. Bicuculline and Gabazine Are Allosteric Inhibitors of Channel Opening of the GABA<sub>A</sub> Receptor. *J. Neurosci.* **1997**, *17*, 625–634. [CrossRef]
43. Lee, V.; Maguire, J. The impact of tonic GABA<sub>A</sub> receptor-mediated inhibition on neuronal excitability varies across brain region and cell type. *Front. Neural Circuits* **2014**, *8*, 3. [CrossRef]
44. Farhy-Tselnicker, I.; Allen, N.J. Astrocytes, neurons, synapses: A tripartite view on cortical circuit development. *Neural Dev.* **2018**, *13*, 7. [CrossRef] [PubMed]
45. Grainger, A.I.; King, M.C.; Nagel, D.A.; Parri, H.R.; Coleman, M.D.; Hill, E. In vitro Models for Seizure-Liability Testing Using Induced Pluripotent Stem Cells. *Front. Neurosci.* **2018**, *12*, 590. [CrossRef] [PubMed]
46. Sokal, D.M.; Mason, R.; Parker, T.L. Multi-neuronal recordings reveal a differential effect of thapsigargin on bicuculline- or gabazine-induced epileptiform excitability in rat hippocampal neuronal networks. *Neuropharmacology* **2000**, *39*, 2408–2417. [CrossRef]
47. Bradley, J.A.; Luithardt, H.H.; Metea, M.R.; Strock, C.J. In Vitro Screening for Seizure Liability Using Microelectrode Array Technology. *Toxicol. Sci.* **2018**, *163*, 240–253. [CrossRef]
48. Young, S.Z.; Platel, J.-C.; Nielsen, J.V.; Jensen, N.A.; Bordey, A. GABA<sub>A</sub> increases calcium in subventricular zone astrocyte-like cells through L- and T-type voltage-gated calcium channels. *Front. Cell. Neurosci.* **2010**, *4*, 8. [CrossRef]
49. Halassa, M.M.; Fellin, T.; Haydon, P.G. The tripartite synapse: Roles for gliotransmission in health and disease. *Trends Mol. Med.* **2007**, *13*, 54–63. [CrossRef]
50. Turovskaya, M.V.; Epifanova, E.A.; Tarabykin, V.S.; Babaev, A.A.; Turovsky, E.A. Interleukin-10 restores glutamate receptor-mediated Ca<sup>2+</sup>-signaling in brain circuits under loss of *Sip1* transcription factor. *Int. J. Neurosci.* **2020**, 1–12. [CrossRef]
51. Turovsky, E.A.; Varlamova, E.G.; Plotnikov, E.Y. Mechanisms Underlying the Protective Effect of the Peroxiredoxin-6 Are Mediated via the Protection of Astrocytes during Ischemia/Reoxygenation. *Int. J. Mol. Sci.* **2021**, *22*, 8805. [CrossRef]
52. Dietrich, M.; Hartung, H.-P.; Albrecht, P. Neuroprotective Properties of 4-Aminopyridine. *Neurol. Neuroimmunol. Neuroinflamm.* **2021**, *8*, e976. [CrossRef]
53. Hu, D.; Liu, J.; Keblesh, J.; Xiong, H. Involvement of the 4-aminopyridine-sensitive transient A-type K<sup>+</sup> current in macrophage-induced neuronal injury. *Eur. J. Neurosci.* **2010**, *31*, 214–222. [CrossRef]
54. Smith, A.J.; Tauskela, J.S.; Stone, T.W.; Smith, R.A. Preconditioning with 4-aminopyridine protects cerebellar granule neurons against excitotoxicity. *Brain Res.* **2009**, *1294*, 165–175. [CrossRef] [PubMed]
55. Hu, C.; Liu, Z.; Liu, Z.-Q.; Zeng, X.-M.; Chen, X.-H.; Zhang, Z.-H.; Mei, Y.-A. 4-Aminopyridine, a Kv channel antagonist, prevents apoptosis of rat cerebellar granule neurons. *Neuropharmacology* **2006**, *51*, 737–746. [CrossRef] [PubMed]
56. Zhao, Y.-M.; Sun, L.-N.; Zhou, H.-Y.; Wang, X.-L. Voltage-dependent potassium channels are involved in glutamate-induced apoptosis of rat hippocampal neurons. *Neurosci. Lett.* **2006**, *398*, 22–27. [CrossRef] [PubMed]
57. Tukker, A.M.; Van Kleef, R.G.D.M.; Wijnolts, F.M.J.; De Groot, A.; Westerink, R.H.S. Towards animal-free neurotoxicity screening: Applicability of hiPSC-derived neuronal models for in vitro seizure liability assessment. *ALTEX* **2020**, *37*, 121–135. [CrossRef] [PubMed]
58. Genocchi, B.; Lenk, K.; Hyttinen, J. Influence of Astrocytic Gap Junction Coupling on in Silico Neuronal Network Activity. In *XV Mediterranean Conference on Medical and Biological Engineering and Computing—MEDICON 2019*; Henriques, J., Neves, N., de Carvalho, P., Eds.; IFMBE Proceedings; Springer International Publishing: Cham, Switzerland, 2020; Volume 76, pp. 480–487. ISBN 978-3-030-31634-1.
59. Vincent, K.; Tauskela, J.S.; Mealing, G.A.; Thivierge, J.-P. Altered Network Communication Following a Neuroprotective Drug Treatment. *PLoS ONE* **2013**, *8*, e54478. [CrossRef]
60. Murakami, S.; Kurachi, Y. Mechanisms of astrocytic K<sup>+</sup> clearance and swelling under high extracellular K<sup>+</sup> concentrations. *J. Physiol. Sci.* **2016**, *66*, 127–142. [CrossRef]
61. Mahmoud, S.; Gharagozloo, M.; Simard, C.; Gris, D. Astrocytes Maintain Glutamate Homeostasis in the CNS by Controlling the Balance between Glutamate Uptake and Release. *Cells* **2019**, *8*, 184. [CrossRef]
62. Bellot-Saez, A.; Stevenson, R.; Kékesi, O.; Samokhina, E.; Ben-Abu, Y.; Morley, J.; Buskila, Y. Neuromodulation of Astrocytic K<sup>+</sup> Clearance. *Int. J. Mol. Sci.* **2021**, *22*, 2520. [CrossRef]
63. Bartolomei, F.; Chauvel, P.; Wendling, F. Epileptogenicity of brain structures in human temporal lobe epilepsy: A quantified study from intracerebral EEG. *Brain* **2008**, *131*, 1818–1830. [CrossRef]

64. Aroniadou-Anderjaska, V.; Fritsch, B.; Qashu, F.; Braga, M.F. Pathology and pathophysiology of the amygdala in epileptogenesis and epilepsy. *Epilepsy Res.* **2008**, *78*, 102–116. [CrossRef]
65. Olude, M.A.; Mustapha, O.A.; Aderounmu, O.A.; Olopade, J.O.; Ihunwo, A.O. Astrocyte morphology, heterogeneity, and density in the developing African giant rat (*Cricetomys gambianus*). *Front. Neuroanat.* **2015**, *9*, 67. [CrossRef] [PubMed]
66. Allevi Protocols. Live/Dead Quantification Using Fiji—Step-by-Step Guide. Available online: <https://www.allevi3d.com/livedead-assay-quantification-fiji/> (accessed on 24 September 2021).
67. Chaure, F.; Rey, H.; Quiroga, R.Q. A novel and fully automatic spike-sorting implementation with variable number of features. *J. Neurophysiol.* **2018**, *120*, 1859–1871. [CrossRef] [PubMed]
68. Väلكki, I.A.; Lenk, K.; Mikkonen, J.E.; Kapucu, F.E.; Hyttinen, J.A.K. Network-Wide Adaptive Burst Detection Depicts Neuronal Activity with Improved Accuracy. *Front. Comput. Neurosci.* **2017**, *11*, 40. [CrossRef] [PubMed]
69. Kapucu, F.E.; Tanskanen, J.M.A.; Mikkonen, J.E.; Ylä-Outinen, L.; Narkilahti, S.; Hyttinen, J.A.K. Burst analysis tool for developing neuronal networks exhibiting highly varying action potential dynamics. *Front. Comput. Neurosci.* **2012**, *6*, 38. [CrossRef] [PubMed]
70. Kapucu, F.E.; Väلكki, I.; Mikkonen, J.E.; Leone, C.; Lenk, K.; Tanskanen, J.; Hyttinen, J. Spectral Entropy Based Neuronal Network Synchronization Analysis Based on Microelectrode Array Measurements. *Front. Comput. Neurosci.* **2016**, *10*, 112. [CrossRef] [PubMed]
71. Fagerland, M.W. T-tests, non-parametric tests, and large studies—a paradox of statistical practice? *BMC Med. Res. Methodol.* **2012**, *12*, 78. [CrossRef] [PubMed]
72. Lin, M.; Lucas, H.C.; Shmueli, G. Research Commentary—Too Big to Fail: Large Samples and the p-Value Problem. *Inf. Syst. Res.* **2013**, *24*, 906–917. [CrossRef]
73. Smith, M.L.; Glass, G.V. Meta-analysis of psychotherapy outcome studies. *Am. Psychol.* **1977**, *32*, 752–760. [CrossRef]
74. Lakens, D. Calculating and reporting effect sizes to facilitate cumulative science: A practical primer for *t*-tests and ANOVAs. *Front. Psychol.* **2013**, *4*, 863. [CrossRef]
75. Hentschke, H.; Stüttgen, M.C. Computation of measures of effect size for neuroscience data sets. *Eur. J. Neurosci.* **2011**, *34*, 1887–1894. [CrossRef]

# PUBLICATION

## V

**Astrocytes induce desynchronization and reduce predictability in  
neuron-astrocyte networks cultured on microelectrode arrays**

**Genocchi, B., Ahtiainen, A., Niemi, A., Barros, M. T., Tanskanen, J. M.,  
Lenk, K., Hyttinen, J., and Subramaniam, N. P.**

*Submitted*

**Publication reprinted with the permission of the copyright holders.**



